Models and methods extending the composite fermion theory

A thesis submitted in partial fulfillment of the requirement for the degree of
Doctor of Philosophy
by

Abhishek Anand
Reg. ID : 20183620

Indian Institute of Science Education and Research,
Pune
October 31, 2023

To my family

CERTIFICATE

It is certified that the work documented in the thesis titled "**Models and methods extending the composite fermion theory**" submitted by **Abhishek Anand** was carried out by the candidate under my supervision. The work presented here has not been included in any other thesis submitted previously for the award of any degree or diploma from any other university or institution.

Supervisor:

Sreejith

Date: April 13, 2023 Sreejith G J

DECLARATION

I, **Abhishek Anand**, declare that the written submission titled "**Models and methods extending the composite fermion theory**" contains my ideas which are presented in my own words. Wherever ideas by others are used, I have made sure that the original sources are adequately cited. I also declare that I have adhered to all principles of academic integrity and not misrepresented, fabricated or falsified any idea/data/source in the submission. I understand that violation of the above will be a cause for disciplinary action by the institute or a penal action from the sources whose work has not been properly cited or has been presented without proper permissions. The work reported in this thesis was performed under the guidance of Dr. Sreejith G J.

Abhishek Anand

Abhishek Anand
Reg. ID : 20183620
Date : October 31, 2023

Acknowledgments

The work presented in this thesis began at IISER Pune under the supervision of Dr. Sreejith GJ. I thank him for guiding me through the years of my PhD. His encouragement and constructive criticism have always led me toward a better direction. I am also thankful for allowing me to work in the quantum Hall effect, a field that exposed me to a good mixture of analytical and numerical methods. Our discussions made learning many interesting computational techniques easy, which I immensely enjoyed.

I thank Jainendra K Jain for all the insightful discussions and encouragement during our collaborative work and Rushikesh A Patil for working out the cumbersome algebra of edge currents, leading to a fascinating joint project. Fabien Alet's suggestion to use PETSc for exact diagonalization proved pivotal in studying the model interaction's spectra. Sunil Mukhi's insights on affine Lie algebra have helped us a lot. I thank Ajit C Balram for lending his expertise on parton states. Discussions on the details of torus geometry with Songyang Pu have benefited me a lot. I thank Aditya for all the helpful discussions on his DMRG calculation on cylinder geometry and Mohd Ali for helping me with concepts in affine Lie algebra. All high-performance computations were performed on the PARAM Brahma supercomputing facility made accessible through the National Supercomputing Mission. I want to thank Nisha Kurkure, S. Suresh Kumar, and Naveen N. from the IT department for their constant support in streamlining the computational facilities. I also thank my research advisory committee members, Rejish Nath and Sourin Das, for their constructive comments.

Finally, I would like to thank my family and friends, who were always there behind the curtain, keeping me grounded. I am grateful to Naveen and Sandeep, whose help and company made me feel welcome in the group. I want to mention Pragya, Habeeb, Arnab, Saurabh, and Mayank, whose friendship I will cherish for years. Words fail to convey my gratitude to Keerti and Priti for constantly reminding me that there is always a silver lining. Finally, I wish all the best to Sandipan and Ojasvi, whose childlike enthusiasm never fails to motivate me.

The work was supported by CSIR-JRF fellowship.

Abhishek Anand

Abstract

This thesis attempts to abstract and generalize some key features of the composite fermion (CF) wavefunctions. CF theory successfully explains the experimentally observed fractional quantum Hall effect (FQHE) in the lowest Landau level. We present a short-range strongly interacting model for 2D electron gas in a magnetic field. The model is exactly solvable on the disk, and the eigenstates abstract several key features of the CF wavefunctions. Exact diagonalization of the interaction shows that it produces FQHE at the Jain sequence of filling fractions. Unlike parent Hamiltonians for Laughlin, Moore Read, Read Rezayi, and projected 2/5 states, the model allows exact solutions for all charged excitations, neutral modes, and incompressible states. The model interaction can be extended to other geometries, and the low-energy spectrum shows the same qualitative features you see in the disk. However, the disk eigenfunctions do not generalize to compact geometries like the sphere and torus. Eigenfunctions in these geometries can nevertheless be written for QPs of $1/m$ state.

In the second half, we study the properties of a generalization of CF states, namely parton states. Parton states are seen as a candidate for many non-Abelian filling fractions in FQHE, which require multiple Landau levels. Specifically, we study the real space entanglement spectra (RSES) of these states using an efficient Monte Carlo method. By computing the RSES of simple non-Abelian parton states, namely Φ_2^2, Φ_2^3 and Φ_3^2, we verify that the edge-spectra of partons states of kind Φ_n^k are indeed given by highest-weight representation of $\widehat{su}(n)_k$ Kac-Moody algebra. Finally, we perform extensive benchmarks of the accuracy of the Monte Carlo technique by comparing the RSESs of 2/5 CF state computed using the efficient Monte Carlo method and brute force methods. We present an approximate projection method that generalizes the Jain-Kamilla projection method, allowing efficient computation of RSES of projected CF states for systems as large as 100 particles.

List of publications

Exactly Solvable Model for Strongly Interacting Electrons in a Magnetic Field
Abhishek Anand, J. K. Jain, and G. J. Sreejith
Phys. Rev. Lett. 126, 136601 (2021)

Real-space entanglement spectra of parton states in fractional quantum Hall systems
Abhishek Anand, Rushikesh A. Patil, Ajit C. Balram, and G. J. Sreejith
Phys. Rev. B 106, 085136 (2022)

Real-space entanglement spectra of lowest Landau level projected fractional quantum Hall states using Monte Carlo methods
Abhishek Anand and G. J. Sreejith
Phys. Rev. B 107, 085101 (2023)

Torus geometry eigenfunctions of an interacting multi-Landau level Hamiltonian
Abhishek Anand, Songyang Pu, and G. J. Sreejith
Phys. Rev. B 107, 195126 (2023)

Table of Contents

List of Figures

Chapter 1

Introduction

The physics of complex many-body systems is best described in terms of emergent degrees of freedom that depend on the scale at which we want to understand their behavior. In weakly interacting systems, perturbation theory can typically be used to infer the emergent structures. Quasiparticles of Fermi liquids and Cooper pairs in superconductors are examples of such emergent degrees of freedom. The effective description of phenomena in terms of them is enormously simpler and tractable when compared to the fundamental degrees of freedom.

The fractional quantum Hall effect (FQHE) is a quintessential example of a many-body phenomenon where the only microscopic energy scale in the system comes from the strong interaction; perturbative approaches completely fail in the absence of small parameters. In FQHE, a 2-dimensional system of strongly interacting electrons in a large magnetic field B condenses to a diverse set of gapped quantum liquid ground states called Hall liquids, exhibiting universal features independent of substrate.

Each of the FQH phases occurs near a characteristic electronic filling fraction ν, which is electron density written as a fraction of magnetic flux density. Despite the challenging, strongly interacting nature of the problem, much progress has been made thanks to variational methods that rely on emergent particles. The occurrence of these ground states can be explained in terms of weakly interacting emergent particles, called *composite fermions* (CFs). These are the bound states of each electron with an even number of vortices of all other electrons. FQHE of electrons is a manifestation of the integer quantum Hall effect (IQHE) of these weakly-interacting composite fermions in a reduced magnetic field B^* different from the actual magnetic fields seen by the electrons. The IQH state of these CFs hosts further emergent entities with qualitatively different properties: quasiparticles in the IQH phases of CFs are *anyons* which, unlike fermions or bosons, follow fractional exchange statistics [6, 7, 8, 9]. In addition to IQHE, the CFs can form other phases such as Fermi sea (at $\nu = 1/2p$, where p is a positive integer), superconductors (at $\nu = 5/2$) [10, 11, 12, 13] and Wigner crystals [14, 15, 16, 17, 18, 19, 20].

Composite fermions that experience an effective field B^* are not merely a theoretical construct to describe FQHE; they have been experimentally observed by studying the cyclotron orbits of FQH systems [21, 22, 23] where it was found that particles in FQH system at $\nu = 1/2$ move under an effective magnetic field B^*. Other signatures, for instance, Fermi sea at half-filled Landau level [24, 25, 21, 22], Shubnikov de Haas oscillations [26, 27] and most importantly, the ability to predict the filling fraction ν at which FQHE occurs to confirm the veracity and usefulness of CF description.

However, CFs are formed from strongly interacting electrons. A microscopic description that starts from the electron will need to deal with the calculational difficulties ubiquitously encountered in the study of all strongly interacting systems. In this thesis, we study an effective simplified model interaction that describes the FQHE of electrons at the Jain sequence of filling fractions given by $\nu = \frac{n}{2np+1}$ where n, p are positive integers. Exact solutions are rare in most problems involving strong interactions. Though the model interaction is different from physically relevant Coulomb interaction, it is still an appealing model as its exact eigenfunctions can be written, which share many key properties with the actual CF wavefunctions. We also present refined special numerical methods which allow efficient computation of the key characteristic property called Entanglement Spectra of the CF wavefunctions and the more general parton states. Here, we begin by briefly reviewing the necessary background on the quantum Hall effect.

This chapter is organized as follows. We first review the phenomenon of classical Hall effect in Sec. 1.1. In Sec. 1.2, we introduce the integer quantum Hall effect and discuss some conventional system geometries. In this section, we also explain the importance of disorder in the observed phenomenon. Sec 1.3 introduces the fractional quantum Hall effect and some important variational wavefunctions that successfully explain the effect for different filling fractions. Finally, in Sec. 1.4, the idea of Haldane's pseudopotentials is reviewed, which is used to write the model interaction in Part I of the thesis.

1.1 Classical Hall effect

Before embarking on a description of the quantum Hall effect, a quick review of the classical Hall effect will be helpful. The typical setup consists of free electrons in a rectangular sheet in the xy-plane (see Fig. 1.1) such that a current I_x flows in the x-direction. A constant magnetic field $\boldsymbol{B} = B\hat{e}_z$ is applied perpendicular to the system. The magnetic field induces a voltage difference V_H along the direction perpendicular to the current, which is called the *Hall effect*. A schematic of the Hall system is given below.

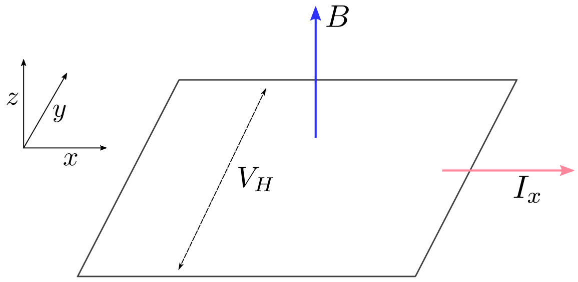

Figure 1.1: Schematic of classical Hall effect

We can use the Drude model of electrons to study the system where elastic collisions of an electron with the hard-core lattice points (which represent heavy ions in the background) are effectively modeled as the addition of a linear dissipative term in the equation of motion. The equation of motion of an electron in the system is thus given by

$$m\frac{\mathrm{d}\boldsymbol{v}}{\mathrm{d}t} = -e(\boldsymbol{E} + \boldsymbol{v} \times \boldsymbol{B}) - \frac{m}{\tau}\boldsymbol{v} \tag{1.1}$$

where m is the mass and charge $-e$ is the charge of the electron; τ is the *relaxation time* which represents average time between two successive collisions. At equilibrium, we expect a steady current of electrons *i.e.* $\frac{\mathrm{d}\boldsymbol{v}}{\mathrm{d}t} = 0$. The current density is given by $\boldsymbol{J} = -ne\boldsymbol{v}$ where n is the density of electrons. Using Ohm's law *i.e.* $\boldsymbol{J} = \sigma\boldsymbol{E}$, we get the value for conductivity σ at steady current as

$$\sigma = \frac{\sigma_{\mathrm{dc}}}{1 + \omega_B^2\tau^2}\begin{pmatrix} 1 & -\omega_B\tau \\ \omega_B\tau & 1 \end{pmatrix} \tag{1.2}$$

where $\sigma_{\mathrm{dc}} = \frac{ne^2\tau}{m}$ is the conductivity in absence of a magnetic field. Since resistivity ρ is the inverse of conductivity, it can be checked using Eq. (1.2) that the transverse resistivity in classical Hall system is linearly proportional to the magnetic field strength, given by

$$\rho_{xy} = R_H B \tag{1.3}$$

where coefficient of proportionality $R_H = 1/ne$ is called the *Hall coefficient*. In materials with multiple carriers, the R_H is modified systematically such that it can be used to understand the carrier type and their densities [28, Ch. 6]. The linear resistivity remains constant with B as shown in Fig. 1.4.

Moreover, advances in material synthesis methods allowed the construction of almost two-dimensional samples, particularly in GaAs-AlGaAs heterostructures and, more recently, in graphene. Access to extremely low temperatures and very large magnetic fields allowed the quantum effects to appear in the picture. As we will see next, this results in the integer quantum Hall effect (IQHE) phenomenon.

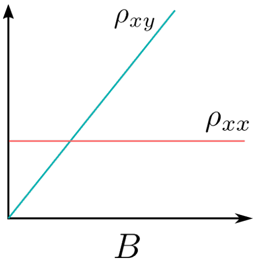

Figure 1.2: In the classical Hall effect, the transverse resistivity ρ_{xy} of the system increases linearly with the strength of magnetic field B. In contrast, the linear resistivity ρ_{xx} remains invariant.

1.2 Quantum Hall effect

In 1980, von Klitzing used the high mobility GaAs-AlGaAs sample prepared by Dorda and Pepper, to study the Hall effect in quantum regime [1]. The Metal-Oxide-Silicon device used in the experiment was 400 μm long and 50 μm wide, under a magnetic field of $B = 18$ T and temperature around 1.8 K. In a thin sample, quantum effects become important at low-temperature and high magnetic field. He found that, instead of increasing linearly, the transverse resistivity ρ_{xy} increases in steps as magnetic field strength is increased. Between the jumps, ρ_{xy} remains constant, as shown in the following figure,

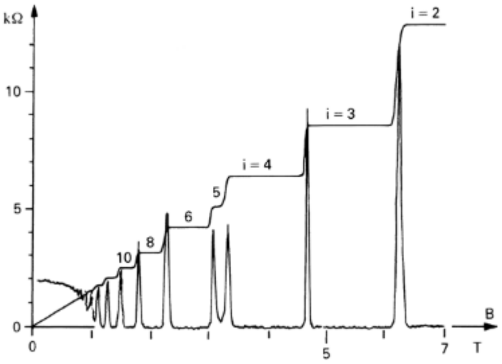

Figure 1.3: Quantized resistivity ρ_{xy} increases in steps of $h/e^2\nu$ with magnetic field B, where $\nu \in \mathbb{Z}^+$ (represented in the figure by i). Between the jumps, ρ_{xy} remains constant for a range of magnetic field strength, forming a plateau or step like structure. In these plateau regions, the longitudinal resistivity ρ_{xx} vanishes and only shows sharp peaks when ρ_{xy} changes value. [1]

This phenomenon of the quantized increment in the transverse resistivity ρ_{xy} with magnetic field in steps of $h/e^2\nu$ where $\nu \in \mathbb{Z}^+$, is called the integer quantum Hall effect (IQHE). As the name suggest, it is a purely quantum phenomena which cannot be explained using classical picture. Also, the effect is universal and independent of the microscopic details of the system. Quantization of the Hall plateaus is accurate up to few parts in 10^9 [29]. This phenomenon can be fully understood as a combined effect of:

1. *Formation of Landau levels :* In quantum limit, the kinetic energy of free electrons in the presence of a magnetic field gets quantized into discrete energy levels which are highly degenerate. These are called Landau levels.

2. *Presence of disorder :* Experimental samples always contain random disorder. Counter intuitively, it is the disorder which ensures that the plateaus are quantized to such high precision.

The quantization of Hall conductivity can also be understood from topological point of view: the transverse conductance is given by $\sigma_{xy} = -\frac{e^2}{h}C$, where C is called the Chern number [30]. This Chern number is a topological quantum number and always takes an integer value. Topological quantum numbers remain invariant under small changes in the Hamiltonian, which makes the edge modes carrying the current *topologically protected* to small disorders in the system.

1.2.1 Landau Quantization

Before we study the quantum picture of an electron in a magnetic field, let us remind ourselves how a classically charged particle behaves in a magnetic field. The Lagrangian of a free electron with charge $-e$ and mass m, in presence of a magnetic field $\boldsymbol{B} = \nabla\times\boldsymbol{A}(\boldsymbol{r})$, is given by

$$\mathcal{L} = \frac{m\dot{\boldsymbol{r}}^2}{2} - e\dot{\boldsymbol{r}}\cdot\boldsymbol{A} \tag{1.4}$$

where $\boldsymbol{r}$ is the position vector of electron and $\boldsymbol{A} \equiv \boldsymbol{A}(\boldsymbol{r})$. We can write the corresponding Hamiltonian using the Legendre transformation, which is given by

$$\mathcal{H} = \dot{\boldsymbol{r}}\cdot\boldsymbol{p} - \mathcal{L} = \frac{1}{2m}(\boldsymbol{p} + e\boldsymbol{A})^2 \tag{1.5}$$

where $\boldsymbol{p} = m\dot{\boldsymbol{r}} - e\boldsymbol{A}$ is the canonical momenta of the electron. Notice, in the presence of magnetic field, canonical momentum $\boldsymbol{p}$ and mechanical momentum are related by $m\dot{\boldsymbol{r}} = \boldsymbol{p} + e\boldsymbol{A}$ and hence, are not equal. Poisson bracket for the components of this mechanical momentum is given by

$$\{m\dot{r}_i, m\dot{r}_j\} = -e\left(\frac{\partial A_j}{\partial r_i} - \frac{\partial A_i}{\partial r_j}\right) = -e\epsilon_{ijk}B_k \tag{1.6}$$

The Hamiltonian in Eq. (1.5) is converted to quantum mechanical picture by replacing physical variables by corresponding operators:

$$\hat{\mathcal{H}} = \frac{1}{2m}(\hat{\boldsymbol{p}} + e\hat{\boldsymbol{A}})^2 \tag{1.7}$$

where symbols with ˆ represent the corresponding operators. System consists of a two-dimensional plane where $\boldsymbol{r} = (x, y)$ with a magnetic field passing perpendicular to the (x, y)-plane, given by $\nabla\times\boldsymbol{A} = B\hat{e}_z$. For simplicity, we will assume the the spin degree of freedom of electrons are frozen. Using Eq. (1.6), we can get the commutation relations between the components of mechanical momentum $\hat{\boldsymbol{\pi}} = \hat{\boldsymbol{p}} + e\hat{\boldsymbol{A}}$, given by

$$[\hat{\pi}_x, \hat{\pi}_y] = -ie\hbar B \tag{1.8}$$

We construct following ladder operators

$$\begin{aligned} \hat{a} =& \frac{1}{\sqrt{2e\hbar B}} \left(\hat{\pi}_x - i\hat{\pi}_y\right) \\ \hat{a}^\dagger =& \frac{1}{\sqrt{2e\hbar B}} \left(\hat{\pi}_x + i\hat{\pi}_y\right) \end{aligned} \tag{1.9}$$

which follow $[a, a^\dagger] = 1$. The Hamiltonian can be written in terms of these ladder operators as

$$\hat{\mathcal{H}} = \frac{\hat{\boldsymbol{\pi}}^2}{2m} = \hbar\omega_B \left(\hat{a}^\dagger\hat{a} + \frac{1}{2}\right) \tag{1.10}$$

where $\omega_B = \frac{eB}{m}$ is the cyclotron frequency.

Similar to the case of simple harmonic oscillator, we first define a vacuum state $|0\rangle$ which obeys $\hat{a}\,|0\rangle = 0$. All other eigenstates $|n\rangle$ for $n = 0, 1, 2, \ldots$ can be generated using the ladder operators.

$$\hat{a}^\dagger\,|n\rangle = \sqrt{n+1}\,|n+1\rangle \tag{1.11}$$

The state $|n\rangle$ has energy

$$E_n = \hat{\mathcal{H}}\,|n\rangle = \hbar\omega_B \left(n + \frac{1}{2}\right) \tag{1.12}$$

where $n = 0, 1, 2, \ldots$ labels the energy levels. Notice that the gap between the levels is proportional to magnetic field strength B. These energy levels are called *Landau levels.* We will see next that unlike simple harmonic oscillator, each Landau level is highly degenerate.

We can define a gauge-dependent operator $\tilde{\boldsymbol{\pi}} = \boldsymbol{p} - e\boldsymbol{A}$. The new operator follows

$$[\tilde{\pi}_x, \tilde{\pi}_y] = ie\hbar B \tag{1.13}$$

and its commutation with mechanical momentum is given by

$$[\pi_x, \tilde{\pi}_y] = [\pi_y, \tilde{\pi}_x] = ie\hbar \left(\frac{\partial A_x}{\partial y} + \frac{\partial A_y}{\partial x}\right) \tag{1.14}$$

In the RHS of Eq. (1.14), the terms inside the parenthesis cancel each other if we use symmetric gauge *i.e.* $\boldsymbol{A} = -\frac{1}{2}(\boldsymbol{r} \times \boldsymbol{B})$. Hence, in symmetric gauge, the operator $\tilde{\boldsymbol{\pi}}$ commutes with the Hamiltonian. We construct new ladder operators which are given by

$$\begin{aligned} \hat{b} =& \frac{1}{\sqrt{2e\hbar B}} \left(\tilde{\pi}_x + i\tilde{\pi}_y\right) \\ \hat{b}^\dagger =& \frac{1}{\sqrt{2e\hbar B}} \left(\tilde{\pi}_x - i\tilde{\pi}_y\right) \end{aligned} \tag{1.15}$$

which satisfy $[\hat{b}, \hat{b}^\dagger] = 1$. The complete Hilbert space is generated by repeated action of $a^\dagger$ and $b^\dagger$ on the vacuum. If we define the ground state as $|0,0\rangle$ which satisfies $\hat{a}\,|0,0\rangle = \hat{b}\,|0,0\rangle = 0$, the general state in the Hilbert space is $|n,m\rangle$ defined by

$$\phi_{n,m} \equiv |n,m\rangle = \frac{(\hat{b}^\dagger)^{m+n}(\hat{a}^\dagger)^n}{\sqrt{n!m!}}\,|0,0\rangle \tag{1.16}$$

where $m = -n, -n+1, \ldots, 0, 1, \ldots$ and $n = 0, 1, \ldots$.

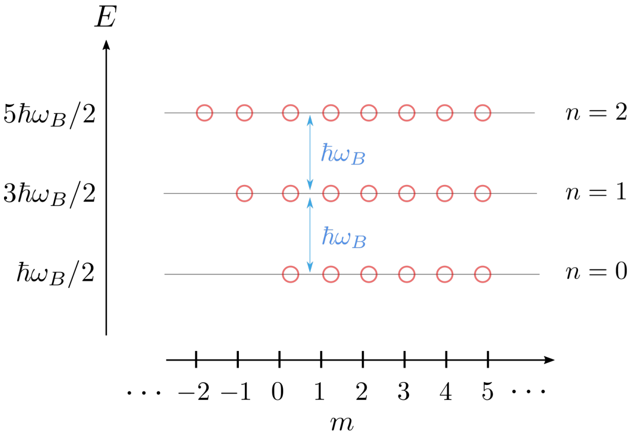

Figure 1.4: Schematic showing Landau orbitals (red circles) with their angular momentum indices along the x-axis and energies along the y-axis.

As the ladder operator $\hat{b}$ commutes with the Hamiltonian, energy of the system is independent of index m. Thus, for nth Landau level, states $|n,m\rangle$ are degenerate for all possible values of m. The value of degeneracy is fixed by system size.

Let us take a rectangular system with sides of lengths L_x and L_y. We choose to work in Landau gauge *i.e.* $\boldsymbol{A} = xB\hat{e}_y$ ($\hat{e}_y$ is the unit vector along y-axis) for which the Hamiltonian in Eq. (1.7) is given by

$$\hat{\mathcal{H}} = \frac{1}{2m}\left(\hat{p}_x^2 + (\hat{p}_y + e\hat{x}B)^2\right) \tag{1.17}$$

In this gauge, Hamiltonian remains invariant under translation in the y-direction. Thus, the eigenfunctions for the Hamiltonian are labeled by the y-momentum $\hbar k$ and can be written as $\psi_k(x,y) = e^{\imath ky} f_k(x)$. The function $f_k(x)$ satisfies $h_k f_k(x) = \epsilon_k f_k(x)$ where

$$h_k = \frac{p_x^2}{2m} + \frac{1}{2m}\left(\hbar k + exB\right)^2 \tag{1.18}$$

which can be rewritten as a displaced simple harmonic oscillator (SHO) as shown below

$$h_k = \frac{p_x^2}{2m} + \frac{1}{2}m\omega_B^2\left(x + k\ell^2\right)^2 \tag{1.19}$$

where $\ell = \sqrt{\hbar/eB}$ is called *magnetic length* which is the characteristic length scale of the system. Eq. (1.19) resembles a quantum SHO centered at $X_k = -k\ell^2$ and for each value of y-momentum quantum number k, energy of the eigenstates is given by $\epsilon_{nk} = \hbar\omega_B \left(n + \frac{1}{2}\right)$ which does not depend on the value of k. $f(x)$ are the known eigenfunctions of the displaced SHO problem. The complete eigenfunctions (unnormalized) $\psi_{nk}(x,y)$ for the system are given by

$$\psi_{nk}(x,y) = e^{\iota ky} H_n(x + k\ell^2) e^{-\frac{1}{2\ell^2}(x+k\ell^2)^2} \tag{1.20}$$

where $H_n(x)$ is the nth Hermite polynomial and $\psi_{nk}(x,y)$ is the Landau orbital for electron in nth LL with kth y-momentum state. The Gaussian factor implies the particle remains localized in the x-direction around the mean position given by $X_k = -k\ell^2$. If we assume a periodic boundary condition along y-direction, which converts the rectangle into cylinder, the allowed values of y-momentum gets constrained such that $k = \frac{2\pi n}{L_y}$, where n takes integer values.

Conventionally, for the study of any QH system, a few geometries are preferred. Geometries with open boundaries like disk and cylinder are useful for the study of edge physics whereas compact geometries like sphere and torus are better for the bulk study. A quick review of these geometries and form of Landau orbitals is given below:

Spherical geometry : Unlike disk geometry, the sphere is a closed manifold; absence of any edge makes it suitable for the study of bulk properties [31]. Perpendicular magnetic field with $2Q$ flux quanta ($\hbar/e$) is generated by placing a Dirac magnetic monopole of strength Q at the center of sphere. The electronic wavefunction is only well-defined for integer values of $2Q$. Due to rotational symmetry, angular momentum l and its z-component m are good quantum numbers. Their allows values are

$$l = |Q|, |Q| - 1, \ldots \tag{1.21}$$

$$m = -l, -l+1, \ldots, l-1, l \tag{1.22}$$

Different angular momentum sectors corresponding to quantum number l are different Landau levels, with $l = |Q|$ representing the LLL. The degeneracy of each LL is independent of system size in spherical geometry, which is equal to $2|Q| + n + 1$ for nth LL. In spherical geometry, Landau orbitals are given by monopole harmonics $Y_{Qlm}(\mathbf{\Omega})$ where $\mathbf{\Omega} \equiv (\phi, \theta)$ [32, 33]. Conventionally, coordinates of the particle are written in spinor variable (u, v) given by

$$u = \cos(\theta/2) e^{\iota\phi/2} \tag{1.23}$$

$$v = \sin(\theta/2) e^{-\iota\phi/2} \tag{1.24}$$

and the form of Y_{Qlm} [31, 4] is given by

$$Y_{Qlm} = N_{Qlm}(-1)^{l-m} v^{Q-m} u^{Q+m} \times \\ \sum_{s=0}^{l-Q} (-1)^s \binom{l-Q}{s} \binom{l+Q}{l-m-s} (v^* v)^{l-Q-s} (u^* u)^s \tag{1.25}$$

where $\binom{j}{k}$ is zero if either $k < 0$ or $k < j$ and the normalization factor N_{Qlm} is given by

$$N_{Qlm} = \frac{(2l+1)(l-m)!(l+m)!}{4\pi(l-Q)!(l+Q)!}^{1/2} \tag{1.26}$$

Disk geometry :

In disk geometry, for symmetric gauge $\boldsymbol{A} = \frac{1}{2}\boldsymbol{B} \times \boldsymbol{r}$, unnormalized Landau orbitals are given by

$$\phi_{nm}(\boldsymbol{r}) = \frac{(-1)^n}{\sqrt{2\pi}} \sqrt{\frac{n!}{2^m (n+m)!}}\; e^{-\frac{r^2}{4\ell_B^2}} \left(\frac{z}{\ell_B}\right)^m L_n^m \left(\frac{r^2}{2\ell_B^2}\right) \tag{1.27}$$

where $n = 0, 1, 2, \ldots$ labels the Landau level and $m = -n, -n+1, \ldots, 0, 1, \ldots$ is the angular momentum quantum number of the electron in nth LL; $L_n^m(x)$ represents associated Laguerre polynomial.

Torus geometry : Torus geometry is another example of a compact geometry, which can be constructed if we enforce periodicity along the length of cylinder [34]. Thus, any planar system with periodicity along two directions can be thought as a torus.

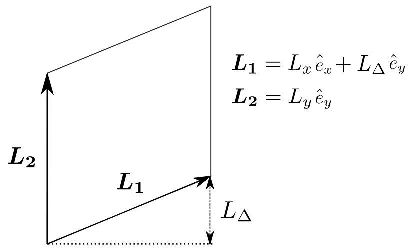

Figure 1.5: A general torus generated by $\boldsymbol{L}_1$ and $\boldsymbol{L}_2$. The skewness L_Δ parametrizes the deviation from a rectangular torus.

For symmetric gauge $\boldsymbol{A} = \frac{1}{2}\boldsymbol{B} \times \boldsymbol{r}$, unnormalized Landau orbitals [34, 35] for torus in the Figure below are given by

$$\phi_{n,k}(z, \bar{z}) = e^{-\frac{z^2+|z|^2}{2\ell^2}} \frac{(a_f^\dagger)^n}{\sqrt{n!}} \left[\vartheta \begin{bmatrix} \frac{k}{N_\phi} + \frac{\theta_2}{2\pi N_\phi} \\ \frac{\theta_1}{2\pi} \end{bmatrix} \left(\frac{N_\phi z}{L_2} \middle| N_\phi \tau \right) \right] \tag{1.28}$$

where $0 \leq k < N_\phi$ is a y-momentum and $n = 0, 1, \ldots$ is the LL-index. Here $z = x + \iota y$ is the complex position vector (assuming $\boldsymbol{B} = -B\hat{e}_z$), $\tau = -L_1/L_2$ and $a_f^\dagger = \sqrt{2}\ell \left(\frac{\bar{z}+z}{2\ell^2} - \partial_z\right)$ is the ladder operator for LL index such that its action of the exponential pre-factor is already taken into account. For given complex numbers z and τ, Jacobi theta function [36] is defined as

$$\vartheta \begin{bmatrix} a \\ b \end{bmatrix} (z|\tau) = \sum_{j=-\infty}^{\infty} e^{i\pi(j+a)^2\tau} e^{i2\pi(j+a)(z+b)} \tag{1.29}$$

where a, b are rational numbers and j is an integer.

Now that we understand the quantum mechanical picture of free electron in a magnetic field, we add an electric field to make it a Hall system. Specifically, we add a uniform electric field $\boldsymbol{E} = E\hat{e}_x$ in x-direction which gives us the following Hamiltonian

$$\hat{\mathcal{H}} = \frac{1}{2m}\left(\hat{p}_x^2 + (\hat{p}_y + e\hat{x}B)^2\right) + eEx \tag{1.30}$$

Solving it by completing the square gives us another SHO which is centered now at $X_k = -k\ell^2 - eE/m\omega_B^2$ and the eigenvalues now depend on the k quantum number. For instance, energies for LLL $i.e.\, n = 0$ are given by

$$\epsilon_k = \frac{1}{2}\hbar\omega_B + eEX_k + \frac{1}{2}m\left(\frac{E}{B}\right)^2 \tag{1.31}$$

As we see, eigenvalues depend linearly on k quantum number, which will tilt the Landau levels. It can be checked that there is a net current in y-direction given by $\langle J_y \rangle = eE/B$.

Physically, the tilt in LLs is small. Hence fine tuning of chemical potential to keep it between two LLs is not possible because as chemical potential reaches $\hbar\omega_B(n+\frac{1}{2})$, when nth LL is filled completely. If we add one extra electron it has to go to $(n+1)$th LL and the chemical potential will sharply jump to $\hbar\omega_B(n+1+\frac{1}{2})$. Thus, the LLs alone do not explain the formation of plateaus and the quantized values of ρ_{xy} in the IQHE (see Fig. 1.3). This is explained by the disorder in the system which localizes all the Landau orbitals except one state (per LL), which is extended along the system. Next section gives a sketch of the underlying physics.

1.2.2 Importance of disorder

In order to explain the formation of plateaus in the ρ_{xy}, some amount of local disorder $V(\boldsymbol{r})$ is required. Presence of disorder breaks the degeneracy in the LL and the divergent density of states in each LL broadens into finite width peaks, as shown in Fig. 1.6. Out of all the orbitals in band of each LL, only one state (in the thermodynamic limit) can transport current through the sample and all others are localized. States *localize* around the local disorder which can be imagined as slow varying ($\nabla V(\boldsymbol{r}) \ll \frac{\hbar\omega_B}{\ell_B}$) forming hills or valleys. States in the band drift along the equipotential lines of V, which form closed loops as shown in Fig. 1.7.

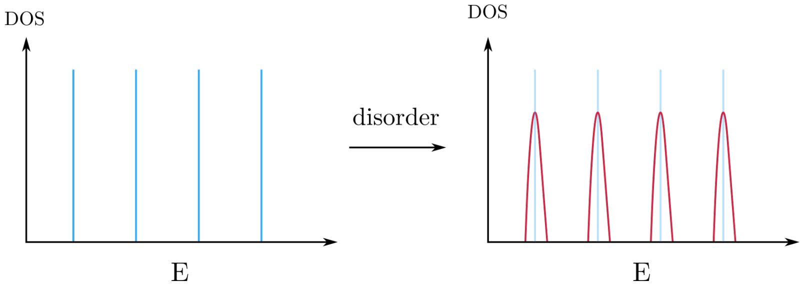

Figure 1.6: Landau levels have sharp density of states (blue in right panel), with all the states in nth LL having exact energy $\hbar\omega_B(n+1/2)$. Introducing the disorder breaks this degeneracy and spreads the states in each LL into set of bands (shown in red in the left panel).

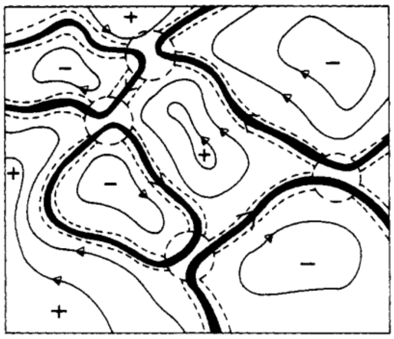

Figure 1.7: Schematic showing a typical potential $V(x,y)$ where the loops with arrow represent the drift of localized states along the equipotential contours. Direction of drift along the hills (+ve potential) and valleys ($-ve$ potential) are opposite as expect. Contours shown in bold represent the extended states which are present near the middle of LL band (blue lines in left panel of Fig. 1.6) [2]

Somewhere in the middle of each LL band, one conducting state which is *extended* along the sample contributes to the current [37]. The existence of this extend state can be understood using a percolation picture [2]. As we fill electrons in the system, states at the lower end of the LL band are filled, which get localized on equipotential cureves around the minima or valleys of the potential. As Fermi energy reaches center of the band, the equipotential lines extend across the sample, transporting current. As we further increase the energy, states are localized in equipotential contours around maxima or hills of the potential. As long as the electrons at the fermi energy fill these localized states, the Hall resistance remains fixed forming plateaus. Only when an electron is removed from the extended state, we see a jump in the Hall resistance which explains the IQHE.

1.3 Fractional quantum Hall effect

In 1981, Tsui, Stormer and Gossard found additional plateaus at a set of fractional values of filling fraction ν by studying GaAs-AlGaAs heterojunctions with electron densities

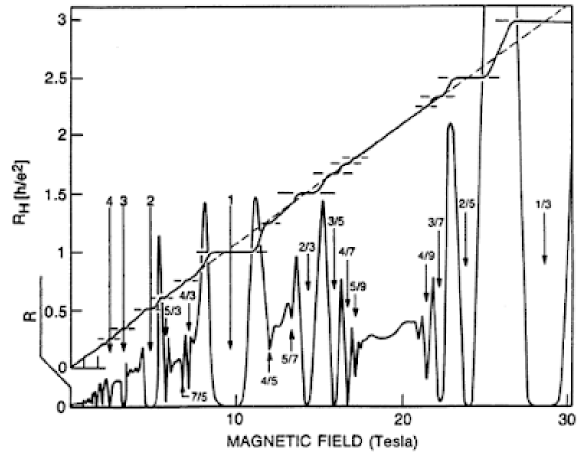

Figure 1.8: In larger magnetic field and cleaner sample, transverse resistance ρ_{xy} increases in quantized steps with B, such that the values of ρ_{xy} at plateaus is given by $h/e^2\nu$ where filling fraction ν also takes fractional values. [3]

$n = 1.1 \times 10^{11}$ to 1.4×10^{11} cm^2 and mobility $\mu = 8 \times 10^4$ to 10×10^4 cm^2/V. The study was conducted in higher magnetic field (~ 20 T) and much lower temperatures (around 0.42 K) and at filling fraction $\nu < 1$. This novel phenomena, where an excitation gap seems to appear even at rational filling, is known as fractional Hall effect (FQHE) (see Fig. 1.8). It appears that as electrons come close to each other due to large magnetic field, gaps open up inside otherwise gapless Landau bands at a set of fractional fillings. Opening of these gaps is attributed to Coulomb interaction between electrons. The Coulomb interaction between two electrons is given by

$$V_{\text{Coulomb}} = \frac{e^2}{4\pi|\boldsymbol{r}_1 - \boldsymbol{r}_2|} \tag{1.32}$$

This makes the system strongly-correlated and convetional methods like perturbation theory cannot be used to study the model. Instead, as we shall see in the next section, an indirect approach is taken to study the FQHE.

1.3.1 Laughlin's states

In 1983, based on educated guesswork, Laughlin directly wrote trial wavefunctions representing the ground states at filling fraction of form $\nu = 1/m$, where m is an odd integer [38]. Although Laughlin states are not exact eigenfunctions of the FQHE Hamiltonian given by

$$\mathcal{H}_{\text{FQHE}} = \sum_{i}^{N_e} \frac{\hat{\boldsymbol{\pi}}_i^2}{2m} + \hat{V}_{\text{Coulomb}} \tag{1.33}$$

but, for small number of particles, the Laughlin state has large overlaps with the exact ground states of $\mathcal{H}_{\text{FQHE}}$ at that electron density.

Coulomb interaction is central which implies $V_{\text{Coulomb}}(\boldsymbol{r}_1 - \boldsymbol{r}_2) = V_{\text{Coulomb}}(|\boldsymbol{r}_1 - \boldsymbol{r}_2|)$. Since it is rotationally symmetric, it shares its eigenstates with angular momentum operator. Using symmetric gauge *i.e.* $\boldsymbol{A} = \frac{1}{2}\boldsymbol{B} \times \boldsymbol{r}$ makes the FQHE Hamiltonian rotationally symmetric. It can be checked that in symmetric gauge, Landau orbitals in the lowest Landau level (LLL) have following form (see Eq. (1.27))

$$\psi_m(z) \sim z^m e^{-|z|^2/4\ell_B^2} \tag{1.34}$$

where m is the angular momentum of the state and $z = x - \imath y$ is coordinate of the particle in complex form. Using the rotational symmetry of $\mathcal{H}_{\text{FQHE}}$, we can write a general two-particle solution for it as

$$\psi(z) \sim (z_1 + z_2)^M (z_1 - z_2)^{m_{\text{rel}}} e^{(-|z_1|^2 - |z_2|^2)/4\ell_B^2} \tag{1.35}$$

where M and m_{rel} represent the center-of-mass and relative angular momentum of the pair of particles, respectively.

Laughlin proposed that ground state at filling fraction $1/m$ is given by

$$\psi_{1/m}(z) = \prod_{i<j}^{N} (z_i - z_j)^m e^{-\sum_i |z_i|^2/4\ell_B^2} \tag{1.36}$$

The wavefunction is anti-symmetric for odd values of m which is consistent for electrons (fermions). It can be checked that the wavefunction returns correct filling fraction. More impressively, the wavefunction has around 99% overlap with exact ground state for small number of particles. It starts decreasing as number of particles are increased in the system. Hence, instead of looking at these wavefunction as candidate for exact solutions, we should think of them as describing the 'universality' class, which implies that Laughlin states have same long wavelength properties of the excitations and topological order as that of the exact ground state.

1.3.2 Composite Fermion wavefunctions

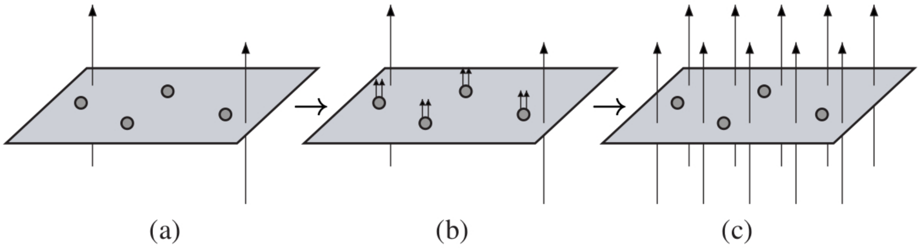

Figure 1.9: Figure shows the map from the IQHE to the FQHE. Panel (a) shows the IQHE with total flux represented by number of pointed arrows. Panel (b) shows conversion of each electron into a composite fermion by attaching $2p = 2$ flux. Finally, spreading out the attached flux gives us the corresponding FQHE state (c) of electron in a higher magnetic field. [4]

Jain's composite fermion (CF) [39] wavefunctions describe FQHE of electrons at sequence of filling fractions given by $\nu = n/(2pn + 1)$, where n and p are positive integers, using a picture of weakly interacting emergent particles. The emergent particle called *composite fermion* is understood as a bound state of an electron and $2p$ flux quanta. Using CF construction, FQHE for N_e electrons in flux N_ϕ at filling fraction $\nu = n/(2pn + 1)$ can be mapped to the integer quantum Hall effect (IQHE) of CFs in a reduced flux $N^*_\phi = N_\phi - 2pN_e$ at $\nu^* = n$. This IQHE-to-FQHE map for $2p = 2$ is schematically shown in Fig. 1.9.

In disk geometry, the CF wavefunction for the electrons is obtained by multiplying the IQHE state of CFs at filling fraction ν^*—represented by a Slater determinant Φ_{ν^*}—by the Jastrow factor $\mathcal{J}^{2p} = \prod_{j<k}^{N}(z_j - z_k)^{2p}$, which attaches $2p$ vortices to each particle. The CFs inside the Slater determinant see a reduced magnetic field $B^* = B - 2p\rho\phi_0$. The second term can be understood as the average berry phase arising from the vortices on the other particles. The Jastrow factor also increases the *relative* angular momentum of each pair of particles in the Slater determinant, denoted by m, by $2p$ units. The CF wavefunction is given by

$$\Psi_{\frac{\nu^*}{2p\nu^*+1}} = \mathcal{P}_{\text{LLL}}\Phi_{\nu^*}\prod_{j<k}(z_j - z_k)^{2p}, \tag{1.37}$$

where $\mathcal{P}_{\text{LLL}}$ denotes projection into the lowest Landau level. The Jastrow factor $\mathcal{J}^{2p}$ suppresses the probability of 2 particles being too close to each other resulting in a screened effective interaction. The operation of projection is motivated from the fact that in a high magnetic field regime *i.e.* $|B| \to \infty$, most of the particles will be in the LLL. It can be verified that, for $2p = m - 1$ and $\nu^* = 1$, CF state returns Laughlin wavefunction for $\nu = 1/m$.

CF wavefunction in different geometries:

Spherical geometry : Composite fermion wavefunction generalizes to spherical geometry as follows

$$\Psi_Q = \mathcal{P}_{\text{LLL}} \Phi_{Q^*} \Phi_1^{2p} \tag{1.38}$$

where the Slater determinant Φ_{Q^*} corresponds to IQH state of CFs in a reduced magnetic flux of $2Q^*$ and the Jastrow factor is given by

$$\Phi_1^{2p} = \prod_{j<k} (u_i v_j - v_j u_k)^{2p} \tag{1.39}$$

and reduced flux is related to actual flux via $2Q^* = 2Q - 2p(N-1)$.

Cylinder geometry : Composite fermion wavefunction in cylinder geometry is given by

$$\Psi_{\frac{\nu^*}{2p\nu^*+1}} = \mathcal{P}_{\text{LLL}} \prod_{i<j} \left(e^{\frac{2\pi z_i}{L}} - e^{\frac{2\pi z_j}{L}} \right)^{2p} \Phi_{\nu^*} \tag{1.40}$$

where the Slater determinant Φ_{ν^*} corresponds to IQH state of CFs in a filling fraction ν^*. The number of orbitals in each LL are fixed by N_ϕ which is equivalent to fixing the length of cylinder along the non-periodic direction.

Torus geometry : Composite fermion wavefunction on torus [40] is given by

$$\Psi_{\nu=\frac{\nu^*}{2p\nu^*+1}} = \mathcal{P}_{\text{LLL}} \left[F_1(Z_{\text{cm}})\right]^{2p} \mathcal{J}^{2p} \, e^{-\sum_i \frac{z_i^2+|z_i|^2}{2\ell^2}} \, \Phi_{\nu^*} \tag{1.41}$$

where $Z_{\text{cm}} = \sum_i z_i$ and the Jastrow factor is given by

$$\mathcal{J}(\{z\}) = \prod_{i<j} \vartheta \begin{bmatrix} 1/2 \\ 1/2 \end{bmatrix} \left(\frac{z_i - z_j}{L_2} \middle| \tau \right) \tag{1.42}$$

where the Jacobi theta functions [36] are defined as

$$\vartheta \begin{bmatrix} a \\ b \end{bmatrix} (z|\tau) = \sum_{j=-\infty}^{\infty} e^{i\pi(j+a)^2\tau} e^{i2\pi(j+a)(z+b)} \tag{1.43}$$

such that a, b are rational numbers and j is an integer. For the torus in Fig. 1.5, we have $\tau = -L_1/L_2$. $F_1(Z_{\text{cm}})$ represents the center-of-mass dependent part of the filled lowest Landau level [34], given by

$$F_1(Z_{\text{cm}}) = \vartheta \begin{bmatrix} \frac{\theta_2}{2\pi} + \frac{N_e-1}{2} \\ \frac{\theta_1}{2\pi} + \frac{N_e-1}{2} \end{bmatrix} \left(\frac{Z_{\text{cm}}}{L_2} \middle| \tau \right) \tag{1.44}$$

where θ_1 and θ_2 determine the Hilbert space representations of translations along the periodic directions $\boldsymbol{L}_1$ and $\boldsymbol{L}_2$, respectively.

1.3.3 Parton wavefunctions

Parton theory of FQHE was introduced by Jain as a generalization to the idea of composite fermion [41]. In this theory, we imagine that each electron can be divided into k different fictitious particles called partons. The final wavefunction is constructed by placing each parton in an IQHE state n_β where $\beta = 1, 2, \ldots, k$, given by

$$\Psi_\nu^{n_1 n_2 n_3 \cdots} = \mathcal{P}_{\text{LLL}} \prod_{\beta=1}^{k} \Phi_{n_\beta}(z_i) \tag{1.45}$$

Shorthand for a parton state can be denoted by a string $(n_1 n_2 n_3 \ldots)$. Partons can see an effective field that is antiparallel to that experienced by the electrons, in which case the corresponding Slater state is denoted by $\Phi_{\bar{n}} = \Phi_{-n} = \Phi_n^*$.

All k partons share the same coordinates as that of electrons *i.e.* $z_i^\beta = z_i$ for all β. Charge of at excitation of each parton is related to charge of electron by $e_\beta = -\nu e / n_\beta$ and the net electronic filling fraction is given by $\nu = [\sum_{\beta=1}^{k} n_\beta^{-1}]^{-1}$ in terms of the parton fillings. As an example, 2/5 CF state can written as (211) parton state as $\Psi_{2/5}^{CF} = \Psi_{2/5}^{211} = \mathcal{P}_{\text{LLL}} \Phi_2 \Phi_1^2$.

1.4 Haldane's pseudopotentials

Any interaction of $V(|\boldsymbol{r}_1 - \boldsymbol{r}_2|)$ in a rotationally symmetric system can be written in angular momentum basis. In the disk, we denote the state of two electrons that occupy the n_1th and n_2th LLs and have a relative angular momentum m_{rel} and center of mass angular momentum M by $|n_1 n_2; M m_{\text{rel}}\rangle$. It is evident that the state labeled by these quantum numbers, if allowed by symmetry, is unique. It can be generated by exact diagonalization of a rotationally invariant interaction in the appropriate Hilbert space. In fact, given the wave function for the minimum relative angular momentum pair for a given n_1 and n_2, the states may be generated by repeated application of $(\hat{z}_1 \pm \hat{z}_2)$. More specifically, we write

$$|n_1 n_2; M m_{\text{rel}}\rangle \equiv (\hat{z}_1 + \hat{z}_2)^M (\hat{z}_1 - \hat{z}_2)^{m_{\text{rel}}} |(n_1, -n_1)(n_2, -n_2 + \delta_{n_1 n_2})\rangle \tag{1.46}$$

where $\hat{z}_i$ represents the position operator of ith particle and $|(n_1, -n_1)(n_2, -n_2 + \delta_{n_1 n_2})\rangle = |n_1, -n_1\rangle \otimes |n_2, -n_2 + \delta_{n_1 n_2}\rangle$ is the two-particle state (see Eq. 1.16) with the minimum relative angular momentum and zero center of mass momentum.

Any rotationally symmetric interaction $\hat{V}(|\vec{r}_1 - \vec{r}_2|)$ can be characterized by the generalized Haldane's pseudopotentials [31], given by

$$V_{m_{\text{rel}}}^{n_1 n_2; n_1' n_2'} = \langle n_1' n_2'; M m_{\text{rel}} | \hat{V}(|\vec{r}_1 - \vec{r}_2|) | n_1 n_2; M m_{\text{rel}}\rangle \tag{1.47}$$

The pseudopotential does not depend on M, but, in general, has matrix elements involving LL transitions. Relative angular momentum m_{rel} takes even and odd values for bosons and fermions, respectively. In LLL, eigenvalues of $V(|\boldsymbol{r}_1 - \boldsymbol{r}_2|)$ in this basis are given by

$$V_{m_{\text{rel}}} = \frac{\langle M, m_{\text{rel}}| V |M, m_{\text{rel}}\rangle}{\langle M, m_{\text{rel}} |M, m_{\text{rel}}\rangle} \tag{1.48}$$

Any two-particle central potential can be written in terms of pseudopotentials as

$$V = \sum_{m'_{\text{rel}}} V_{m'_{\text{rel}}} \mathcal{P}_{m'_{\text{rel}}} \tag{1.49}$$

where $\mathcal{P}_{m'_{\text{rel}}} = |m'_{\text{rel}}\rangle \langle m'_{\text{rel}}| \otimes \mathbb{I}_{\text{COM}}$ is the projector in m'_{rel}th relative angular momentum. The following figure shows the pseudopotentials of Coulomb interaction in LLL for a few small relative angular momentum values.

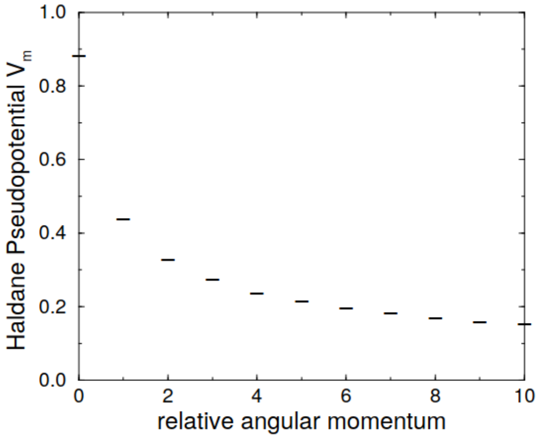

Figure 1.10: The Haldane pseudopotentials $V_{m_{\text{rel}}}$ (in the units of $e^2/\epsilon\ell_B$) for Coulomb interaction corresponding to different relative angular momentum m_{rel} quantum numbers of two-particles in LLL. Pseudopotentials at even m_{rel} are for bosons. [5]

We can design a general interaction by tuning the values of these pseudopotentials [31]. The $V(r)$ corresponding to such toy interactions is rarely physical. This idea can be generalized to n-body interactions with rotational symmetry [42].

On the spherical geometry, the rotational and translation symmetry maps to full $SO(3)$ rotational symmetry. Here $|l_1, l_2, L, L_z\rangle$ is the unique two-particle state of total angular momentum quantum number L and z-component angular momentum L_z, constructed from two particles in LL given by $n_1 = l_1 - Q$ and $n_2 = l_2 - Q$ LLs. With this, the matrix element of interactin V between the two-particle states $|(l'_1, m'_1), (l'_2, m'_2)\rangle$ and $|(l_1, m_1), (l_2, m_2)\rangle$ is given by

$$\delta_{(l_1,l_2)(l'_1,l'_2)} V_L^{l_1,l_2} C^{L,L_z}_{(l_1,m_1)(l_2,m_2)} C^{L,L_z}_{(l_1,m'_1)(l_2,m'_2)} \tag{1.50}$$

where $C^{L,L_z}_{(l_1,m_1)(l_2,m_2)}$ is the Clebsch Gordan coefficient and pseudopotentials $V_L^{l_1,l_2}$ are given by

$$V_L^{l_1,l_2} = \frac{\langle l_1, l_2; L, L_z| \, V \, |l_1, l_2; L, L_z\rangle}{\langle l_1, l_2; L, L_z \, |l_1, l_2; L, L_z\rangle} \tag{1.51}$$

By carefully inspecting the Laughlin wavefunction for filling fraction $1/m$, Haldane realized that all two particles in the wavefunction have relative angular momentum $m_{\text{rel}} \geq m$. Based on this, he constructed a toy interaction with pseudopotentials where

$$v_{m_{\text{rel}}} = \begin{cases} 1 & m_{\text{rel}} < m \\ 0 & m_{\text{rel}} \geq m \end{cases} \tag{1.52}$$

This implies that only those pairs of particles are penalized with energy cost with relative angular momentum $m_{\text{rel}} < m$. Since these angular momentum modes are missing in the Laughlin state by construction, it becomes a unique zero-energy eigenstate of this toy interaction. Similarly, the idea of pseudopotential has been generalized to write Parent Hamiltonians for other variational wavefunctions.

1.5 Structure of the thesis

The thesis is structured as follows. In Chapter 2, we introduce the strong short-range model interaction for rotationally symmetric systems, namely disk, and sphere. We present the low-energy spectra of the model Hamiltonian for spherical geometry, which looks identical to the spectra of the non-interacting system. We also show that the ground state corresponding to different species of FQHE adiabatically connects to the ground state of LLL projected Coulomb interaction. Chapter 3 introduces the exact eigenfunction of the model interaction for the disk geometry. Although disk eigenfunction cannot be directly generalized for spherical geometry, a simplification of eigenfunctions for QPs (quasi-particles) of 1/3 can be written. We numerically verify that these exactly match the ED ground state. The explicit form of the eigenfunction allows us to study various properties of the excitations, like fractional charge and exchange statistics.

In the next two chapters, we present the study of this model interaction in torus and cylinder geometries which are not rotationally symmetric. We introduce notations and symmetries associated with the torus geometry in Chapter 4. The calculation of matrix-element for torus and cylinder is also discussed. Chapter 5 explains how model interaction written for rotationally symmetric geometry can be extended to torus and cylinder. We present the low-energy spectra of the model interaction for both torus and cylinder geometry. Apart from the characteristic topological degeneracy in torus spectra, the low-energy spectra in both geometries come out to be identical to spectra of non-interacting systems. We generalize the exact eigenfunctions for the case of the cylinder. Eigenfunctions could not be directly generalized for the case of a torus, but similar to the spherical case, we could write eigenfunctions for the QPs of the 1/3 state.

In Chapter 6, we study an efficient numerical method based on Monte Carlo techniques for the computation of the real-space entanglement spectra of a class of FQHE wavefunctions. This method allows us to study systems as large as ~ 100 particles in a much shorter time than the direct methods. We use this method to efficiently compute the RSES of a set of simple parton states, namely ϕ_2^2, ϕ_3^2 and ϕ_2^3, which show non-Abelian excitations. Using the RSES of these parton states, we verify that the RSES of parton states of type ϕ_n^k has a one-to-one correspondence with highest weight representations of $\widehat{su}(n)_k$ affine Lie algebra. To verify that this efficient method produces correct entanglement spectra, in Chapter 7, we compare the RSES of projected and unprojected 2/5 CF state for small system sizes. We verify that the efficient method based on the Monte-Carlo technique produces correct spectra. Analytically, it becomes cumbersome to find the exact LLL projection of FQHE states for a large number of particles, limiting the usage of this method to smaller systems only. We circumvent this problem by introducing an efficient approximate LLL projection method based on the Jain-Kamilla projection of CF states. We show that the RSES computed using this approximation for the case of projected 2/3 CF state has identical counting to the RSES of the exactly projected state. Since this approximation allows the usage of the Monte Carlo method, RSES of the projected CF state for a much larger system size can be computed in a time which are orders of magnitude faster.

Finally, we list down the conclusion of our study and provide possible directions for further studies in the Conclusion Chapter.

Part I

A Model Interaction for FQHE

Chapter 2

An Exactly Solvable Model (I) : Exact diagonalization

Strong correlations give rise to exciting phenomena of fundamental interest in all areas of physics. One such phenomenon is the topological phases of matter with exotic emergent properties. Hence, models of strongly correlated systems that can be exactly solved are of particular importance. In this thesis, we consider the phenomenon of fractional quantum Hall effect (FQHE) [43], namely quantization of Hall resistance at $R_H = h/fe^2$ where f is a fraction, that occurs when two-dimensional (2D) electrons are subject to a strong magnetic field. Close to a hundred fractions have been experimentally observed in various 2D electron systems in semiconductor quantum wells and graphene. Several themes in contemporary condensed matter physics, such as fractional charge [38] and fractional statistics [44], composite fermions [39], non-Fermi liquids [45], topological superconductivity with Majorana particles [10, 46], and proposals for topological quantum computation [7], have originated in the context of FQHE.

Theoretical investigations of FQHE begin with the Hamiltonian of 2D electrons in a magnetic field:

$$\hat{H} = \sum_{j=1}^{N} \frac{\hat{\boldsymbol{\pi}}_j^2}{2m_b} + \sum_{j<k=1}^{N} \hat{V}(|\vec{r}_j - \vec{r}_k|), \tag{2.1}$$

where $\hat{\boldsymbol{\pi}}_j = \hat{\mathbf{p}}_j + \frac{e}{c}\vec{A}(\hat{\mathbf{r}}_j)$ is the kinetic momentum, $\vec{A}(\vec{r}) = (B/2)(-y, x, 0)$ is the vector potential producing a magnetic field B in the $+z$ direction, m_b is the electron band mass, N is the number of electrons, and $\hat{V}$ is the interaction between the electrons. The traditional practice since the early works [38, 31] has been to consider the limit where the interaction energy is weak compared to the cyclotron energy, i.e., $\kappa \equiv V_C/\hbar\omega_c \to 0$, where $V_C = e^2/\epsilon\ell$ is the Coulomb interaction scale, ϵ being the dielectric constant of the host material. The reason the system becomes strongly correlated is that, in this limit, electrons are confined to the lowest LL (LLL), leaving the interaction as the only energy scale in the problem. The problem with Coulomb interaction is not exactly solvable. Haldane introduced [31] a model interaction that obtains the Laughlin wave function at $\nu = 1/3$ as the exact ground state (GS). Other model interactions have been designed for several known trial wave functions [47, 48, 49, 50, 51, 52, 53, 54, 55, 56]. These models, however, are not fully solvable, in that each model produces incompressibility only at one fraction, and only the zero energy solutions are known.

In this chapter, we introduce a model interaction that can be solved exactly for all eigenstates at arbitrary filling factors $\nu < 1/2p$ and yields FQHE at all fractions of the form $n/(2pn+1)$, where n and p are integers. Specifically, we will discuss the construction of matrix elements of the model interaction and its exact diagonalization spectrum in the current chapter. We will also discuss interesting topological features of exact diagonalization ground states of the model interaction. We will keep the discussion of its exact eigenfunctions for the next chapter.

A fundamental departure from the previous approaches is that we consider the opposite limit where the interaction is infinitely strong compared to the cyclotron energy, leaving the cyclotron energy as the only energy scale in the problem. The role of the interaction is to impose a nontrivial constraint on the allowed (finite energy) space of many-particle wave functions, which is responsible for FQHE within our model.

This chapter is organized as follows. We first introduce the model interaction on disk geometry in Sec. 2.1. In Sec. 2.2, we discuss the matrix element calculation of the Coulomb and the model interaction on a spherical geometry. We present exact diagonalization spectra of the model interaction for various systems in Sec 2.3. In Sec. 2.4, we present the study of adiabatic connection between the exact diagonalization ground states of model interaction and the ground of (lowest Landau level projected) Coulomb interaction. We compare the model interaction with Trugman-Kivelson Hamiltonian, that is another important short-range interaction in FQHE, in Sec. 2.5. Finally, we conclude our results in Sec. 2.6.

2.1 The Model Hamiltonian

In this section, we will introduce a model interaction that is motivated by the composite fermion (CF) wavefunctions (see Sec. 1.3.2). Constructing a model interaction $\hat{V}$ so that the CF wavefunctions are zero-interaction energy eigenstates of Hamiltonian $H = H_{\text{KE}} + \hat{V}$ is challenging due to several reasons, one of which is that multiplication with the Jastrow factor scatters particles in different LLs. Although LL occupation of the CF wavefunction after the multiplication of Jastrow factor cannot be known, we know that the Jastrow factor increases the relative angular momentum of each pair of particles by $2p$. We use this information to write a strong short-range interaction in terms of pseudopotentials such that its zero-energy eigenfunctions, which are very similar to CF wavefunctions in construction, can be written on disk geometry. We assume fully spin-polarized electrons in the disk geometry; generalization to spinful electrons or bosons is straightforward. Next, we will describe how the interaction is constructed.

In the disk geometry, for two electrons in the nth and n'th LLs, the smallest value of $m_{\rm rel}$ is $-n-n'+\delta_{n,n'}$. We increase $m_{\rm rel}$ of each pair by $2p$, motivated by the Jastrow factor in CF wavefunction, *but in a manner that preserves their LL indices.* In the resulting state, the smallest $m_{\rm rel}$ for a pair with one electron in the nth and the other in n'th LLs is $-n-n'+\delta_{n,n'}+2p$. In other words, pairs with $-n-n'+\delta_{n,n'} \leq m_{\rm rel} < -n-n'+\delta_{n,n'}+2p$ will be absent. This information motivates us to construct an interaction that imposes an energy penalty on these pairs:

$$\hat{V} = \sum_{n\leq n'=0}^{\infty} \sum_{m_{\rm rel}=-n-n'+\delta_{n,n'}}^{-n-n'+\delta_{n,n'}+2p-1} V^{n,n'}_{m_{\rm rel}} |n,n';m_{\rm rel}\rangle\langle n,n';m_{\rm rel}|. \tag{2.2}$$

Here $|n,n';m_{\rm rel}\rangle$ represents the state of a pair of electrons from the nth and n'th LLs, with relative angular momentum $m_{\rm rel}$. $V^{n,n'}_{m_{\rm rel}} = \langle n,n';m_{\rm rel}|\hat{V}|n,n';m_{\rm rel}\rangle$ is the interaction energy of this pair, a generalization of the Haldane pseudopotentials including intra- as well as inter-LL pairs. Our model interaction preserves LLs, and thus keeps only the diagonal pseudopotentials $V^{n_1n_2;n_1n_2}_{m_{\rm rel}} \equiv V^{n_1n_2}_{m_{\rm rel}}$. (Note that pairs with certain $m_{\rm rel}$'s may not be allowed due to exchange symmetry; the corresponding terms are automatically absent in the Hamiltonian. For ease of notation, we have suppressed the center-of-mass degree of freedom, which does not affect the pseudopotentials.) The above interaction conserves the number of electrons in each LL (denoted N_n for the nth LL) and therefore, kinetic energy. Each eigenstate is labeled by the total angular momentum $m_{\rm total} = \sum_j m_j$, and LL occupation $(N_0, N_1, N_2, \ldots)$. To describe the low-energy physics of a given fraction at $\nu = \nu^*/(2p\nu^*+1)$, terms containing only a finite number of LLs need to be kept in the above summation; this restricted interaction is thus local.

Although the interaction given in Eq. (2.2) is for the disk geometry, we can also write it for the sphere. Since exact diagonalization is more straightforward in spherical geometry due to its compactness, we describe the construction of interaction matrix elements on a sphere in the next section.

2.2 Matrix elements in the spherical geometry

A general two-particle interaction between particles on a sphere can be written as follows

$$\sum_{l_1,l_2=|Q|}^{\infty} \sum_{m_1=-l_1}^{l_1} \sum_{m_2=-l_2}^{l_2} c^{\dagger}_{l_1m_1} c^{\dagger}_{l_2m_2} V_{12;1'2'} c_{l'_2m'_2} c_{l'_1m'_1} \tag{2.3}$$

where $V_{12;1'2'}$ is a shorthand for the matrix element of the interactions between two-particle states ie

$$V_{12;1'2'} \equiv \langle (l_1,m_1),(l_2,m_2)|\hat{V}|(l'_1,m'_1),(l'_2,m'_2)\rangle \tag{2.4}$$

where $|(l_1,m_1),(l_2,m_2)\rangle$ is a two-particle state on sphere with particles occupying m_1 and m_2 angular momentum states in the LLs l_1 and l_2 respectively.

We can fully characterize any two-particle interaction by its matrix elements. In the remainder of this section, we first describe the calculation of the matrix elements for the Coulomb interaction [57], as well as for our model interaction for electrons residing on the surface of a sphere.

2.2.1 Coulomb interaction

The Coulomb interaction between particles on the surface of a sphere is $1/r$ where r is the chord distance $|\mathbf{r}_a - \mathbf{r}_b|$ between the positions $\mathbf{r}_a \equiv (\theta_a, \phi_a)$ and $\mathbf{r}_2 \equiv (\theta_b, \phi_b)$. The radius of the sphere is $R = \sqrt{Q}$ in units of the magnetic length $\ell = \sqrt{\hbar c/eB}$, $B = 2Q\Phi_0/4\pi R^2$ is the field strength on the surface of the sphere, and $2Q$ is the (integer) number of flux quanta emanating from a monopole placed at the center of the sphere. Eigenstates of the single particle Hamiltonian $\hat{\boldsymbol{\pi}}^2/2m_b$ in this geometry are called the monopole spherical harmonics Y_{Qlm} [32, 33]. The quantity $l = |Q| + n$ is the angular momentum of the orbitals in the nth LL ($n = 0, 1, \dots$) and $m = -l, -l+1, \dots l$ labels the degenerate states in the nth LL.

The Coulomb potential can be expanded in terms of the Legendre polynomials as

$$\frac{1}{r} = \frac{1}{\sqrt{Q}} \sum_{l=0}^{\infty} P_l(\cos\theta),$$

where θ is the angle subtended by $\mathbf{r}_a$ and $\mathbf{r}_b$ at the origin. The Legendre Polynomial can be expressed in terms of the monopole spherical harmonics (Eq. 14.30.9 of Ref. [58]) resulting in the expression

$$\frac{1}{r} = \frac{1}{\sqrt{Q}} \sum_{l=0}^{\infty} \frac{4\pi}{2l+1} \sum_{m=-l}^{l} Y^*_{0lm}(a) Y_{0lm}(b). \tag{2.5}$$

Here the arguments a and b of the monopole Harmonics are a short-hand notation to represent the coordinates (θ_a, ϕ_a) and (θ_b, ϕ_b). The matrix element (Eq. 2.4) of the Coulomb interaction between a pair of (antisymmetrized) two-particle fermionic states $|(l_1, m_1)(l_2, m_2)\rangle$ and $|(l'_1, m'_1)(l'_2, m'_2)\rangle$ is given by

$$V_{12;1'2'} \equiv V^{(l'_1 m'_1)(l'_2 m'_2)}_{(l_1 m_1)(l_2 m_2)} - V^{(l'_2 m'_2)(l'_1 m'_1)}_{(l_1 m_1)(l_2 m_2)} + V^{(l'_2 m'_2)(l'_1 m'_1)}_{(l_2 m_2)(l_1 m_1)} - V^{(l'_1 m'_1)(l'_2 m'_2)}_{(l_2 m_2)(l_1 m_1)} \tag{2.6}$$

where

$$V^{(l'_1 m'_1)(l'_2 m'_2)}_{(l_1 m_1)(l_2 m_2)} = \int Y^*_{Ql_1 m_1}(a) Y^*_{Ql_2 m_2}(b) V(r) Y_{Ql'_1 m'_1}(a) Y_{Ql'_2 m'_2}(b) d\Omega_a d\Omega_b. \tag{2.7}$$

Theorems 1 and 3 from Ref [33] can be used to evaluate the integrals involved in terms of Wigner 3j symbols, yielding the following expression for $V^{(l'_1 m'_1)(l'_2 m'_2)}_{(l_1 m_1)(l_2 m_2)}$:

$$\sum_{l=0}^{\infty}\nu_l\sum_{m=-l}^{l}\sqrt{(2l_1+1)(2l_2+1)(2l_1'+1)(2l_2'+1)}(-1)^{2Q+m_1+m_2+l_1+l_2+l_1'+l_2'}$$
$$\begin{pmatrix} l_1 & l & l_1' \\ -m_1 & -m & m_1 \end{pmatrix}\begin{pmatrix} l_2 & l & l_2' \\ -m_2 & m & m_2 \end{pmatrix}\begin{pmatrix} l_1 & l & l_1' \\ -Q & 0 & Q \end{pmatrix}\begin{pmatrix} l_2 & l & l_2' \\ -Q & 0 & Q \end{pmatrix} \quad (2.8)$$

where $\nu_l = 1/\sqrt{Q}$. The series can be summed numerically to obtain the Coulomb matrix elements. The series terminates at sufficiently large l as the Wigner 3j-symbols are nonzero only for those arguments that satisfy certain constraints (Sec 34.2 of Ref [58]).

2.2.2 Model interaction

We obtain the matrix elements (Eq. 2.4) of the model interaction introduced in this chapter by sandwiching the interaction shown in Eq. (2.2) between two-particle states. For convenience, we reproduce full details of the interaction here

$$\hat{V} = \sum_{l_1<l_2=0}^{\infty}\ \sum_{L=2Q+l_1+l_2-\delta_{l_1l_2}-2p+1}^{2Q+l_1+l_2-\delta_{l_1l_2}}\ \sum_{L_z=-L}^{L} V_L^{l_1,l_2}\ \times\ |l_1,l_2,L,L_z\rangle\langle l_1,l_2,L,L_z| \quad (2.9)$$

Here $|l_1, l_2, L, L_z\rangle$ is the unique two-particle state of total angular momentum quantum number L and z-component angular momentum L_z, constructed from two particles in LLs indexed by $n_1 = l_1 - Q$ and $n_2 = l_2 - Q$. With this, the matrix element (Eq. 2.4) between the two-particle states $|(l_1', m_1'), (l_2', m_2')\rangle$ and $|(l_1, m_1), (l_2, m_2)\rangle$ is given by

$$\delta_{(l_1,l_2)(l_1',l_2')}V_L^{l_1,l_2}C^{L,L_z}_{(l_1,m_1)(l_2,m_2)}C^{L,L_z}_{(l_1,m_1')(l_2,m_2')} \quad (2.10)$$

where $C^{L,L_z}_{(l_1,m_1)(l_2,m_2)}$ is the Clebsch Gordan coefficient.

2.3 Exact spectrum of Model interaction on sphere

For diagonalization studies, we find it convenient to employ Haldane's spherical geometry [31], where N electrons move on a sphere with a total radial magnetic flux of $2Q\phi_0$, where $2Q$ is an integer. The single-particle orbitals in the nth LL have angular momentum $l = |Q| + n$. The eigenstates are labeled by the total angular momentum L. The relative pair angular momentum M of the disk geometry corresponds to pair angular momentum $L = 2Q - M$ on the sphere. The interaction [Eq.(2.2)] therefore translates to

$$\hat{V} = \sum_{n\leq n'=0}^{\infty}\ \sum_{L=2Q+n+n'-\delta_{n,n'}-2p+1}^{2Q+n+n'-\delta_{n,n'}} V_L^{n,n'}|n,n';L\rangle\langle n,n':L|. \quad (2.11)$$

According to the standard CF theory the interacting system $(N, 2Q)$ of electrons relates to a noninteracting system $(N, 2Q^*)$ of CFs with $Q^* = Q - p(N-1)$. We specialize to $2p = 2$ below. We will now consider the strong interaction limit $V_m^{n,n'}/\hbar\omega_c \to \infty$, so all eigenstates with nonzero interaction energy are projected out. The collection of wave functions that (i) have zero interaction energy and (ii) are eigenstates of the kinetic energy will be referred to as the $\mathcal{V}_\infty$ wave functions.

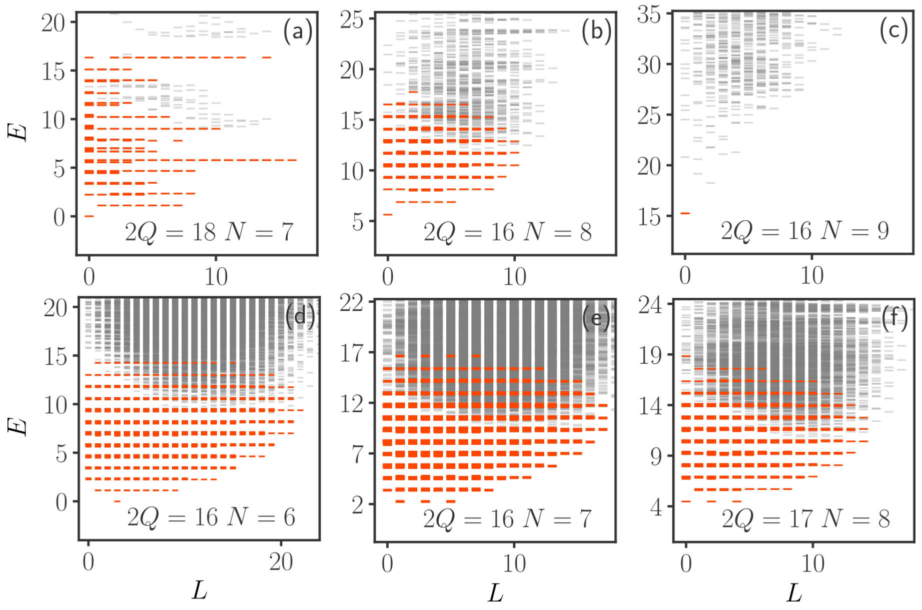

Figure 2.1: Spectra of the model Hamiltonian for representative systems in the spherical geometry, with N particles in $2Q$ flux quanta. All nonzero pseudopotentials [Eq. (2.11)] are set to $V_L^{n,n'} = 20\hbar\omega_c$, and the Hilbert space is restricted to the three lowest LLs. The energy E is in units of $\hbar\omega_c$, measured relative to the zero point energy $N\hbar\omega_c/2$. L is the total orbital angular momentum. Orange markers show the $\mathcal{V}_\infty$ states with zero interaction energy. (Each orange dash may represent many degenerate eigenstates.) Black dashes show eigenstates with nonzero interaction energies; these will be pushed to infinity in the limit $V_L^{n,n'}/\hbar\omega_c \to \infty$. (a)–(c) Spectra for systems at $\nu = 1/3$, $2/5$, and $3/7$; for $\nu = 3/7$ the spectrum has no orange-colored excited states, as we have kept only the three lowest LLs in our study. (d)–(f) Spectra for N and $2Q$ for which the GS is not incompressible. Panel (a) shows only a subset of the higher energy states due to difficulty in diagonalization of Hamiltonians with large degeneracies. The slight broadening of the orange bands is a finite size effect, resulting from the fact that for finite systems in the spherical geometry, the inter-LL gap depends slightly on the LL index.

We have performed exact diagonalization of this Hamiltonian for many systems $(N, 2Q) = (5, 12)$, $(5, 11)$, $(6, 11)$, $(6, 12)$, $(6, 15)$, $(6, 16)$, $(7, 16)$, $(8, 16)$, $(9, 16)$, $(8, 17)$, and $(7, 18)$ in the Hilbert space restricted to the three lowest LLs. In many cases the full Hilbert space is too large to perform efficient numerical calculations, but the calculation is possible because diagonalization can be performed in each (N_0, N_1, N_2) sector separately. The resulting spectra are shown in Fig. 2.1. In our calculations, we have set all nonzero pseudopotentials to unity and $\hbar\omega_c = 0.05$. The states with zero interaction energy (in the

$\mathcal{V}_\infty$-sector) are highlighted in orange. The high-energy parts of the spectra in Fig. 2.1 also show states outside the $\mathcal{V}_\infty$-sector (black dashes), which will be pushed to infinity in the strong interaction limit *i.e.* $V_m^{n,n'}/\hbar\omega_c \to \infty$.

The states in the $\mathcal{V}_\infty$-sector display IQHE-like structure of bands of states separated by $\sim \hbar\omega_c$ ($\sim$ is needed because the LL spacing in the spherical geometry is not exactly $\hbar\omega_c$ for finite systems [59]). In fact, for each case, including those shown in Fig. 2.1, the spectrum is identical to that for N noninteracting electrons at flux $Q^* = Q - p(N-1)$. The restriction to three LLs is purely for feasibility of numerics and is not a limitation for the ansatz solutions. We have tested close to 200 different $(N_0, N_1, N_2, 2Q)$ systems (see 3.3), and in each case the dimension of the $\mathcal{V}_\infty$ space in the exact spectrum matches that of noninteracting fermions at $(N_0, N_1, N_2, 2Q^*)$.

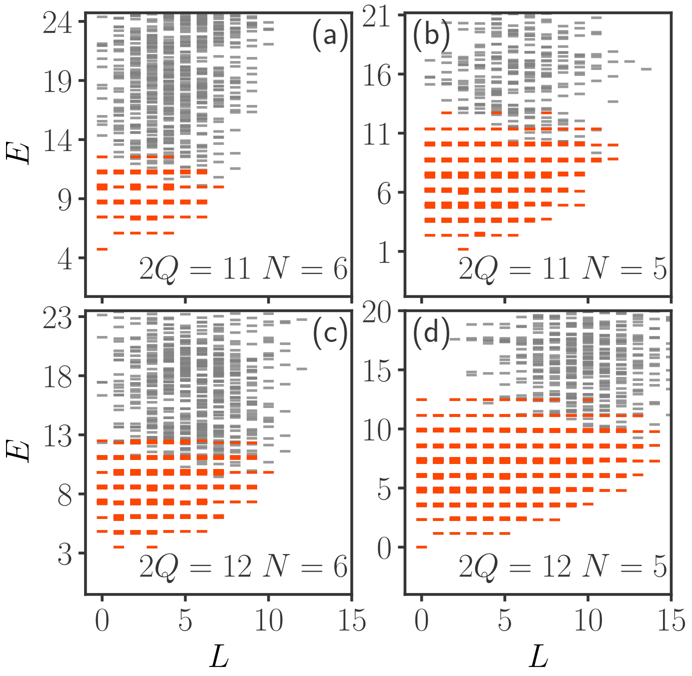

Figure 2.2: Spectra for our model interaction for different $(N, 2Q)$ systems on the sphere. Orange markers indicate eigenstates with zero interaction energies. $\hbar\omega$ is set to 1 and all non-zero pseudopotentials are set to 20. The black dashes show eigenstates that have nonzero interaction energy, i.e. are outside the $\mathcal{V}_\infty$ sector.

Figure 2.2 shows additional representative spectra, all evaluated within the Hilbert space of the lowest 3 LLs. All nonzero pseudopotentials of the interaction are set to 20 in units of $\hbar\omega_c = 1$. The zero interaction energy states (*i.e.* the states belonging to $\mathcal{V}_\infty$-sector) are indicated using orange markers and the remaining states are indicated with gray markers; the latter will be pushed to infinity in strong interaction limit. Panel (a) shows the system $(N, 2Q) = (6, 11)$, which maps into noninteracting fermion system $(N, 2Q^*) = (6, 1)$. Here, the spectrum contains a single incompressible ground state with $(N_0, N_1, N_2) = (2, 4, 0)$, followed by neutral excitations at $\hbar\omega_c$ at $L = 1, 2, 3, 4$ in the $(N_0, N_1, N_2) = (2, 3, 1)$ sector. Panel (b) shows the spectrum of $(N, 2Q) = (5, 11)$, which maps into $(N, 2Q^*) = (5, 3)$. The ground state corresponds to $(N_0, N_1, N_2) = (4, 1, 0)$, *i.e.* describes a single quasiparticle of the 1/3 state. The angular momentum of this quasiparticle is predicted to be $L = 5/2$. Panel (c) shows the spectrum of $(N, 2Q) = (6, 12)$, which maps into $(N, 2Q^*) = (6, 2)$. The ground state sector, with $(N_0, N_1, N_2) = (3, 3, 0)$, has two quasiholes of the 2/5 state, each carrying an angular momentum of $l = 2$. Addition of their angular momentum produces low energy states at total $L = 1, 3$, precisely as seen in panel (c). Panel (d) shows the $(N, 2Q) = (5, 12)$ which corresponds to the one filled LL state $(N, 2Q^*) = (5, 4)$. In all cases low energy states show same structure as what is expected in the LLL Coulomb spectrum.

Thus, we have energies not just for the incompressible GSs but also for their quasiholes (QHs), quasiparticles (QPs), neutral excitations, and, in fact, all $\mathcal{V}_\infty$ eigenstates. The exact mapping to noninteracting fermions at filling ν^* is lost if we set some of the $V_L^{n,n'}$ in Eq. (2.11) to zero or include additional pseudopotentials; in particular, the inter-LL pseudopotentials are necessary.

2.4 Topological properties

While $\kappa \equiv V_C/\hbar\omega_c$ was small in the early experiments [43], FQHE is routinely seen for $\kappa \sim 5-7$ in p-doped GaAs [60] and ZnO quantum wells [61] and is seen to survive even up to $\kappa \sim 40$ in high-quality AlAs quantum wells [62]. The limit of strong interactions is thus not entirely unphysical for FQHE. While intention of our model is not to produce a quantitative theory of experiments for large κ, we now show that it shares topological features with the FQHE of Coulomb electrons in the LLL.

Our theory reproduces the prominent qualitative features of the phenomenology, namely gapped states at $\nu = n/(2pn+1)$ and, by extension to the $n \to \infty$ limit, the compressible Fermi sealike states [45] at $\nu = 1/2p$. Many topological properties follow from the counting of lowest energy excitations, which our model produces exactly. The fractional charge of magnitude $e^* = e/(2pn+1)$ for the QPs and QHs follows from the presence of gap at $\nu = n/(2pn+1)$ but can also be deduced from the mapping into $2Q^* = 2Q - 2p(N-1)$ [4]. We have confirmed fractional charge by explicit evaluation in finite-size systems (see Sec. 3.4.1). The one-to-one correspondence with IQHE implies that the excitations obey Abelian braid statistics, because the wave function Φ^α, and thus also Ψ^α, is uniquely determined by specifying the positions of the QPs or QHs. The edge physics of the FQHE state $\nu = n/(2pn+1)$ is analogous to that of the IQHE state at $\nu^* = n$, described by n chiral edge modes. Real space or momentum space entanglement spectra should also reflect these edge modes [63], but the currently accessible system sizes are insufficient to reveal the characteristic features (except for $\nu = 1/3$) [64, 65]. Another topological quantity is the shift S, or the orbital spin [66], defined by the relation $2Q = \nu^{-1}N - S$ for the flux where FQHE states occur in the spherical geometry. Our model produces the same shift, $S = n + 2p$, as the standard CF theory.

We next ask whether a path exists in the space of Hamiltonians that takes the gapped states of the model to those of the LLL Coulomb Hamiltonian without gap closing. This parameter space is large, consisting of the cyclotron energy and many pseudopotentials, leaving us with many different paths to consider. If we simply increase the cyclotron energy while retaining the model interaction, the orange states in Fig. 2.1 will float up, resulting in many level crossings. (The only exceptions are the GS and QH states at $\nu = 1/3$, which are already in the LLL, and also ground states of the V_1 pseudopotential; these remain ground states throughout.) However, a more general interaction will convert the level crossings into anticrossings, for any finite system, thus opening a gap everywhere. We ask if we can identify a path where the gap remains robust throughout. We have studied the evolution of the GS, the QP state and the QH state as the Hamiltonian is continuously deformed from our model to the Coulomb interaction with large cyclotron energy for $\nu = 1/3$ and $\nu = 2/5$.

We will show how the model Hamiltonian (in the spherical geometry) evolves as the Hamiltonian is continuously changed to the LLL Coulomb Hamiltonian along a particular path in the parameter space. Each row of the figure shows the evolution of the spectrum within a single total angular momentum sector. The Hamiltonian is parametrized by two parameters λ and β as follows

$$\hat{H}(\beta, \lambda) = \frac{\beta}{\hbar\omega_c} \sum_{i=1}^{N} \frac{\hat{\boldsymbol{\pi}}_i^2}{2m} + (1-\lambda)\hat{V} + \lambda \hat{V}_{\text{Coulomb}} \tag{2.12}$$

where $\hat{V}$ is the model Hamiltonian and $\hat{V}_{\text{Coulomb}}$ is the Coulomb Hamiltonian. All energies are quoted in units of $e^2/(\epsilon\ell)$. Nonzero pseudopotentials of the model Hamiltonian are all set to 1.

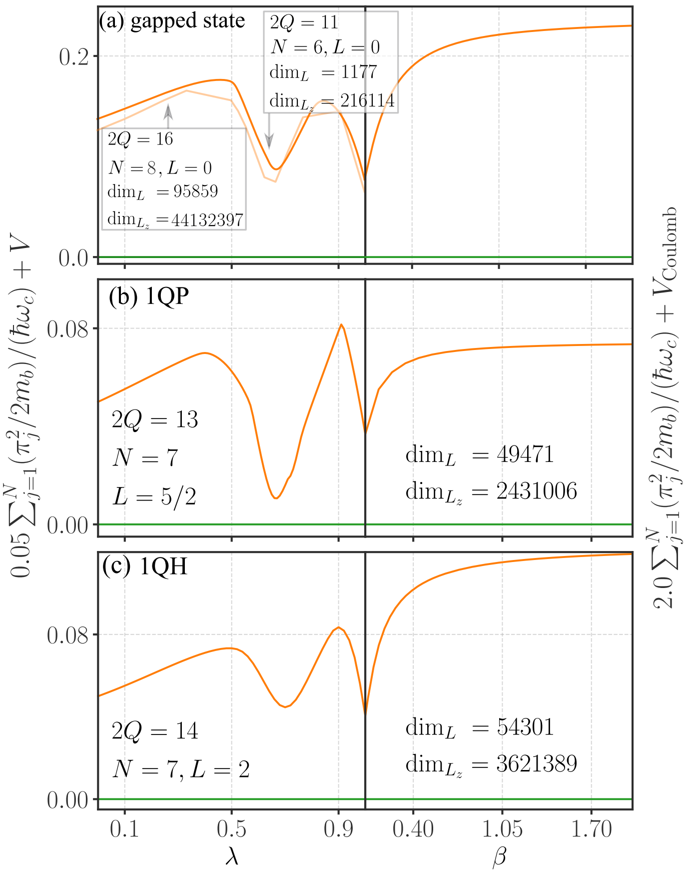

Figure 2.3: Adiabatic connection between the model and Coulomb Hamiltonian at $\nu = 2/5$. The Hamiltonian is defined by $H = \frac{\beta}{\hbar\omega_c}\sum_{j=1}^{N}\frac{\hat{\boldsymbol{\pi}}_j^2}{2m_b} + (1-\lambda)V + \lambda V_{\text{Coulomb}}$, where all energies are in units of $e^2/\epsilon\ell$, V is our model interaction in which all nonzero pseudopotentials are set to unity, and V_{Coulomb} is the Coulomb interaction. Panel (a) shows the lowest two energies (green, orange) in the $L = 0$ sector in a system with an incompressible GS as the Hamiltonian is varied. On the left side, the interaction Hamiltonian is varied (parametrized by λ) from the model interaction to the Coulomb interaction, keeping $\beta = 0.05$. On the right side, the cyclotron energy (parametrized by β) is sent to a large value ($\beta = 2$), with the interaction fixed at its Coulomb value. All energies are measured relative to the GS energy. The darker (lighter) shade line shows the data for $N = 6$ (8) particles. For $N = 8$, evolution in only the initial half was calculated. Panels (b) and (c) correspond to the evolution of a single QP and a single QH state of 2/5 that occur at angular momenta 5/2 and 2. In all cases, the gap is seen to remain finite throughout. In row (a), at small λ, the simplest excitation in the $L = 0$ corresponds to two particle-hole pairs whose energy above ground state is given by $2\beta(1+1/Q)$; the deviation from 2β arises because, in the spherical geometry, the LL separation has a finite size deviation from $\hbar\omega_c$. The dimensions of the Hilbert space in the relevant L and L_z sectors are shown on the figures, denoted $\dim_L$ and $\dim_{L_z}$, respectively.

Figure 2.3 shows the evolution of the incompressible GS, the single QP state, and the single QH state at filling factor $\nu = 2/5$ along the following path: we first vary parameters to go from our model interaction continuously to Coulomb (left side), and then increase

$\hbar\omega_c$ (right side). The GS, single QP and single QH states of the model evolve continuously into the corresponding LLL Coulomb states.

Fig. 2.4 shows how low-energy neutral excitation states in the model adiabatically connect to that of LLL projected Coulomb interaction at filling fraction $\nu = 2/5$. Adiabatic continuity for the low-energy states is seen in all cases; the qualitatively different behavior for $L = 1$ (note the different energy scale for this row), for which the states are pushed to very high energies, captures the absence of a low-energy neutral mode in the LLL Coulomb spectrum.

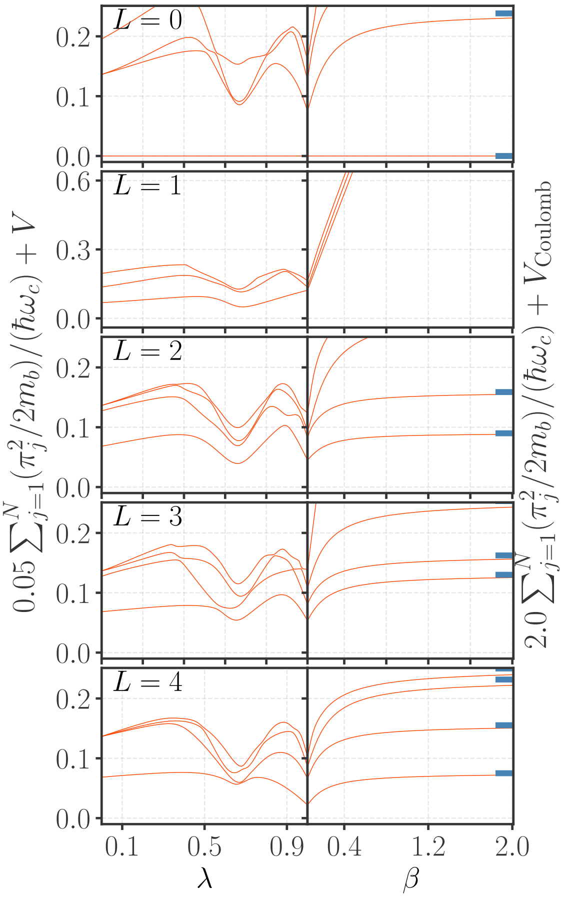

Figure 2.4: Demonstration of adiabatic continuity between the ground state and the low energy neutral excitations of the model Hamiltonian and the lowest Landau level Coulomb Hamiltonian for $N = 6$ particles at $\nu = 2/5$.

Figure 2.5 shows the same for $\nu = 1/3$. The left panels show the change in the spectrum as λ is changed from 0 to 1 with $\beta = 0.05$. At the left end, the Hamiltonian $\hat{H}(\beta = 0.05, \lambda = 0)$ represents a system with a small cyclotron gap of 0.05 and particles interacting via the model Hamiltonian $\hat{V}$. At the right end of the left panels, $\hat{H}(\beta = 0.05, \lambda = 1)$ represents the Hamiltonian of the system with the same cyclotron gap but instead interacting via the Coulomb interaction. The right panels show the spectral transformation as β is varied from 0.05 to 2 keeping $\lambda = 1$. At the rightmost end, on account of the relatively large cyclotron energy, particles predominantly reside in the LLL.

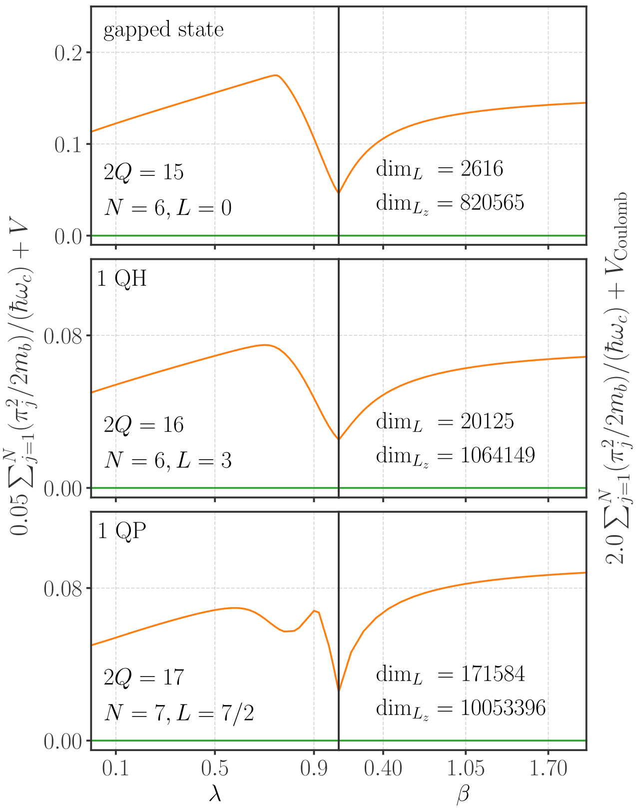

Figure 2.5: Demonstration of adiabatic connectivity of GS (top), single QH (middle) and single QP (bottom) states of our model Hamiltonian and the those of the LLL Coulomb Hamiltonian for a finite system near $\nu = 1/3$. The form of Hamiltonian is $\hat{H} = \beta\sum_{j=1}^{N}(\hat{\boldsymbol{\pi}}_j^2/2m_b)/(\hbar\omega_c) + (1-\lambda)\hat{V} + \lambda\hat{V}_{\text{Coulomb}}$. Three LLs were included in the calculation. The left panels show the change in the spectra as λ changes from 0 to 1 keeping $\beta = 0.05$ and the right panels show the variation as β changes from 0.05 to 2. Note that the single QP and single QH states have an angular momentum of $L = N/2 + 1$ and $N/2$ respectively. All the energies are relative to the GS in the corresponding system.

For $\nu = 1/3$, single quasihole state occurs with an angular momentum of $L = N/2$ in a system with $2Q = 3N - 2$. This state is again identical to the single QH state of the Laughlin state and we do find that along the path that we have studied, the single QH of the model and Coulomb interactions are connected without gap closing (middle panel of Fig 2.5). Most importantly, the single QP of the model which occurs with angular momentum $L = N/2 + 1$ in a system $2Q = 3N - 4$ is also adiabatically connected to the corresponding state of the Coulomb Hamiltonian (Fig 2.5, bottom).

Fig. 2.6 shows the adiabatic continuity between neutral excitations states of model interaction and LLL Coulomb interaction at $\nu = 1/3$. Different rows shows the spectra in different L sectors. The ground state of the model Hamiltonian adiabatically connects to ground state for LLL Coulomb Hamiltonian. The same is true from neutral excitations, with the exception of level-crossing at $L = 2$.

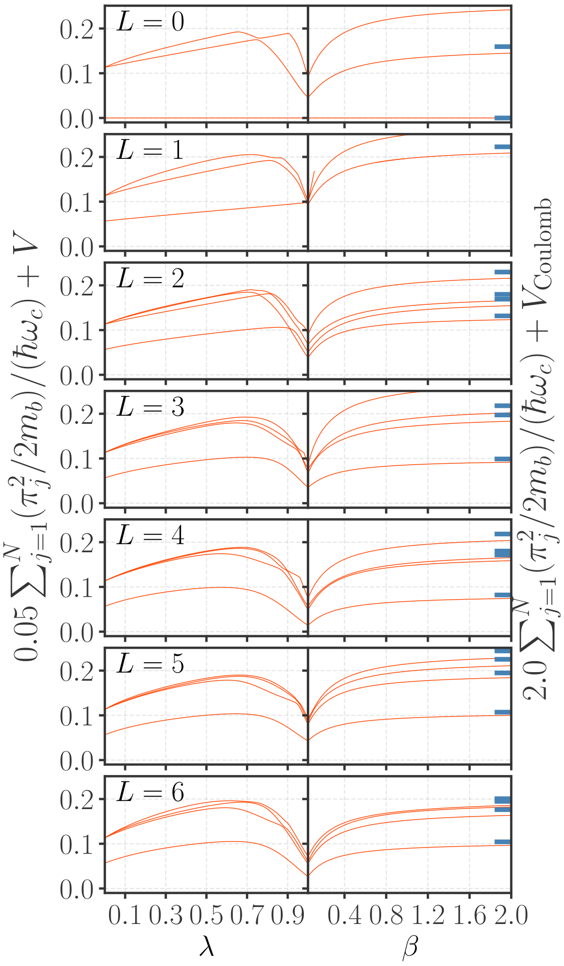

Figure 2.6: Demonstration of adiabatic connectivity of low energy eigenstates of our model Hamiltonian and the those of the LLL Coulomb Hamiltonian for a six particle system at $\nu = 1/3$.

The spectrum of the model interaction closely match the spectrum of the Coulomb interaction for particles strictly confined to the LLL, which occurs to the limit of infinite cyclotron gaps (Fig 2.7 (bottom)). The uniform ground state of the model Hamiltonian ($L = 0$ sector shown in the top) at $2Q = 3N - 3$ is identical to the Laughlin state, and we expect that it is adiabatically connected to the Coulomb Hamiltonian. We do find that along the path that we have chosen, the two are indeed connected without gap closing (Fig 2.5 top). As discussed below, the simplest low energy states namely single QH and QP states also appear to be adiabatically connected to each other (Fig 2.7).

For the largest systems at $\nu = 1/3$ and $2/5$ that we could diagonalize, the physics of the model and the LLL Coulomb Hamiltonian are adiabatically connected. Nonetheless, as with all numerical results, we cannot definitively assert that adiabatic continuity will survive in the thermodynamic limit.

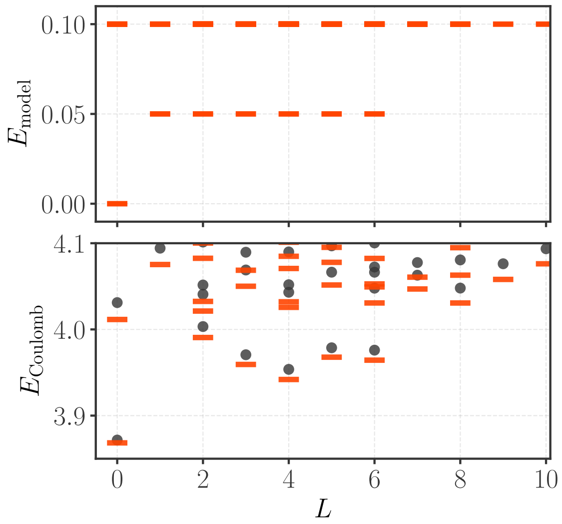

Figure 2.7: Low energy spectra of the Hamiltonians $\hat{H}(\beta = 0.05, \lambda = 0)$ (top) and $\hat{H}(\beta = 2.0, \lambda = 1)$ (bottom, dashes) for a systen of $N = 6$ particles and $2Q = 15$, at $\nu = 1/3$. Dots in the bottom figure represent the LLL Coulomb spectrum. For simplicity the subleading $1/Q$ dependent part of the cylotron energy on the sphere was omitted in the top panel.

2.5 Comparison to Trugman-Kivelson Hamiltonian

Trugman and Kivelson [47] (TK) introduced the interaction

$$V_{\text{TK}}(r) = \nabla^2 \delta(r), \tag{2.13}$$

which obtains Laughlin's wave function as the unique solution at $\nu = 1/3$ in the LLL Hilbert space. Interestingly, if one sets the lowest two LLs degenerate while sending the remaining higher LLs to infinity, then the unprojected Jain state at $\nu = 2/5$:

$$\Psi^{\text{CF}}_{2/5} = \prod_{i<j=1}^{N} (z_i - z_j)^2 \, \Phi_2(\{z_i\}), \tag{2.14}$$

where $\Phi_2(\{z_i\})$ is the spin polarized integer quantum Hall state at filling fraction $\nu = 2$, appears as the unique zero-energy ground state for the TK interaction [48, 49, 50]. This state occurs at flux $2Q = 5N/2 - 4$ on the sphere. It is interesting to ask in what sense the TK interaction is different from the one considered here.

On the sphere, the TK interaction can be expanded in spherical Harmonics as (compare with Eq. 2.5)

$$\nabla^2 \delta(\mathbf{r}_a - \mathbf{r}_b) = -\sum_{l=0}^{\infty} \sum_{m=-l}^{l} \frac{l(l+1)}{Q} Y_{0lm}(a) Y^*_{0lm}(b) \tag{2.15}$$

where we have expanded the Dirac delta function in monopole spherical harmonics (Eq. 1.17.25 of Ref [58]). The matrix elements of the TK Hamiltonian can be found in a manner similar to that for the Coulomb Hamiltonian and have the same form as Eq. 2.6 and Eq. 2.8 but with $\nu_l = -l(l+1)(2l+1)/4\pi Q$.

It is interesting to ask in what way the TK Hamiltonian is different from ours. To address this, we consider the system of particles living in the Hilbert space of the two lowest LLs. Our model Hamiltonian introduced in this chapter

1. imposes an energy penalty on all two-particle states of relative angular momenta $L = 2Q+1$ and $2Q$ on the sphere; and on the unique multiplet of two-particle states of angular momenta $2Q-1$ in the LLL.
2. It is an LL conserving Hamiltonian.

Like our model Hamiltonian, the TK Hamiltonian also

1. imposes an energy penalty on all states in the $L = 2Q+1$ and $2Q$ sectors.
2. In the $L = 2Q-1$ sector, however, it imposes a penalty on a particular two-particle multiplet in the three dimensional (multiplet) space of the $L = 2Q-1$ states. This multiplet is a linear combination of two-particles states in multiple LLs. *That makes TK Hamiltonian LL non-conserving.*

The "forbidden" two-particle multiplet of the TK Hamiltonian in the $L = 2Q-1$ sector can be inferred from numerically studying the two-particle spectrum of the TK Hamiltonian, using the matrix elements evaluated as described above.

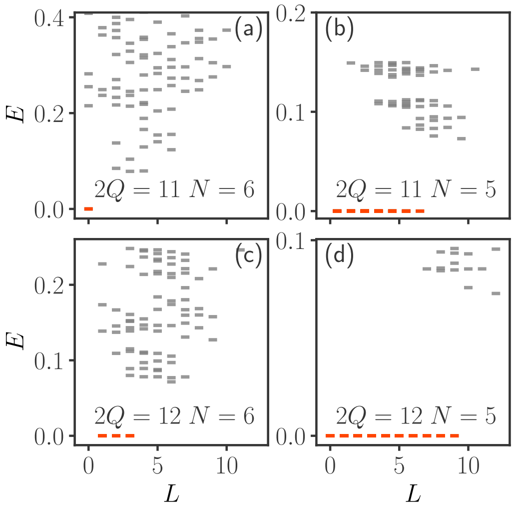

Figure 2.8: Spectra for the Trugman-Kivelson interaction for several $(N, 2Q)$ systems (same as in Fig. 2.2) obtained by exact diagonalization. Only two lowest Landau levels are included, which are assumed to be degenerate. Zero energy states are shown in orange. The energy is quoted in arbitrary units (set by the TK interaction), but all four plots are in the same units.

Figure 2.8 depicts spectra for the TK Hamiltonian for the same $(N, 2Q)$ systems as in Fig. 2.2. Only the two lowest LLs (taken as degenerate) are included in the diagonalization. The unique zero energy state occurring in the panel (a) is identical to the Jain unprojected wave function in Eq. 2.14. The zero energy states in the remaining panels are highly degenerate; their counting matches with that of the corresponding $(N, 2Q^{*})$ system of non-interacting fermions with the lowest two LLs taken as degenerate.

When compared to the TK Hamiltonian, the model interaction produces identical low-energy spectra to the corresponding non-interacting system, not just for filling fraction 2/5 but all Jain sequence of filling fractions. Thus, it works for systems with an arbitrary number of LLs, not just the lowest two. The choice to work with the lowest 3 LLs in our calculations is purely for numerical feasibility.

2.6 Conclusion

In summary, we introduce an exactly solvable model for a strongly correlated system of electrons in a magnetic field. An appealing aspect of this model is that it exactly implements the physics of "noninteracting CFs," in that the spectrum of strongly interacting electrons at $\nu = \nu^*/(2p\nu^* + 1)$ matches that of noninteracting fermions at ν^*. For finite systems, the exact diagonalization ground states of the model interaction for various systems adiabatically connect to the corresponding ground states of the LLL projected Coulomb interaction. Due to the sharp increase in the Hilbert space dimension, we could not perform a finite-size scaling study of this adiabatic gap. Without this check, we cannot conclude that the model and the LLL projected Coulomb interactions are in the same topological class.

Although the interaction is presented employing the relative angular momentum quantum numbers, which require rotational symmetry, the interaction is local, and its physics is expected to be independent of the boundary conditions in the thermodynamic limit. Generalization to the torus geometry [67, 34, 68, 40] is a natural question in this context and will be addressed in Chapter 5. The wave functions in this chapter can be extended to accommodate an anisotropic electron mass [69, 70]; construction of a suitable anisotropic interaction for these states is an interesting open question.

Chapter 3

An Exactly Solvable Model (II) : Study of exact eigenfunctions

In the previous chapter, we introduced a model interaction that describes FQHE at the Jain sequence of filling fraction and claimed that it is *exactly solvable.* In this chapter, we will introduce the form of exact zero-energy eigenfunctions for model interaction on disk geometry. Using numerical methods, we explicitly count and verify that the disk eigenfunctions span the entire $\mathcal{V}_\infty$ space, which is the eigenspace of parent Hamiltonian in the strong interaction limit $i.e.\, V \to \infty$. Although we cannot directly generalize the disk eigenfunctions for spherical geometry, we could construct eigenfunctions for quasiparticles of filling fractions $1/m$ using an alternate method. In addition, we show that the excitations generated in the eigenfunctions have correct fractional charges and exhibit expected fractional statistics.

This chapter is organized as follows. In Sec. 3.1, we introduce the idea of guiding center coordinates in the quantum Hall effect. Sec. 3.2 explains the construction of exact eigenfunctions on disk geometry using the guiding center coordinates. This section also describes how disk eigenfunctions can be generalized to spherical geometry, where guiding center coordinates are not well defined. In Sec. 3.3, by explicit counting using numerical methods, we verify that these eigenfunctions indeed span the complete $\mathcal{V}_\infty$ space. Study of topological features like fractional charge and berry phase of charged excitations of exact eigenfunctions are studied in Sec. 3.4. Conclusion of the chapter is presented in Sec. 3.5.

3.1 Guiding center coordinates

While explaining Landau quantization, we defined a constant of motion for IQHE Hamiltonian (Eq. 1.15), which in position coordinates is given by

$$\hat{Z} = \hat{z} - i\sqrt{2}\ell\hat{a}, \tag{3.1}$$

This is called the guiding center coordinate. Action of this operator changes a state without altering its energy, indicating that it affects degrees of freedom different from those captured by the energy ladder operators. $\hat{Z}$ and $\hat{a}$ together satisfy the following commutation relations

$$[\hat{a}, \hat{a}^\dagger] = 1;\ [\hat{a}, \hat{Z}] = [\hat{a}^\dagger, \hat{Z}] = 0;\ [\hat{Z}^\dagger, \hat{Z}] = 2\ell^2 \tag{3.2}$$

The space in which this algebra acts is spanned by the energy states of the form

$$|n, s-n\rangle = \frac{(\hat{a}^\dagger)^n}{\sqrt{n!}} \frac{(\hat{Z}/\sqrt{2}\ell)^s}{\sqrt{s!}} |0,0\rangle\,; n, s = 0, 1, \dots \infty \tag{3.3}$$

where $|0,0\rangle$ is annihilated by both $\hat{a}$ and $\hat{Z}^\dagger$. This state has an energy $(n+1/2)\hbar\omega_c$ and angular momentum $m = s - n$. The LL index $n = 0, 1, 2\dots$ and the angular momentum $m = -n, -n+1, \dots \infty$ are eigenvalues of the LL index operator $\hat{n} = \hat{a}^\dagger\hat{a}$ and the angular momentum operator $\hat{m} = \hat{Z}\hat{Z}^\dagger/2\ell^2 - \hat{n}$. The guiding center coordinates $\hat{Z}$ and $\hat{Z}^\dagger$ act as raising and lowering operators for the angular momentum.

The discussion so far is gauge independent. Guiding center coordinate $\hat{Z}$ can be written in real space representation once a choice for the gauge $\mathbf{A}$ has been made. In the symmetric gauge $\mathbf{A} \equiv B(-y, x)/2$, the guiding center coordinate is given by

$$\hat{Z} = \hat{z} - i\sqrt{2}\ell\hat{a} = \hat{z} - i\frac{\ell^2}{\hbar}(\hat{\pi}_x - i\hat{\pi}_y) \equiv \frac{x - iy}{2} - \ell^2(\partial_x - i\partial_y) = \frac{z}{2} - 2\ell^2\partial_{\bar{z}} \tag{3.4}$$

3.2 $\mathcal{V}_\infty$ wave functions

As defined in Sec. 2.3, zero interaction energy eigenstates of the model interaction in limit $V_m^{n,n'}/\hbar\omega_c \to \infty$, are referred to as the $\mathcal{V}_\infty$ wave functions. We will describe the construction of $\mathcal{V}_\infty$ wave functions in disk geometry first. In the spherical geometry, where guiding-center coordinate is not well-defined, we show an alternate method for constructing $\mathcal{V}_\infty$ eigenfunctions.

3.2.1 On disk geometry

The physics of the model interaction (Eq. (2.2)) motivates the following construction of $\mathcal{V}_\infty$ wave functions. We denote by Φ^α the distinct kinetic energy eigenstates, labeled by α, of noninteracting fermions; these are simple Slater determinants. To construct the $\mathcal{V}_\infty$ states, we must increase the relative angular momentum of each pair by $2p$ units in a LL-conserving manner. The standard composite fermionization through multiplication by $\mathcal{J}^{2p}(\{z\}) = \prod_{j<k}(z_j - z_k)^{2p}$ does not conserve the LL index as position operators z_i may

scatter particle to different LLs. Instead consider:

$$\Psi^{\alpha} = \prod_{j<k} (\hat{Z}_j - \hat{Z}_k)^{2p} \times \Phi^{\alpha} \tag{3.5}$$

where $\hat{Z} = \hat{z} - i(\hat{\pi}_x - i\hat{\pi}_y)/\hbar$ is the guiding center coordinate. That Ψ^{α} is a $\mathcal{V}_{\infty}$ state follows from two facts:

1. Unlike the position coordinate operators $\hat{z}$, the guiding center coordinate operator $\hat{Z}$ does not have matrix elements that scatter between LLs. As a result, $\hat{Z}$ conserves the LL indices of the particles. Ψ^{α} thus has the same kinetic energy as Φ^{α}.

2. The angular momentum operator for a single particle [Eq.(1.16)] can be written as $\hat{m} = \hat{Z}\hat{Z}^{\dagger}/2 - \hat{n}$, $\hat{n}$ being the LL index. The guiding center coordinate acts as a raising operator for $\hat{m}$ due to the commutation relation $[\hat{m}, \hat{Z}] = \hat{Z}$. Thus $\hat{Z}$ raises the single-particle angular momentum. In the symmetric gauge, the guiding center coordinate has a real space representation of $\hat{Z} \equiv z/2 - 2\partial_{\bar{z}}$. For a pair of particles, $\hat{Z}_1 - \hat{Z}_2$ does not change the center-of-mass angular momenta, because it commutes with the center of mass $(\hat{z}_1 + \hat{z}_2)/2$ and its angular momentum. The Jastrow operator $\mathcal{J}^{2p}(\{Z\}) = \prod_{j<k}(\hat{Z}_j - \hat{Z}_k)^{2p}$ thus increases the relative angular momentum of every pair of particles by $2p$.

Because Ψ^{α}_{ν} does not contain pairs with relative angular momenta for which $\hat{V}$ imposes a penalty, Ψ^{α} has zero interaction energy.

The action of the Jastrow operator increases the largest occupied single-particle angular momentum by $2p(N-1)$ such that the state Φ^{α} at ν^* produces a state Ψ^{α} at $\nu = \nu^*/(2p\nu^* + 1)$ [39, 4]. We next make the conjecture that the states in Eq. (3.5) provide a complete basis for the $\mathcal{V}_{\infty}$ space. This conjecture implies that the excitation spectrum of our model Hamiltonian at any filling $\nu = \nu^*/(2p\nu^* + 1)$ is identical to that of noninteracting fermions at filling ν^*. Extensive diagonalization studies, discussed below, provide a compelling and nontrivial confirmation of the completeness of Ψ^{α}_{ν}. As a corollary, our model produces FQHE at $\nu = n/(2pn + 1)$, in analogy with the IQHE at $\nu^* = n$.

3.2.2 On spherical geometry

Even though the exact eigenfunctions for the model interaction on the disk geometry can be written in a compact form, given in Eq. (3.5), these do not immediately generalize to the case of the spherical geometry as guiding center coordinates are not well defined in all geometries. In this section we describe a form of the ansatz that is equivalent to Eq. (3.5) for the special case of quasiparticles of 1/3. The alternate form presented here has the advantage of generalizing to other geometries. In this section, we restrict to the case where all particles are in the lowest two LLs *i.e.* $n = 0, 1$ as is appropriate when considering quasiparticles of 1/3. We present the steps to get the alternate form of ansatz here.

On disk, the single particle state with angular momentum m in nth LL has the form

$$\phi_{n,m}(z,\bar{z}) = F_{n,m}(z,\bar{z})\, e^{-|z|^2/4\ell^2} \tag{3.6}$$

where $F_{n,m}(z,\bar{z})$ is a polynomial of z and $\bar{z}$. Highest power of $\bar{z}$ in $F_{n,m}(z,\bar{z})$ is equal to the LL-index n. The action of the guiding center coordinate $\hat{Z} = z/2 - 2\ell^2\partial_{\bar{z}}$ on the single particle states $\phi_{n,m}$'s can be reduced to the action of an operator on $F_{n,m}$:

$$\hat{Z}\phi_{n,m}(z,\bar{z}) = \left(z/2 - 2\ell^2\partial_{\bar{z}}\right) F_{n,m}(z,\bar{z})\, e^{-|z|^2/4\ell^2} = e^{-|z|^2/4\ell^2}\left(z - 2\ell^2\partial_{\bar{z}}\right) F_{n,m}(z,\bar{z}) \tag{3.7}$$

In the remaining calculations we will omit the exponential factor from the expressions. We will now consider the state describing N QPs of 1/3 given by,

$$\Psi^{\mathrm{N-QPs}}_{\nu=1/3} = \mathcal{J}^2(\{\hat{Z}\})\,\Phi^{\mathrm{N-QPs}}_1,$$

where the $\Phi^{\mathrm{N-QPs}}_1$ contains N particles in LL1. Any ansatz state is called a *proper state* when, for each occupied Landau orbital in the Slater determinant Φ_{ν^*} with LL index n and momentum state k, kth momentum Landau orbitals in all lower LLs are also filled [40]. Hence, quasiparticle states are proper states. In a determinant $\Phi^{\mathrm{N-QPs}}_1$ corresponding to a proper state, the orbitals in the 2nd LL can be written as $F_{1,m}(z_i,\bar{z}_i) = z_i^m\bar{z}_i$ for all i, without affecting the Slater determinant $\Phi^{\mathrm{N-QPs}}_1$. Hereafter we will use this as the definition of $F_{1,m}(z_i,\bar{z}_i)$. The terms excluded in $F_{1,m}$ do not contribute to the determinant.

Since all particles in Φ are in the lowest two LLs $\Phi^{\mathrm{N-QPs}}_1$ will at most be linear in $\bar{z}_i$'s, for each i. This implies that we only need to expand the Jastrow factor $\mathcal{J}^2(\{\hat{Z}\})$ up to linear terms in $\partial_{\bar{z}}$'s:

$$\begin{aligned}
\mathcal{J}^2(\{\hat{Z}\})\Phi^{\mathrm{N-QPs}}_1 &= \prod_{i<j}(\hat{Z}_i - \hat{Z}_j)^2\Phi^{\mathrm{N-QPs}}_1 \\
&= \left[\mathcal{J}^2(\{z\}) - 2\ell^2\sum_i \partial_{\bar{z}_i}\partial_{z_i}\mathcal{J}^2(\{z\})\right]\Phi^{\mathrm{N-QPs}}_1 \\
&= \prod_i\left[1 - 2\ell^2\partial_{\bar{z}_i}\partial_{z_i}\right]\Phi^{\mathrm{N-QPs}}_1\mathcal{J}^2(\{z\})
\end{aligned} \tag{3.8}$$

Here $\mathcal{J}(\{z\}) = \prod_{i<j}(z_i - z_j)$ is the Jastrow factor of normal position coordinates. Note that in the last expression the derivatives ∂_{z_i}'s act only on the Jastrow factor $\mathcal{J}^2(\{z\})$ and $\partial_{\bar{z}_i}$ acts only on the Slater determinant $\Phi^{\mathrm{N-QPs}}_1$. For instance, the above expression acts trivially on lowest Landau level states of the Slater Determinant:

$$\left[1 - 2\ell^2\partial_{z_i}\,\partial_{\bar{z}_i}\right] z_i^{m_i}\mathcal{J}^2(\{z\}) = z_i^{m_i}\mathcal{J}^2(\{z\}) \tag{3.9}$$

When there are states from the second LL in the Slater determinant it acts as

$$\left[1-2\ell^2\partial_{z_i}\,\partial_{\bar{z}}\right]\bar{z}_i z_i^{m_i}\mathcal{J}^2(\{z\}) = \left[\bar{z}_i-2\ell^2\partial_{z_i}\right]z_i^{m_i}\mathcal{J}^2(\{z\}) = P_{LL1}\bar{z}_i z_i^m\mathcal{J}^2(\{z\}) \tag{3.10}$$

where $\mathcal{P}_{LL1}=\mathbb{I}-\mathcal{P}_{LLL}$ is the projection to the second LL. Combining these results, the ansatz simplifies to the following expression for the case of N quasiparticles of $1/3$.

$$\mathcal{J}^2(\{\hat{Z}_i\})\,\Phi_1^{\text{N}-\text{QPs}} = \hat{\Phi}_1^{\text{N}-\text{QPs}}\mathcal{J}^2(\{z_i\}) \tag{3.11}$$

where the Slater determinant $\hat{\Phi}_1^{\text{N}-\text{QPs}}$ is constructed by replacing all LL1 Landau orbitals $F_{1,m}(z,\bar{z})$, inside $\Phi_1^{\text{N}-\text{QPs}}$ by $F_{1,m}(z,\bar{z})-\hat{F}_{1,m}(z,\bar{z}\rightarrow 2\ell^2\partial_z)$. Here the operator $\hat{F}_{1,m}(z,\bar{z}\rightarrow 2\ell^2\partial_z)$ represents LLL projection of the LL1 Landau orbital $F_{1,m}(z,\bar{z})$ constructed by replacing $\bar{z}\rightarrow 2\ell^2\partial_z$. A normal ordering is required such that all $\bar{z}$ are moved to the left before making the replacement $\bar{z}\rightarrow 2\ell^2\partial_z$ where it is understood that the derivatives do not act on the exponentials (see Sec. 5.14.4 of Ref. [4]). The exact eigenfunction given in Eq. (3.5) can be rewritten in this way for neutral excitations of 1/3 as well, as long as the Slater determinant state Φ_1^α is a proper state.

This implies, that ansatz in Eq. (3.5) for N QPs of 1/3 can be written as

$$\Psi_{1/3}^{\text{N}-\text{QPs}} = \hat{\Phi}_1^{\text{N}-\text{QPs}}\mathcal{J}^2(\{z\}) \tag{3.12}$$

The operator $\hat{\Phi}_1^{\text{N}-\text{QPs}}$ which acts on $\mathcal{J}^2(\{z\})$ can be constructed by replacing any LL1 orbitals $F_{1,m}$, inside $\Phi_1^{\text{N}-\text{QPs}}$ with $\hat{G}_{1,m}=F_{1,m}-\hat{F}_{1,m}$ such that the operator $\hat{\Phi}_1^{\text{N}-\text{QPs}}$ in last expression of Eq. (3.12) is given by

$$\hat{\Phi}_1^{\text{N}-\text{QPs}} = \begin{vmatrix} F_{0,0}(z_1) & F_{0,0}(z_2) & \dots & F_{0,0}(z_{N_e}) \\ F_{0,1}(z_1) & F_{0,1}(z_2) & \dots & F_{0,1}(z_{N_e}) \\ \vdots & \vdots & \vdots & \vdots \\ F_{0,N_\phi^*-1}(z_1) & F_{0,N_\phi^*-1}(z_2) & \dots & F_{0,N_\phi^*-1}(z_{N_e}) \\ \hat{G}_{1,m_1}(z_1,\partial_{z_1}) & \hat{G}_{1,m_1}(z_2,\partial_{z_1}) & \dots & \hat{G}_{1,m_1}(z_{N_e},\partial_{z_{N_e}}) \\ \vdots & \vdots & \ddots & \vdots \\ \hat{G}_{1,m_N}(z_1,\partial_{z_1}) & \hat{G}_{1,m_N}(z_2,\partial_{z_1}) & \dots & \hat{G}_{1,m_N}(z_{N_e},\partial_{z_{N_e}}) \end{vmatrix} \tag{3.13}$$

The operator $\hat{F}_{1,m}$ is defined such that

$$\hat{F}_{1,m}F_{0,k} = \mathcal{P}_{\text{LLL}}\left[F_{1,m}F_{0,k}\right] \tag{3.14}$$

where $\mathcal{P}_{\text{LLL}}$ is the LLL projection operator. It should be noted that the derivatives ∂_z's do not act on the exponential factor. The operator $\hat{G}_{1,m}$ can be better understood as

$$\begin{aligned} \hat{G}_{1,m}F_{0,k} &= \left[F_{1,m}-\hat{F}_{1,m}\right]F_{0,k} \\ &= F_{1,m}F_{0,k}-\mathcal{P}_{\text{LLL}}\left[F_{1,m}F_{0,k}\right] = \mathcal{P}_{\text{LL1}}\left[F_{1,m}F_{0,k}\right] \end{aligned} \tag{3.15}$$

Although, it is not as easy to see that the alternate form of Ψ^α defined in Eq. (3.12) are zero-energy eigenfunctions of the model interaction, these can be numerically evaluated for small systems. Upon comparison with exact diagonalization spectrum of the model Hamiltonian given in Eq. (2.2) on the disk, we could explicitly verify that these are the right eigenfunctions.

More importantly, the expression in Eq. (3.12) can be written for sphere as well:

$$\Psi_{1/3}^{\mathrm{N-QPs}} = \hat{\Phi}_{1/3}^{\mathrm{N-QPs}} \left(Y_{Q^*1m} \rightarrow Y_{Q^*1m} - \hat{Y}^{q}_{Q^*1m} \right) \mathcal{J}^2 \tag{3.16}$$

where monopole harmonics Y_{Qnm} represent single-particle Landau orbitals with angular momentum m in nth LL, in flux given by $2Q$. For a given LLL state Y_{q0k}, the operator $\hat{Y}^{q}_{Q^*1m}$ is defined using

$$\hat{Y}^{q}_{Q1m} Y_{q0k} = \mathcal{P}_{\mathrm{LLL}} \left[Y_{Q1m} Y_{q0k} \right] \tag{3.17}$$

The explicit form of $\hat{Y}^{q}_{Qnm}$ is given in Appendix J of Ref. [4]. Again, we could explicitly compare this with ED eigenfunctions for small systems and verify that the ansatz in Eq. (3.16) gives correct eigenfunctions. In summary, Eq. (3.12) and (3.16) describe QPs of the 1/3 state on disk and sphere geometries.

3.3 Counting of $\mathcal{V}_\infty$ states

In this section we present results comparing the number of numerically obtained zero energy $\mathcal{V}_\infty$ states $(N, 2Q)$ with the dimension of the Hilbert space of the corresponding noninteracting system at $(N, 2Q^*)$, with $2Q^* = 2Q - 2p(N-1)$. All exact diagonalizations are performed in the space of the lowest three LLs.

$\mathcal{V}_\infty$ states are constructed by acting $\hat{\mathcal{J}} = \prod_{i<j=1}^{N} (\hat{Z}_i - \hat{Z}_j)^{2p}$ on the slater determinant states Φ^α with a fixed number of particles (N_0, N_1, N_2) in each LL. Maximum angular momenta of the particles in the slater determinant is less than that in the corresponding $\mathcal{V}_\infty$ state as the Jastrow factor $\hat{\mathcal{J}}$ adds an angular momentum of $2p(N-1)$ for each particle.

While the states constructed in this manner definitely belong to the $\mathcal{V}_\infty$ sector, one can ask:

1. Do different rearrangements of particles in a given LL occupation sector $(N_0, N_1, N_2 \cdots)$ produce linearly independent $\mathcal{V}_\infty$ states? This seems likely, as the resulting states are very complex, but we do not have an analytic proof.
2. Are there other $\mathcal{V}_\infty$ states that are not captured by this construction? We have failed to find such states, but rigorously speaking, we cannot rule out this possibility a priori.

We have conjectured that the states obtained in this fashion are all linearly independent

N_0, N_1, N_2	$2Q = 11$	$2Q = 12$	N_0, N_1, N_2	$2Q = 11$	$2Q = 12$
0,0,5	6	12	2,0,3	35	76
0,1,4	41	74	2,1,2	103	222
0,2,3	80	146	2,2,1	79	178
0,3,2	56	108	2,3,0	17	40
0,4,1	14	31	3,0,2	13	36
0,5,0	1	3	3,1,1	23	64
1,0,4	29	56	3,2,0	9	26
1,1,3	130	246	4,0,1	1	5
1,2,2	165	322	4,1,0	1	5
1,3,1	70	147	5,0,0	0	1
1,4,0	9	21			

Table 3.1: The number of independent $L_z = 1/2$ zero interaction energy ($\mathcal{V}_\infty$) eigenstates in exact-diagonalization spectra for many different (N_0, N_1, N_2) sectors for several values of $2Q$. The total number of particles is $N = 5$. In every single case, the number of numerically obtained zero interaction energy eigenstates matches exactly with the number of slater determinant states for noninteracting electrons in the (N_0, N_1, N_2) sector at $2Q^* = 2Q - 2(N - 1)$.

and provide a complete basis for the $\mathcal{V}_\infty$ space. In other words, in the spherical geometry, the $\mathcal{V}_\infty$ eigenstates in exact diagonalization spectrum of $(N, 2Q)$ have an exact one-to-one correspondence with the eigenstates of noninteracting fermions at $(N, 2Q^*)$, with $2Q^* = 2Q - 2p(N - 1)$. Alternatively: (i) all $\mathcal{V}_\infty$ states are of this form (or linear combinations of them), and (ii) $\mathcal{V}_\infty$ states constructed from different slater determinant states are linearly independent, *i.e.* the action of $\hat{\mathcal{J}}$ does not not annihilate any wave function.

L^2, L_z, N_0, N_1, N_2 form good quantum numbers of the eigenstates of the model Hamiltonian. In the tables, we have have presented the comparison of the number of $\mathcal{V}_\infty$ states at each (N_0, N_1, N_2) with the total number of non-interacting electronic eigenstates at $2Q^*$. We provide convincing numerical evidence for this conjecture by explicitly diagonalizing our model interaction in various (N_0, N_1, N_2) sectors at several values of $2Q$ to obtain their zero interaction energy eigenstates. The results are shown in the tables 3.1, 3.2 and 3.3. In every case the number matches the number of different slater determinant states at $2Q^*$ in the (N_0, N_1, N_2) sector. Only the number of the $L_z = 0$ states is shown. In addition to the cases shown in the tables, the expected counting is obtained for the $(N, 2Q) = (9, 16)$ system, where only a single $\mathcal{V}_\infty$ state occurs in the sector $(N_0 = 1, N_1 = 3, N_2 = 5)$, corresponding to the $\nu = 3/7$ ground state. The one-to-one correspondence is seen for all cases we have studied.

N_0, N_1, N_2	$2Q = 11$	12	15	16	N_0, N_1, N_2	$2Q = 11$	12	15	16
6,0,0	0	0	1	1	2,2,2	14	74	1372	2662
5,1,0	0	0	6	19	3,0,3	0	5	186	393
4,2,0	0	0	44	108	0,5,1	0	1	48	102
5,0,1	0	0	6	21	1,3,2	18	74	1086	2054
3,3,0	0	2	106	236	2,1,3	12	61	1028	1971
4,1,1	0	0	106	265	0,4,2	3	13	236	452
2,4,0	1	3	100	210	1,2,3	34	118	1396	2556
3,2,1	0	10	452	978	2,0,4	3	13	236	452
4,0,2	0	0	59	143	0,3,3	12	40	470	858
1,5,0	0	1	34	74	1,1,4	18	61	708	1292
2,3,1	4	28	656	1328	0,2,4	14	40	410	728
3,1,2	0	13	550	1165	1,0,5	2	9	114	214
0,6,0	0	0	4	8	0,1,5	4	13	146	264
1,4,1	2	15	334	674	0,0,6	1	1	18	32

Table 3.2: The number of independent $L_z = 0$ zero interaction energy ($\mathcal{V}_\infty$) eigenstates in exact-diagonalization spectra for many different (N_0, N_1, N_2) sectors for several values of $2Q$. The total number of particles is $N = 6$. In every single case, the number of numerically obtained zero interaction energy eigenstates matches exactly with the number of slater determinant states for noninteracting electrons in the (N_0, N_1, N_2) sector at $2Q^* = 2Q - 2(N-1)$.

N_0, N_1, N_2	$2Q = 16$	N_0, N_1, N_2	$2Q = 16$
7,0,0	0	0,2,5	210
0,7,0	1	3,0,4	108
0,0,7	4	1,5,1	91
6,1,0	0	0,4,3	236
6,0,1	0	0,3,4	344
1,6,0	5	1,1,5	356
0,6,1	7	4,2,1	91
1,0,6	38	4,1,2	114
0,1,6	52	2,4,1	286
5,2,0	3	1,4,2	520
5,0,2	4	3,3,1	286
2,5,0	26	2,1,4	700
0,5,2	68	1,2,4	1016
4,3,0	21	3,1,3	482
5,1,1	7	1,3,3	1136
2,0,5	108	3,2,2	628
3,4,0	40	2,3,2	1022
4,0,3	38	2,2,3	1372

Table 3.3: The number of independent $L_z = 0$ zero interaction energy ($\mathcal{V}_\infty$) eigenstates in exact-diagonalization spectra for different (N_0, N_1, N_2) sectors within the $(N, 2Q) = (7, 16)$ system. In every single case, the number of numerically obtained zero interaction energy eigenstates matches exactly with the number of slater determinant states of noninteracting electrons in the (N_0, N_1, N_2) sector at $2Q^* = 2Q - 2(N-1)$.

In the Fig 3.1, Fig 3.2 and Fig 3.3 we have shown a comparison of the noninteracting spectrum at $2Q^*$ and model Hamiltonian spectrum at $2Q$. The degeneracy of each orange dash ($\mathcal{V}_\infty$ state) is shown next to it. The degeneracy indicates the number of independent states with a given energy and and given angular momentum L. In these plots L_z is fixed at 0 and (N_0, N_1, N_2) can take any value. In all cases we find that the degenaracies in the spectra match identically. Zero energy space dimensions were computed using Krylov-Schur algorithm [71] and setting large Krylov subspace dimensions.

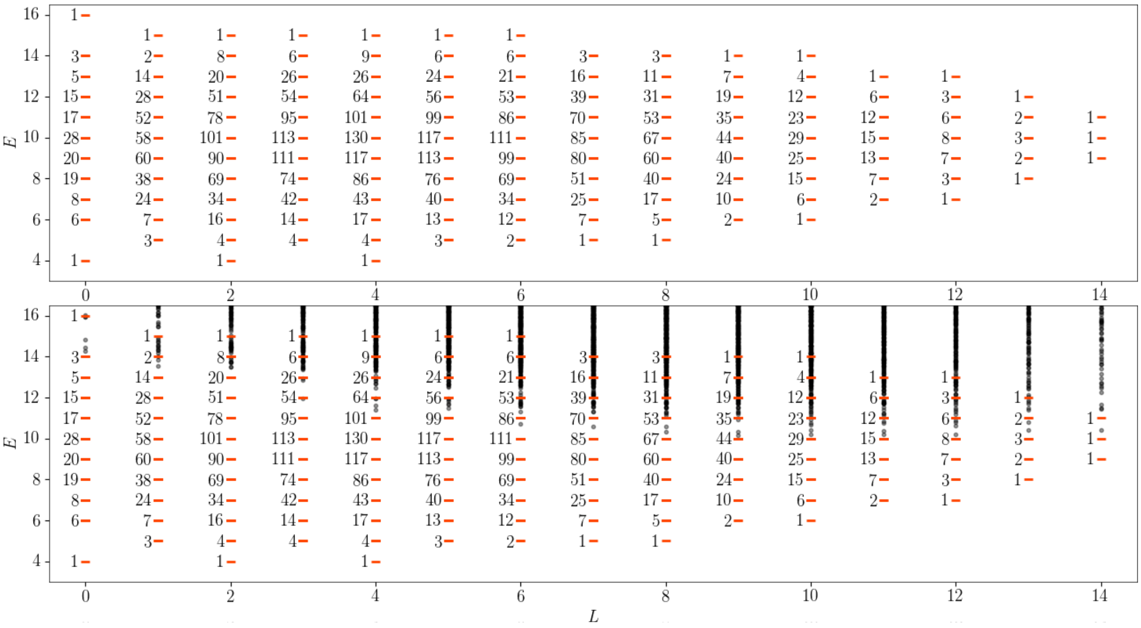

Figure 3.1: (top): The spectrum of $N = 8$ non-interacting electrons at flux $2Q^* = 3$ in the Hilbert space of three LLs, with the cyclotron energy set to $\hbar\omega = 1$. (bottom) The spectrum of the model Hamiltonian for $N = 8$ electrons at flux $2Q = 17$ in the Hilbert space of three LLs, with the cyclotron energy set to $\hbar\omega = 1$. All interaction pseudopotentials are set to 20. Orange dashes show $\mathcal{V}_\infty$ states, and the black dots show the finite interaction energy states. The numbers next to the orange dashes show the degeneracy of each line. The flux values are related by $2Q^* = 2Q - 2(N-1)$. In every case, the degeneracies in the two spectra match.

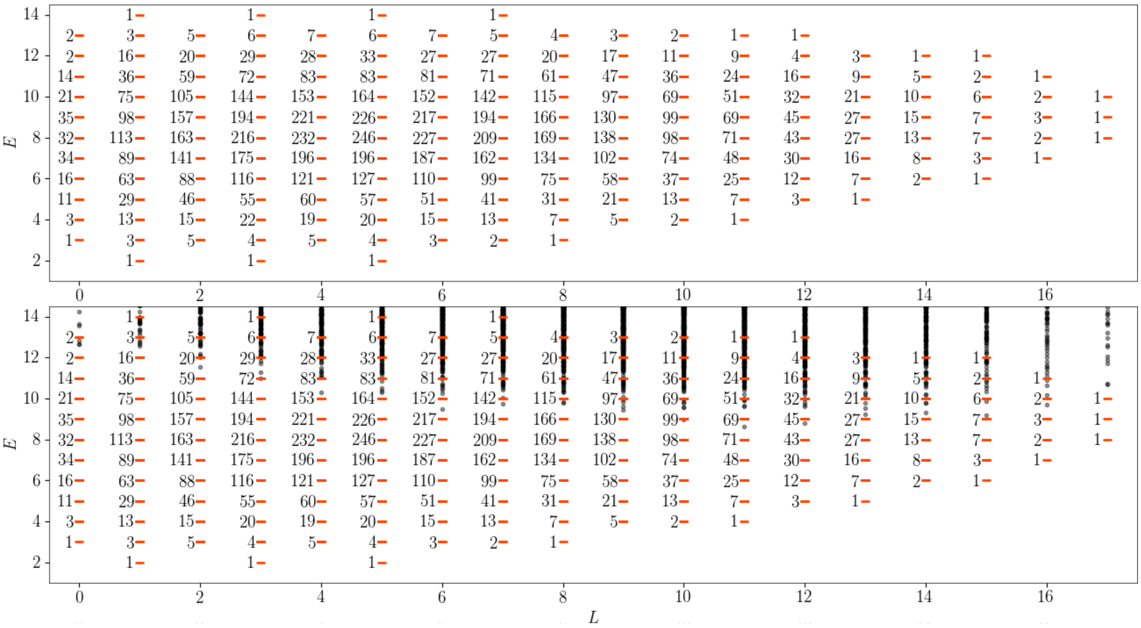

Figure 3.2: Similar comparison for a system of size $N = 7$. Bottom panel shows the spectrum of the model interaction at $2Q = 16$ and the top panel shows the spectrum of non-interacting electrons at $2Q^* = 2Q - 2(N-1) = 4$.

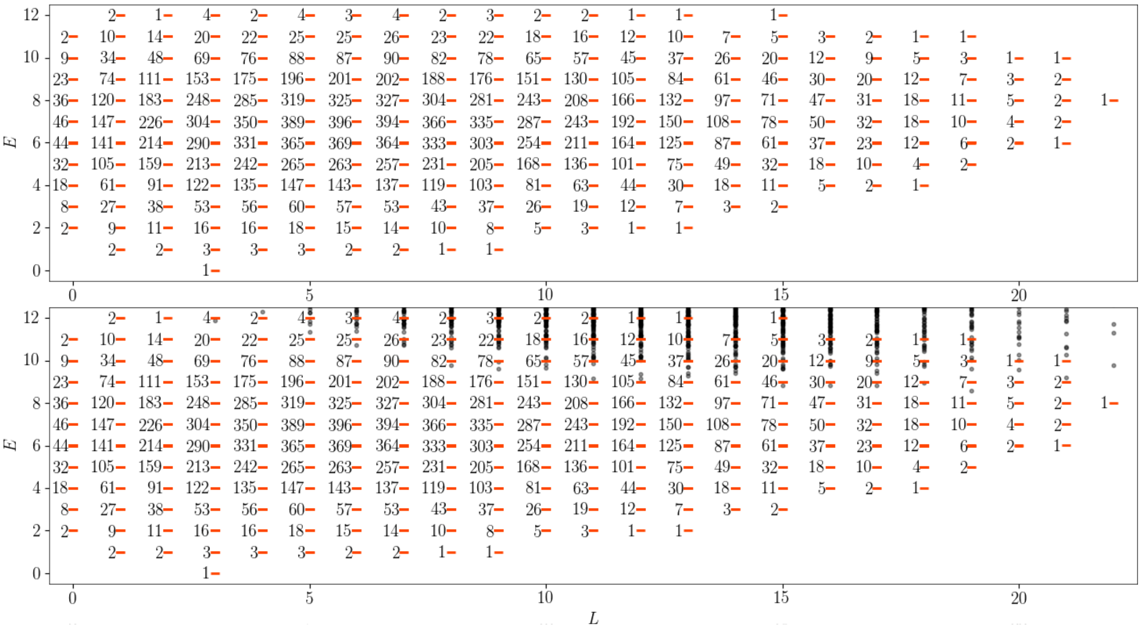

Figure 3.3: Similar comparison for a system of size $N = 6$. Bottom panel shows the spectrum of the model interaction at $2Q = 16$ and the top panel shows the spectrum of non-interacting electrons at $2Q^* = 2Q - 2(N-1) = 6$.

3.4 Topological properties

Many topological properties follow from counting the low energy levels, which we know precisely for our model through its one-to-one correspondence with the noninteracting

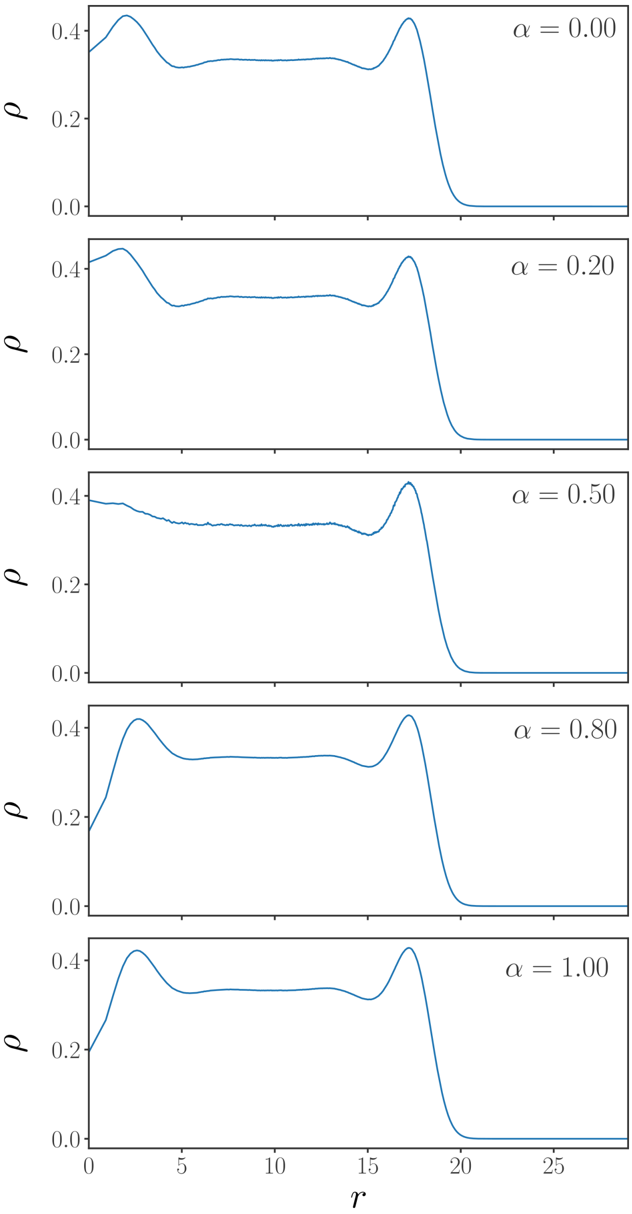

Figure 3.4: Radial density $\rho(r)$ of exact eigenfunction $\Psi^{1-\mathrm{QP}}_{1/3}$ corresponding to 1 QP of 1/3 for different values of α (see Eq. 3.18). The QP is at angular momentum state $m = 0$ in LL1.

problem of electrons at an effective filling factor. We discuss these in some detail in this section.

3.4.1 Fractional charge

As reviewed in Ref. [4], the fractional charge for the quasiparticle (quasihole) can be obtained from an analogy to the noninteracting system. Essentially, one asks the question: How many quasiparticles (quasiholes) are created when one adds a single electron to (removes a single electron from) the system? Following verbatim the discussion in Ref. [4],

$2pn+1$ quasiparticles are created when one electron is added to the system, thus producing a charge of magnitude $e^* = 1/(2pn+1)$, in units of the electron charge, for each quasiparticle.

The charge can also be obtained from the density profile. Let us go back to the exact eigenfunction on disk corresponding to 1 QP of 1/3, discussed in Sec. 3.2.2. In Eq. 3.10, we insert a parameter α as follows

$$\left[\alpha \bar{z}_i - (1-\alpha) 2\ell^2 \partial_{z_i}\right] z_i^{m_i} \mathcal{J}^2(\{z\}) \tag{3.18}$$

such that tuning $\alpha = 0 \to 1$ takes the QP from completely projected in LLL to entirely residing in 2nd LL; $\alpha = 0.5$ of course corresponds to the exact eigenfunction. Figure 3.4 shows the density $\rho(r)$ of $\Psi_{1/3}^{\text{N-QPs}}$ (see Eq. 3.12) with 1 QP at angular momentum $m = 0$ in LL1, for different values of α.

We consider here the single quasiparticle state of 2/5 for $N = 9$, which occurs for a system with $2Q = 18$ at an angular momentum of $L = 3$. When placed in an $L_z = L$ state, the excess charge is maximally moved to one of the poles of the system. The net charge accumulated due to the quasiparticle can be calculated as the saturation value (at large θ) of

$$Q(\theta) = \int_0^\theta \left[\rho(\theta') - \rho(\pi)\right] 2\pi \sin x dx \tag{3.19}$$

where θ is the polar angle, $\rho(x)$ is the local charge density at a polar angle x (which will be azimuthally symmetric, ie independent of azimuthal angle ϕ) and $\rho(\pi)$ is density at the south pole.

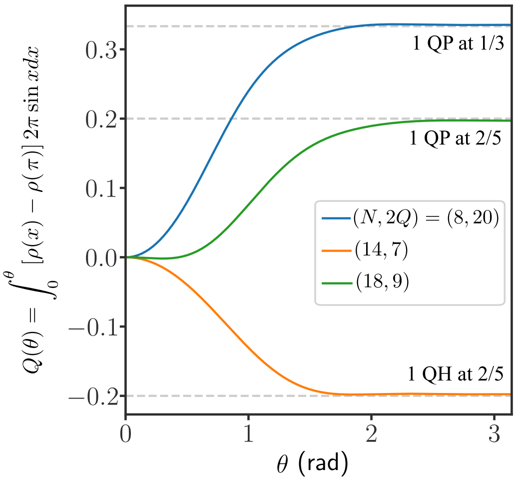

Figure 3.5: Cumulative charge inside a region defined by angle θ for a QP and a QH of the 2/5 FQH state and for a QP of the 1/3 FQH state. The plot shows excess charge near the north pole (measured relative to the density at the south pole) in a system where there is a single QP/QH placed in a highest weight ($L_z = L$) state, corresponding to the QP/QH located at the north pole. In all cases we find that the magnitude of the net charge in the around the north pole is $1/(2p\nu^* + 1)$ in units of the electron charge.

Fig 3.5 shows the result for $Q(\theta)$ indicating that the total charge accumulated around the pole is $1/5$ as expected. Similar analysis of the QH of $2/5$ shows its charge to be $1/5$ in magnitude again. The single QH state of $1/3$ in our model is identical to that of the Laughlin quasihole state and therefore has a charge of $1/3$. The single quasiparticle is found to have a charge of $1/3$ as shown by the blue line of the figure, evaluated for a system of $N = 8$ electrons at $2Q = 20$.

3.4.2 Fractional statistics

The one-to-one analogy between our solutions and the integer quantum Hall states implies that QP/QH excitations of our solutions will also obey Abelian statistics. This implication follows because, just as for the integer quantum Hall state, specifying the positions produces a unique wave function, and thus, any braidings may only produce a phase factor. Furthermore, general arguments discussed in Ref. [4] also fix the value of the statistics.

3.4.3 Edge states

The counting of edge excitations of the $n/(2pn+1)$ states in our model is identical to that of the $\nu^* = n$ integer quantum Hall state. This implies that the edge excitations for our model system are exactly described in terms of n chiral bosonic modes, which is also believed to be the case for the lowest Landau level FQH states at these filling factors.

3.4.4 Computation of Berry Phase using Monte Carlo

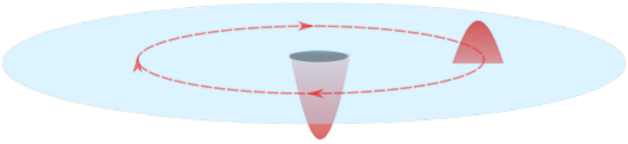

Figure 3.6: Schematic for Berry phase calculation of a quasi-hole (center) and quasi-particle pair on a disk.

Berry phase for a wavefunction $\psi(\{z\}, \eta)$ along a closed path Γ in parameter space of η is given by

$$\gamma(\Gamma, \eta) = i \int_{\Gamma} \mathrm{d}\eta \, \langle \psi(\{z\}, \eta)| \frac{\mathrm{d}}{\mathrm{d}\eta} |\psi(\{z\}, \eta)\rangle \tag{3.20}$$

For a circular path, $\eta = |\eta| e^{-i\theta}$, hence $\mathrm{d}\eta = -i\eta \mathrm{d}\theta$. The berry phase is then given by

$$\gamma(\Gamma, \eta) = i \int_{\Gamma} \mathrm{d}\theta \, \langle \psi(\{z\}, \eta)| \frac{\mathrm{d}}{\mathrm{d}\theta} |\psi(\{z\}, \eta)\rangle \tag{3.21}$$

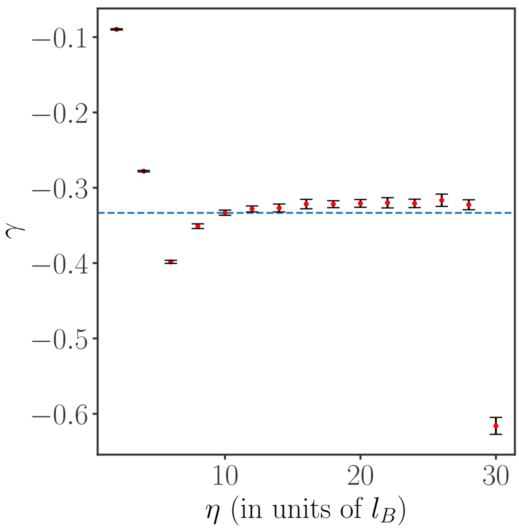

Figure 3.7: Berry phase $\gamma(\eta)$ for anstaz eigenfunction (Eq. (5.2)) which contains a coherent state QP at radius η and a QH at the center. We see that the $\gamma(\eta)$ saturates to the expected value of $-1/3$ as distance η of QP is increased from the center.

We studied the Berry phase associated to charged excitations of model interaction at 1/3 filling on a disk. We know that (see Eq. (3.5)) the exact eigenfunction of model interaction at 1/3 is given by

$$\Psi^{\alpha}_{1/3} = \prod_{j<k} (\hat{Z}_j - \hat{Z}_k)^2 \times \Phi^{\alpha}_{1} \tag{3.22}$$

where α labels the type of excitation. The Slater determinant for a QP at center and another at radius η is given by

$$\Phi^{\mathrm{QP-QP}}_{0,\eta}(\{z\}) = \begin{vmatrix} \phi_{0,0}(z_1) & \phi_{0,0}(z_2) & \phi_{0,0}(z_3) & \dots & \phi_{0,0}(z_N) \\ \vdots & \vdots & \vdots & \dots & \vdots \\ \phi_{0,N-2}(z_1) & \phi_{0,N-2}(z_2) & \phi_{0,N-2}(z_3) & \dots & \phi_{0,N-2}(z_N) \\ \phi^{\mathrm{coh-qp}}_{0}(z_1) & \phi^{\mathrm{coh-qp}}_{0}(z_2) & \phi^{\mathrm{coh-qp}}_{0}(z_3) & \dots & \phi^{\mathrm{coh-qp}}_{0}(z_N) \\ \phi^{\mathrm{coh-qp}}_{\eta}(z_1) & \phi^{\mathrm{coh-qp}}_{\eta}(z_2) & \phi^{\mathrm{coh-qp}}_{\eta}(z_3) & \dots & \phi^{\mathrm{coh-qp}}_{\eta}(z_N) \end{vmatrix} \tag{3.23}$$

where $\phi_{n,m}$ are the Landau orbital in disk (see Sec. 1.27) and $\phi^{\mathrm{coh-qp}}_{\eta}(z)$ is the coherent state wavefunction projected in 2nd LL, given by

$$\begin{aligned} \phi^{\mathrm{coh-qp}}_{\eta}(z) &= \mathcal{P}_{\mathrm{LL1}} \delta(z-\eta) \mathcal{P}_{\mathrm{LL1}} = \mathcal{P}_{\mathrm{LL1}} \left[\sum_{n,m} \phi_{n,m}(z) \bar{\phi}_{n,m}(\eta) \right] \mathcal{P}_{\mathrm{LL1}} \\ &= \frac{1}{4\pi\ell^2_{B^*}} \left((\bar{z}-\bar{\eta})(\eta - z) + 2\ell^2_{B^*} \right) \exp\left(\frac{z\bar{\eta}}{2\ell^2_{B^*}} - \frac{|z|^2}{4\ell^2_{B^*}} - \frac{|\eta|^2}{4\ell^2_{B^*}} \right) \end{aligned} \tag{3.24}$$

where the coherent state QP is centered at position η. All single particle states in the Slater determinant Φ^α in Eq. (3.5) will use the modified magnetic length $\ell_{B^*}^2 = \frac{1}{\ell_B^2}(1-2p\nu)$, which for $\nu = 1/3$ is $\ell_{B^*}^2 = 1/3\ell_B^2$. As a side note, it is important to point that single particle states in the Slater determinant of the exact eigenfunction see the actual magnetic field B, instead of a reduced field B^* like the CFs. This implies, the area of Hall droplet represented by Φ^α in the exact eigenfunction is contracted by a factor of $(1-2p\nu)$ when compared to the CF state. Multiplication with the modified Jastrow factor results in expansion of this area by exactly $1/(1-2p\nu)$. This increases the flux through the system, giving us the correct magnetic length ℓ_B and filling fraction ν.

3.5 Conclusion

In Chapter 2, we had introduced a model interaction which, as the electron density is changed, produces incompressible states at Jain filling fractions of the form $n/(2pn+1)$ and allows exact eigenfunctions not just for the incompressible and quasihole states but also the quasiparticle and neutral excitations. In this chapter, we present the exact zero-interaction (ZIE) energy eigenfunctions of the model interaction in disk geometry. Using extensive numerical checks, we verify that these eigenfunction, which are closely related to the CF wavefunctions, form a linearly independent complete basis for the ZIE eigenspace, $\mathcal{V}_\infty$, of the model interaction. Although direct generalization of disk eigenfunctions to spherical geometry fails, we could write exact eigenfunctions for QPs of $1/m$. Exactness of these eigenfunctions was numerically verified by comparing them with the exact diagonalization eigenstates.

The exact eigenfunctions of model interaction capture many important features of CF wavefunctions. We numerically verified that the QP and QH excitations of these ansatz wavefunctions at given filling fraction indeed produce the correct fractional charge. In addition, by Monte Carlo computation of the Berry phase between the QP-QH pair of exact eigenfunction we verify that the charged excitations follow correct fractional statistics. We found that Berry phase associated to QP-QP converges much slower due to finite spread in the densities of the QP of exact eigenfunction (see panel corresponding to $\alpha = 0.5$ in Fig. 3.4).

Chapter 4

Review of Quantum Hall systems on Torus and Cylinder geometry

The choice of system geometry in quantum Hall (QH) systems depends on the nature of the study we are interested in. While geometries with open boundaries, like a disk or a plane, allow the analysis of edge physics, closed geometries, like a sphere or a torus, are better suited for studying bulk properties. In addition to that, the ground states in FQHE are not unique on surfaces with non-trivial topology like torus. To be precise, at filling fraction $\nu = p/q$, the number of degenerate ground states must be multiple of q [67]. Thus, by studying the model interaction on a torus, we can verify whether it gives correct degeneracy. Also, torus geometry is suitable for studying a non-dissipative viscous response in Hall fluids, called *Hall viscosity*, as we can simulate a constant strain by shearing the torus [72].

This chapter reviews the basic ideas necessary to study the quantum Hall effect on periodic geometries, namely torus and cylinder. In addition to the discrete translation symmetry inherent in the boundary conditions, emergent many-body translation symmetries can be constructed in torus for QH systems.

This chapter is organized as follows. Sec. 4.1 reviews the basic single particle symmetries in QH systems on torus geometry and its Landau orbitals. Sec. 4.2 describes other many-body translation symmetries in torus geometry, which are helpful in the exact diagonalization of the model interaction. Sec. 4.3 introduces similar ideas for cylinder geometry. Finally, the matrix element of any rotationally symmetric two-particle interaction on torus geometry is calculated in Sec. 4.4. Matrix elements for the cylinder geometry turn out to be of the same form.

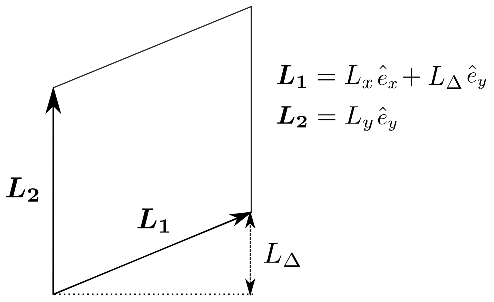

Figure 4.1: A general torus generated by $\boldsymbol{L}_1$ and $\boldsymbol{L}_2$. The skewness L_Δ parameterizes the deviation from a rectangular torus.

4.1 Quantum Hall effect on Torus geometry

We consider a quantum Hall system of N_e electrons with $-e$ charge in the presence of magnetic field $\boldsymbol{B} = -B\hat{e}_z$ on a torus. A torus represents a system with periodic boundary conditions along lattice vectors $\boldsymbol{L}_1$ and $\boldsymbol{L}_2$, as shown in Fig. 4.1. A two-dimensional vector $\boldsymbol{a}$ in quantum Hall systems is conventionally represented as a complex number given by $a = a_x + \imath a_y$. Using this, we can parameterize the torus in Fig. 4.1 by $L_1 = \tau L_2$, where $L_1 = L_x + \imath L_\Delta$, $L_2 = \imath L_y$ and $\tau = -L_1/L_2$. Unless represented by boldface symbol, all vectors will be treated as complex numbers henceforth.

The periodicity in torus geometry implies that all observables of the system must remain invariant under lattice translations of type $\boldsymbol{L}_{mn} = m\boldsymbol{L}_1 + n\boldsymbol{L}_2$ where $m,\, n \in \mathbb{Z}$. Although this looks similar to Bloch electrons, the kinetic energy of a charged particle in a magnetic field does not commute with standard lattice translations. Instead, we use magnetic translation operators introduced in the following section.

4.1.1 Magnetic Translsation Operators

In a system of charged particles in a magnetic field, the normal spatial translations $T(\boldsymbol{a}) = e^{\frac{\imath}{\hbar}\boldsymbol{a}\cdot\boldsymbol{p}}$ generated by canonical momenta $\boldsymbol{p} = -\imath\hbar\nabla$ do not commute with the kinetic energy H_{KE}. For N_e electrons in a magnetic field $\boldsymbol{B} = -B\hat{e}_z$, the kinetic energy is given by

$$H_{\text{KE}} = \frac{1}{2m_e}\sum_{i}^{N_e} \boldsymbol{\Pi}_i^2 \tag{4.1}$$

where the quantity $\boldsymbol{\Pi}_i = \boldsymbol{p}_i + e\boldsymbol{A}(\boldsymbol{r}_i)$ is defined as the kinetic momenta for the i^{th} electron. The electron mass is m_e and the gauge field $\boldsymbol{A}(\boldsymbol{r})$ satisfies $\nabla \times \boldsymbol{A}(\boldsymbol{r}) = -B\hat{e}_z$. Instead we have another operator $\boldsymbol{K}$, called guiding-center momentum, given by

$$\boldsymbol{K} = \boldsymbol{\Pi} - \frac{\hbar}{\ell^2}\left(\hat{e}_z \times \boldsymbol{r}\right) \tag{4.2}$$

which commutes with H_{KE}. Guiding-center momentum $\boldsymbol{K}$ is the generator of translations in the presence of magnetic field, which are called magnetic translation operators (MTOs) defined as $t(\boldsymbol{a}) = e^{\frac{i}{\hbar}\boldsymbol{a}\cdot\boldsymbol{K}}$ [73]. MTO for a sum of two vectors $\boldsymbol{a}$ and $\boldsymbol{b}$ is given by

$$t(\boldsymbol{a}+\boldsymbol{b}) = e^{\frac{i}{2\hbar}\hat{e}_z\cdot(\boldsymbol{a}\times\boldsymbol{b})}t(\boldsymbol{a})t(\boldsymbol{b}) \tag{4.3}$$

which implies that unlike normal translations, MTOs generally do not commute. Using Eq. (4.3), it can be shown that states will remain invariant under translations by lattice vectors $t_i(\boldsymbol{L}_1)$ and $t_i(\boldsymbol{L}_2)$ only if the number of flux quanta through the unit cell — given by $N_\phi = |\boldsymbol{L}_1 \times \boldsymbol{L}_2|/2\pi\ell^2$ — is an integer.

MTOs for lattice translations $\boldsymbol{L}_{mn}$ commute with any Hamiltonian $H = H_{\mathrm{KE}} + V(\boldsymbol{r})$ as long as the interaction is also periodic in torus *i.e.* $V(\boldsymbol{r}+\boldsymbol{L}_{mn}) = V(\boldsymbol{r})$. This implies that the many-body eigenstates $\psi_\alpha(\{\boldsymbol{r}\})$ of the Hamiltonian H will also be the eigenstates of MTOs, such that

$$t_i(\boldsymbol{L}_j)\psi_\alpha(\{\boldsymbol{r}\}) = e^{i\theta_j^i}\psi_\alpha(\{\boldsymbol{r}_i\}) \tag{4.4}$$

where $\{\boldsymbol{r}_i\} \equiv \{\boldsymbol{r}_1, \boldsymbol{r}_2, \ldots, \boldsymbol{r}_{N_e}\}$ and $t_i(\boldsymbol{L}_j)$ only acts on the i^{th} particle. Using Eq. (4.3) and (4.4), it can be checked that

$$t_i(\boldsymbol{L}_{mn})\psi_\alpha(\{\boldsymbol{r}\}) = e^{i\theta_{mn}^i}\psi_\alpha(\{\boldsymbol{r}\}) \tag{4.5}$$

such that $\theta_{mn}^i = \pi mnN_\phi + m\theta_1^i + n\theta_2^i$. Since these eigenstates are anti-symmetric (symmetric for bosons), θ's in the eigenvalues are independent of particle index *i.e.* $e^{i\theta_{mn}^i} = e^{i\theta_{mn}^j} = e^{i\theta_{mn}}$.

4.1.2 Single-particle Hilbert space

For symmetric gauge $\boldsymbol{A}(\boldsymbol{r}) = \frac{B}{2}\boldsymbol{r} \times \hat{e}_z$, an MTO $t_i(\boldsymbol{a})$, is related to the corresponding normal translation operator $T_i(\boldsymbol{a})$, by following relation

$$t_i(\boldsymbol{a}) = e^{-\frac{i}{2\ell^2}\hat{e}_z\cdot(\boldsymbol{a}\times\boldsymbol{r}_i)}T(\boldsymbol{a}) \tag{4.6}$$

In this gauge, the Landau orbital for a particle in LLL with momentum k on a torus (see Fig. 4.1), is given by

$$\phi_{0,k}(z,\bar{z}) = e^{-\frac{z^2+|z|^2}{2\ell^2}}\vartheta\begin{bmatrix}\frac{k}{N_\phi}+\frac{\theta_2}{2\pi N_\phi}\\ \frac{\theta_1}{2\pi}\end{bmatrix}\left(\frac{N_\phi z}{L_2}\middle| N_\phi\tau\right) \tag{4.7}$$

where $0 \le k < N_\phi$ denotes y-momentum, z is the position and $\tau = -L_1/L_2$. The orbitals are written in terms of Jacobi theta functions [36], which are defined as

$$\vartheta\begin{bmatrix}a\\ b\end{bmatrix}(z|\tau) = \sum_{j=-\infty}^{\infty} e^{i\pi(j+a)^2\tau}e^{i2\pi(j+a)(z+b)} \tag{4.8}$$

such that a, b are rational numbers and j is an integer. Ladder operator for LL-index in symmetric gauge are given by $a^\dagger = \sqrt{2}\ell\left(\bar{z}/4\ell^2 - \partial_z\right)$. For convenience, we can separate out its action on the exponential pre-factor as follows

$$a^\dagger e^{-\frac{z^2+|z|^2}{2\ell^2}} = e^{-\frac{z^2+|z|^2}{2\ell^2}} a_f^\dagger \tag{4.9}$$

such that $a_f^\dagger = \sqrt{2}\ell\left(\frac{\bar{z}+z}{2\ell^2} - \partial_z\right)$ is the effective ladder operator for LL index which does not act on the exponential pre-factor. Landau orbitals for higher LLs can then be written as

$$\phi_{n,k}(z,\bar{z}) = e^{-\frac{z^2+|z|^2}{2\ell^2}} \frac{(a_f^\dagger)^n}{\sqrt{n!}} \left[\vartheta\begin{bmatrix}\frac{k}{N_\phi}+\frac{\theta_2}{2\pi N_\phi}\\ \frac{\theta_1}{2\pi}\end{bmatrix}\left(\frac{N_\phi z}{L_2}\middle| N_\phi\tau\right)\right] \tag{4.10}$$

where LL-index $n = 0, 1, 2, \ldots$ and so on. Using Eq. (4.6) and the following properties of Jacobi theta functions, given by

$$\begin{aligned}\vartheta\begin{bmatrix}a\\ b\end{bmatrix}(z\pm 1|\tau) &= e^{\pm i2\pi a}\vartheta\begin{bmatrix}a\\ b\end{bmatrix}(z|\tau)\\ \vartheta\begin{bmatrix}a\\ b\end{bmatrix}(z\pm \tau|\tau) &= e^{-i\pi[\tau\pm 2(z+b)]}\vartheta\begin{bmatrix}a\\ b\end{bmatrix}(z|\tau)\end{aligned} \tag{4.11}$$

it can be checked that Landau orbital $\phi_{n,k}(z,\bar{z})$ are the eigenstates of lattice translations $t_i(\boldsymbol{L}_1)$ and $t_i(\boldsymbol{L}_2)$ with eigenvalues $e^{i\theta_1}$ and $e^{i\theta_2}$, respectively. The Hilbert space representation of the MTOs $t_i(\boldsymbol{L}_1)$ and $t_i(\boldsymbol{L}_2)$ is labeled by the choice of θ_1 and θ_2 values, respectively.

Next we will see that, the single-particle lattice translation symmetry in a QH system on torus geometry gives rise to other useful many-body translation symmetries. Hamiltonians of much larger dimensions can be exactly diagonalized in symmetry blocks of these translation operators. We will see in the next chapter that the characteristic degeneracy in FQH spectra in torus can be better understood using the quantum numbers of these many-body operators.

4.2 Many-body Symmetries on torus

For a QH system on torus, two many-body translation operators can be defined as

$$\begin{aligned}t_{\text{cm}}(\boldsymbol{a}) &= \prod_i t_i(\boldsymbol{a})\\ \tilde{t}_i(\boldsymbol{a}) &= t_i\left(\frac{(N_e-1)\boldsymbol{a}}{N_e}\right)\prod_{j\neq i} t_j\left(-\frac{\boldsymbol{a}}{N_e}\right)\end{aligned} \tag{4.12}$$

where $\tilde{t}_i$ and t_{cm} are named *relative* and *center-of-mass* translation operators, respectively. The action of these operators is schematically shown in Fig. 4.2. In order to preserve the Hilbert space representation fixed by (θ_1, θ_2), $t_{\text{cm}}(\boldsymbol{a})$ and $\tilde{t}_i(\boldsymbol{a})$ need to commute with discrete lattice translations $t_j(\boldsymbol{L}_1)$ and $t_j(\boldsymbol{L}_2)$, $\forall\, i,\, j$. Since we want the eigenfunctions to

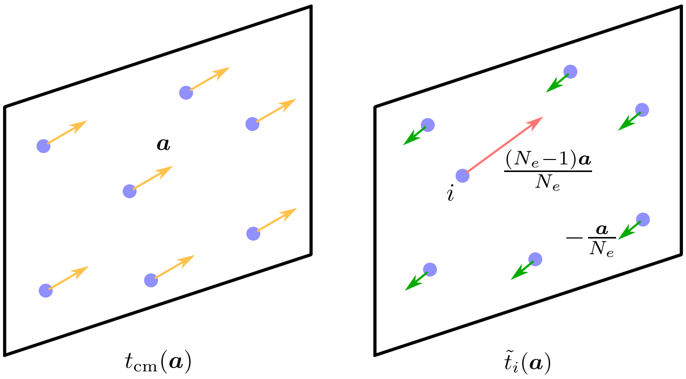

Figure 4.2: Schematic for center-of-mass (left) and relative (right) many-body translations on torus, represented by $t_{\text{cm}}(\boldsymbol{a})$ and $\tilde{t}_i(\boldsymbol{a})$, respectively. While $t_{\text{cm}}(\boldsymbol{a})$ translates all particles by same vector $\boldsymbol{a}$, relative translation $\tilde{t}_i(\boldsymbol{a})$ translates ith particle by $(N_e-1)\boldsymbol{a}/N_e$ and the rest are translated by $-\boldsymbol{a}/N_e$.

be simultaneously labeled with quantum numbers of $\tilde{t}_i(\boldsymbol{a})$ and $t_{\text{cm}}(\boldsymbol{a})$, following conditions are required:

1. $[\tilde{t}_i(\boldsymbol{a}), t_{\text{cm}}(\boldsymbol{b})] = 0$
2. $[\tilde{t}_i(\boldsymbol{a}), \tilde{t}_i(\boldsymbol{b})] = 0$
3. $[t_{\text{cm}}(\boldsymbol{a}), t_{\text{cm}}(\boldsymbol{b})] = 0$

It turns out that apart from the first condition, other two are not true $\forall\, \boldsymbol{a}, \boldsymbol{b}$. Hence, we form a maximally commuting subset of these operators by restricting the translations.

For a system of $N_e = pN$ particles in $N_\phi = qN$ flux quanta, where $N = \gcd(N_e, N_\phi)$, this maximally commuting subset is given by

$$\bigcup_{m,n} \left\{ \tilde{t}_i(p\boldsymbol{L}_{m,n}), t_{\text{cm}}\left(\frac{q\boldsymbol{L}_{m,n} + r\boldsymbol{L}_2}{N_\phi}\right) \,\middle|\, 0 \le r < q \right\} \tag{4.13}$$

Although this gives us infinite number of quantum numbers, these quantum numbers are fully determined by the eigenvalues of $\tilde{t}_i(p\boldsymbol{L}_1)$, $\tilde{t}_i(p\boldsymbol{L}_2)$ and $t_{\text{cm}}(\boldsymbol{L}_2/N_\phi)$.

4.2.1 Eigenfunctions of Many-body translation operators

Many-body basis states can be written as $|\{k_i\}\rangle \equiv |k_1, k_2, \ldots, k_{N_e}\rangle$ such that $|k\rangle \equiv \phi_{n,k}(z,\bar{z})$ defined in Eq. (4.10); the LL-indices n's, are suppressed for brevity. It is easy to check that many-body basis states $|\{k_i\}\rangle$ are already eigenfunctions of $t_{\text{cm}}(\boldsymbol{L}_2/N_\phi)$ with quantum number $K_2 = \sum_i k_i (\bmod N_\phi)$, such that

$$t_{\text{cm}}(\boldsymbol{L}_2/N_\phi)\,|\{k_j\}, K_2\rangle = e^{2\pi i K_2/N_\phi}\,|\{k_j\}, K_2\rangle \tag{4.14}$$

If we denote a basis state in a given K_2-sector by $|\{k_i\}, K_2\rangle$, the action of $\tilde{t}_j\,(p\boldsymbol{L}_1)$ is given by

$$\tilde{t}_i(p\boldsymbol{L}_1)\,|\{k_j\}, K_2\rangle = |\{(k_j + q) \bmod N_\phi\}, K_2\rangle \tag{4.15}$$

Although $\tilde{t}_i(p\boldsymbol{L}_1)$ increments k_i for each particle by q, the state remains in the same K_2-sector. Eigenfunctions for $\tilde{t}_i(p\boldsymbol{L}_1)$ are constructed by linearly combining states from a given K_2-sector as

$$\left|\tilde{K}_1, K_2\right\rangle = \sum_{j=0}^{N_\phi} e^{i2\pi\tilde{K}_1 j/N}\,|\{(k_i + jq) \bmod N_\phi\}, K_2\rangle \tag{4.16}$$

Eigenvalues of $\tilde{t}_i(p\boldsymbol{L}_1)$ are given by $e^{-i2\pi\tilde{K}_1/N}$ where $\tilde{K}_1$ can take values from $0, 1, \ldots, N-1$.

We first exact diagonalize the Hamiltonian in a fixed K_2-sector. In order to label the eigenfunctions with $\tilde{K}_1$ quantum numbers, we explicitly construct the $\tilde{t}_i(p\boldsymbol{L}_1)$ operator using Eq. (4.15), and compute its expectation value for the eigestates. $\tilde{K}_1$ and K_2 can be used to label the eigenfunctions of Hamiltonian invariant under lattice translations of torus.

4.3 Cylinder geometry

Any geometry with periodicity along one of the direction can be treated as a cylinder. Fig. 4.3 shows a cylinder with length L along the periodic direction.

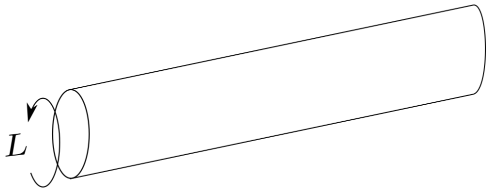

Figure 4.3: Schematic of cylinder geometry with period L

Single-particle states for cylinder are given by

$$\phi_{n,k}(\boldsymbol{r}) = \frac{1}{\sqrt{2^n n!\sqrt{\pi}L}}\exp\left[-i\frac{2\pi k}{L}y\right]\exp\left[-\frac{1}{2}\left(\frac{x}{\ell} - \frac{2\pi\ell}{L_y}k\right)^2\right]H_n\left[\frac{2\pi\ell}{L}k - \frac{x}{\ell}\right] \tag{4.17}$$

where L is the length of circumference. Length of the cylinder fixed by putting a cut-off on k values such that it can only take N_ϕ consecutive values in each LL with $k_{\text{min}} = 0$ and $k_{\text{max}} = N_\phi - 1$.

4.4 Calculation of Matrix elements

4.4.1 For torus

In this section, we show the calculation of matrix elements of the model interaction on torus. We will restrict to a rectangular torus with $L_1/L_2 = iL_x/L_y$ and $L_\Delta = 0$. The matrix elements of an interaction $V(|\boldsymbol{r}|)$ on torus can be written using its Fourier transform $V(|\boldsymbol{q}|)$ as

$$\begin{aligned} V^{n_1n_2-n_3n_4}_{j_1j_2-j_3j_4} =& \frac{1}{L_xL_y}\sum_q V(\boldsymbol{q}) \iint \mathrm{d}\boldsymbol{r}_1\mathrm{d}\boldsymbol{r}_2 \left[\phi^*_{n_1,j_1}(\boldsymbol{r_1})\phi^*_{n_2,j_2}(\boldsymbol{r_2}) - \phi^*_{n_1,j_1}(\boldsymbol{r_2})\phi^*_{n_2,j_2}(\boldsymbol{r_1})\right] \\ & \times \left[\phi_{n_3,j_3}(\boldsymbol{r_1})\phi_{n_4,j_4}(\boldsymbol{r_2}) - \phi_{n_3,j_3}(\boldsymbol{r_2})\phi_{n_4,j_4}(\boldsymbol{r_1})\right] e^{i\boldsymbol{q}\cdot(\boldsymbol{r}_1-\boldsymbol{r}_2)} \end{aligned} \tag{4.18}$$

where the form of single-particle orbitals on torus $\phi_{n,j}$, is given in Eq. (4.10) and the summation is over reciprocal vectors $\boldsymbol{q}$ of torus lattice vectors, given by $\boldsymbol{q} = 2\pi\left[\frac{s}{L_x}, \frac{t}{L_y}\right]$, such that $s, t \in \mathbb{Z}$. We define

$$\begin{aligned} &\langle n_1, j_1; n_2, j_2|\, e^{i\boldsymbol{q}\cdot(\boldsymbol{r}_1-\boldsymbol{r}_2)}\, |n_3, j_3; n_4, j_4\rangle = \\ &\qquad = \iint \mathrm{d}\boldsymbol{r}_1\phi^*_{n_1,j_1}(\boldsymbol{r_1})\phi^*_{n_2,j_2}(\boldsymbol{r_2})e^{i\boldsymbol{q}\cdot(\boldsymbol{r}_1-\boldsymbol{r}_2)}\mathrm{d}\boldsymbol{r_2}\phi^*_{n_3,j_3}(\boldsymbol{r_1})\phi^*_{n_4,j_4}(\boldsymbol{r_2}) \end{aligned} \tag{4.19}$$

where $|n_1, j_1; n_2, j_2\rangle$ is a two-particle state for particles in LL n_1 and n_2 with momentum j_1 and j_2, respectively. Note that, this two-particle state does not represent an antisymmetrized state.

In Sec. 5.1, we provide the details for construction of the model interaction for torus. The model interaction on torus is written such that calculation of intra and inter-LL matrix elements uses different forms of $V(|\boldsymbol{q}|)$. For nth LL, the intra-LL matrix element is given by

$$\begin{aligned} V^{nn-nn}_{j_1j_2-j_3j_4} =& \frac{1}{L_xL_y}\sum_{s,t\in\mathbb{Z}} V(q) \left[\mathcal{L}_n\left(\frac{q^2\ell^2}{2}\right)\right]^2 e^{-\frac{(q\ell)^2}{2}} \times \\ & \times \left[e^{\frac{i2\pi s}{N_\phi}(j_1-j_4)} - e^{\frac{i2\pi s}{N_\phi}(j_2-j_4)} - e^{\frac{i2\pi s}{N_\phi}(j_1-j_3)} + e^{\frac{i2\pi s}{N_\phi}(j_2-j_3)}\right] \end{aligned} \tag{4.20}$$

where $\mathcal{L}_n$ is nth Laguerre polynomial and the form of $V(q) = V^{nn-nn}_1(q)$ for intra-LL matrix elements is given in Eq. (5.3). Using the notation defined in Eq. (4.19), inter-LL matrix element for LLs n and n' can be written as

$$\begin{aligned} V^{nn'-nn'}_{j_1j_2-j_3j_4} =& \frac{1}{L_xL_y}\sum_{s,t\in\mathbb{Z}} V(q)\times \\ & \Big\{\langle n, j_1; n', j_2|\, e^{i\boldsymbol{q}\cdot(\boldsymbol{r}_1-\boldsymbol{r}_2)}\, |n, j_3; n', j_4\rangle + \langle n', j_2; n, j_1|\, e^{i\boldsymbol{q}\cdot(\boldsymbol{r}_1-\boldsymbol{r}_2)}\, |n', j_4; n, j_3\rangle \\ & - \langle n', j_2; n, j_1|\, e^{i\boldsymbol{q}\cdot(\boldsymbol{r}_1-\boldsymbol{r}_2)}\, |n, j_3; n', j_4\rangle - \langle n, j_1; n', j_2|\, e^{i\boldsymbol{q}\cdot(\boldsymbol{r}_1-\boldsymbol{r}_2)}\, |n', j_4; n, j_3\rangle\Big\} \end{aligned} \tag{4.21}$$

where the explicit form of terms inside the parenthesis is following

$$\begin{aligned}
\left\langle n, j_1; n', j_2\right| e^{i\boldsymbol{q}\cdot(\boldsymbol{r}_1-\boldsymbol{r}_2)} \left|n, j_3; n', j_4\right\rangle =&\mathcal{L}_{n_1}\left(\frac{q^2\ell^2}{2}\right)\mathcal{L}_{n_2}\left(\frac{q^2\ell^2}{2}\right)e^{\frac{i2\pi s}{N_\phi}(j_1-j_4)}\\
\left\langle n', j_2; n, j_1\right| e^{i\boldsymbol{q}\cdot(\boldsymbol{r}_1-\boldsymbol{r}_2)} \left|n', j_4; n, j_3\right\rangle =&\mathcal{L}_{n_1}\left(\frac{q^2\ell^2}{2}\right)\mathcal{L}_{n_2}\left(\frac{q^2\ell^2}{2}\right)e^{\frac{i2\pi s}{N_\phi}(j_2-j_3)}\\
\left\langle n', j_2; n, j_1\right| e^{i\boldsymbol{q}\cdot(\boldsymbol{r}_1-\boldsymbol{r}_2)} \left|n, j_3; n', j_4\right\rangle =&\frac{(q\ell)^2}{2}e^{\frac{i2\pi s}{N_\phi}(j_1-j_3)}\\
\left\langle n, j_1; n', j_2\right| e^{i\boldsymbol{q}\cdot(\boldsymbol{r}_1-\boldsymbol{r}_2)} \left|n', j_4; n, j_3\right\rangle =&\frac{(q\ell)^2}{2}e^{\frac{i2\pi s}{N_\phi}(j_2-j_4)}
\end{aligned}\tag{4.22}$$

4.4.2 For cylinder

On a cylinder with length L along periodic y-direction, the Fourier transform of an interaction V given by

$$V = \frac{1}{(2\pi L)}\sum_k \int \mathrm{d}q_x\ V(\boldsymbol{q})e^{iq_x(\hat{x}_1-\hat{x}_2)}e^{i\frac{2\pi k}{L}(\hat{y}_1-\hat{y}_2)} \tag{4.23}$$

such that y-momentum is quantized as $q_y = \frac{2\pi k}{L}$, where k is integer. Similar to torus, Landau orbitals given in Eq. (4.17) can be used to calculate the matrix-elements of V in cylinder geometry. It can be checked that the form of matrix-element $V^{n_1n_2-n_3n_4}_{j_1j_2-j_3j_4}$ for cylinder comes out to be identical to torus matrix-elements, for both inter and intra-LL cases.

Chapter 5

Torus geometry eigenfunctions of an interacting multi-Landau level Hamiltonian

In this chapter, we complete the calculations in Chapter 2 and 3, which focused on the disk and spherical geometry, by studying the spectra and the eigenfunctions of the Hamiltonian in torus and cylinder geometries. We motivate structure of the Hamiltonian in the torus using the analogy with the multilayer model. Direct generalization of disk eigenfunction to the torus is not possible as the function do not satisfy the necessary boundary conditions. Nonetheless, an alternative ansatz can be written for the torus and the sphere which describes the ground state and charged excitations at Laughlin filling fraction $1/(2p+1)$. For the case of cylinder, an ansatz can be constructed by direct generalization of the disk ansatz.

This chapter is organized as follows. The model interaction for torus is given in Sec. 5.1. In Sec. 5.2, we extend the known disk eigenfunctions to the cylinder geometry. We show that, although these eigenfunctions do not extend to the torus, alternate ansatz eigenfunctions on torus can be constructed nevertheless for low-energy quasi-particle (QP) and some neutral excitations of $\nu = 1/3$. Numerical results are presented in Sec. 5.3 where various features of low-energy spectra of the model interaction for torus and cylinder are discussed. Finally, we summarize our results in Sec. 5.4.

Notations – In the chapter, unless we mention otherwise, we use symmetric gauge $\boldsymbol{A}(\boldsymbol{r}) = \frac{B}{2}\boldsymbol{r} \times \hat{e}_z$ corresponding to a magnetic field $\boldsymbol{B} = -B\hat{e}_z$. The magnetic length is defined as $\ell = \sqrt{\hbar/eB}$ and the magnetic flux is counted in the units of flux quanta $\phi_0 = hc/e$. When positions are represented in complex form, we use the convention $z = x + iy$. For calculations in the disk geometry, angular momentum k takes values in $0, 1, 2, \ldots$ in all

LLs. For given complex numbers z and τ, Jacobi theta function [36] is defined as

$$\vartheta\begin{bmatrix}a\\b\end{bmatrix}(z|\tau) = \sum_{n=-\infty}^{\infty} e^{i\pi(n+a)^2\tau}e^{i2\pi(n+a)(z+b)} \tag{5.1}$$

where a, b are rational numbers and n is an integer.

5.1 Model Interaction on Torus

The model interaction (Eq. 2.2) described in Chapter 2 was originally written in terms of pseudo-potentials for rotationally symmetric systems like a disk, which means that it assigns energy to a pair of particles based on their relative angular momentum given by m. The natural way to map the interaction into the torus geometry is to first reconstruct the real space form $V(r)$ of the interaction (or its Fourier transform $V(q)$). The interaction matrix elements on the torus can be calculated from $V(r)$. Unfortunately, the interaction shown in Eq. (2.2) is unlikely to be diagonal in the real-space representation. This is indicated by the fact that the projection of the interaction into each LL has the same number of non-zero psueodpotentials.

We can nevertheless define torus matrix elements of an interaction that produces the same features in the following way. We construct a different real space form for different terms of the interaction in Eq. (2.2). For instance, for $2p = 2$, the interaction within the nth LL imposes an energy cost for the state $|n, n; m = 1\rangle = (a_1^\dagger)^n(a_2^\dagger)^n(b_1^\dagger - b_2^\dagger)\,|0, 0\rangle$, which is a two particle state where both particles are in nth LL with relative momentum $m = 1$, and a_i and b_i are ith-particle ladder operators for LL and angular momentum respectively. We seek an interaction whose Fourier transform $V(|\boldsymbol{q}|)$ satisfies

$$\int \mathrm{d}\boldsymbol{q}\, V(|\boldsymbol{q}|)\langle n, n; m|e^{i\boldsymbol{q}\cdot(\hat{\boldsymbol{r}}_1-\hat{\boldsymbol{r}}_2)}|n, n; m\rangle = \delta_{m,1}. \tag{5.2}$$

The expectation value $\langle n, n; m|e^{i\boldsymbol{q}\cdot(\hat{\boldsymbol{r}}_1-\hat{\boldsymbol{r}}_2)}|n, n; m\rangle$ can be evaluated to be $\left\langle n|e^{A_1}|n\right\rangle \left\langle n|e^{A_2}|n\right\rangle$ $\langle m|B|m\rangle$ where $\hat{\boldsymbol{r}}_i$ are the position operators, $A_i = \frac{i\ell}{\sqrt{2}}(qa_i^\dagger + \bar{q}a_i)$, $B = e^{(q\ell)^2/2}e^{i\bar{q}\ell b_r^\dagger}e^{iq\ell b_r}$ and $b_r = (b_1 - b_2)/\sqrt{2}$ is the ladder operator for relative angular momentum. Here the reciprocal vector is written as a complex number $q = q_x + iq_y$ (note that, this is unrelated from parameter q for FQH system defined in the previous section). A solution is found to be

$$V_{m=1}^{nn-nn}(q) = \frac{\mathcal{L}_{m=1}(q^2\ell^2)}{\left\langle n|e^{A_1}|n\right\rangle \left\langle n|e^{A_2}|n\right\rangle} \tag{5.3}$$

where $\mathcal{L}_m$ is the mth Laguerre polynomial. The two particle interaction matrix elements on the torus for this component of the interaction can be calculated from the real space form $V(r) = \int \mathrm{d}\boldsymbol{q}\, V(|\boldsymbol{q}|)\, e^{i\boldsymbol{q}\cdot(\hat{\boldsymbol{r}}_1-\hat{\boldsymbol{r}}_2)}$. We find that all LL dependent information vanishes when the matrix elements are computed; so we get identical interaction matrix elements between momentum states of the torus in every LL.

The inter-LL interactions (again assuming $2p = 2$) associates an energy cost whenever particles in two different LLs have a relative angular momentum $m = 0$ or 1 in the disk ie for states $|n, n', m = 1\rangle = ((a_1^\dagger)^n (a_2^\dagger)^{n'} + (a_1^\dagger)^{n'} (a_2^\dagger)^n)(b_1^\dagger - b_2^\dagger)\,|0, 0\rangle$ and $|n, n', m = 0\rangle = ((a_1^\dagger)^n (a_2^\dagger)^{n'} - (a_1^\dagger)^{n'} (a_2^\dagger)^n)\,|0, 0\rangle$. Here the solutions for $V(q)$ can be taken to be

$$V_{m=1}^{n_1n_2-n_3n_4}(q) = \frac{\mathcal{L}_{m=1}(q^2\ell^2)(\delta_{n_1n_3}\delta_{n_2n_4} + \delta_{n_1n_4}\delta_{n_2n_3})}{\langle n_1|e^A|n_3\rangle\,\langle n_2|e^A|n_4\rangle}$$

$$V_{m=0}^{n_1n_2-n_3n_4}(q) = \frac{\mathcal{L}_{m=0}(q^2\ell^2)(\delta_{n_1n_3}\delta_{n_2n_4} - \delta_{n_1n_4}\delta_{n_2n_3})}{\langle n_1|e^A|n_3\rangle\,\langle n_2|e^A|n_4\rangle}$$

Again this leads to an interaction where matrix elements in the momentum space are independent of the LLs. Explicit form of the final matrix elements are given in the next section.

The general form of torus matrix elements is given in Sec. 4.4. For the case of inter-LL term, we use $V(\boldsymbol{q}) = V_0^{n_1n_2-n_3n_4}(q) + V_1^{n_1n_2-n_3n_4}(q)$. Putting the corresponding form of V(q) given in Sec. 5.1, intra and inter-LL matrix elements are given by

$$\begin{aligned} V_{j_1j_2-j_3j_4}^{nn-nn} =& \frac{1}{L_xL_y}\sum_{s,t\in\mathbb{Z}} e^{-\frac{q^2}{2}}\,\mathcal{L}_1(q^2\ell^2)\times \\ & \left(e^{\frac{i2\pi s}{N_\phi}(j_1-j_4)} + e^{\frac{i2\pi s}{N_\phi}(j_2-j_3)} - e^{\frac{i2\pi s}{N_\phi}(j_1-j_3)} - e^{\frac{i2\pi s}{N_\phi}(j_2-j_4)}\right) \end{aligned} \tag{5.4}$$

and

$$\begin{aligned} V_{j_1j_2-j_3j_4}^{nn'-nn'} =& \frac{1}{L_xL_y}\sum_{s,t\in\mathbb{Z}} e^{-\frac{q^2}{2}}\;\Bigg[(\mathcal{L}_1(q^2\ell^2) + \mathcal{L}_0(q^2\ell^2))\left(e^{\frac{i2\pi s}{N_\phi}(j_1-j_4)} + e^{\frac{i2\pi s}{N_\phi}(j_2-j_3)}\right) \\ & -(\mathcal{L}_1(q^2\ell^2) - \mathcal{L}_0(q^2\ell^2))\left(e^{\frac{i2\pi s}{N_\phi}(j_1-j_3)} + e^{\frac{i2\pi s}{N_\phi}(j_2-j_4)}\right)\Bigg] \end{aligned} \tag{5.5}$$

Both intra and inter-LL matrix elements are independs of LL-indices.

Cylinder geometry : For calculation of cylinder matrix elements, we use the same form of $V(q)$ which was used in the case of torus geometry.

5.2 Exact Eigenfunctions

As was argued in Sec 3.2, exact eigenfunctions of the model Hamiltonian can be constructed on the disk geometry. In this section, we first show how to generalize these eigenfunctions to the cylinder geometry. We then discuss the sphere and torus geometries and show that similar generalization does not work in these cases. Eigenfunctions can nevertheless be written down for low-energy QP type excitations of FQH system at filling 1/3 for both the geometries.

5.2.1 Generalizing disk eigenfunctions to cylinder

The unprojected CF state on the cylinder is given by

$$\Psi_{\nu=\frac{\nu^*}{2p\nu^*+1}} = \prod_{i<j}\left(e^{\frac{2\pi z_i}{L}} - e^{\frac{2\pi z_j}{L}}\right)^{2p} \Phi_{\nu^*} \tag{5.6}$$

where L is the length along the periodic direction of cylinder, and Φ_{ν^*} is the Slater determinant state with Landau orbitals in reduced flux N_ϕ^*. For the Landau gauge $\boldsymbol{A} = -xB\hat{e}_y$, the single-particle state $\phi_{n,k}(\boldsymbol{r})$ with momentum k in nth LL, is given by

$$\begin{aligned}\phi_{n,k}(\boldsymbol{r}) = \mathcal{N}\exp\left(\frac{i2\pi k}{L}y\right)\exp\left[-\frac{1}{2}\left(\frac{x}{\ell}-\frac{2\pi\ell}{L}k\right)^2\right]\times \\ \times H_n\left(\frac{2\pi\ell}{L}k-\frac{x}{\ell}\right)\end{aligned} \tag{5.7}$$

where $\mathcal{N}$ is normalization, H_n is the nth Hermite polynomial and k is the momentum quantum number which takes value in $0, 1, \ldots, N_\phi - 1$.

In the spirit of the eigenfunction to our model Hamiltonian in the disk geometry, we replace the coordinates in the Jastrow factor with the guiding-center coordinates, to get

$$\Psi_{\nu=\frac{\nu^*}{2p\nu^*+1}} = \prod_{i<j}\left(e^{\frac{2\pi \hat{Z}_i}{L}} - e^{\frac{2\pi \hat{Z}_j}{L}}\right)^{2p} \Phi_{\nu^*} \tag{5.8}$$

For the given gauge, the action of $\hat{Z}$ on $\phi_{n,k}(z)$ is manifested through

$$e^{\frac{2\pi\hat{Z}_i}{L}}\phi_{n,k}(z) = e^{\frac{2\pi^2}{L^2}(2k+1)}\phi_{n,k+1}(z) \tag{5.9}$$

Although multiplication with Jastrow factor changes the momentum state of orbitals in Φ_{ν^*}, it does not change their LL-index. Thus, it is easy to see from Eq. (5.9), just like Slater determinant Φ_{ν^*}, the ansatz Ψ_ν is also an eigenfunction of the kinetic energy. Kinetic energy of the state Ψ_ν is identical to that of Φ_{ν^*}, as in the case of disk geometry.

It is not straightforward to see that the ansatz defined in Eq. (5.8) is a zero-energy eigenfunction of the model interaction in the cylinder geometry, however, for a few QPs at filling $\nu = 1/3$, we numerically verified that the eigenfunctions in Eq. (5.8) match exactly with the ED eigenfunctions of the model interaction. Also, as will be shown in the Sec. 5.3.2, the counting of low energy states match that the 1 QH spectrum, as one would expect from the ansatz in Eq. (5.8).

5.2.2 Attempt to generalize disk eigenfunctions to torus

Motivated by the exact eigenfunctions in the disk and cylinder geometry, we consider similar construction of the ansatz on the torus by replacing the coordinates in the Jastrow factor of the unprojected CF states, [40, 34] with the guiding-center coordinates. For the torus geometry, the resulting ansatz is given by

$$\Psi_{\nu=\frac{\nu^*}{2p\nu^*+1}} = \left[F_1(\hat{Z}_{\rm cm})\right]^{2p} \mathcal{J}^{2p}(\{\hat{Z}\})\; e^{-\sum_i \frac{z_i^2+|z_i|^2}{2\ell^2}}\; \Phi_{\nu^*} \tag{5.10}$$

where

$$\mathcal{J}(\{\hat{Z}\}) = \prod_{i<j} \vartheta \begin{bmatrix} 1/2 \\ 1/2 \end{bmatrix} \left(\frac{\hat{Z}_i - \hat{Z}_j}{L_2} \middle| \tau \right) \tag{5.11}$$

is the Jastrow factor of guiding-center coordinates. In section, we will write $\mathcal{J}^{2p}(\{\hat{Z}\})$ as $\hat{\mathcal{J}}$ for brevity. $\hat{Z}_{\rm cm} = \sum_i \hat{Z}_i$ is the center-of-mass of guiding-centers and Φ_{ν^*} is the Slater determinant of Landau orbitals defined in Eq. (4.10) at flux N_ϕ^* instead of N_ϕ. For the torus in Fig. 4.1, we have $\tau = -L_1/L_2$. $F_1(\hat{Z})$ represents the center-of-mass dependent part of the filled lowest Landau level, [34] given by

$$F_1(\hat{Z}_{\rm cm}) = \vartheta \begin{bmatrix} \frac{\theta_2}{2\pi} + \frac{N_e-1}{2} \\ \frac{\theta_1}{2\pi} + \frac{N_e-1}{2} \end{bmatrix} \left(\frac{\hat{Z}_{\rm cm}}{L_2} \middle| \tau \right) \tag{5.12}$$

where θ_1 and θ_2 determine the Hilbert space representations of MTOs $t_i(L_1)$ and $t_i(L_2)$ respectively (see Sec. 4.1.1). In what follows, we show that the generalization of Eq. (5.10) does not yield an eigenfunction of $t_i(L_1)$ and is, therefore, not a valid eigenfunction.

To verify the boundary conditions of the ansatz, we calculate the action of the MTOs on each piece of the ansatz one-by-one. A MTO, $t_i(\boldsymbol{a})$, can be written in terms of normal translation operators, $T_i(\boldsymbol{a})$, in the symmetric gauge as

$$t_i(\boldsymbol{a}) = e^{-\frac{i}{2\ell^2}\hat{e}_z\cdot(\boldsymbol{a}\times\boldsymbol{r}_i)} T_i(\boldsymbol{a}) \tag{5.13}$$

The guiding-center coordinate, $\hat{Z}_i$, transform under $t_i(a)$ like normal position coordinates (z) transform under $T_i(\boldsymbol{a})$. The action of $t_i(L_2)$ on various pieces of the ansatz is given as

$$t_i(L_2) F_1(\hat{Z}_{\rm cm}) t_i^\dagger(L_2) = e^{i\theta_2} F_1(\hat{Z}_{\rm cm}) \tag{5.14}$$

$$t_i(L_2) \hat{\mathcal{J}} t_i^\dagger(L_2) = \hat{\mathcal{J}} \tag{5.15}$$

The action of MTOs on functions of normal position coordinates can be calculated using Eq. (5.13), which gives us

$$t_i(L_2) \left[e^{-\frac{\sum_i z_i^2+|z_i|^2}{2\ell^2}} \Phi_{\nu^*} \right] = e^{i\theta_2} \left[e^{-\frac{\sum_i z_i^2+|z_i|^2}{2\ell^2}} \Phi_{\nu^*} \right] \tag{5.16}$$

By putting them together, we get

$$t_i(L_2) \Psi_{\frac{\nu^*}{2p\nu^*+1}} = e^{i\alpha\theta_2} \Psi_{\frac{\nu^*}{2p\nu^*+1}} \tag{5.17}$$

where $\alpha = (2p+1)$. This implies that Ψ is an eigenfunction of $t_i(L_2)$. Now we consider the action of $t_i(L_1)$ on the ansatz Ψ. It is easy to check that

$$t_i(L_1)F_1(\hat{Z}_{\text{cm}})t_i^\dagger(L_1) = e^{i\theta_1}e^{-i\pi\tau}e^{\frac{i2\pi\hat{Z}_{\text{cm}}}{L_2}}F_1(\hat{Z}_{\text{cm}}) \tag{5.18}$$

$$t_i(L_1)\hat{\mathcal{J}}t_i^\dagger(L_1) = e^{-i\pi(N_e-1)\tau}e^{-\frac{i2\pi\hat{Z}_{\text{cm}}}{L_2}}e^{\frac{i2\pi N_e\hat{Z}_i}{L_2}}\hat{\mathcal{J}} \tag{5.19}$$

and

$$\begin{aligned} t_i(L_1)\left[e^{-\frac{\sum_i z_i^2+|z_i|^2}{2\ell^2}}\Phi_{\nu^*}\right] = \\ e^{i\theta_1}e^{i2\pi pN_e\tau}e^{-\frac{i4\pi pN_e\hat{Z}_i}{L_2}}\left[e^{-\frac{\sum_i z_i^2+|z_i|^2}{2\ell^2}}\Phi_{\nu^*}\right] \end{aligned} \tag{5.20}$$

By combining these results together, the action of $t_i(L_1)$ on the ansatz is found to be

$$t_i(L_1)\Psi_{\frac{\nu^*}{2p\nu^*+1}} = e^{i\alpha\theta_1}e^{\frac{i4\pi pN_e}{L_2}(\hat{Z}_i-z_i)}\Psi_{\frac{\nu^*}{2p\nu^*+1}} \tag{5.21}$$

Since the action of $t_i(L_1)$ on ansatz results in a factor which contains the guiding-center operator $\hat{Z}_i$, the ansatz is not an eigenfunction of $t_i(L_1)$ and hence not a valid state on torus. Using Eq. (5.18)-(5.20) it can be verified that, similar factor will arise even if we use $F_1(Z_{\text{cm}})$ with normal center-of-mass coordinate instead, in the ansatz. In summary, this implies that the ansatz obtained by straightforward generalization of Eq. (3.5) valid on disk and Eq. (5.8) valid on cylinder, does not yield an eigenfunction on torus.

5.2.3 Exact Eigenfunction for QPs of $\nu = 1/3$

As shown in the previous section the disk ansatz Eq. (3.5) does not generalize to the torus. It is also not possible to generalize it to spherical geometry as the form of the guiding-center coordinate is not known for sphere. In this section, we show that for a subset of states namely quasiparticles of the 1/3 state, the ansatz can be written in a simplified form, which generalizes to sphere and torus geometries. For the disk and the spherical geometry we could verify that the results from the ED of the Hamiltonian (Sec. 2.1) match with the form of the eigenfunction presented here. Finally, we show that a similar generalization leads to a valid state on torus, as it satisfies the periodic boundary conditions.

Ansatz for torus geometry

Motivated by the applicability of ansatz in Eq. (3.11) to the spherical geometry, in this section we ask whether it also gives a valid state on torus. For N QPs on $\nu = 1/3$ with N_e particles in N_ϕ flux quanta, the analogue of Eq. (3.11) in torus geometry is

$$\Psi_{1/3}^{\text{N−QPs}} = e^{-\frac{\sum_i^{N_e} z_i^2+|z_i|^2}{2\ell^2}}\left[F_1(Z_{\text{cm}})\right]^2\hat{\mathcal{D}}_1^{\text{N−QPs}}\left(\{f_i^k,\hat{g}_j^q\}\right)\mathcal{J}^2(\{z\}) \tag{5.22}$$

where $Z_{\text{cm}} = \sum_i z_i$ and $\mathcal{J}(\{z\})$ is the Jastrow factor, given by

$$\mathcal{J}(\{z\}) = \prod_{i<j}^{N_e} \vartheta \begin{bmatrix} 1/2 \\ 1/2 \end{bmatrix} \left(\frac{z_i - z_j}{L_2} \middle| \tau \right) \tag{5.23}$$

All states inside the determinant $\hat{\mathcal{D}}\left(\{f_i^k, \hat{g}_j^q\}\right)$ see reduced flux $N_\phi^* = N_\phi - 2N_e$ and the corresponding magnetic length is given by ℓ^*, defined as $(\ell^*)^2 = \ell^2 N_\phi / N_\phi^*$. For N QPs in 2LL, the operator $\hat{\mathcal{D}}_1^{\text{N-QPs}}\left(\{f_i^k, \hat{g}_j^q\}\right)$ is defined as

$$= \begin{vmatrix} f_0^0(z_1) & f_0^0(z_2) & \dots & f_0^0(z_{N_e}) \\ f_0^1(z_1) & f_0^1(z_2) & \dots & f_0^1(z_{N_e}) \\ \vdots & \vdots & \vdots & \vdots \\ f_0^{N_\phi^*-1}(z_1) & f_0^{N_\phi^*-1}(z_2) & \dots & f_0^{N_\phi^*-1}(z_{N_e}) \\ \hat{g}_1^{q_1}(z_1, \bar{z}_1) & \hat{g}_1^{q_1}(z_2, \bar{z}_2) & \dots & \hat{g}_1^{q_1}(z_{N_e}, \bar{z}_{N_e}) \\ \vdots & \vdots & \ddots & \vdots \\ \hat{g}_1^{q_{N_2}}(z_1, \bar{z}_1) & \hat{g}_1^{q_{N_2}}(z_2, \bar{z}_2) & \dots & \hat{g}_1^{q_{N_2}}(z_{N_e}, \bar{z}_{N_e}) \end{vmatrix} \tag{5.24}$$

where $f_0^k(z)$ and $f_1^k(z, \bar{z})$ represent the single particle wave functions in LLL and LL1 respectively, and are defined as [40]

$$\begin{aligned} f_0^k(z) &= \vartheta \begin{bmatrix} \frac{k}{N_\phi^*} + \frac{\theta_2}{2\pi N_\phi^*} \\ \frac{\theta_1}{2\pi} \end{bmatrix} \left(\frac{N_\phi^* z}{L_2} \middle| N_\phi^* \tau \right) \\ f_1^k(z, \bar{z}) &= \sqrt{2}\ell^* \left[\frac{\bar{z} + z}{2(\ell^*)^2} - \partial_z \right] f_0^k(z) \end{aligned} \tag{5.25}$$

The operator $\hat{g}_1^q(z, \bar{z}) = f_1^q(z, \bar{z}) - \hat{f}_1^q(z, \bar{z})$ is analogous to the $\hat{G}$ operator defined in Eq.(3.13). The operator $\hat{f}_1^q(z, \bar{z})$ is defined as

$$\hat{f}_1^q(z, \bar{z}) = \sqrt{2}\ell^* \left[-2\nu \partial_z f_0^q(z) + (1 - 2\nu) f_0^q(z) \partial_z \right] \tag{5.26}$$

which implies that $\hat{g}_1^q(z, \bar{z})$ is given by

$$\hat{g}_1^q(z, \bar{z}) = \frac{\sqrt{2} N_\phi^* \ell^*}{N_\phi} \left[\frac{\bar{z} + z}{2\ell^2} f_0^q(z) - \partial_z f_0^q(z) - f_0^q(z) \partial_z \right]$$

such that $\hat{g}_1^q f_0^k = \mathcal{P}_{LL1}\left[f_1^q f_0^k \right]$.

Now we show that the state defined in Eq. (5.22) satisfies the periodic boundary conditions. We calculate the action of MTOs $t_i(L_1)$ and $t_i(L_2)$ on different parts of the ansatz. First, the action on the exponential factor is given by

$$t_i(L_2) e^{-\frac{\sum_i z_i^2 + |z_i|^2}{2\ell^2}} = e^{-\frac{\sum_i z_i^2 + |z_i|^2}{2\ell^2}} \tag{5.27}$$

$$t_i(L_1) e^{-\frac{\sum_i z_i^2 + |z_i|^2}{2\ell^2}} = e^{i\pi N_\phi \left(\tau - \frac{2z_i}{L_2} \right)} e^{-\frac{\sum_i z_i^2 + |z_i|^2}{2\ell^2}} \tag{5.28}$$

Their action on $F_1(Z_{\rm cm})$ is given by

$$t_i(L_2)F_1(Z_{\rm cm})t_i^\dagger(L_2) = e^{i\theta_2}F_1(Z_{\rm cm}) \tag{5.29}$$

$$t_i(L_1)F_1(Z_{\rm cm})t_i^\dagger(L_1) = e^{i\theta_1}e^{-i\pi\tau}e^{\frac{i2\pi Z_{\rm cm}}{L_2}}F_1(Z_{\rm cm}) \tag{5.30}$$

Since the Slater determinant $\hat{\mathcal{D}}_1^{\text{N}-\text{QPs}}\left(\{f_i^k,\hat{g}_j^q\}\right)$ contains operators, the action of MTOs is rather calculated on the combined piece *i.e.* $\hat{\mathcal{D}}_1^{\text{N}-\text{QPs}}\left(\{f_i^k,\hat{g}_j^q\}\right)\mathcal{J}^2$.

In the expansion of the Slater determinant, the ith particle can either be in LLL, in which case it will be represented by some state $f_0^{k_j}(z_i)$, or it can be in second LL, where it will be an operator $\hat{g}_1^{q_j}(z_i)$. The operators $\hat{g}_1^{q_j}(z_i)$'s commute with each other for different particles. Since, the single particle MTO, $t_i(a)$, only affects the ith particle, we only need to check the action on $f_0^{k_j}(z_i)\mathcal{J}^2$ and $\hat{g}_1^{q_j}(z_i)\mathcal{J}^2$, which are given by

$$t_i(L_2)f_0^{k_j}(z_i)\mathcal{J}^2 = e^{i\theta_2}f_0^{k_j}(z_i)\mathcal{J}^2 \tag{5.31}$$

$$t_i(L_2)\hat{g}_1^{q_j}(z_i)\mathcal{J}^2 = e^{i\theta_2}\hat{g}_1^{q_j}(z_i)\mathcal{J}^2 \tag{5.32}$$

Using Eqs. (5.27), (5.29), (5.31) and (5.32), we get

$$t_i(L_2)\Psi_{\frac{\nu^*}{2p\nu^*+1}} = e^{i3\theta_2}\Psi_{\frac{\nu^*}{2p\nu^*+1}} \tag{5.33}$$

Similarly, the action of $t_i(L_1)$ is given by

$$t_i(L_1)f_0^{k_j}(z_i)\mathcal{J}^2 = e^{i\theta_1}e^{i\pi(2-N_\phi)\tau}e^{\frac{i2\pi}{L_2}(N_\phi z_i-2Z_{\rm cm})}f_0^{k_j}(z_i)\mathcal{J}^2 \tag{5.34}$$

$$t_i(L_1)\hat{g}_1^{q_j}(z_i)\mathcal{J}^2 = e^{i\theta_1}e^{i\pi(2-N_\phi)\tau}e^{\frac{i2\pi}{L_2}(N_\phi z_i-2Z_{\rm cm})}\left[\hat{g}_1^{q_j}(z_i)-\frac{i4\pi A(N_e-1)}{L_2}f_0^{q_j}(z_i)\right]\mathcal{J}^2 \tag{5.35}$$

where $A=\sqrt{2}N_\phi^*\ell^*/N_\phi$. There are two terms which could cause the boundary conditions to not be satisfied: First, in the Eq. (5.35), we get an addition term $-i4\pi A(N_e-1)f_0^q(z_i)/L_2$ along with $\hat{g}_1^q(z_i)$ inside the square bracket. Secondly, if there are more that 1 QPs in the system, $\hat{g}_1^q(z_j)$'s for other QPs will act on the factor $e^{-\frac{i4\pi Z_{\rm cm}}{L_2}}$ and produce further terms. These are equivalent to replacing $\hat{g}_1^{q_j}(z_i)$ for the ith particle with $\hat{g}_1^{q_j}(z_i)+af_0^{q_j}(z_i)$ and $\hat{g}_1^{q_j}(z_k)$'s for $k\neq i$ with $\hat{g}_1^{q_j}(z_k)+bf_0^{q_j}(z_k)$ in the Slater determinant $\hat{\mathcal{D}}\left(\{f_i^k,\hat{g}_j^q\}\right)$, where a and b are constants for a given problem. Since all the LLL states $f_0^{q_j}$'s are filled, the terms of kind $af_0^{q_j}(z_i)$ and $bf_0^{q_j}(z_k)$ can be removed without affecting the determinant $\hat{\mathcal{D}}_1^{\text{N}-\text{QPs}}$. Putting everything together from Eqs. (5.28), (5.30), (5.34) and (5.35), we get

$$t_i(L_1)\Psi_{\frac{\nu^*}{2p\nu^*+1}} = e^{i3\theta_1}\Psi_{\frac{\nu^*}{2p\nu^*+1}} \tag{5.36}$$

which means that it satisfies the torus boundary conditions. Note that we have shown that the wave function in Eq. (5.22) is a valid torus state. The state is an eigenfunction of kinetic energy $H_{\rm KE}$, however we have not been able to check that the state is a zero energy eigenfunction of the model interaction on torus. Hence this is a conjecture supported by the validity of ansatz expression in the disk and more importantly in the spherical geometry.

5.3 Numerical Results

In Chapter 2, we explored the spectra of the model Hamiltonian in the spherical geometry and explicitly demonstrated the correspondence between spectrum of the model Hamiltonian and the IQH spectrum. In this chapter, we compute the same in torus and cylinder geometries.

First, we present and discuss the features low-energy spectra for the model interaction on the torus geometry. In the results shown below, we consider different Hall liquids are labeled by (N_ϕ, N_e) configurations. The eigenfunctions are labeled using K_2 and $\tilde{K}_1$ which are quantum numbers associated to MTOs $t_{\text{cm}}\,(\boldsymbol{L}_2/N_\phi)$ and $\tilde{t}_i(p\boldsymbol{L}_1)$ (Sec. 4.2). The following results are for a square torus where $|L_1| = |L_2|$ and $L_\Delta = 0$, which implies $\tau = \imath$.

5.3.1 Spectra on the torus geometry

The CF wave functions [39] describe FQHE systems at Jain sequence filling fraction $\nu = n/(2pn+1)$ by mapping the interacting system of N_e electrons, in flux N_ϕ (in the units of flux quanta $\phi_0 = 2\pi\hbar/e$), to a non-interacting system of CFs in a reduced flux given by $N_\phi^* = N_\phi - 2pN_e$. While in Chapter 2, we showed that in spherical geometry there is a one-to-one correspondence between IQH and model Hamiltonian spectra, in this section we will show that a similar map exists for torus geometry as well, but instead there is a one-to-$(2pn+1)$ mapping present in the IQH and FQH spectra for the torus geometry.

From the spectra shown presented in the subsequent section, we infer the following key results. For a system with $N_e = pN$ particles in $N_\phi = qN$ flux quanta, where $N = \gcd(N_\phi, N_e)$, the low-energy spectra of the model Hamiltonian, in a given $(\tilde{K}_1, K_2)$-sector, is identical to the $(\tilde{K}_1, K_2^I)$-sector spectra of a non-interacting system in a reduced flux N_ϕ^*, where K_2 and K_2^I are related by

$$K_2 = K_2^I + rN \qquad r = 0, 1, \ldots, q-1 \tag{5.37}$$

where $K_2 \in [0, N_\phi)$; $K_2^I \in [0, N_\phi^*)$ is the quantum number corresponding to $t_{\text{cm}}(\boldsymbol{L}_2/N_\phi^*)$ for the IQHE system. We show this equivalence between spectra in several cases below.

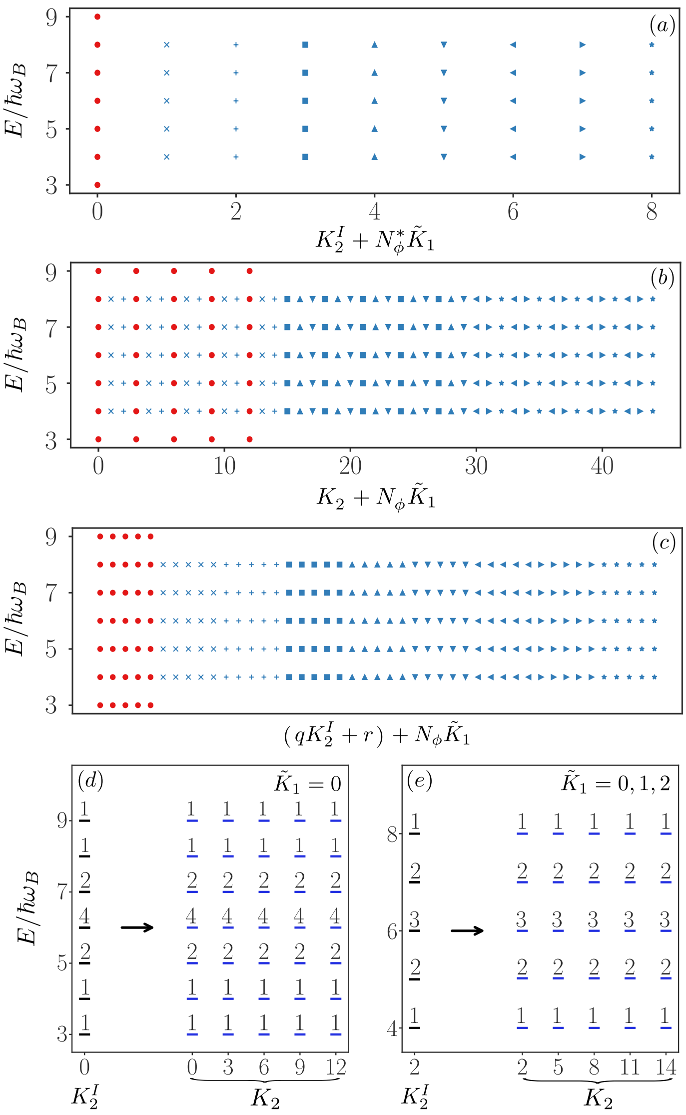

Figure 5.1: Panel (a) shows the spectrum for a non-interacting system (IQH) at integer filling factor $\nu^* = 2$, with $N_e = 6$ particles in flux $N_\phi^* = 3$. Pair of quantum numbers $(\tilde{K}_1, K_2^I)$ label each state along the x-axis. Spectrum in each $(\tilde{K}_1, K_2^I)$-sector is represented by a different marker. In addition, different colors are assigned for unique degeneracy patterns along the y-axis. Spectra with red and blue markers have degeneracy pattern of $(1, 1, 2, 4, 2, 1, 1)$ and $(1, 2, 3, 2, 1)$, respectively. The state with energy $E/\hbar\omega_B = 3$ represents the incompressible ground state at integer filling factor $\nu^* = 2$ whereas states with $E/\hbar\omega_B = 4$ contain a single neutral excitation. Panel (b) shows the spectra for ZIE eigenspace of the model interaction (FQH) for system with $N_e = 6$ particles in flux $N_\phi = 15$ at $\nu = p/q = 2/5$. The states are labeled with quantum numbers $(\tilde{K}_1, K_2)$ along the x-axis and are represented by the same markers used for the $(\tilde{K}_1, K_2^I)$-sector of IQH spectrum if K_2 and K_2^I satisfy Eq. (5.37). We see that, apart from the 5-fold topological degeneracy, the spectra is identical to the IQH spectra. Panel (c) shows the same spectra using a different arrangement of $(\tilde{K}_1, K_2)$ along the x-axis where the 1-to-5 correspondence with IQH spectra in panel (a) is more evident. Here definitions of r, q are same as in Eq. (5.37). Panels (d) and (e) show maps of IQH spectra (black) in two different $(\tilde{K}_1, K_2^I)$-sectors, representing 2 unique degeneracy patterns present in the full spectra. This is juxtaposed with the spectrum of the FQH system at corresponding $(\tilde{K}_1, K_2)$-sectors satisfying Eq. (5.37).

Incompressible state at $\nu = 2/5$: In Fig. 5.1, in panels (a) and (b), we show the spectra of non-interacting system at $\nu^* = 2$ with low-energy spectra of model interaction at $\nu = 2/5$, respectively. FQH and IQH systems have $N_e = 6$ particles in flux $N_\phi = 15$ and $N_\phi^* = 3$, respectively. Each marker represents an eigenfunction (or eigenfunctions, when degenerate) with its energy shown along y-axis. The sectors which these eigenfunction (or eigenfunctions) belong to are represented by a unique combination of quantum numbers $(\tilde{K}_1, K_2^I)$ and $(\tilde{K}_1, K_2)$, along the x-axis, for IQH and FQH system respectively. For clarity, eigenfunctions in $(\tilde{K}_1, K_2^I)$-sectors are color-coded according to their degeneracy pattern along the energy axis.

For instance, the spectra for sector $(\tilde{K}_1, K_2^I) = (0, 0)$ of IQH has a degeneracy pattern of $(1, 1, 2, 4, 2, 1, 1)$ at energies $E/\hbar\omega_B = (3, 4, 5, 6, 7, 8, 9)$. We have shown all sectors with this pattern in red color. The same degeneracy pattern is seen in the model Hamiltonian spectrum, in $(\tilde{K}_1 = 0, K_2)$-sectors where the K_2-values are given by $0, 3, 6, 9, 12$, as expected from Eq. (5.37). There can be more than one $(\tilde{K}_1, K_2^I)$-sectors with the same degeneracy pattern. Eq. (5.37) suggests that FQH states in each $(\tilde{K}_1, K_2)$-sector can be uniquely labeled by $(\tilde{K}_1, K_2^I, r)$. All FQH states labeled with same $(\tilde{K}_1, K_2^I)$ have the same spectrum and r takes values in $0, 1, \ldots, q-1$. In panel (c) of Fig. 5.1, the choice of x-axis ensures that sectors with same $\tilde{K}_1$ and K_2^I appear together, allowing us to clearly see the 1-to-5 correspondence. Fig. 5.1 (c,d) show the spectra at one $(\tilde{K}_1, K_2^I)$-sector of IQH together with the spectrum at sector $(\tilde{K}_1, K_2^I + rN)$ for $r = 0, 1, \ldots, q-1$. We note that these sectors have identical spectrum validating the relation in Eq. (5.37).

Incompressible state at $\nu = 1/3$: Fig. 5.2 shows the mapping between $(\tilde{K}_1, K_2^I)$-sectors in IQH spectra and $q = 3$ different $(\tilde{K}_1, K_2)$-sectors in the FQH for 1/3 state. There are four panels, one for each $(\tilde{K}_1, K_2^I)$-sector of IQH spectra representing a unique degeneracy-pattern present in the full IQH spectra (Fig. 5.4). All of these map to $q = 3$ different K_2-sectors in FQH, which follow Eq. 5.37. Results for $\nu = 3/7$ are given in Fig. 5.3.

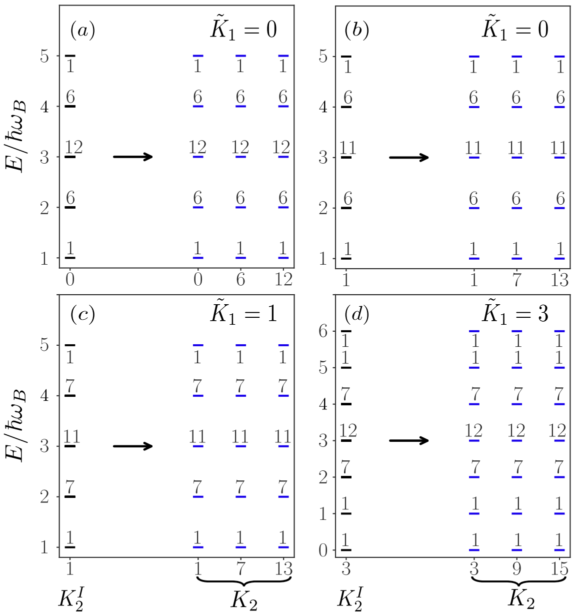

Figure 5.2: Plot showing the IQH-to-FQH mapping in low-energy spectra for IQH system (black) with $(N_\phi^*, N_e) = (6, 6)$, at filling fraction $\nu^* = 1$, to the corresponding FQH spectra (orange) with $(N_\phi, N_e) = (18, 6)$ at $\nu = 1/3$. The full IQH spectra consists of four different degeneracy patterns, and each panel shows their mapping to the corresponding K_2-sectors for FQH system: (a) in $\tilde{K}_1 = 0$ sector, IQH spectra for $K_2^I = 0$ sector maps to those with $K_2 = 0, 6, 12$ sectors in FQH system. Panels (b) and (c) show similar maps for other unique spectra in given sectors. Panel (d) shows map of spectra which contains zero-energy state corresponding to the incompressible ground state of $\nu = 1/3$. Full spectrum is shown in Fig. 5.4.

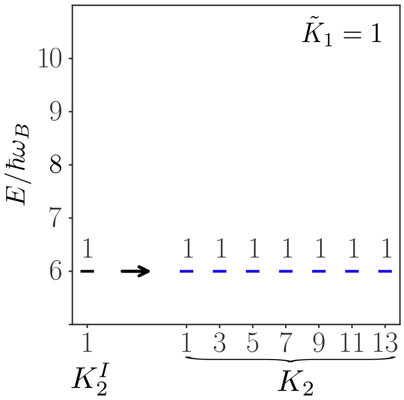

Figure 5.3: Map for low-energy spectra of non-interacting system (black) for $(N_\phi^*, N_e) = (2, 6)$, at $\nu^* = 3$ to the corresponding spectra of interacting (blue) system for $(N_\phi, N_e) = (14, 6)$ at $\nu = 3/7$. The map clearly shows a 7-fold degeneracy. Since our calculations are restricted to lowest 3 LLs, only 3/7 ground states are present in the spectra.

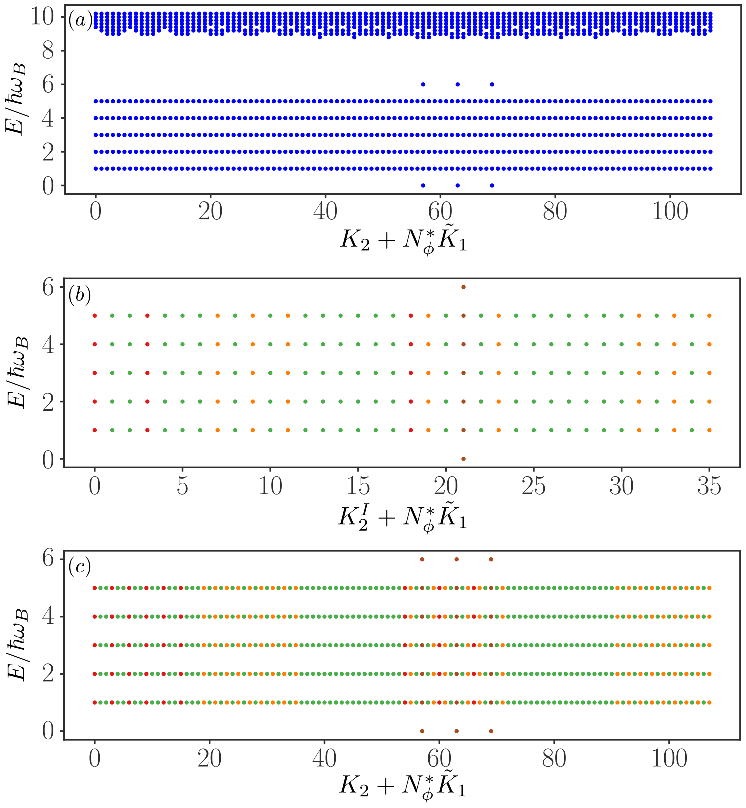

Figure 5.4: In panel (a), we show the spectrum of model interaction for system on the torus with the configuration $(N_\phi, N_e) = (18, 6)$ corresponding to filling fraction $\nu = 1/3$, where the states are labeled by a pair of quantum numbers $(\tilde{K}_1, K_2)$ along the x-axis and the y-axis represents their energy which is rescaled such that $\hbar\omega_B \to 1$. In this panel, we see that the spectrum of the interacting system (FQH) has a clear gap, which separates the spectrum of the ZIE eigenspace of the interaction, from the finite interaction energy states. The states with finite interaction energy are higher in the spectra, and only a few of them are visible in the given energy range. These states do not map to the spectra of non-interacting (IQH) system and hence are not of our interest. In panel (b), we show the spectrum of IQH system at $\nu^* = 1$ for configuration $(N^*_\phi, N_e) = (6, 6)$. The states in a given $(\tilde{K}_1, K^I_2)$-sector of the IQH spectra are color coded for each unique degeneracy pattern. For instance, the eigenfunctions in red have a degeneracy of $(1, 6, 12, 6, 1)$ from low to high energy bands. For system with $N_e/N_\phi = p/q$ where p, q are coprime, each $(\tilde{K}_1, K^I_2)$-sector of IQH system is mapped to q different sectors of FQH, such that $(\tilde{K}_1, K_2) = (\tilde{K}_1, K^I_2 + r \times \text{gcd}(N_e, N_\phi))$ where $r = 0, 1, \ldots, q - 1$. This 3-fold multiplicity in FQH spectrum relative to the IQH spectra is demonstrated in the panel (c).

For charged excitations of $\nu = 1/3,\ 2/5$: The 1-to-q mapping between corresponding sectors in the IQH and FQH spectra also holds for quasi particles (QPs) and quasi-holes (QHs) of filling fractions $\nu = 1/3$ and $2/5$. The spectra are given in Fig. 5.5.

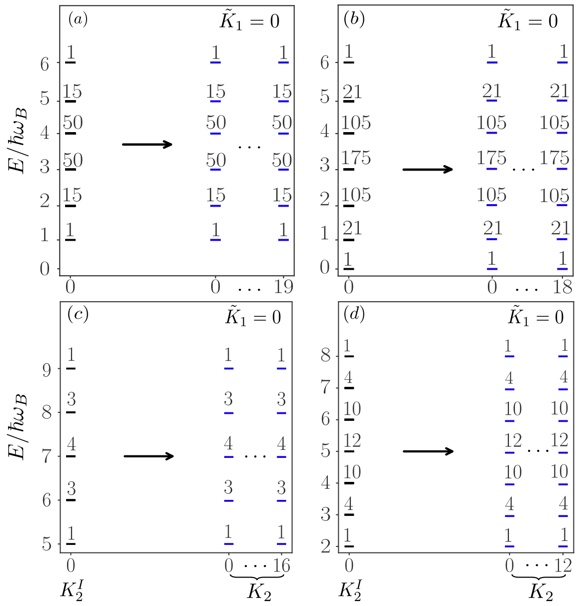

Figure 5.5: Plot shows the maps between IQH specta and FQH spectra for single charged excitations (QP/QH) at fillings $\nu = 1/3$ and $2/5$. Since $\gcd(N_\phi, N_e) = 1$ for all these cases, FQH spectra shows $q = N_\phi$ fold degeneracy. (a) Spectrum for a system hosting a single QP of IQH at $\nu^* = 1$ for $N_e = 7$ and flux $N_\phi^* = 6$ maps to the corresponding FQH spectra at $\nu = 1/3$ with flux $N_\phi = 20$. The dots ($\dots$) along the x-axis indicate that the FQH system has identical spectra for all intermediate K_2 values. Panel b) shows the similar map in system hosting a single QH instead of a QP where IQH spectra for $N_e = 6$ and flux $N_\phi^* = 7$, at $\nu^* = 1$, maps to the corresponding FQH spectra at $\nu = 1/3$ with $N_\phi = 19$. Panels (c) and (d) show similar mapping for a single QP and QH between FQH at $\nu = 2/5$ with configurations $(N_\phi = 17, N_e = 7)$ and $(N_\phi = 13, N_e = 5)$ to the corresponding IQH spectra for configurations $(N_\phi^* = 3, N_e = 7)$ and $(N_\phi^* = 3, N_e = 5)$, respectively.

Panels (a) and (b), show the IQH-FQH map for the spectra of a single QP and QH at FQH filling $\nu = 1/3$, respectively. Similarly, panels (c) and (d), give the maps for a single QP and QH at FQH filling $\nu = 2/5$, respectively. Since $\gcd(N_\phi, N_e) = 1$ in all of these cases, there is only one degeneracy pattern in the IQH spectra, hence only one map for any representative $(\tilde{K}_1, K_2^I)$-sector of the IQH spectra is sufficient. As the panel shows, in all four cases, each IQH K_2^I-sector maps to N_ϕ K_2-sectors of FQH. Since $\gcd(N_\phi^*, N_e) = 1$ in all of these cases, all $(\tilde{K}_1, K_2^I)$-sectors in IQH spectra have identical degeneracy pattern [67].

5.3.2 Spectra on cylinder geometry

In cylinder geometry, the single particle state is labeled by linear momentum k due to translation invariance along circumference of size L. Unlike torus, the cylinder does not have any non-trivial many-body translation symmetries, hence the spectra of model interaction is only indexed by $K_{\text{total}} = \sum_i k_i$ where $k_i \in [0, N_\phi)$ and N_ϕ is the maximum number of orbitals in each LL. The minimum and maximum values of k_i are $k_{\text{min}} = 0$ and $k_{\text{max}} = N_\phi - 1$.

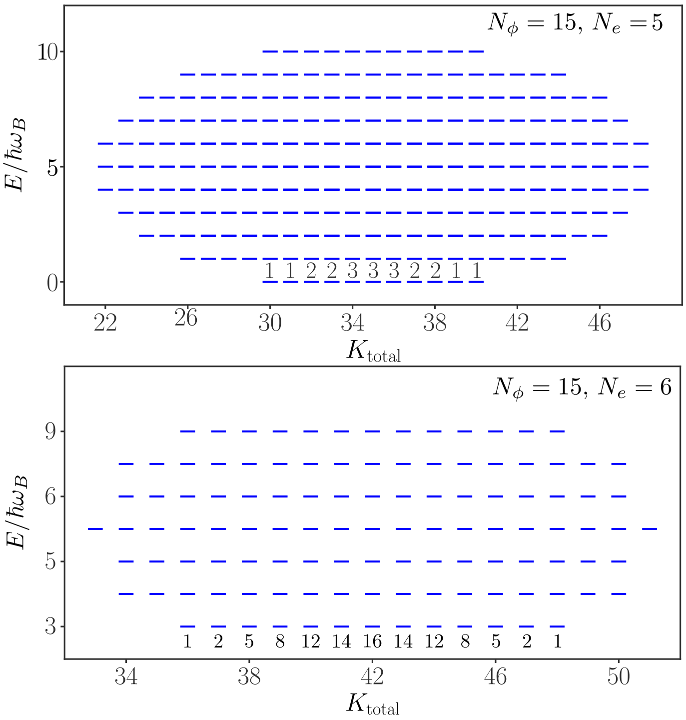

Figure 5.6: Spectra for the model Hamiltonian in cylinder geometry, for FQH systems at filling $\nu = 1/3$ (panel (a)) and 2/5 (panel (b)). The x-axis labels the K_{total} quantum number, and energy $E/\hbar\omega_B$ is along the y-axis. Lowest 3 LLs are used in these calculations. Panel (a) shows the spectrum for system with $N_\phi = 15$ and $N_e = 5$. The numbers above states with $E/\hbar\omega_B = 0$ represent their degeneracy. The state at $K_{\text{total}} = 30$ corresponds to the incompressible ground state at filling $\nu = 1/3$ and other states are its QH/edge and center-of-mass excitations. States at higher energy correspond to neutral excitations of 1/3. Similarly, panel (b) shows the spectrum for system with $N_\phi = 15$ and $N_e = 6$. Here the state at $K_{\text{total}} = 36$ with $E/\hbar\omega_B = 3$ is the ground state for $\nu = 2/5$.

In the top panel of Fig. 5.6, we show the spectrum for system with $N_e = 5$ in flux $N_\phi = 15$, at filling fraction $\nu = 1/3$. The eigenfunction with zero energy at $K_{\text{total}} = 30$ corresponds to the incompressible ground state of 1/3. At the same energy, the eigenfunctions at higher K_{total} are the quasi-hole/edge excitations as well as center-of-mass excitations where the numbers represent the degeneracy at a given K_{total}-value. The counting at small momenta match that of the edge excitation of $\nu = 1/3$. At large momenta the counting deviates due to finite system size. The states in the higher energy bands are the neutral excitations of $\nu = 1/3$. Similarly, the lower panel shows the spectra of state at $\nu = 2/5$ filling, with $N_e = 6$ at flux $N_\phi = 15$. Here the incompressible ground state with energy $E/\hbar\omega_B = 3$ is at $K_{\text{total}} = 36$. Again, the same energy band shows QH/edge and center-of mass excitations at larger K_{total} values, and the higher energy band hosts neutral excitations of the 2/5 FQH state.

5.4 Conclusion

In this chapter, we extend the ideas presented in Chapter 2 and 3 to torus and cylinder geometries. The model Hamiltonian (Sec. 2.1) introduced in there was written in the disk geometry and studied in the disk and spherical geometries. The Hamiltonian has some appealing features - a single Hamiltonian produces incompressible states at all Jain filling fractions of the form $n/(2pn + 1)$ and allows exact eigenfunctions for the incompressible states, quasihole states, quasiparticle and neutral excitations. The spectrum of the system at filling fraction $n/(2pn+1)$ has a one-to-one correspondence with the IQH states at filling fraction n. Only the low relative angular momentum sectors appeared in the Hamiltonian, so we expected that the interaction must be short ranged and that the qualitative results obtained in the disk/spherical geometry should extend to other geometries as well. The interaction presented is not diagonal in position representation and therefore usual approaches to mapping the Hamiltonian from disk geometry to torus/cylinder geometry do not work. Nevertheless, we could construct a Hamiltonian that is motivated by the disk Hamiltonian and has qualitatively the same structure.

The Hamiltonian can be interpreted as that of a multilayer model where different layers have different chemical potentials but each layer is treated as a different LL of same particles. The eigenfunctions of the Hamiltonian when written in the momentum Fock space is then similar to that of a multilayer model. The real space wave functions for multi-Landau level eigenfunctions can be written in a compact form on the disk geometry.

We showed that the structure of this wave function generalizes in a natural way to the cylinder geometry but not to the torus or spherical geometry. On the torus geometry, we showed that the generalization fails to have the right boundary condition. However we could construct the low energy QP excitations of the Laughlin $1/(2p + 1)$ state in the spherical geometry (Eq. (3.16)); by generalizing a simplified form (Eq. (3.12)) of the general eigenfunction on the disk. On the disk, cylinder and spherical geometry we could verify the eigenfunction by comparing with the numerical (ED) results. This wave function when generalized to the torus geometry produces a wave function (Eq. (5.22)) with the correct boundary conditions and expected total kinetic energy. We conjecture that this is also an eigenfunction of the full interacting Hamiltonian. Explicit verification of the result is challenging due to difficulty in explicit evaluation of the wave function.

The model interaction captures some key features of the FQH phases and excitations at the Jain sequence filling fractions and produces exact eigenfunctions with wave functions closely similar in structure to the CF excitations. We could ask if a similar model interaction can be written which describes more complex FQH liquids. Interestingly the ideas can be generalized, as shown in Ref [74], to the case of the Moore Read states and allows construction of exact low energy eigenfunctions analogous to the structure of the bipartite composite fermion excitations [75, 76, 77]. Degeneracy on the torus geometry of the Moore Read states have a non-Abelian component in addition to what is expected from the q fold degeneracy due to the center of mass translations. It is interesting ask how this degeneracy will be manifested in a torus geometry generalization of the results in Ref. [74].

Part II

Numerical Study of Entanglement spectra of FQH systems

Chapter 6

Entanglement Spectra of Partons

The entanglement spectrum (ES) serves as a useful probe of the topological properties of FQH states [63]. It has been argued that the ES has a one-to-one correspondence with the low-energy edge spectrum providing a natural way to understand the edge theory [63, 78, 79]. Exact analytical calculation of ES can be done for Slater determinant states including the IQH states [80]. Direct numerical calculation of ES of correlated FQH states requires a numerical calculation of the reduced density matrix. The dimension of this matrix grows exponentially with subsystem size, making it infeasible to evaluate the spectra for large systems.

However, for trial wave functions that can be written as a product of Slater determinants (or LLL-projections of that product), the ES across a rotationally symmetric real-space cut can be evaluated in a computationally efficient manner [65, 81]. Such wave functions include the Jain CF wave functions as well the more general set of parton states. In the parton theory, which is a generalization of composite fermion theory of FQHE, the electron is envisaged as being made of k partons, each of which goes into an IQH ground state at filling fraction n_β [41], where β labels the parton species. The LLL-projected k-parton state, labeled by a sequence of integers $(n_1, n_2, \cdots, n_k)$, has the general formgeos

$$\Psi_\nu^{n_1 n_2 \cdots n_k} = \mathcal{P}_{\text{LLL}} \prod_{\beta=1}^{k} \phi_{n_\beta}(\{z_i\}), \tag{6.1}$$

where $z_q = x_q + iy_q$ is the complex representation of the two-dimensional coordinate of the q^{th} electron, ϕ_n is the Slater determinant wave function of N particles that completely fill the lowest n LLs and $\mathcal{P}_{\text{LLL}}$ projects the state into the LLL, as is appropriate in the large magnetic field limit, i.e., $B \to \infty$. For negative n_β, the state is taken to be $\phi^*_{|n_\beta|}$. Since each of the partons have the same density as the parent electrons and all the partons are exposed to the external magnetic field, the β^{th} parton is associated with a charge of $(-e)\nu/n_\beta$, where $-e$ is the charge of the electron. The constraint that the charges of the partons should add up to that of electron relates the electronic filling ν to the parton filling as $\nu = \left[\sum_\beta n_\beta^{-1}\right]^{-1}$.

The Laughlin wave function [38] $\psi^{\text{Laughlin}}_{1/(2p+1)} \equiv \phi_1^{2p+1}$ at filling $\nu = 1/(2p+1)$ can be viewed as a parton wave function where $2p+1$ partons, each form a $n_\beta = 1$ IQH state. The Jain CF wave functions $\psi^{\text{Jain}}_{n_1/(2pn_1\pm1)} \equiv \mathcal{P}_{\text{LLL}}\phi_1^{2p}\phi_{\pm n_1}$ at filling $\nu = n_1/(2pn_1 \pm 1)$ for positive integers n_1, p are states with $2p+1$ partons, where $2p$ of them are at filling $n_\beta = 1$ and one of them is at filling $\pm n_1$. The edge theory of such a state is described by n_1 bosons [82]. The low energy edge modes, as well as the entanglement spectrum [63], show that the state counting can be interpreted as generated by n_1 bosonic fields. More generally, edge theory of parton states of the form $(n_1, n_2, \ldots, n_k)$ which are Abelian, i.e., where none of the n_β's that are greater than one repeat, are described by $c = \sum_\beta n_\beta - (k-1)$ bosons. This can be seen by noting that each IQH state n_β is made of n_β bosonic edge modes, yielding in total $\sum_\beta n_\beta$ bosonic edge modes. However, the density fluctuations of the k-partons should be identified which results in a set of $k-1$ constraints. It manifests in a reduction of the number of bosonic degrees of freedom at the edge by $k-1$, leading to above-mentioned value of chiral central charge c. This procedure of gluing the unphysical partons back into the physical electrons is already implemented in the wave function of Eq. (6.1) by identifying the coordinates of the different species of partons with the electronic coordinate, i.e., setting $z_q^\beta = z_q \ \forall\beta$ (each parton IQH wave function is made up of *all* the electrons).

This motivates us to consider the edge structure for the simplest non-Abelian parton states which contain repeating n_β's with $n_\beta \geq 2$. The edge spectrum of a quantum Hall system generically depends on the confinement potential and the details of the electronic interactions. A simple approach to access the universal properties of the edge is to look at the entanglement spectrum of the bulk state [63]. In this chapter, we consider the entanglement spectra of states $(22) \equiv \phi_2^2$, $(222) \equiv \phi_2^3$, and $(33) \equiv \phi_3^2$ which represents states at filling fractions $\nu = 1$, $2/3$, and $3/2$ respectively. States ϕ_2^2 and ϕ_3^2 are bosonic whereas ϕ_2^3 represents a fermionic parton state. Unlike the states with non-repeating n_β's where the edge theories are made of multiple bosons, the edge theories of ϕ_n^k are described by, edge currents that satisfy an $\widehat{su}(n)_k$ Kac-Moody algebra, and a $u(1)$ boson [83] yielding a central charge of $k(n^2-1)/(k+n)+1$ (Eq 15.61 of Ref. [84]). Up to a $u(1)$ boson, the edge theory of these states is identical to that of the k-cluster Read-Rezayi states [42]. The momentum-space entanglement spectrum of the Read-Rezayi states has been previously studied in Ref. [85]. We mention here that a formalism has recently been developed to rigorously study certain unprojected parton states such as ϕ_2^2 and ϕ_2^3 [54, 86].

The real-space entanglement spectra (RSES) of the parton wave functions have been efficiently evaluated for the case of Jain CF states, thanks to an idea originally introduced in Ref. [65]. The algorithm in general applies to wave functions that can be written as the product of Slater determinants or their LLL-projections, and thus can also be used to evaluate the RSES of certain parton states. In this chapter, we employ the algorithm to unprojected and projected partons states, as well as a few of their bulk excited states and explicitly demonstrate a one-to-one correspondence of the RSES with representations of their edge current algebra.

The chapter is organized as follows. Numerical details of the RSES computation are explained at length in Sec. 6.1. There we provide details of the RSES computation algorithm for parton states and discuss the prescription used for LLL-projection. In that section, we also present the calculation of edge current algebra of ϕ_n^k parton states using representations of $\widehat{su}(n)_k$ Kac-Moody algebra. All the results of the chapter are presented in Sec. 6.2. First, RSES for three parton states which are unprojected ϕ_2^2, ϕ_2^3 and ϕ_3^2 are presented. We also present the RSES for parton states ϕ_2^2 and ϕ_2^3 when they have a quasihole excitation. RSES of LLL-projected $[\phi_1^2\phi_2]^2$ is also provided. Edge spectra for unprojected ϕ_2^2, ϕ_2^3, and ϕ_3^2 are presented which is computed by exact diagonalization of the overlap matrix sectors where LL occupation number is restricted. Finally, we conclude the chapter with a summary of our findings in Sec. 6.3.

6.1 Numerical details

6.1.1 RSES for parton states

The key computational simplification in the computation of RSES arises from the specific structure of the parton wave functions (Eq. (6.1)), which allows us to identify a small set of states whose span contains all the eigenstates of the reduced density matrix with non-zero eigenvalues. The dimension of this subspace does not scale with the subsystem size. The task then reduces to evaluating the matrix elements of the reduced density matrix between these special sets of states. The simple structure of these basis states allows us to explicitly evaluate these matrix elements using Monte Carlo methods. The method makes it possible to efficiently obtain the ES in a few dominant angular momentum sectors in large systems with hundreds of particles. In comparison, exact diagonalization can compute the momentum-space ES for about 20 particles [87]. Infinite DMRG methods can produce the momentum-space ES for a nominally infinite system if the parent Hamiltonian is known. The latter is not true for the general parton states or the general Jain CF states [88].

The method presented here was introduced in Ref. [89] and has been previously employed to obtain scaling properties of the entanglement Hamiltonian for the Jain CF states [81]. Here we provide details of the method and point out the changes needed when specializing to the case of parton states.

6.1.2 Construction of entanglement wave functions

We will work in a disk geometry with a rotationally symmetric cut, shown schematically in Fig. 6.1. Since the full state has a fixed total number of particles N, the reduced density matrix is block diagonal in (N_A, N_B) sectors, where N_A and $N_B = N - N_A$ are the particles in the subsystem A and B on the two sides of the real-space cut. We will work in one of these blocks where $N_{A/B}$ are close to the expected number of particles in that subsystem ($\nu/2\pi$ times the area in units of the magnetic length $\ell = \sqrt{\hbar c/(eB)}$). We assume $\ell = 1$

in our calculations. Due to rotational symmetry, the eigenstates of the reduced density matrix can be labeled by the angular momentum eigenvalues. The entanglement spectrum is obtained as the negative logarithm of the eigenvalues of the angular momentum blocks of the reduced density matrix plotted as a function of the angular momenta.

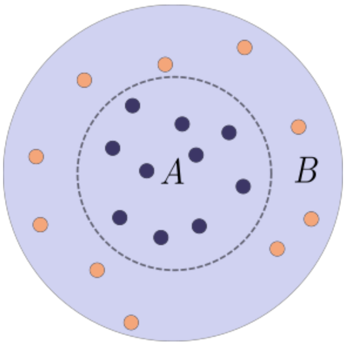

Figure 6.1: A rotationally symmetric real-space cut on disk geometry dividing the full system into A and B subsystems.

Now we proceed to give details of the method. Any Slater determinant wave function of N particles occupying angular momentum orbitals $(k_1, k_2, k_3 \ldots, k_N)$ can be expanded as an antisymmetrization of the product of smaller Slater determinants of N_A and N_B particles as follows:

$$S_{k_1 \ldots k_N}(Z) = \sum_{\sigma \in P} \epsilon(\sigma)\, S_{k_{\sigma(1)} \ldots k_{\sigma(N_A)}}(Z_A)\, S_{k_{\sigma(N_A+1)} \ldots k_{\sigma(N)}}(Z_B) \tag{6.2}$$

where $Z_A \equiv (z_1, \ldots, z_{N_A})$ and $Z_B \equiv (z_{N_A+1}, \ldots, z_N)$; P is the set of $(N!/N_A!N_B!)$ permutations of the ordered set $(1, \ldots, N)$ such that first N_A and the last N_B entries of the $P(1, \ldots, N)$ are in an increasing order, and $\epsilon(\sigma)$ is the sign for a permutation represented by σ.

Each orbital k_i refers to a pair of quantum numbers (n_i, m_i) namely the LL-index n and angular momentum quantum-number m. In the disk geometry, these orbitals have the form (up to normalization):

$$\eta_{n,m}(z) = z^m L_n^m \left(\frac{|z|^2}{2} \right) \mathrm{e}^{-\frac{|z|^2}{4}} \tag{6.3}$$

where $L_n^m(z)$ is the associated Laguerre polynomial. To keep track of the signs of permutations, we will associate some order within the set of orbitals.

The product of two Slater determinants S_M and S_R where $M = (m_1, m_2, \ldots, m_N)$ and $R = (r_1, r_2, \ldots, r_N)$ can be written as (using Eq. (6.2))

$$\psi = \sum_{\lambda} \epsilon(\lambda) \xi_\lambda^A(Z_A) \xi_\lambda^B(Z_B). \tag{6.4}$$

Here λ goes over all $(N!/N_A!N_B!)^2$ possible ways to split the ordered set M into two disjoint ordered sets M_A and M_B and the ordered set R into two disjoint ordered sets R_A and R_B. Here M_A and R_A have sizes N_A and M_B and R_B have sizes N_B. The sign $\epsilon(\lambda)$ is the sign of the permutation that takes the set (M, R) into (M_A, M_B, R_A, R_B). The entanglement wave functions (EWFs), ξ, are defined as

$$\begin{aligned} \xi^A_\lambda &= S_{M_A}(Z_A)S_{R_A}(Z_A), \\ \xi^B_\lambda &= S_{M_B}(Z_B)S_{R_B}(Z_B). \end{aligned} \tag{6.5}$$

The generalization to the case where the product consists of more than two Slater determinants is straightforward. The product $S_{M^1}S_{M^2}\ldots S_{M^q}$ can be written in the form of Eq. (6.4) where the EWFs are given by

$$\xi^A_\lambda = \prod_{i=1}^{q} S_{M^i_A}(Z_A), \quad \xi^B_\lambda = \prod_{i=1}^{q} S_{M^i_B}(Z_B) \tag{6.6}$$

Here λ corresponds to one of the $(N!/N_A!N_B!)^q$ ways to split every M^i into disjoint ordered subsets M^i_A and M^i_B of sizes N_A and N_B.

If a wave function ψ contains more than one copy of the same Slater determinant (for instance, the unprojected Jain CF states $\phi_1^{2p}\phi_n$), then different splittings λ can result in the same EWFs. To clarify this, consider a 10-particle state ϕ_1^2 which contains the two copies of the Slater determinant $\phi_1 = S_{(0,1,2,3\ldots,9)}$ (all orbitals are in the LLL so the LL indices have been suppressed). Here $M^1 = M^2 = (0, 1, 2\ldots, 9)$. Two distinct splittings, given by

$$\begin{aligned} M^1_A &= (0, 1, 2, 3, 5),\ M^1_B = (4, 6, 7, 8, 9) \\ M^2_A &= (0, 1, 2, 4, 5),\ M^2_B = (3, 6, 7, 8, 9) \end{aligned}$$

and

$$\begin{aligned} M^1_A &= (0, 1, 2, 4, 5),\ M^1_B = (3, 6, 7, 8, 9) \\ M^2_A &= (0, 1, 2, 3, 5),\ M^2_B = (4, 6, 7, 8, 9) \end{aligned}$$

result in the same EWFs ξ^A_λ and ξ^B_λ. This allows simplification of Eq. (6.4) to

$$\psi = \sum_i s_i\, \xi^A_i(Z_A)\xi^B_i(Z_B) \tag{6.7}$$

where i indexes the distinct EWFs and s_i is the sum of $\epsilon(\lambda)$ for all splittings λ that result in the same EWFs ξ^A_i, ξ^B_i.

6.1.3 Diagonalizing L^A_z-blocks of ρ_A

The RSES can be calculated by diagonalizing the reduced density matrix obtained as $\rho_A = \sum_{j,k} s_j s_k \left|\xi^A_j\right\rangle \langle \xi^B_k|\xi^B_j\rangle \left\langle \xi^A_k\right|$. Exhaustive enumeration of all splittings λ of the resulting

EWFs is computationally infeasible. However, we are typically interested only in the specific small angular momentum sectors. To calculate a block of reduced density matrix ρ_A in a fixed L_z^A-sector, we only need to consider a restricted sum of only those EWFs which have the desired angular momentum. This is given by

$$\rho_A^{L_z^A} = \sum_{j,k}{}^{\prime} s_j s_k \left|\xi_j^A\right\rangle \left\langle\xi_k^B|\xi_j^B\right\rangle \left\langle\xi_k^A\right| \tag{6.8}$$

where $L_z^A = \sum_i M_A^{i,\text{tot}}$, and $M_A^{i,\text{tot}}$ is total momenta of A subsystem for the i^{th} splitting. For clarity, consider the case of the ϕ_1^2 wave function. In a given (N_A, N_B)-sector of ρ_A, there are no EWFs with L_z^A less than $L_{z,\text{min}}^A = N_A(N_A-1)$ but for angular momenta $0, 1, 2$ and 3 above $L_{z,\text{min}}^A$, the numbers of distinct EWFs are $1, 2, 5$ and 10 respectively.

It can be shown that the non-zero eigenvalues of $\rho_A^{L_z^A}$ are the same as those of the following finite-dimensional matrix:

$$M_{jk} = \sum_i{}^{\prime} s_j s_i \langle\xi_i^A|\xi_j^A\rangle\langle\xi_i^B|\xi_k^B\rangle \tag{6.9}$$

If the set of the EWFs are overcomplete, then M has excess zero eigenvalues compared to $\rho_A^{L_z^A}$. The excess zero eigenvalues do not affect the entanglement spectra.

The matrix elements of M can be evaluated in terms of the overlaps between the EWFs:

$$\begin{aligned}\langle\xi_i^A|\xi_j^A\rangle &= \int_A \bar{\xi}_i^A(Z_A)\xi_j^A(Z_A)dZ_A \\ \langle\xi_i^B|\xi_j^B\rangle &= \int_B \bar{\xi}_i^B(Z_B)\xi_j^B(Z_B)dZ_B\end{aligned} \tag{6.10}$$

Standard Metropolis Monte Carlo methods can be used to estimate these overlaps up to a proportionality constant. For given N_A, we choose one of the EWFs with smallest L_z^A value, ξ_0^A, as the sampling wave function to estimate the overlap ratio $\langle\xi_\lambda^A|\xi_\mu^A\rangle/\langle\xi_0^A|\xi_0^A\rangle$. For computing $\langle\xi_\lambda^B|\xi_\mu^B\rangle/\langle\xi_0^B|\xi_0^B\rangle$, we use ξ_0^B, which is complementary EWF to ξ_0^A. Since we use the same sampling wave function for all the L_A sector, we get the overlap matrix M upto a multiplicative factor of $|\xi_0^A\xi_0^A|^{-2}$. This also implies that the entire entanglement spectrum can be obtained up to an overall vertical shift.

Lastly, we would like to point out that the above algorithm and its justification also generalize if the product of determinants is replaced by an LLL-projection of the same product wave function. The EWFs should, in this case, be replaced with the corresponding LLL-projected counterparts.

6.1.4 Approximation in LLL-projection

The algorithm described in Sec. 6.1.3 is exact up to statistical uncertainty from the Monte Carlo estimations of the matrix elements. The main set of results presented in this chapter is for the unprojected parton states. For these states, the algorithm provides a faithful estimator for the entanglement spectra. However, approximations are needed when calculating the spectra for the projected parton states. In this section, we describe the approximate projection which we used to obtain the LLL EWFs.

In this chapter we consider the ES of the projected wave function of the following form

$$\psi_{1/5}^{2^2 1^4} = \mathcal{P}_{\text{LLL}}\ [\phi_1^2\phi_2]^2 \sim \left(\mathcal{P}_{\text{LLL}}\ [\phi_1^2\phi_2]\right)^2 \equiv [\psi_{2/5}^{\text{Jain}}]^2. \tag{6.11}$$

The wave functions on either side of the $\sim$ sign in Eq. (6.11) differ in the details of how the LLL-projection is implemented. We expect such details to not affect the universality class of the phase described by the wave functions [90, 91]. Only the form given on the rightmost side of Eq. (6.11) is amenable to a numerical evaluation for large system sizes and thus this is the form that will be used in this chapter.

Projecting state to LLL in the disk geometry is equivalent to replacing any $\bar{z}$ by $2\partial_z$ in the Slater determinant after taking all the terms with z to the right hand side of the $\bar{z}$ (the derivatives do not act on the Gaussian part of the wave function) [92], i.e.,

$$\psi_{1/5}^{2^2 1^4} = \left[\phi_2\left(\{z, \bar{z} \to 2\partial_z\}\right)\phi_1^2\right]^2. \tag{6.12}$$

Same replacements need to be applied in the EWFs to obtain their LLL-projections. Getting the exact analytical form of the LLL-projected state is not feasible beyond the case of ~ 10 particles. To make progress, we consider an approximate projection scheme where we replace $\bar{z}_i$ by the following.

$$\bar{z}_i \to \sum_{j \neq i}^{N} \frac{2}{z_i - z_j} \tag{6.13}$$

For the Jain composite wave functions, this is a highly reliable way to perform the LLL-projections [4]. This has also been used in the case of parton wave functions previously [93, 94]. We employ the same approximation to the case of the EWFs here. This produces wave function in the LLL with correlations similar to that of the unprojected wave functions. Thus, in general, we have our approximate projected parton state as

$$\psi_{n/[m(n+1)]}^{n^m 1^m} = \left[\phi_1 \times \phi_n\left(\left\{z, \bar{z}_i \to \sum_{j \neq i}^{N} \frac{2}{z_i - z_j}\right\}\right)\right]^m \tag{6.14}$$

which is used for RSES calculation.

6.1.5 Edge counting from edge current algebra representations

The parton states considered in this chapter namely $[\phi_1^a \phi_n]^k$ have edge mode currents carrying a representation of the $\widehat{su}(n)_k \times u(1)$ algebra. Algorithms discussed in the previous sections calculate the entanglement spectra reflecting the edge spectra of the states. To compare the entanglement spectra with the counting expected from the current algebra, in this section, we summarize the construction of the representations of the $\widehat{su}(n)_k$ algebra, which has the form

$$[J_l^a, J_m^b] = \imath \sum_c f^{abc} J_{l+m}^c + kl\delta_{l+m,0}\delta_{a,b}. \tag{6.15}$$

Here the indices $l, m \in \mathbb{Z}$, $1 \leq a, b \leq \dim(su(n))$ and f^{abc} are the structure factors for the $su(n)$ Lie algebra. We provide a simplified picture of the construction, presented in parallel with ideas from the more familiar case of the highest weight representations of the $su(2)$ algebra. Further details on these ideas can be found in Chapters 13 and 14 of Ref. [84].

As in the case of $su(2)$, the highest weight representations are labeled by the quantum numbers of the highest weight state, and the remaining basis states in the representation can be obtained by repeated action of ladder operators. The dominant highest weight representations of $\widehat{su}(n)_k$ are labeled by the Dynkin labels $\vec{\mu} = [\mu^{(0)}, \mu^{(1)}, \ldots, \mu^{(r)}]$ of the highest weight state $|\text{hw}\rangle$. Here r is the dimension of the maximal commuting sub-algebra of $\widehat{su}(n)_k$, and $\mu^{(i)}$'s are non-negative integers that add up to k. Thus the highest weight representations of $\widehat{su}(2)_2$ (for which $r = 1$) are labeled by Dynkin labels $[1, 1]$, $[2, 0]$ and $[0, 2]$.

Having discussed the highest weight states, we now discuss the ladder operators. The ladder operators arise from identifying linear combinations of $\{J_n^a\}$ that form $su(2)$ sub-algebras of $\widehat{su}(n)_k$. There are $r + 1$ independent ladder operators $\{E_0, E_1 \ldots E_r\}$ that can be constructed (See Sec 13.1.3 and 14.1.4 of Ref. [84]). An infinite tower of basis states is generated by the ladder operators acting on the highest weight state. The action of a ladder operator on a basis state reduces the Dynkin label of the state by a fixed integral vector; each ladder operator E_i is labeled by this integral vector $\vec{\alpha}_i$. These integral directions are determined by details of the algebra encoded in f^{abc}. For $\widehat{su}(2)_k$ these are given by $\vec{\alpha}_0 = [2, -2]$ and $\vec{\alpha}_1 = [-2, 2]$. (See Sec. 14.1.7 of Ref. [84]).

Repeated action of E_i on $|\text{hw}\rangle \equiv |\vec{\mu}\rangle$ creates an $su(2)$ multiplet. The dimension of this multiplet is $\mu^{(i)} + 1$; thus each E_i can act on the state $\mu^{(i)}$ times producing basis states $|\vec{\mu}\rangle, E_i^1|\vec{\mu}\rangle, E_i^2|\vec{\mu}\rangle, \ldots, E_i^{\mu^i}|\vec{\mu}\rangle$ with Dynkin labels $\vec{\mu}, \vec{\mu} - \vec{\alpha}_i, \vec{\mu} - 2\vec{\alpha}_i \ldots \vec{\mu} - \mu^{(i)}\vec{\alpha}_i$. Any state $|\vec{\lambda}\rangle$ obtained by action of one of the ladder operators, say E_i, on any basis state is a highest weight state for the remaining r ladder operators E_j, $(j \neq i)$, and the corresponding multiplets have dimensions $\lambda^{(j)} + 1$. Note that when referring to the Dynkin labels of the highest weight state characterizing the representation we use the symbol μ; the symbol λ is used to refer to a general state in the representation.

We illustrate this for the special case of $\widehat{su}(2)_2$. The ideas are summarized in Fig. 6.2 where

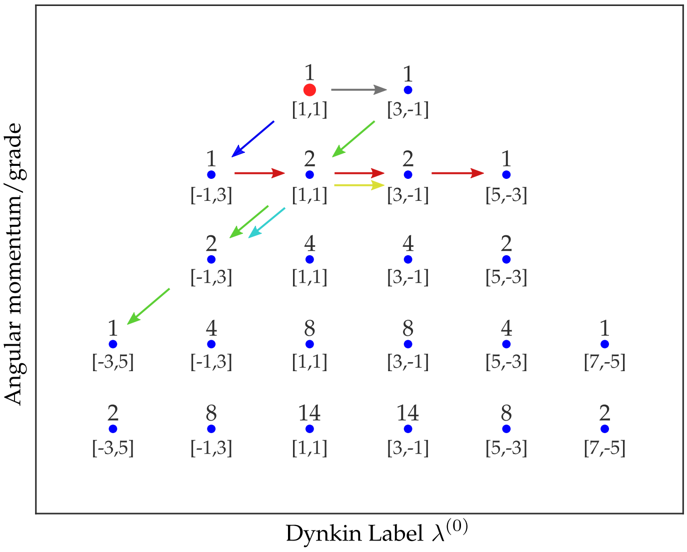

Figure 6.2: Representation of $\widehat{su}(2)_2$ generated from the highest weight state with Dynkin label $[1,1]$ (red dot). Other states in the representation are generated by action of ladder operators E_0 and E_1. Action of E_0 on any state is represented by a diagonal arrow and the horizontal arrows show the action of E_1. Arrows with same colors are used to illustrate successive application of either ladder operators to form an $su(2)$ multiplet.

we show the representation generated from the highest weight state $\vec{\mu} = [1,1]$ shown in the figure with a red dot. The action of E_1 is indicated by a horizontal arrow. This generates an $su(2)$ multiplet of dimension $\mu^{(1)} + 1 = 2$. The action of the E_0 ladder operator is indicated by a diagonal arrow going down to the lower left. This creates a multiplet of dimension $\mu^{(0)} + 1 = 2$.

The state $E_1|\vec{\mu}\rangle$ is a highest weight state for E_0. It has a Dynkin label $[3,-1]$ and thus is the highest weight state of a dimension 4 $su(2)$ multiplet generated by E_0 (indicated by the sequence of states connected by the green arrows). The state $E_0|\vec{\mu}\rangle$ has a Dynkin label $[-1,3]$ and is the highest weight state of a dimension 4 $su(2)$ multiplet generated by E_1 (indicated by the sequence of states connected by the red arrows). The Dynkin label $[1,1]$ can be created by two paths in the diagram representing the states $E_1E_0|\vec{\mu}\rangle$ and $E_0E_1|\vec{\mu}\rangle$. Whether they are distinct states or linearly dependent is decided by the commutation relation between E_1 and E_0, encoded in the structure constants f^{abc}. In general, when a Dynkin label can be arrived at by multiple paths in the diagram, the multiplicity of that Dynkin label is determined by the number of linearly dependent combinations of E_i's that reach there starting from $|\vec{\mu}\rangle$, which in turn is determined by the commutation relations between the ladder operators.

Getting the multiplicities, taking into account all commutation relations can be difficult; thankfully the multiplicities can be obtained directly using the Freudenthal Recursion formula (See Eq 14.136 of Ref. [84]). The formula allowed us to evaluate the multiplicities using simple computational combinatorics. The multiplicities are shown in Fig. 6.2 as an integer above the dot.

The coordinates of the dots in the Fig. 6.2 are chosen as follows. The x-axis represents $\lambda^{(0)}$ (note that the Dynkin label $\lambda^{(1)}$ is automatically determined as $k - \lambda^{(0)}$) and the y coordinate called the "grade" is determined by the number of actions of E_0 required to reach the state. We empirically identify the E_0 with angular momentum raising operator in the edge spectrum. Thus the y-coordinate is identified as angular momentum in the spectrum, which means the total number of states at angular momenta 0, 1, 2 are 2, 6, 12 respectively.

The edge current algebra is $\widehat{su}(n)_k \times u(1)$. The multiplicities at the angular momenta $L_z = 0, 1, 2\ldots$ for the u_1 boson is given by the integer partitions of L_z, namely $1, 1, 2, 3, 5\ldots$ (See Sec 14.4.3 of Ref. [84]). The total multiplicity is given by the convolution $\mathcal{M}(L) = \sum_{m=0}^{M} \mathcal{M}_{\widehat{su}(n)_k}(m)\mathcal{M}_{u(1)}(L-m)$ considering all possible ways of partitioning the angular momenta.

6.1.6 Representations of $\widehat{su}(2)_2$, $\widehat{su}(2)_3$ and $\widehat{su}(3)_2$ Kac-Moody algebra

A complete summary of root systems of affine extensions of $su(2)$ and $su(3)$ can be found in Ref. [84] (Also see explicit tables in Ref. [95]). We used these ideas to construct the explicit multiplicities for the cases we are interested in. The representation of $\widehat{su}(2)_2$ and $\widehat{su}(2)_3$ are given in Fig. 6.3 and 6.4 respectively.

For $su(2)$ affine algebra, the simple roots in the Dynkin label basis are given by $E_0 = [2, -2]$ and $E_1 = [-2, 2]$. In case of $\widehat{su}(2)_2$, the possible highest weights are $[2, 0]$, $[1, 1]$ and $[0, 2]$. Following the procedure described, we get their highest weight representations (Fig. 6.3).

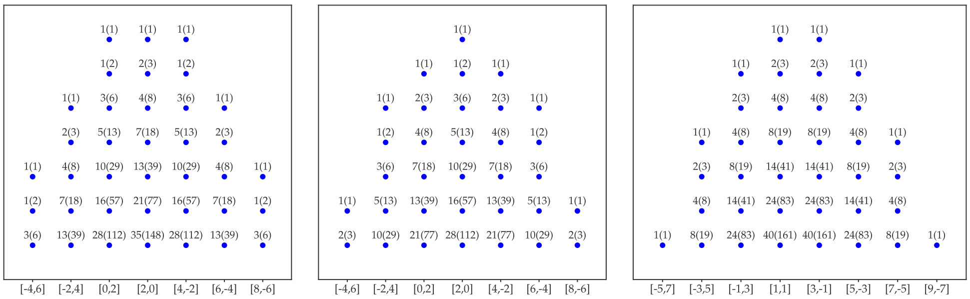

Figure 6.3: Representations of $\widehat{su}(2)_2$ for all three highest weight states given by Dynkin label $[0, 2]$ (left), $[2, 0]$ (middle) and $[1, 1]$. Dynkin labels for each state are labeled along the x-axis. The number above each marker shows the multiplicity of the state whereas the number inside the parenthesis shows the multiplicity corresponding to $\widehat{su}(2)_2 \times u(1)$.

Similarly for $\widehat{su}(2)_3$, the possible highest weights are $[3, 0]$, $[2, 1]$, $[1, 2]$ and $[0, 3]$. The highest weight representations are presented in Fig. 6.4.

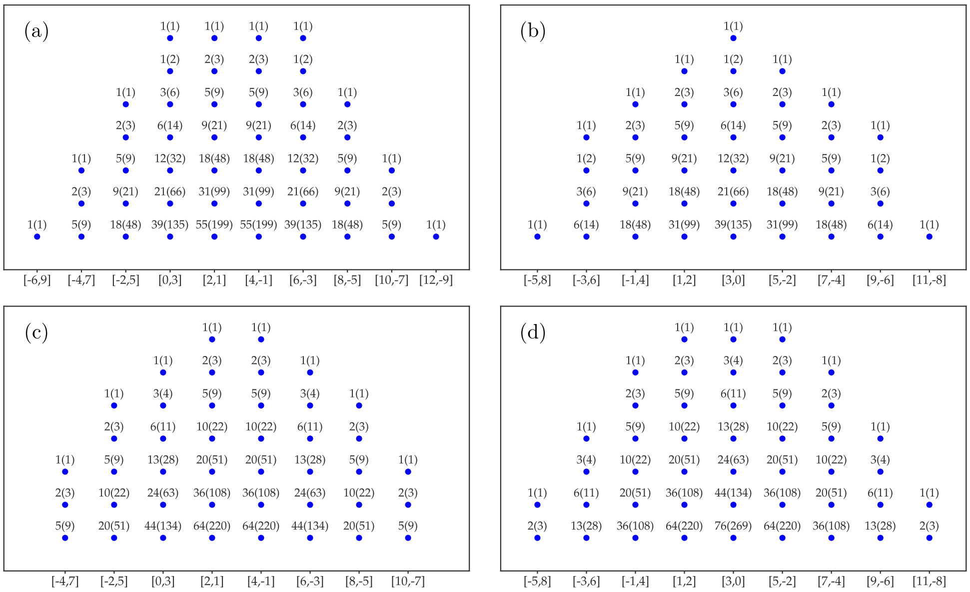

Figure 6.4: Representations of $\widehat{su}(2)_3$ for all possible highest weight states given by Dynkin label: (a) $[0,3]$, (b) $[3,0]$, (c) $[2,1]$ and (d) $[1,2]$. Dynkin labels for each state are labeled along the x-axis. The number inside the parenthesis shows the multiplicity corresponding to $\widehat{su}(2)_3 \times u(1)$.

Figure 6.5 shows the representation of $\widehat{su}(3)_2$ for highest weight state given by Dynkin label $[2,0,0]$. In these figures, multiplicity $\mathcal{M}_{\widehat{su}(n)_k}$ for each Dynkin label is shown above the dot whereas the full multiplicity $\mathcal{M}(L)$ is given in the parenthesis. Other highest weight representations are presented in Figs. 6.6 $-$ 6.8.

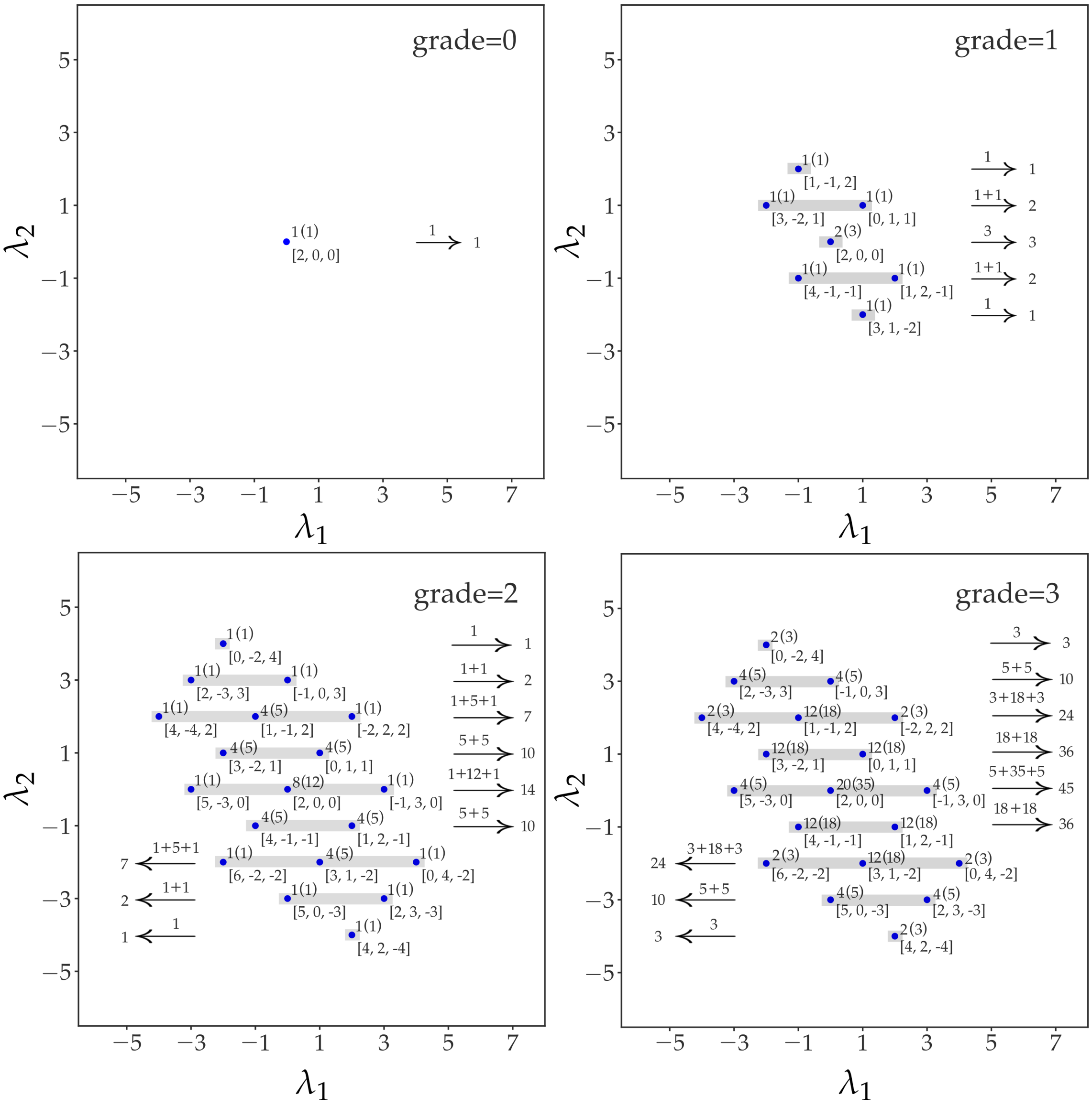

Figure 6.5: Representation of $\widehat{su}(3)_2$ characterized by the highest weight state with Dynkin label $[2,0,0]$. In each panel, which is labeled by the grade quantum number, action of E_1 and E_2 changes the Dynkin label without changing the grade. Highest weight state with Dynkin label $[2,0,0]$ has $\mu^{(1)}, \mu^{(2)} = 0$, hence action of E_1 and E_2 annihilates the state. Therefore only one state exists for grade $= 0$ which is represented by the blue marker in the top left panel. The number above each marker represents the multiplicity of the state whereas the number inside the parentheses corresponds to the same after adding 1 boson. Since $\mu^{(0)} = 2$, E_0 can act twice to produce states with Dynkin labels $[0,1,1]$ and $[-2,2,2]$ which have grade 1 and 2 respectively. In the top right panel, we get six new Dynkin labels after E_1 and E_2 act on $[0,1,1]$. If we think of grade as L_z^A quantum number in RSES, representation in each panel can be mapped to RSES in different L_z^A sectors. The arrows give combined multiplicities (with 1 boson) of states spanned by the gray boxes. It turns out that these combined multiplicities are one-to-one mapped with the counting in ϕ_3^2 RSES, shown in Fig. 6.12 (middle panel).

For $su(3)$ affine algebra, the simple roots are $E_0 = [2, -1, -1]$, $E_1 = [-1, 2, -1]$ and $E_2 = [-1, -1, 2]$. For $\widehat{su}(3)_2$ the possible highest weights are $[2, 0, 0]$, $[0, 2, 0]$, $[0, 0, 2]$, $[1, 1, 0]$, $[1, 0, 1]$ and $[0, 1, 1]$. Figs. 6.6, 6.7, and 6.8 show the representation of $\widehat{su}(3)_2$ for different highest weight states:

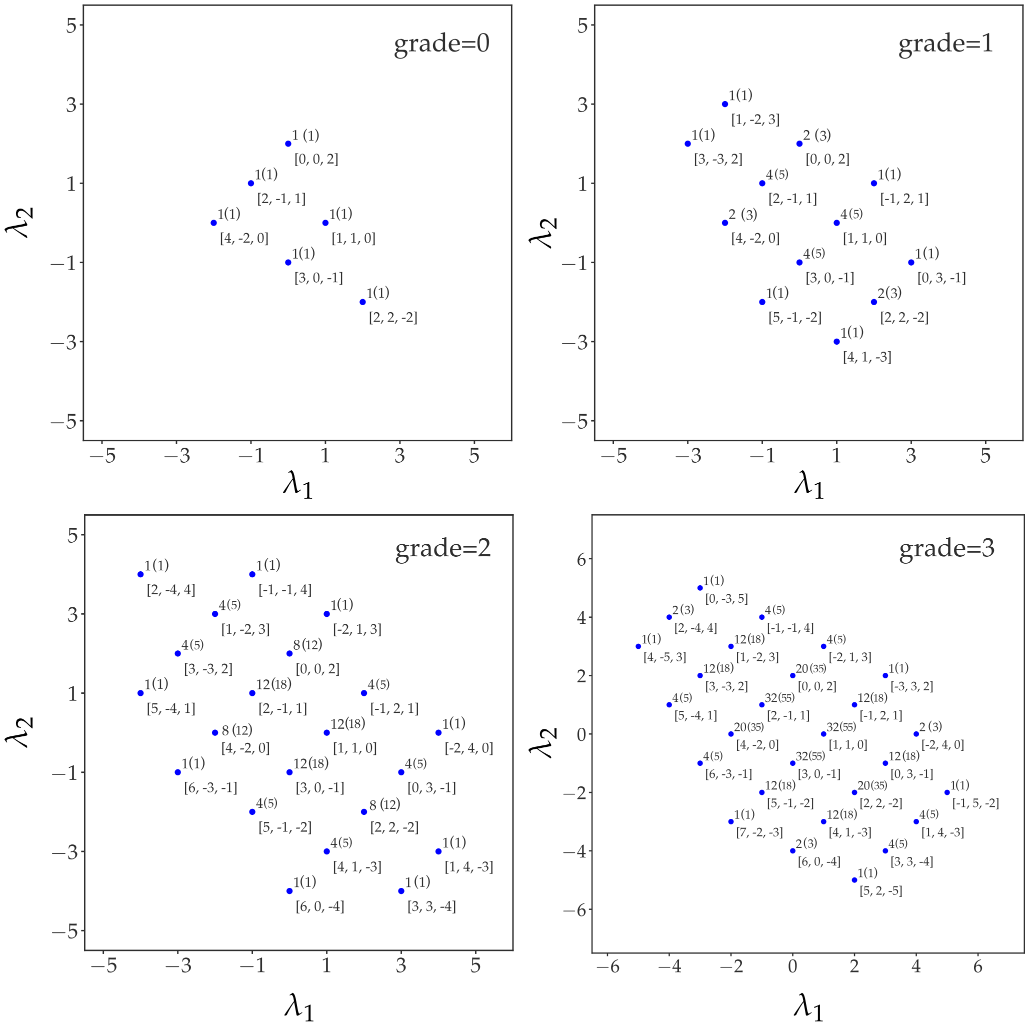

Figure 6.6: Representation of $\widehat{su}(3)_2$ for highest weight state given by Dynkin label $[0, 0, 2]$. This representation is identical to that for highest weight state given by Dynkin label $[0, 2, 0]$, but with a rotation. Each panel shows a particlular slice of the full representation labeled by grade quantum number.

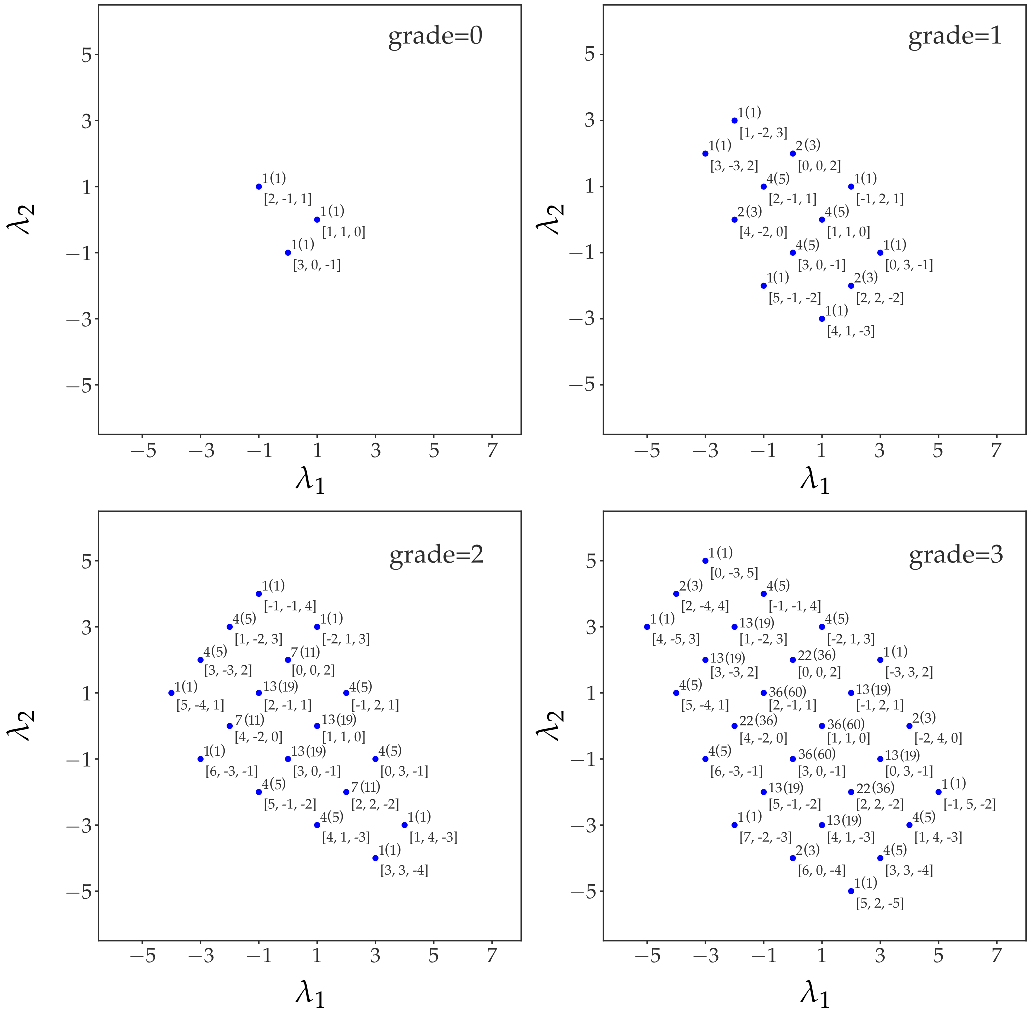

Figure 6.7: Representation of $\widehat{su}(3)_2$ for highest weight state given by Dynkin label $[1, 1, 0]$. This representation is identical to that for highest weight state given by Dynkin label $[1, 0, 1]$, but with a rotation. Each panel shows a particlular slice of the full representation labeled by the grade quantum number.

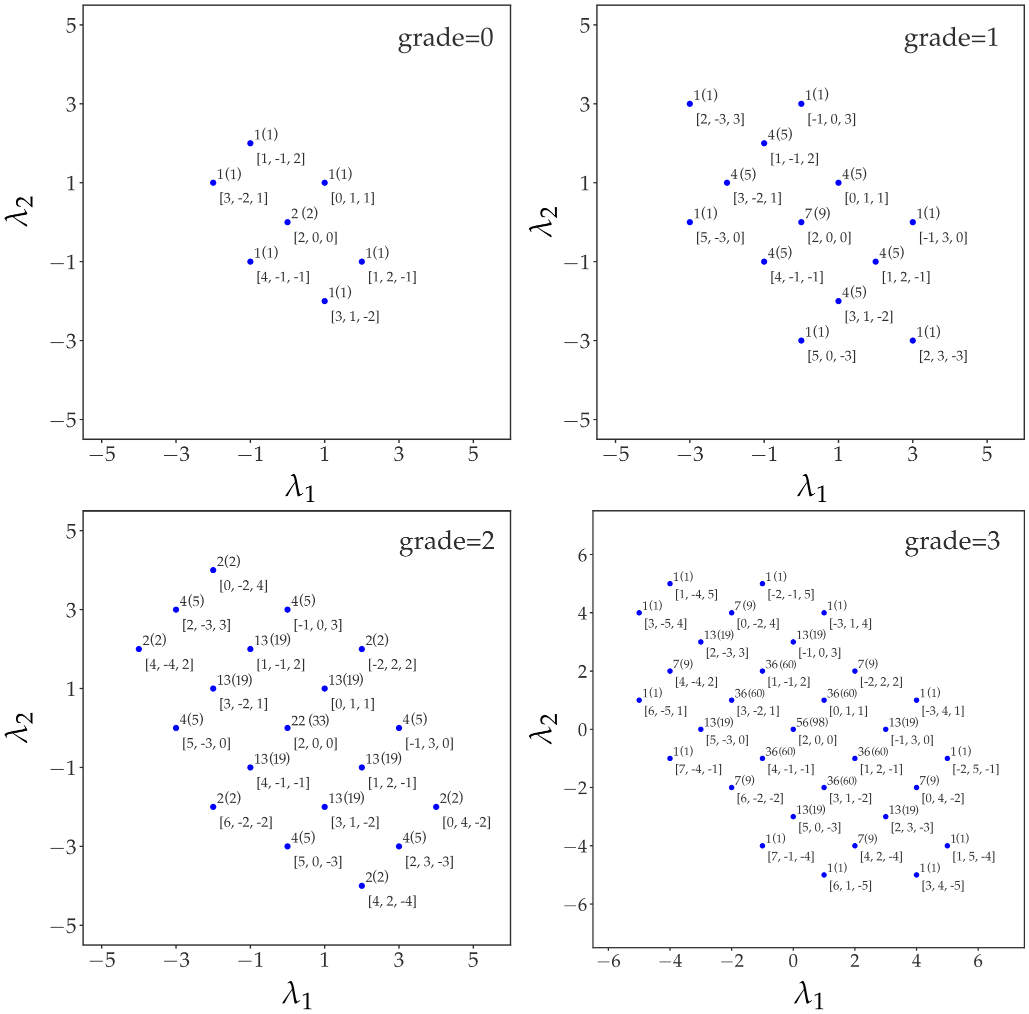

Figure 6.8: Representation of $\widehat{su}(3)_2$ for highest weight state given by Dynkin label $[0, 1, 1]$. Each panel shows a particlular slice of the full representation labeled by the grade quantum number. Action of E_1 and E_2 on $[0, 1, 1]$ state creates large number of states in grade $= 0$.

6.2 Results

In this section, we present the numerically obtained RSES for three different parton states as well as for their quasihole excitations. We compare the structure of RSES with the representations of the corresponding edge current algebra. It is found that the RSES contains multiple distinct branches. This is true for Jain CF states as well where it has been found that the different branches can be associated with the different number of composite fermions occupying the different Lambda levels [96]. We can attribute a similar origin to the different branches in RSES of these partons as well. For this, we find the number of linearly independent edge states after fixing the number of particles in the different LLs in each parton.

6.2.1 Real-space entanglement spectra of parton states

Fig. 6.9 shows the RSES of the ϕ_2^2 state across a rotationally symmetric cut (schematically shown in Fig. 6.1). The left panel shows the RSES corresponding to a block of the reduced density matrix with $N_A = 40$ and the right panel is for the block with $N_A = 41$. RSES is qualitatively unchanged when N_B is varied without changing N_A. For other nearby N_A sectors, the RSES is qualitatively the same as the ones shown here - depending on the parity (odd/even) of N_A.

The density matrix ρ_A within an N_A block is itself block diagonal in angular momentum sectors. The x-axis shows the angular momentum eigenvalues (L_z^A) of different blocks. The y-axis shows the (negative logarithm of) eigenvalues of that block of the reduced density matrix.

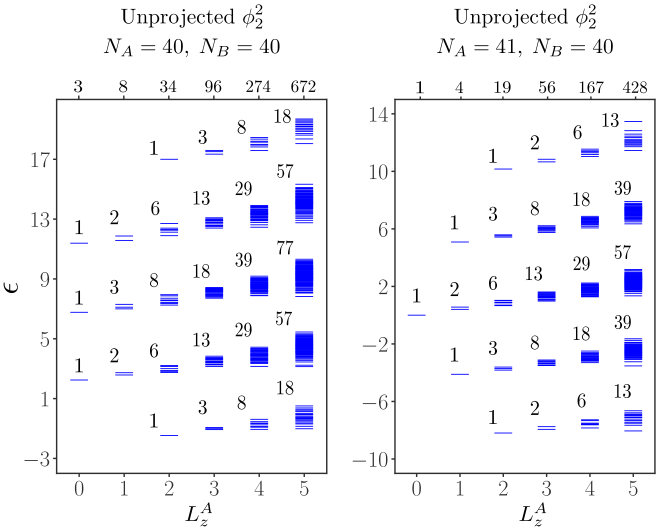
Unprojected ϕ_2^2
$N_A = 40,\ N_B = 40$

Unprojected ϕ_2^2
$N_A = 41,\ N_B = 40$

Figure 6.9: RSES of the parton wave function unprojected ϕ_2^2. The two different panels show the RSES in two different blocks of ρ_A corresponding to $N_A = N_B = 40$ (left) and $N_A = 41$, $N_B = 40$ (right). Entanglement energies ϵ are the negative logarithm of eigenvalues corresponding to L_z^A-blocks of ρ_A in a given (N_A, N_B)-block. Each marker thus is labeled by its L_z^A quantum number on x-axis which is shifted such that $L_{z,\min}^A = 0$. The number next to clusters of markers represents the number of eigenvalues in that cluster. Total number of distinct EWFs in any given L_z^A-block is shown just above the top axis.

In the expansion shown in Eq. (6.4), the EWF ξ_λ^A with the smallest angular momentum corresponds to that in which all the N_A particles in each parton compactly occupy the smallest single-particle angular momentum states. All possible compact LL configurations for ϕ_2^2 are shown in Fig. 6.10. In the case of ϕ_2^2 with odd N_A, the lowest angular momentum is obtained when both the partons have $(N_A - 1)/2$ particles in the LLL and $(N_A + 1)/2$ in the 2nd LL. This is the only state with this angular momentum. When N_A is even, there are three distinct EWFs, all with an angular momentum equal to the lowest angular momentum. There are no EWFs with L_z^A below these angular momenta, and hence the RSES contains no states for $L_z^A < L_{z,\min}^A$. The L_z^A values across the x-axis in these figures are relative to this minimum angular momentum $L^A_{z\text{min}}$.

(a) Unprojected ϕ_2^2; odd N_A

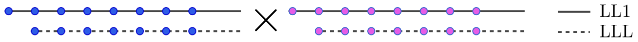

(b) Unprojected ϕ_2^2; even N_A

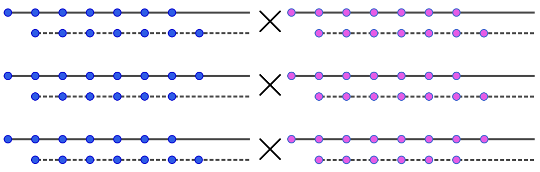

(c) Unprojected ϕ_2^2 with 1 qh; even N_A

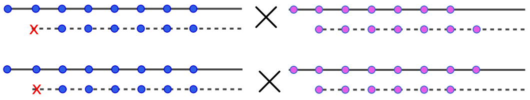

Figure 6.10: Schematic diagram showing all compact LL configurations for unprojected ϕ_2^2 in even and odd N_A sectors. Different partons are represented with different colors. For (a) odd N_A, there is only one configuration with $L^A_{z,\text{min}}$ whereas for (b) even N_A, three distinct LL configurations are possible. We also study RSES for parton states with one quasihole excitation. (c) Shows two possible compact LL configurations for unprojected ϕ_2^2 with one quasihole in LLL, when N_A is even.

The entanglement energies in the RSES appear in several nearly-degenerate clusters. In Fig. 6.9, the number of entanglement energies in a cluster is shown right next to the cluster. The total number of distinct EWFs with a given L^A_z (and N_A) obtained by simple enumeration (as described in Sec. 6.1.3) increases quite rapidly with L^A_z. This number is shown just above the top axis of each panel. The total number of entanglement energies in each L^A_z sector is much less than the number of EWFs. This is due to the extensive number of linear dependencies between the EWFs. As discussed in Sec. 6.1.3, these linear dependencies are reflected as 0 eigenvalues of the matrix M.

In general, the total number of the EWFs, total number of linear dependencies, and the total number of entanglement energies in each L^A_z sector grow rapidly with L^A_z. Due to the proliferation of EWFs, reliable numerical calculation of the matrix M is possible only up to $L^A_z \sim 5$. These sectors were sufficient to make a comparison with the representations of the current algebra. Quad-precision arithmetic in C codes reliably estimates M in systems as large as 80 particles. Statistical uncertainties in the estimated eigenvalues can be inferred by considering the results of many independent Monte Carlo trials. These error bars are typically comparable to the width of the marker and therefore are not shown.

The y-axes of the RSES plots are shifted by an arbitrary constant. This is because the matrix M and therefore its eigenvalues can be calculated only up to a proportionality constant in the Monte Carlo techniques (see Sec 6.1.3). This factor depends only on the Monte Carlo sampling distribution. Since the same distribution is used for all L^A_z sectors within a single plot, the different L^A_z sectors are shifted by the same amount. For the calculations presented in each plot, the Monte Carlo sampling wave function was chosen to be equal to the square of the absolute value of one of the EWFs with angular momentum $L^A_{z,\text{min}}$. Since the sampling function is different across different plots (for instance the two panels in Fig. 6.9), the ES in different plots are shifted by different constants.

The radius of the circular cut, (Fig. 6.1) was chosen to be approximately equal to the radius of EWF with the most compact configuration i.e. with a total angular momentum $L^A_{z,\text{min}}$. For example, in the case of ϕ_2^2, the largest single-particle momenta of the most compact configuration is approximately N_A. Hence the radius of the cut was chosen as $\sqrt{2N_A}$ (in magnetic length units).

RSES of ϕ_2^2*:* Fig. 6.9 shows the RSES of unprojected ϕ_2^2 where the left and right panels correspond to even and odd N_A-blocks respectively. Across different L^A_z sectors, the clusters in entanglement energies appear as distinct branches. Different arrangement of these branches give the RSES a particular structure. RSES of unprojected ϕ_2^2 for even and odd N_A consist of different arrangements of two distinct branches $(1, 2, 6, 13, \dots)$ and $(1, 3, 8, 18 \dots)$ as shown in Fig. 6.9. The counting and structure of RSES for even N_A exactly matches to the $\widehat{su}(2)_2 \times u(1)$ representation corresponding to Dynkin label $[0, 2]$ whereas for odd N_A, it matches with representation corresponding to Dynkin label $[2, 0]$ (left and middle panels in Fig. 6.3).

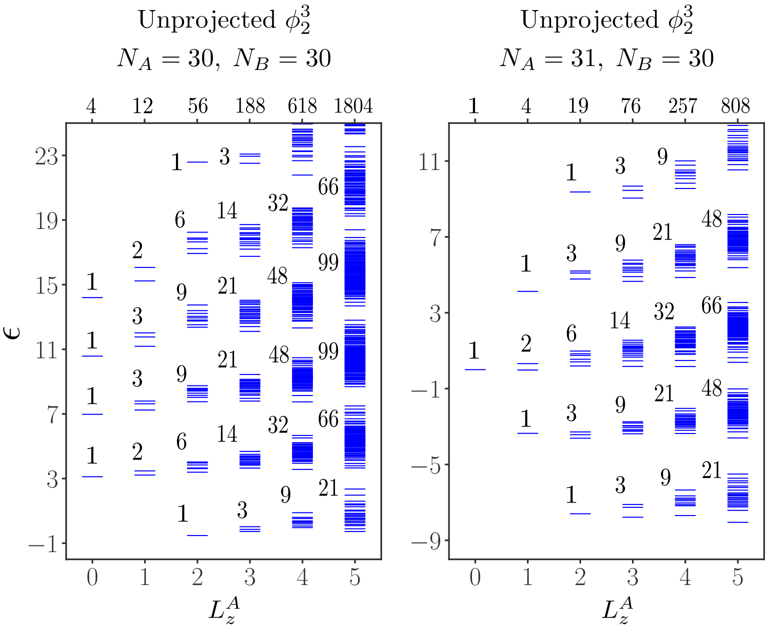

Figure 6.11: RSES of unprojected ϕ_2^3 for $N_A = N_B = 30$ (left) and $N_A = 31, N_B = 30$ (right) blocks of ρ_A. Number of distinct EWFs for L^A_z-sectors are much larger than that for ϕ_2^2 parton state, and hence spread in clusters in more, partly due to numerical errors.

RSES of ϕ_2^3*:* The RSES of unprojected ϕ_2^3 is shown in Fig. 6.11 with the left panel showing the spectrum for $(N_A = 30, N_B = 30)$ sector and right panel for $(N_A = 31, N_B = 30)$. Similar to the case of ϕ_2^2, we find that the RSES arrangement of unprojected ϕ_2^3 only depends on the parity (even or odd) of N_A. These arrangement consists of two distinct branches which have counting $(1, 2, 6, 14, 32, 66, \dots)$ and $(1, 3, 9, 21, 48, 99, \dots)$. We find that the RSES arrangement for even N_A exactly matches the highest weight representation of $\widehat{su}(2)_3 \times u(1)$ corresponding to Dynkin label $[0, 3]$ and the representation corresponding to Dynkin label $[3, 0]$ matches spectrum for odd N_A (Fig. 6.4).

RSES of ϕ_3^2: Figure 6.12 shows the RSES of unprojected ϕ_3^2 where the left, middle and right panels show the RSES for $(N_A = 29, N_B = 29)$, $(N_A = 30, N_B = 31)$ and $(N_A = 31, N_B = 31)$ blocks respectively. Three different branches are present in the RSES corresponding to $(N_A = 29, N_B = 29)$ and $(N_A = 31, N_B = 31)$-sectors, with counting $(2, 8, 31, 93, ..)$, $(1, 4, 17, 54, ..)$ and $(1, 6, 24, 78, ..)$. For the case of $(N_A = 30, N_B = 31)$, we find branches with counting $(1, 3, 14, 45, ..)$, $(2, 10, 36, ..)$, and $(1, 7, 24, ..)$. We use a grey vertical line in Fig. 6.12 to represent which eigenvalues are clubbed together in the counting.

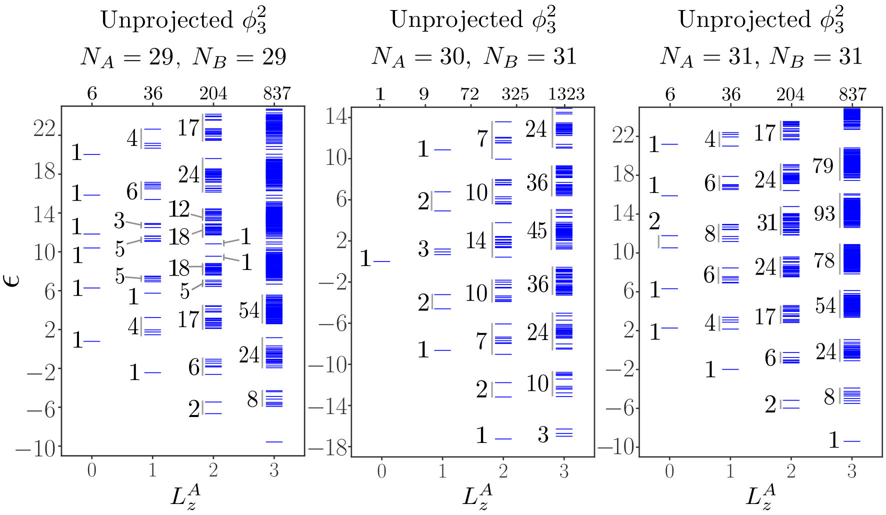

Figure 6.12: RSES of unprojected ϕ_3^2 for three blocks of ρ_A corresponding to $N_A = N_B = 29$ (left), $N_A = 30, N_B = 31$ (mid) and $N_A = 31, N_B = 31$ (right). As multiple branches emerge in close proximity to each other, we use a vertical (grey) line to show which clusters are clubbed together. Total number of states in these collections are shown next to the vertical lines.

Unlike the case of ϕ_2^2 and ϕ_2^3, comparing RSES of ϕ_3^2 to $\widehat{su}(3)_2 \times u(1)$ representation is not straightforward. Let us take an example of RSES for the $(N_A = 30, N_B = 31)$ sector (middle panel of Fig. 6.12). Total number of states at each angular momentum in the RSES match the total number of states at the corresponding grade in Fig. 6.5. We empirically find that the counting in the branches in the RSES is the sum total of counting along a horizontal line in Fig. 6.5 (shaded gray boxes). In this sense, the spectrum for $N_A = 30$ matches the $[2, 0, 0]$ representation of the $\widehat{su}(3)_2 \times u(1)$ algebra. Other highest weight representations of $\widehat{su}(3)_2 \times u(1)$ are given in Figs. 6.6-6.8. We find that the $N_A = 29$ and $N_A = 31$ RSES matches highest weight representations for $[0, 0, 2]$ and $[0, 2, 0]$ Dynkin labels respectively, shown in Fig. 6.6. In all the cases that we tested, we find that the aggregate number of states along a line matches exactly with the spectrum obtained from the current algebra.

The finer structures in each cluster too resemble the counting in the states of individual Dynkin labels. We point this out in the RSES of $N_A = 29$ shown in the left panel of Fig. 6.12. For instance, at $L_z = 1$, we find seven clusters with counting $(1, 4, 6, 8, 6, 4, 1)$, which can be associated with the total number of states along horizontal lines in the top right panel (grade 1) of Fig. 6.6. The number 4 is obtained by adding three states with Dynkin labels $[0, 0, 2]$ and one state with Dynkin label $[3, -3, 2]$. This 3+1 structure is reflected in the RSES as indicated in the left panel of Fig. 6.12.

RSES of ϕ_2^2 and ϕ_2^3 with a quasihole: We also explore the RSES for ϕ_2^2 and ϕ_2^3 when 1 quasihole is added to the system at the origin (Fig. 6.13). Adding a quasihole at the origin is equivalent to having the lowest angular momentum state in any one of the LLs in one of the partons empty. Fig. 6.10 shows a schematic for LL occupation in the two partons of ϕ_2^2 when the quasihole is in the lowest angular momentum state of the LLL. We find that the RSES does not change if the quasihole is added to either LL.

The left panel of Fig. 6.13 shows the RSES for ϕ_2^2 with a quasihole and $N_A = 31$. We found that the same RSES is produced for both odd and even N_A. RSES for ϕ_2^2 with a quasihole exactly matches with the $[1, 1]$ highest weight representation of $\widehat{su}(2)_2 \times u(1)$ (middle panel in Fig. 6.9). RSES for ϕ_2^3 with a quasihole, for $N_A = 30$ (right panel in Fig. 6.13) matches with with $[1, 2]$ highest weight representation of the $\widehat{su}(2)_3 \times u(1)$. RSES spectra changes for $N_A = 31$ which maps exactly to $[2, 1]$ highest weight representation of $\widehat{su}(2)_3 \times u(1)$. The corresponding representations are shown in the bottom panels of Fig. 6.4.

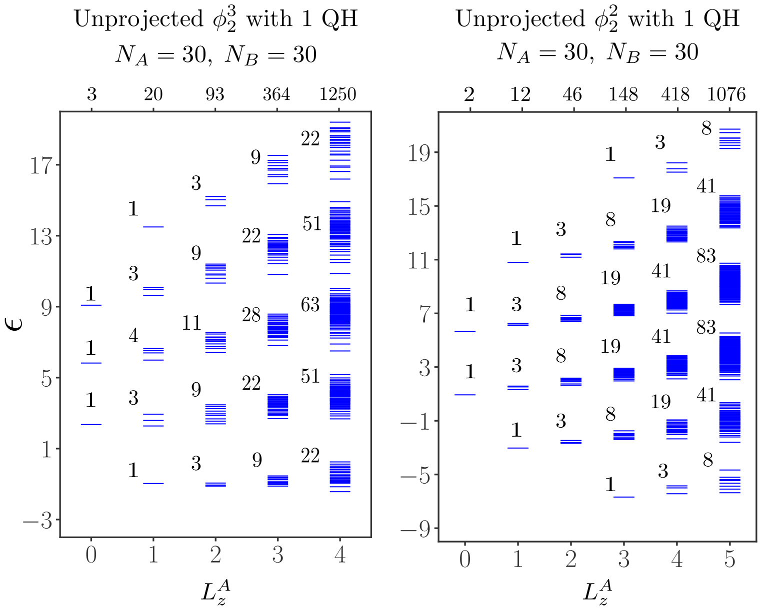
Unprojected ϕ_2^3 with 1 QH
$N_A = 30,\ N_B = 30$

Unprojected ϕ_2^2 with 1 QH
$N_A = 30,\ N_B = 30$

Figure 6.13: RSES of ϕ_2^3 (left) and ϕ_2^2 (right) where both parton states have a single quasihole placed at $m = 0$ angular momentum state of LLL. Both panels show RSES for $N_A = N_B = 30$ block of ρ_A.

6.2.2 RSES for the projected state

Until now we discussed the RSES of unprojected parton states. A natural question is whether the agreement between the RSES and the representations of the edge currents continues to hold even after projection into the LLL. The algorithm that we have used for the calculation extends also to the case of the projected parton states. The calculations run slower due to the computational cost of projection. Moreover, an exact projection into the LLL is not possible except in very small systems. We instead rely on approximate projection as described in Sec. 6.1.4. To enable the use of the projection scheme, we consider a projected state $\psi_{1/5}^{2^2 1^4}$ [see Eq. (6.11)] which is expected to also show the same edge counting as ϕ_2^2.

We indeed find that even after the approximation, the RSES of LLL-projected $\psi_{1/5}^{2^2 1^4}$ state has the same structure ϕ_2^2 as shown in Fig. 6.14. Note that the number of the EWFs (shown above the panels) in each L_z^A block is significantly larger than that for unprojected ϕ_2^2 (Fig. 6.9). This is a result of the excitations associated with the additional Slater determinants ϕ_1 in the wave function. We find a larger spread in the clusters. An exact match with RSES of unprojected ϕ_2^2 suggests that multiplication with factors of ϕ_1 and action of LLL-projection do not alter the topological features (fusion rules of the non-trivial anyons are identical) of a parton state.

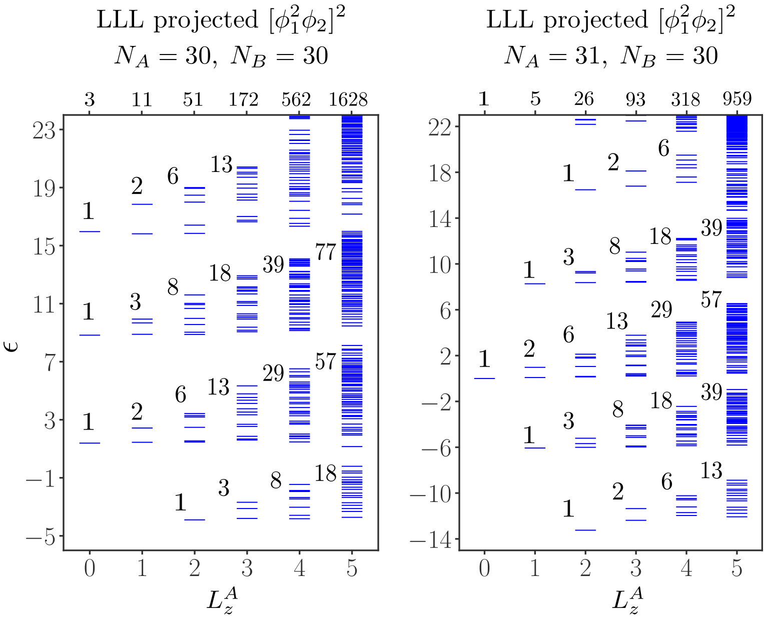

Figure 6.14: RSES of LLL-projected $[\phi_1^2\phi_2]^2$ for two blocks of ρ_A corresponding to $N_A = N_B = 30$ (left) and $N_A = 31, N_B = 30$ (right). The projection is approximated as described in Sec 6.1.4.

6.2.3 Origin of the branches and edge overlap matrix

The branches in the entanglement spectra appear in the case of the edge spectrum of composite fermion states as well [96, 65]. Each branch in that case could be associated with states with a particular occupancy of the composite fermion Landau levels. In this section, we ask whether a similar picture is true in the context of the parton states.

The entanglement spectrum contains states with different occupancy of the Landau levels of each parton. A strategy to address the question could be to expand the Schmidt eigenstates in the EWFs. Then identify the number of particles in each LL in the basis states that contribute predominantly to each Schmidt eigenvector. This strategy does not yield a clear answer as the EWFs are not all linearly independent.

We instead address the problem in the following way. We consider the states with a fixed number of particles in each LL of each parton. We consider the excitations at the edge of the system at each angular momentum. These are the same as the EWFs that we had constructed earlier but with a specific Landau level occupancy of each parton. We consider the overlap matrix of the edge states, $\mathcal{O}$ and plot the (negative logarithm of) eigenvalues for different L_z-blocks of $\mathcal{O}$. The number of dominant eigenvalues is a measure of the linearly independent states in the space of these states, i.e, the dimension of the space.

Interestingly, the number of dominant eigenvalues of $\mathcal{O}$ at different L_z values reproduce the same counting that we saw in the individual branches present in the RSES. The dominant eigenvalues as a function of momentum are plotted in Figs. 6.15 and 6.16 for the case of ϕ_2^2 and ϕ_2^3 respectively, and further results are summarized in Tables 6.1 and 6.2 respectively.

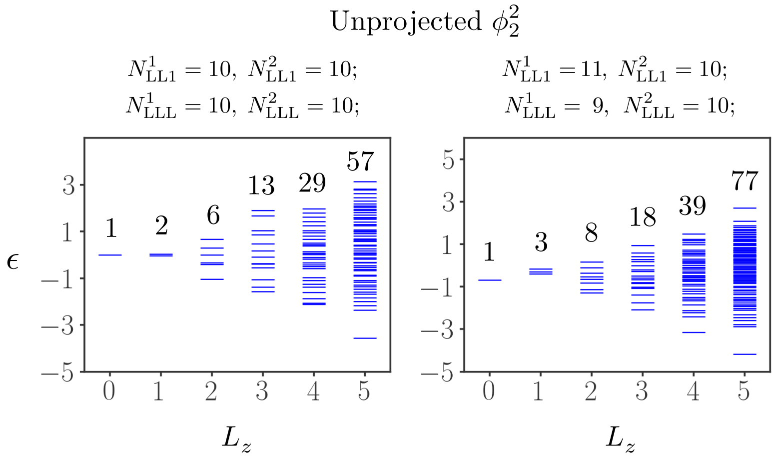

Figure 6.15: Dominant eigenvalues of the overlap matrix $\mathcal{O}$ for two different Landau level occupancies. Left panel shows the spectra when both partons have identical LL occupation $(N_{\mathrm{LLL}}, N_{\mathrm{LL1}}) = (10, 10)$. The right one is for when LL occupation of one of the partons is $(N_{\mathrm{LLL}} + 1, N_{\mathrm{LL1}} - 1)$ and the other one has a configuration $(N_{\mathrm{LLL}}, N_{\mathrm{LL1}})$. The y-axis is the negative logarithm of eigenvalues of different L_z-blocks of $\mathcal{O}$.

For ϕ_2^2: Figure 6.15 shows dominant eigenvalues of the overlap matrix against L_z for two different $(N_{\text{LLL}}, N_{\text{LL1}})$-sectors. The left panel shows the case of $(N^{1,2}_{\text{LLL}}, N^{1,2}_{\text{LL1}}) = (10, 10)$ (where superscript labels different partons). As shown in Table 6.1, as long as both the partons have same LL occupation, the counting remains the same. The right panel shows the case where $(N^1_{\text{LLL}}, N^1_{\text{LL1}}) = (11, 9)$ and $(N^2_{\text{LLL}}, N^2_{\text{LL1}}) = (10, 10)$. This produces a different branch. Similarly, we find that more generally whenever $N^1_{\text{LLL}} = N^2_{\text{LLL}} + 1$ and $N^1_{\text{LL1}} = N^2_{\text{LL1}} - 1$, we get the same counting (see Table 6.1). The counting that we see in these two cases is in agreement with the individual branches seen in the ground state RSES shown in Fig. 6.9.

$(10, 10) \times (10, 10)$	1,2,6,13,29,57
$(11, 9) \times (11, 9)$	
$(12, 8) \times (12, 8)$	
$(11, 10) \times (11, 10)$	
$(11, 9) \times (10, 10)$	1,3,8,18,39,77
$(12, 8) \times (11, 9)$	
$(12, 9) \times (11, 10)$	
$(10, 10+q) \times (10, 10)$	1,3,8,19,41,83
$(11, 9+q) \times (11, 9)$	
$(11, 10+q) \times (11, 10)$	

Table 6.1: Different LL configurations for parton state ϕ_2^2 given by $(N^1_{\text{LLL}}, N^1_{\text{LL1}}) \times (N^2_{\text{LLL}}, N^2_{\text{LL1}})$ along with counting corresponding to the dominant spectra of its overlap matrix $\mathcal{O}$. Here $N_{LLn} + q$ represents the quasihole addition to nth LL.

If we perform a similar calculation of the eigenvalues of the overlap matrix for cases where there is a quasihole at the center, we obtain a counting that matches the individual branches of the RSES shown in the right panel in Fig. 6.13). This counting is independent of the number of the particles in each parton Landau level (Table 6.1). This is consistent with the fact that only one type of branch appear in this RSES.

For ϕ_2^3: Figure 6.16 shows the dominant eigenvalues of the overlap matrix for ϕ_2^3 in two different LL occupation sectors. Counting matches the different branches present in the ϕ_2^3 RSES (Fig. 6.11). The spectra in the left panel corresponds to LL configuration where all partons have same LL occupation $(N^{1,2,3}_{\text{LLL}}, N^{1,2,3}_{\text{LL1}}) = (10, 10)$. We checked that the counting remains same as long as all three partons have same LL occupation (Table 6.2). Similarly, we get the second branch (right panel in Fig. 6.16) in the RSES of ϕ_2^3 when LL occupation is such that $N^1_{\text{LLL}} = N^{2,3}_{\text{LLL}} + 1$ and $N^1_{\text{LL1}} = N^{2,3}_{\text{LL1}} - 1$.

RSES of ϕ_2^3 with the quasihole has two distinct branches given by counting $(1, 3, 9, 22, 51, \dots)$ and $(1, 4, 11, 28, 63, \dots)$ as shown in Fig. 6.13. We get the first branch from the dominant

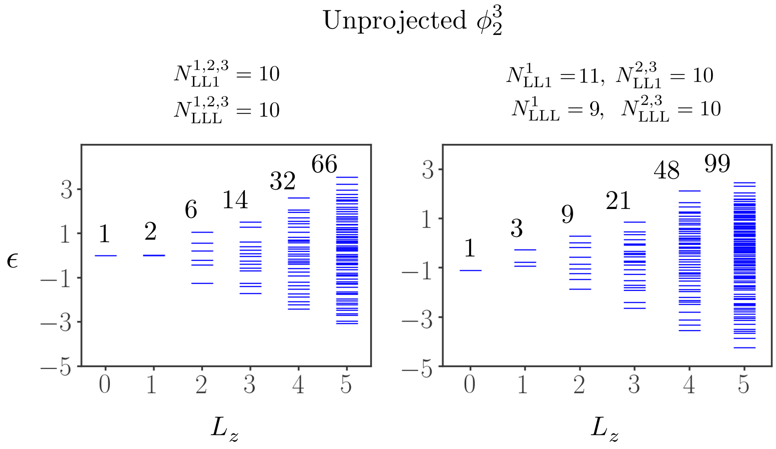

Figure 6.16: Dominant eigenvalues of overlap matrix $\mathcal{O}$ of ϕ_2^3 for different Landau level occupancies. Left panel shows spectra for a configuration when all three partons have identical LL occupation $(N_{\mathrm{LLL}}, N_{\mathrm{LL1}})$. The right one is for a configuration when two partons have same LL occupation $(N_{\mathrm{LLL}}, N_{\mathrm{LL1}})$ and LL configuraion for the third parton is given by $(N_{\mathrm{LLL}}+1, N_{\mathrm{LL1}}-1)$. Two distinct counting we get in these spectra match exactly to those of two distinct branches present in the RSES of ϕ_2^3.

spectra corresponding to the LL configuration in which all three partons have the same LL occupation but one parton has a quasihole in LL1 (see Table 6.2). We get the second branch in configurations where $N_{\mathrm{LLL}}^{1} = N_{\mathrm{LLL}}^{2,3} + 1$ and $N_{\mathrm{LL1}}^{1} = N_{\mathrm{LL1}}^{2,3} - 1$ and the quasihole is in one of the latter (indexed by $2, 3$) partons.

$(10,10)^3$	1,2,6,14,32,66
$(11,9)^3$	
$(11,10)^3$	
$(11,9)\times(10,10)^2$	1,3,9,21,48,99
$(12,8)\times(11,9)^2$	
$(12,9)\times(11,10)^2$	
$(10,10+q)\times(10,10)^2$	1,3,9,22,51,108
$(11,9+q)\times(11,9)^2$	
$(11,10+q)\times(11,10)^2$	
$(11,9)\times(10,10)\times(10,10+q)$	1,4,11,28,63,134
$(12,8)\times(11,9)\times(11,9+q)$	
$(12,9)\times(11,10)\times(11,10+q)$	

Table 6.2: Different LL configurations for parton state ϕ_2^3 given by $(N^1_{\text{LLL}}, N^1_{\text{LL1}}) \times (N^2_{\text{LLL}}, N^2_{\text{LL1}}) \times (N^3_{\text{LLL}}, N^3_{\text{LL1}})$ along with counting corresponding to the dominant spectra of its overlap matrix $\mathcal{O}$. $(N^i_{\text{LLL}}, N^i_{\text{LL1}} + q)$ represents the LL occupation sector where a quasihole is added to LL1 of the ith parton.

6.3 Conclusion

In this chapter, we have studied the RSES of a variety of unprojected parton states given by ϕ_2^2, ϕ_2^3, and ϕ_3^2 for bipartitions of systems with as many as 80 particles. The RSES of ϕ_2^2 and ϕ_2^3 was also computed when the parton states had quasihole excitations in the bulk. We found that counting present in RSES for the unprojected parton wave function of the form ϕ_n^k has a one-to-one mapping with the counting of states in the $\widehat{su}(n)_k \times u(1)$ edge current algebra. RSES counting that matches with different representations of the algebra could be realized by considering sectors of the reduced density matrix with odd and even numbers of particles or by insertion of a quasihole.

We also studied RSES of LLL-projected $[\phi_1^2\phi_2]^2$ state with an approximate projection scheme. We found that the RSES for this state has an identical structure as that of unprojected ϕ_2^2 which suggests that both states are topologically equivalent (up to Abelian anyons). Multiplication with ϕ_1^2 and LLL-projection does not change the topological class of a parton state (to be precise, multiplication by ϕ_1^2 does not change the chiral central charge but does alter other topological quantities like the shift and the charges of the quasiparticles but these can be readily accounted for).

Finally, we computed the spectra of the overlap matrices corresponding to the edge excitations of the parton states while restricting the number of particles in parton Landau levels. The calculations indicate that the different branches seen in the RSES can be associated with different Landau level occupancies of the partons. However, a more thorough study is needed to consider a wider range of Landau-level occupancies to see how they are embedded in the RSES. A careful study of the overlaps between the fixed Landau level occupancy edge state space and the eigenspace of states formed by the individual branches in the RSES can provide a more concrete demonstration of the connection between the Landau level occupancies and the branches. The qualitative similarity in the branch structure of the RSES to the ones previously studied [81] for the Jain sequence states motivates the question of whether these entanglement spectra as well can be associated with a local entanglement Hamiltonian.

Chapter 7

RSES of projected FQH states using Monte Carlo

In the previous chapter, we saw that entanglement spectrum of the unprojected CF state and parton states [39] can be efficiently obtained using Monte Carlo methods [65, 97]. The bottleneck in extending the same technique to the projected CF states (which are energetically more favorable) is the difficulty in implementing the LLL projection. In a large number of studies involving energetics of the CF states, an approximate method introduced by Jain and Kamilla (JK) to perform lowest Landau level (LLL) projection has been found to provide computationally efficient and reliable results [98, 99, 100]. Combining the JK projection with the MC methods for RSES evaluation involves further approximations but this can be used for calculations in systems upto hundred particles [65, 81, 97]. Testing the approximations require comparison with computationally expensive but exact RSES calculated using alternate methods. This is the goal of the chapter.

We identify cases where alternate exact methods can be employed to calculate RSES in relatively large systems. For the fermionic Jain 2/5th state, the Trugman-Kivelson (TK) Hamiltonian [47] can be diagonalized to produce an exact expansion of the unprojected CF state. RSES of the state can be obtained using a generalization of the method presented by Chandran *et al.* in Ref. [101] We use this to show that the MC method indeed produces practically exact results for the RSES.

Construction of exact Hamiltonians for the projected state is an open problem [88], so a similar strategy cannot be employed to test the RSES for the projected state. Instead we consider the case of the bosonic Jain 2/3rd state, where we employ exact projection in a manner that allows us to exactly compute the low momentum entanglement spectrum in systems as large as $N = 24$. We find that as system size increases the results from approximate projection employed in the MC method approach the exact RSES, at least in the low momentum sectors.

We emphasize that the results presented in this chapter is not a comparison of the RSES of the exact projected CF states (ψ_{EX}) and the RSES of the JK projected CF states (ψ_{JK}). Since the two states are nearly identical to each other, we expect their RSES to be nearly the same. Instead what we are testing is the effect of the approximate projection used while implementing the MC method for RSES calculation. The approximation in the latter is similar in spirit to the JK projection but is not the same. Secondly, the results presented compare the approximate results from MC estimates of RSES with the RSES of the ψ_{EX}. The comparison is done with ψ_{EX} rather than with ψ_{JK} because, using methods described in Sec. 7.2.2, RSES of ψ_{EX} can be computed exactly at least for small systems. Doing the same for ψ_{JK} is harder.

This chapter is structured as follows. We begin by presenting the numerical techniques involved. We present, in Sec 7.1, a strategy for a numerically exact computation of the RSES of the unprojected Jain 2/5th state obtained from exact diagonalization of the TK Hamiltonian. We will later use this to demonstrate that the RSES using MC method is practically exact for the unprojected state. In Sec. 7.2, we give a summary of the method for computing RSES of variational states by expanding them in terms of entanglement wavefunctions (EWFs). The details of the method, originally introduced in Ref. [65], can be found in Refs. [81, 97]. Section 7.2.2 provides the details for using this method with exactly projected Jain 2/3rd state of bosons. We could use this to obtain numerically exact RSES in systems up to size 24. Section 7.2.5 details the approximations that are made to perform LLL projection of the EWFs, which makes accessing large systems possible. All numerical results benchmarking the methods are given in Sec. 7.3, and finally we conclude with Sec. 5.4.

Notations: All calculations in the chapter are performed for systems in the spherical geometry where the single particle Landau orbitals for a particle in the nth LL and with angular momentum m are the monopole harmonics, [32, 33, 31] given by

$$Y_{Qnm} = N_{Qnm}(-1)^{Q+n-m} v^{Q-m} u^{Q+m} \times \sum_{s=0}^{n} \binom{n}{s} \binom{2Q+n}{Q+n-m-s} |v|^{2(n-s)} |u|^{2s} \tag{7.1}$$

where u and v are given by $u = \cos(\theta/2)e^{\iota\phi/2}$ and $v = \sin(\theta/2)e^{-\iota\phi/2}$ in terms of coordinates $0 \leq \theta < \pi$ and $0 \leq \phi < 2\pi$ on the sphere, and Q quantifies the strength of monopole which produces a radial magnetic field of flux $2Q$ in units of flux quanta $\phi_0 = hc/e$. The normalization factor is given by

$$N_{Qnm} = \left(\frac{(2Q+2n+1)}{4\pi} \frac{(Q+n-m)!(Q+n+m)!}{n!(2Q+n)!} \right)^{1/2} \tag{7.2}$$

7.1 RSES of state expanded in Slater determinant basis

In this section, we describe the method to calculate RSES for fermionic quantum Hall states which are expressed as linear combinations

$$\psi(\boldsymbol{r}_1, \ldots, \boldsymbol{r}_N) = \sum_{\boldsymbol{\lambda}} c_{\boldsymbol{\lambda}} \mathcal{M}_{\boldsymbol{\lambda}}(\boldsymbol{r}_1, \ldots, \boldsymbol{r}_N) \tag{7.3}$$

where the basis states $\mathcal{M}_{\boldsymbol{\lambda}}$ are Slater determinants of single particle momentum orbitals. The coefficients $c_{\boldsymbol{\lambda}}$'s can, for instance, be from exact diagonalization. The basis states $\mathcal{M}_{\boldsymbol{\lambda}}$ are parametrized by the ordered list of occupied single particle orbitals $\boldsymbol{\lambda} \equiv (\lambda_1, \lambda_2 \ldots)$ and can be expanded as

$$\mathcal{M}_{\boldsymbol{\lambda}}(\boldsymbol{r}_1, \ldots, \boldsymbol{r}_N) = \frac{1}{\sqrt{N!}} \sum_{\sigma \in \mathcal{S}_N} \epsilon(\sigma) \prod_{i=1}^{N} \phi_{\lambda_{\sigma(i)}}(\boldsymbol{r}_i) \tag{7.4}$$

where $\phi_{\lambda_i}(\boldsymbol{r}_i)$'s are the normalized single particle Landau orbitals $\lambda_i \equiv (n_i, m_i)$ specified by the LL-index n_i and the angular momentum m_i, and $\mathcal{S}_N$ is the set of all permutations of $(1, 2, \ldots, N)$. In the spherical geometry, the single particle orbitals are given by monopole harmonics given in Eq. (7.1).

We present a method which enables us to compute RSES for states with particles occupying different LLs. For a real-space cut which respects the rotational symmetry of the system, angular momentum states (projected onto either subsystem) remain orthogonal to each other as long as they are in same LL. However states with same angular momentum but different LLs have non-zero overlap due to restricted limits of integration within each subsystem. The method presented below extends the one given in Ref. [101] which works for states restricted to the LLL, by incorporating non-orthogonal momentum states.

In this chapter, we will use this method to compute the RSES of unprojected Jain 2/5-state, which we get as the ground state (using ED) of Trugman-Kivelson Hamiltonian [47] projected into the lowest 2 LLs treated as degenerate.

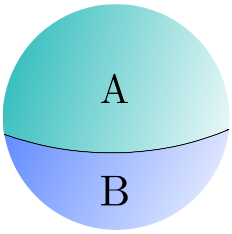

Figure 7.1: Azimuthally symmetric cut for the spherical geometry.

For any wavefunction $\psi(\boldsymbol{r}_1, \ldots, \boldsymbol{r}_N)$ for N particles, the density matrix is given by

$$\rho(\boldsymbol{r}'_1, .., \boldsymbol{r}'_N; \boldsymbol{r}_1, .., \boldsymbol{r}_N) = \frac{\bar{\psi}(\boldsymbol{r}_1, .., \boldsymbol{r}_N)\psi(\boldsymbol{r}'_1, .., \boldsymbol{r}'_N)}{\int \prod_i \mathrm{d}^2\boldsymbol{r}_i \, |\psi(\boldsymbol{r}_1, .., \boldsymbol{r}_N)|^2} \tag{7.5}$$

We partition the system into two subsystems A and B using an azimuthally symmetric cut (Fig. 7.1) and consider the sector where region A contains N_A particles (and B has $N_B = N - N_A$ particles). We use the following shorthands for collections of particle coordinates $\boldsymbol{R} \equiv (\boldsymbol{r}_1, \ldots, \boldsymbol{r}_N)$, $\boldsymbol{R}_A \equiv (\boldsymbol{r}_1, \ldots, \boldsymbol{r}_{N_A})$ and $\boldsymbol{R}_B \equiv (\boldsymbol{r}_{N_A+1}, \ldots, \boldsymbol{r}_N)$.

The reduced density matrix for subsystem A is then given by

$$\begin{aligned}\rho_{N_A}(\boldsymbol{R}_A^{'}; \boldsymbol{R}_A) =& \frac{\int_B \mathrm{d}\boldsymbol{R}_B\, \rho(\boldsymbol{R}_A, \boldsymbol{R}_B; \boldsymbol{R}_A^{'}, \boldsymbol{R}_B)}{\int_A \mathrm{d}\boldsymbol{R}_A \int_B \mathrm{d}\boldsymbol{R}_B\, \rho(\boldsymbol{R}_A, \boldsymbol{R}_B; \boldsymbol{R}_A, \boldsymbol{R}_B)} \\ =& \frac{1}{p_{N_A}} \binom{N}{N_A} \int_B \mathrm{d}\boldsymbol{R}_B\, \rho(\boldsymbol{R}_A, \boldsymbol{R}_B; \boldsymbol{R}_A^{'}, \boldsymbol{R}_B) \end{aligned} \tag{7.6}$$

where p_{N_A} is the probability that subsystem A contains exactly N_A particles. Using Eqs. (7.3) and (7.4), we can rewrite the Eq. (7.6) as

$$\rho_{N_A} = \frac{1}{p_{N_A}} \binom{N}{N_A} \sum_{\boldsymbol{\lambda}, \boldsymbol{\lambda}'} \bar{c}_{\boldsymbol{\lambda}} c_{\boldsymbol{\lambda}'} \int_B \mathrm{d}\boldsymbol{R}_B\, \overline{\mathcal{M}}_{\boldsymbol{\lambda}} \mathcal{M}_{\boldsymbol{\lambda}'} \tag{7.7}$$

To simplify further, we will use the following property

$$\mathcal{M}_{\boldsymbol{\lambda}}(\boldsymbol{R}) = \sqrt{\frac{N_A! N_B!}{N!}} \sum_{\substack{\boldsymbol{\mu}, \boldsymbol{\nu} \\ \langle \boldsymbol{\mu}; \boldsymbol{\nu} \rangle = \boldsymbol{\lambda}}} \epsilon_{\boldsymbol{\mu}\boldsymbol{\nu}}\, \mathcal{M}_{\boldsymbol{\mu}}(\boldsymbol{R}_A) \mathcal{M}_{\boldsymbol{\nu}}(\boldsymbol{R}_B). \tag{7.8}$$

Here the Slater determinant of N particles is expanded as anti-symmetrization of products of Slater determinants corresponding to ordered set of orbitals $\boldsymbol{\mu}$ (of size N_A) and $\boldsymbol{\nu}$ (of size N_B) such that the ordered combination of two is equal to $\boldsymbol{\lambda}$ (this constraint is represented by $\langle \boldsymbol{\mu}; \boldsymbol{\nu} \rangle = \boldsymbol{\lambda}$). The sign corresponding to the permutation σ, which makes $(\lambda_{\sigma(1)}, \ldots, \lambda_{\sigma(N)}) = (\mu_1, \ldots, \mu_{N_A}, \nu_{N_A+1}, \ldots, \nu_N)$ is given by $\epsilon_{\boldsymbol{\mu}\boldsymbol{\nu}} = \epsilon(\sigma)$. This allows us to rewrite ρ_{N_A} as

$$\rho_{N_A}(\boldsymbol{R}_A^{'}, \boldsymbol{R}_A) = \sum_{\boldsymbol{\mu}, \boldsymbol{\mu}'} Q_{\boldsymbol{\mu}, \boldsymbol{\mu}'} \overline{\mathcal{M}}_{\boldsymbol{\mu}}(\boldsymbol{R}_A) \mathcal{M}_{\boldsymbol{\mu}'}(\boldsymbol{R}_A^{'}) \tag{7.9}$$

where

$$\begin{aligned} Q_{\boldsymbol{\mu}, \boldsymbol{\mu}'} &= \frac{1}{p_{N_A}} \sum_{\boldsymbol{\nu}, \boldsymbol{\nu}'} \int_B \mathrm{d}\boldsymbol{R}_B\, \bar{\mathcal{F}}_{\boldsymbol{\nu}}^{\boldsymbol{\mu}}(\boldsymbol{R}_B) \mathcal{F}_{\boldsymbol{\nu}'}^{\boldsymbol{\mu}'}(\boldsymbol{R}_B) \\ \mathcal{F}_{\boldsymbol{\nu}}^{\boldsymbol{\mu}}(\boldsymbol{R}_B) &= \epsilon_{\boldsymbol{\mu}\boldsymbol{\nu}} c_{\langle \boldsymbol{\mu}; \boldsymbol{\nu} \rangle} \mathcal{M}_{\boldsymbol{\nu}}(\boldsymbol{R}_B) \end{aligned} \tag{7.10}$$

This integral contains the overlaps between the angular momentum states which are restricted in B subsystem. As mentioned before, overlap between single particle momentum orbitals in subsystem B is non-zero only when they have same angular momentum. Hence, only those ordered sets $\boldsymbol{\nu}, \boldsymbol{\nu}'$ contribute in the sum in Eq. (7.1) which have identical set of angular momentum quantum numbers. Note that the LL-indices need not be the same. The matrix Q in Eq. (7.10) can be numerically computed by summing over such ordered sets $\boldsymbol{\nu}$ and $\boldsymbol{\nu}'$.

The reduced density matrix ρ_{N_A} is block-diagonal in angular momentum. Its L_z^A-sectors, represented as ρ_{N_A,L_z^A} is

$$\rho_{N_A,L_z^A}(\boldsymbol{R}_A^{'}, \boldsymbol{R}_A) = \sum_{\boldsymbol{\mu},\boldsymbol{\mu}'}{}^{'} \overline{\mathcal{M}}_{\boldsymbol{\mu}}(\boldsymbol{R}_A) Q_{\boldsymbol{\mu},\boldsymbol{\mu}'} \mathcal{M}_{\boldsymbol{\mu}'}(\boldsymbol{R}_A^{'}). \tag{7.11}$$

where we the restricted sum is over ordered sets $\boldsymbol{\mu}$, $\boldsymbol{\mu}'$ of size N_A which have the correct total angular momentum *i.e.* $L_z(\boldsymbol{\mu}) = L_z(\boldsymbol{\mu}') = L_z^A$. As the Slater determinant states $\mathcal{M}_{\boldsymbol{\mu}}$s span the entire Hilbert space of A-subsystem, any eigenvector χ of ρ_{N_A} with eigenvalue k can be written as following linear combination

$$\chi(\boldsymbol{R}_A) = \sum_{\boldsymbol{\mu}} a_{\boldsymbol{\mu}} \mathcal{M}_{\boldsymbol{\mu}}(\boldsymbol{R}_A) \tag{7.12}$$

where the basis $\mathcal{M}_{\boldsymbol{\mu}}$s are generally not orthogonal if they contain states from higher LLs ($n > 1$). Using the eigenvalue equation, given by

$$\int_A \mathrm{d}\boldsymbol{R}_A \, \rho_{N_A}(\boldsymbol{R}_A, \boldsymbol{R}_A^{'}) \chi(\boldsymbol{R}_A) = k\chi(\boldsymbol{R}_A^{'}) \tag{7.13}$$

and Eq. (7.12), it can be shown that a matrix M can be constructed such that it has same set of non-zero eigenvalues as that of ρ_{N_A}, where $M = QP$ where Q is defined in Eq. (7.10) and P is given by

$$P_{\boldsymbol{\mu},\boldsymbol{\mu}'} = \int_A \mathrm{d}\boldsymbol{R}_A \, \overline{\mathcal{M}}_{\boldsymbol{\mu}}(\boldsymbol{R}_A) \mathcal{M}_{\boldsymbol{\mu}'}(\boldsymbol{R}_A) \tag{7.14}$$

which is the overlap matrix (inside A) for EWFs, which can be computed using accurate numerical integration.

The method allows exact computation of RSES for ED eigenstates of various parent QH Hamiltonians where particles are allowed to occupy different LLs [31, 47, 54, 97]. Exponential growth of dimension restricts the usage of this method to only smaller systems ($N \lesssim 10$). Nonetheless, having exact RSES at disposal allows us to benchmark the MC method. In the next section, we discuss an efficient RSES computation method based on the Monte Carlo technique.

7.2 RSES using Entanglement Wavefunctions

Many FQH phases are described by wavefucntions which have a product-of-Slater-determinants form, for instance, the Jain CF states [39] and the partonic QH states [41]. An efficient algorithm for RSES computation has already been studied for such QH states, using Monte Carlo method in Ref. [65]. In this section we present a brief overview of the method for unprojected CF states first followed by description of strategies to deal with projected states.

7.2.1 RSES of unprojected CF states

The unprojected CF state for N-particles at filling fraction $\nu = n/(np+1)$ has the form

$$\psi^{\text{unproj}}_{n/(np+1)}(\boldsymbol{R}) = [\Phi_1(\boldsymbol{R})]^p \, \Phi_n(\boldsymbol{R}) \tag{7.15}$$

where Φ_n is a Slater determinant state where N particles completely fill n LLs. As before, we assume a rotationally symmetric cut in real space which restricts N_A particles in region A and $N_B = N - N_A$ in the B region. Using Eq. (7.8), one can rewrite the state as

$$\psi^{\text{unproj}}_{n/(np+1)}(\boldsymbol{R}) = \text{anti} \sum_{\vec{\boldsymbol{\mu}},\vec{\boldsymbol{\nu}}} s\left(\vec{\boldsymbol{\mu}};\vec{\boldsymbol{\nu}}\right) \xi^A_{\vec{\boldsymbol{\mu}}}(\boldsymbol{R}_A) \xi^B_{\vec{\boldsymbol{\nu}}}(\boldsymbol{R}_B) \tag{7.16}$$

where $\vec{\boldsymbol{\mu}}$ and $\vec{\boldsymbol{\nu}}$ are collections of $p+1$ ordered sets of orbitals $\vec{\boldsymbol{\mu}} = \left(\boldsymbol{\mu}_1, \dots, \boldsymbol{\mu}_p, \boldsymbol{\mu}^*\right)$ and $\vec{\boldsymbol{\nu}} = (\boldsymbol{\nu}_1, \dots, \boldsymbol{\nu}_p, \boldsymbol{\nu}^*)$. Here $\boldsymbol{\mu}_i$ and $\boldsymbol{\nu}_i$ (for each $i = 1, \dots, p$) are disjoint ordered sets of orbitals, of length N_A and N_B respectively, containing single particle orbitals from the Slater determinant Φ_1. Similarly, $\boldsymbol{\mu}^*$ and $\boldsymbol{\nu}^*$ are disjoint ordered sets of lengths N_A and N_B made of occupied single-particle orbitals from Φ_n. Integer valued combinatorical factors $s\left(\vec{\boldsymbol{\mu}};\vec{\boldsymbol{\nu}}\right)$ arise from considering the signs in Eq. 7.8. The entanglement wavefunctions (EWFs) $\xi^A_{\vec{\boldsymbol{\mu}}}$ and $\xi^B_{\vec{\boldsymbol{\nu}}}$ are defined as

$$\begin{aligned} \xi^A_{\vec{\boldsymbol{\mu}}}(\boldsymbol{R}_A) =& \mathcal{M}^A_{\boldsymbol{\mu}^*}(\boldsymbol{R}_A) \prod_{i=1}^{p} \mathcal{M}^A_{\boldsymbol{\mu}_i}(\boldsymbol{R}_A) \\ \xi^B_{\vec{\boldsymbol{\nu}}}(\boldsymbol{R}_B) =& \mathcal{M}^B_{\boldsymbol{\nu}^*}(\boldsymbol{R}_B) \prod_{i=1}^{p} \mathcal{M}^B_{\boldsymbol{\nu}_i}(\boldsymbol{R}_B) \end{aligned} \tag{7.17}$$

where $\mathcal{M}^A_{\boldsymbol{\mu}}$ and $\mathcal{M}^B_{\boldsymbol{\nu}}$ are the Slater determinants where the set of orbitals $\boldsymbol{\mu}$ and $\boldsymbol{\nu}$ are occupied by the particles in A and B.

The reduced density matrix of A is block diagonal with each block characterized by (N_A, N_B) values. Calculation of a specific block

$$\rho_{N_A} = \text{Tr}_B \mathcal{P}_{N_A N_B} |\psi^{\text{unproj}}_{n/(np+1)}\rangle\langle\psi^{\text{unproj}}_{n/(np+1)}| \mathcal{P}_{N_A N_B} \tag{7.18}$$

involves projecting the state into a sector where first N_A particles are inside A subsystem and N_B are in B. The operator $\mathcal{P}_{N_A N_B}$ represents this projection. The projected state is

$$\mathcal{P}_{N_A N_B}\psi^{\text{unproj}}_{n/(np+1)}(\boldsymbol{R}) = \sum_{\vec{\boldsymbol{\mu}},\vec{\boldsymbol{\nu}}} s\left(\vec{\boldsymbol{\mu}};\vec{\boldsymbol{\nu}}\right) \xi^A_{\vec{\boldsymbol{\mu}}}(\boldsymbol{R}_A)\xi^B_{\vec{\boldsymbol{\nu}}}(\boldsymbol{R}_B) \tag{7.19}$$

Using Eq. (7.17), Eq. (7.19) and Eq. (7.18) one can write the reduced density matrix for subsystem A with N_A as

$$\rho_{N_A} = \sum_{\substack{\vec{\boldsymbol{\mu}},\vec{\boldsymbol{\nu}}\\ \vec{\boldsymbol{\mu}}',\vec{\boldsymbol{\nu}}'}} s(\vec{\boldsymbol{\mu}};\vec{\boldsymbol{\nu}})s(\vec{\boldsymbol{\mu}}';\vec{\boldsymbol{\nu}}') \left|\xi^A_{\vec{\boldsymbol{\mu}}}\right\rangle \left\langle\xi^B_{\vec{\boldsymbol{\nu}}'}\right| \left.\xi^B_{\vec{\boldsymbol{\nu}}}\right\rangle \left\langle\xi^A_{\vec{\boldsymbol{\mu}}'}\right| \tag{7.20}$$

It can be shown that the non-zero eigenvalues of ρ_{N_A} is same as that of a matrix M given by

$$M_{\vec{\boldsymbol{\mu}},\vec{\boldsymbol{\nu}}} = \sum_{\vec{\boldsymbol{\alpha}},\vec{\boldsymbol{\beta}}} s(\vec{\boldsymbol{\alpha}};\vec{\boldsymbol{\beta}})s(\vec{\boldsymbol{\mu}};\vec{\boldsymbol{\nu}}) \left\langle\xi^A_{\vec{\boldsymbol{\alpha}}}\right| \left.\xi^A_{\vec{\boldsymbol{\mu}}}\right\rangle \left\langle\xi^B_{\vec{\boldsymbol{\beta}}}\right| \left.\xi^B_{\vec{\boldsymbol{\nu}}}\right\rangle \tag{7.21}$$

Note that the overlaps of EWFs appearing here are computed inside their respective subsystems A and B. We can find eigenvalues of an L^A_z sector of ρ_{N_A} by using only those EWFs which have angular momentum equal to L^A_z, in Eq. (7.20). For every N_A, there is a smallest possible relative momentum L^A_{z0} for the N_A particles inside A. In the remaining text, L^A_z will represent the angular momentum of an EWF ξ^A relative to L^A_{z0}.

For small systems, these overlap matrices can be computed exactly for both unprojected and projected CF states. For large systems, Monte Carlo methods are used to compute RSES for unprojected states.

In following two sections, we describe RSES computation for the cases of exact projection, and approximate projection using Monte Carlo methods, respectively.

7.2.2 RSES for Exactly Projected CF states

The methods described in Sec. 7.2 can be used to calculate the RSES of the projected CF states as well:

$$\psi^{\text{proj}}_{n/(np+1)}(\boldsymbol{R}) = \text{anti}\sum_{\vec{\boldsymbol{\mu}},\vec{\boldsymbol{\nu}}} s\left(\vec{\boldsymbol{\mu}};\vec{\boldsymbol{\nu}}\right) [\mathcal{P}_{\text{LLL}}\xi^A_{\vec{\boldsymbol{\mu}}}(\boldsymbol{R}_A)][\mathcal{P}_{\text{LLL}}\xi^B_{\vec{\boldsymbol{\nu}}}(\boldsymbol{R}_B)] \tag{7.22}$$

which imply that the only change needed is that EWFs in Eq. 7.17 should now be projected to the LLL:

$$\mathcal{P}_{\text{LLL}}\, \mathcal{M}_{\boldsymbol{\mu}^*}(\boldsymbol{R})\, [\mathcal{M}_{\boldsymbol{\mu}}(\boldsymbol{R})]^p \tag{7.23}$$

where $\mathcal{P}_{\text{LLL}}$ represents the LLL projection. Note that the results so far are exact. The exact RSES can be calculated if the LLL projection can be implemented exactly and if the matrix M (Eq. 7.21) is exactly computed.

In the above expression, the ordered set $\boldsymbol{\mu}^*$ may contain orbitals from higher LLs whereas

$\boldsymbol{\mu}$ contains orbitals in the LLL only. Exact LLL projection is implemented by elevating the Slater determinant $\mathcal{M}_{\boldsymbol{\mu}^*}$ to an operator $\widehat{\mathcal{M}}_{\boldsymbol{\mu}^*}$ which acts on $[\mathcal{M}_{\boldsymbol{\mu}}]^p$. The operator $\widehat{\mathcal{M}}_{\boldsymbol{\mu}^*}$ is constructed by replacing each single particle orbitals ϕ_{μ^*} in the determinant $\mathcal{M}^*_{\boldsymbol{\mu}}$ with an operator $\hat{\phi}_{\mu^*}$ [4] that acts on LLL single particle orbitals as defined below. In the spherical geometry, where the single particle orbitals are Y_{Qnm} (Eq. (7.1)), the operator that replaces this, acts on a LLL state $Y_{Q'0m'}$ as

$$\widehat{Y}^{Q'}_{Qnm} = \mathcal{N}_{QQ'} :: Y_{Qnm}\left(\bar{u} \rightarrow \partial_u, \bar{v} \rightarrow \partial_v\right) :: \tag{7.24}$$

where :: Y :: represents a normal ordering where all $\bar{u}$ and $\bar{v}$ are moved to extreme right before replacing them with the corresponding derivatives. The coefficient $\mathcal{N}_{QQ'}$ is given by $\frac{2(Q+Q')+1}{2(Q+Q')+n+1}$.

It is computationally difficult to evaluate the projected state for large enough systems to perform the comparisons that we intend to do. Hence, we will consider the simplest non-trivial case namely that of $n = 2, p = 1$ which corresponds to a bosonic Jain state at filling fraction 2/3. The EWFs (Eq. (7.17)) for this state can be written as

$$\begin{aligned}
\xi^A_{\vec{\boldsymbol{\mu}}}(\boldsymbol{R}_A) =& \widehat{\mathcal{M}}^A_{\boldsymbol{\mu}^*}(\boldsymbol{R}_A)\mathcal{M}^A_{\boldsymbol{\mu}_1}(\boldsymbol{R}_A) \\
\xi^B_{\vec{\boldsymbol{\nu}}}(\boldsymbol{R}_B) =& \widehat{\mathcal{M}}^B_{\boldsymbol{\nu}^*}(\boldsymbol{R}_B)\mathcal{M}^B_{\boldsymbol{\nu}_1}(\boldsymbol{R}_B)
\end{aligned} \tag{7.25}$$

where the ordered sets $\boldsymbol{\mu}^*$ and $\boldsymbol{\mu}_1$ are N_A-sized subsets of orbitals in $\hat{\Phi}_2$ and Φ_1 respectively. Similarly, $\boldsymbol{\nu}^*$ and $\boldsymbol{\nu}_1$ are N_B-sized complements of subsets $\boldsymbol{\mu}^*$ and $\boldsymbol{\mu}_1$ respectively. The action of the operators $\hat{\phi}_{\mu_i^*}(\boldsymbol{r}_i)$ a LLL state $\phi_{\mu_{1,i}}(\boldsymbol{r}_i)$, shown in Eq. (7.24), can be written as

$$\begin{aligned}
\hat{\phi}_{\mu_i^*}\phi_{\mu_{1,i}} \equiv \hat{Y}^{Q'}_{Qn_im_i}Y_{Q'0m_i'} = \\
= F(Q, Q', n_i, m_i, m_i^{'})Y_{Q+Q',0,m_i+m_i'} \equiv F(\mu_i^*, \mu_{1,i})\phi_{\gamma_i}
\end{aligned} \tag{7.26}$$

where the coefficient $F(\mu_i^*, \mu_{1,i})$ for spherical geometry is given in Sec. 7.2.3. The projected EWFs can be conveniently expanded in terms of symmetric many particle states given by

$$\begin{aligned}
\widehat{\mathcal{M}}^A_{\boldsymbol{\alpha}}(\boldsymbol{R}_A)\mathcal{M}^A_{\boldsymbol{\beta}}(\boldsymbol{R}_A) &= \frac{1}{N_A!}\sum_{P,Q\in\mathcal{S}_{N_A}}(-1)^{PQ}\prod_{i=1}^{N_A}\hat{\phi}_{\alpha_{P(i)}}(\boldsymbol{r}_i)\phi_{\beta_{Q(i)}}(\boldsymbol{r}_i) \\
&= \frac{1}{N_A!}\sum_{P\in\mathcal{S}_{N_A}}(-1)^{P}\left[\prod_{i=1}^{N_A}F(\alpha(P)_i, \beta_i)\right]\text{sym}\left(\phi_{\gamma(P)_1}(\boldsymbol{r}_1)\dots\phi_{\gamma(P)_{N_A}}(\boldsymbol{r}_{N_A})\right)
\end{aligned} \tag{7.27}$$

where $\phi_{\boldsymbol{\gamma}(P)_i}$ represents the state obtained from $\hat{\phi}_{\alpha_{P(i)}}\phi_{\beta_i}$ as shown in Eq. (7.2.2). The symmetrization is defined as

$$\text{sym}\left(\phi_{\lambda_1}(\boldsymbol{r}_1)\dots\phi_{\lambda_{N_A}}(\boldsymbol{r}_{N_A})\right) = \sum_{P\in S_{N_A}}\prod_i \phi_{\gamma_i}(\boldsymbol{r}_{P(i)}) \tag{7.28}$$

We can expand all EWFs as linear combinations of orthogonal symmetrized basis states using Eq. (7.27). Using these, we can exactly compute matrix M (Eq. (7.21)), without using Monte Carlo methods as we obtain the EWFs as an expansion in orthogonal states. Eigenvalues of M give the numerically exact RSES for the LLL projected $\psi_{2/3}$.

Exact projection can be performed on EWFs with $N_{A,B} \sim 12$ allowing calculation of exact RSES of the projected 2/3 state in systems of sizes upto $N = N_A + N_B \sim 24$ particles. We will now discuss possible approximations to the LLL projection of the EWFs which can be used instead of the exact projection. We will first discuss the Jain Kamila projection for the 2/3rd state to motivate the approximations used.

7.2.3 Coefficients for exact projection of 2/3 state on sphere

We saw in Sec. 7.2.2, computing the exact projection of bosonic 2/3 CF state requires calculation of coefficients $F(\alpha,\beta)$ arising when performing LLL projection on product of single particle orbitals:

$$\mathcal{P}\phi_\alpha(\boldsymbol{r})\phi_\beta(\boldsymbol{r}) = F(\alpha,\beta)\phi_\gamma(\boldsymbol{r}) \tag{7.29}$$

Here ϕ_β and ϕ_γ are LLL orbitals whereas ϕ_α might occupy any arbitrary LL. For spherical geometry, Landau orbitals are represented by monopole harmonics $Y_{Q,n,m}(u,v)$ [32, 33, 31]. On the sphere, LHS of Eq. (7.29) can be written as

$$\mathcal{P}Y_{Q,n,m}(u,v)Y_{Q',0,m'}(u,v) = \hat{Y}_{Q,n,m}(u,v)Y_{Q',0,m'}(u,v) \tag{7.30}$$

where the operator $\hat{Y}_{Q,n,m}(u,v)$ is defined in Eq. (7.24). Explicit expansion of the above expression produces a LLL orbital upto a proportionality constant:

$$\hat{Y}_{Q,n,m}(u,v)Y_{Q',0,m'}(u,v) = F(Q,Q',n,m,m')Y_{Q+Q',0,m+m'}(u,v) \tag{7.31}$$

where the coefficients $F(\alpha,\beta) \equiv F(Q,Q',n,m,m')$ are defined as

$$F(Q,Q',n,m,m') = \\ \begin{cases} \frac{N^{LLL}_{Q,m}N^{LLL}_{Q',m'}}{N^{LLL}_{Q+Q',m+m'}} & n=0 \\ -\frac{(2(Q+Q')+1)!}{(2(Q+Q')+2)!}\frac{N_{Q,n,m}N^{LLL}_{Q',m'}}{N^{LLL}_{Q+Q',m+m'}}\left(\binom{2Q+1}{Q-m+2}(Q'-m') - \binom{2Q+1}{Q+1-m}(Q'+m')\right) & n=1 \end{cases}$$

where normalization $N_{Q,n,m}$ is defined in Eq. (7.1) and normalization for state in LLL, $N^{LLL}_{Q,m}$, is given as

$$N^{LLL}_{Q,m} = N_{Q,0,m} \times \binom{2Q}{Q+m} \tag{7.32}$$

7.2.4 Jain-Kamilla projection

The LLL projected 2/3 state can be evaluated in an approximate way as $\frac{1}{\Phi_1}\mathcal{P}\psi_{\frac{2}{5}}$. The LLL projected Jain state at filling fraction 2/5 can be evaluated, again in an approximate way, using Jain Kamilla (JK) projection [99]. The latter is computationally efficient and has been found to work well in variational studies [4]. The LLL projected EWFs can be approximated in a similar manner. We give a short summary of the JK projection for the 2/5 state first.

The CF state at filling fraction 2/5 is given by

$$\mathcal{P}\,\Phi_2(\boldsymbol{R})\;[\Phi_1(\boldsymbol{R})]^2 = \hat{\Phi}_2(\boldsymbol{R})[\Phi_1(\boldsymbol{R})]^2 \tag{7.33}$$

which can be evaluated exactly by elevating the first factor to an operator as described Sec. 7.2.2 but evaluating this explicitly is computationally expensive.

In the discussion below, we will only assume that Φ_2 is a Slater determinant where particles occupy at most two Landau levels but not necessarily fully. Φ_1 corresponds to LLL fully occupied by N particles. $[\Phi_1(\boldsymbol{R})]^2$ appearing in the wavefunction above can be rewritten as

$$[\Phi_1(\boldsymbol{R})]^2 = c\prod_i^N J_i, \tag{7.34}$$

where $J_i = \prod_{k\neq i}^N (u_i v_k - u_k v_i)$ and c is some constant. With this, the unprojected CF state can be rewritten as

$$\begin{aligned}\psi_{2/5}^{\text{unproj}}(\boldsymbol{R}) =& \Phi_2(\boldsymbol{R})\;[\Phi_1(\boldsymbol{R})]^2 = c\text{Det}\left[Y_i(\Omega_j)\right]\prod_i J_i,\\ =& c\text{Det}\left[Y_i(\Omega_j)J_j\right].\end{aligned} \tag{7.35}$$

where $\{Y_i(\Omega_j)\}$ represents the single particle orbitals in the Slater determinant Φ_2. The JK projection approximates the projection of this determinant as follows

$$\mathcal{P}\text{Det}\left[Y_i(\Omega_j)J_j\right] \approx \text{Det}\left[\mathcal{P}Y_i(\Omega_j)J_j\right] = \text{Det}\left[\hat{Y}_i(\Omega_j)J_j\right] \tag{7.36}$$

where $\hat{Y}_i$'s are the operators defined in Eq. (7.24). This can be simplified further by defining $\tilde{Y}$ as

$$J_j\tilde{Y}_i = \hat{Y}_i(\Omega_j)J_j. \tag{7.37}$$

For the case, where Φ_2 contains at most two lowest LLs (sufficient for our discussion), $\tilde{Y}_i$ can be shown to have the same form as Eq. (7.24), but with the derivatives ∂_u, ∂_v in $\hat{Y}_i(\Omega_j)$ replaced as follows:

$$\partial_{u_j} \to \sum_{k\neq j}\frac{v_k}{u_j v_k - v_j u_k},$$

$$\partial_{v_j} \to \sum_{k\neq j} \frac{-u_k}{u_j v_k - v_j u_k}. \tag{7.38}$$

In summary, putting Eq. 7.37 and Eq. 7.36 together, the projected state can be approximated as

$$\hat{\Phi}_2 \left[\Phi_1(\boldsymbol{R})\right]^2 \approx \left[\Phi_1(\boldsymbol{R})\right]^2 \mathrm{Det}\left[\tilde{Y}_i(\Omega_j)\right] \tag{7.39}$$

7.2.5 Approximate projection for Monte Carlo method

The JK approximation relied on the possibility of writing the Jastrow Slater determinant Φ_1 as a product of J_i (Eq. 7.34). The Slater determinants $\mathcal{M}^A_{\mu_1}, \mathcal{M}^B_{\mu_1}$ appearing in the EWFs (Eq. 7.25) do not have the same form as Φ_1. We discuss an approximation similar in spirit to the JK projection but which applies to the EWFs.

The EWFs occuring in the case of the RSES calculations of the projected 2/3rd state (Eq. (7.25)) can be written as

$$\xi^A = \mathcal{P}\mathcal{M}^A_{\boldsymbol{\alpha}}\mathcal{M}^A_{\boldsymbol{\beta}} = \widehat{\mathcal{M}}^A_{\boldsymbol{\alpha}}\mathcal{M}^A_{\boldsymbol{\beta}}. \tag{7.40}$$

The state $\mathcal{M}^A_{\boldsymbol{\beta}}$ is a Slater determinant of LLL orbitals:

$$\mathcal{M}^A_{\boldsymbol{\beta}} = c \times \mathrm{anti}[\prod_{i=1}^{N_A}(u_i^{q+m_i} v_i^{q-m_i})] \tag{7.41}$$

where c is a constant, $q = (N-1)/2$, m_i are the angular momenta of the single particle orbitals occupied inside $\mathcal{M}^A_{\boldsymbol{\beta}}$. Factorizing out $\prod_i u_i^{2q}$, defining $z = u/v$, and using the definition of Schur polynomial we get

$$\mathcal{M}^A_{\boldsymbol{\beta}} = c \times \prod_{i<j=1}^{N_A}(z_i - z_j) \times s(\{z_i\}) \times \prod_{i=1}^{N_A} u_i^{2q} \tag{7.42}$$

where s is some Schur polynomial determined by $\boldsymbol{\beta}$ and which has a small degree $\Delta \sim L^A_z$ relative to N_A. Rewriting z in terms of u, v we get

$$\mathcal{M}^A_{\boldsymbol{\beta}} = \Phi^A_1 f^A_{\boldsymbol{\beta}} \prod_{i=1}^{N_A} u_i^{N-N_A-\Delta} \tag{7.43}$$

where

$$\Phi^A_1 = \prod_{i=1}^{N_A}\prod_{j=i+1}^{N_A}(u_i v_j - u_j v_i). \tag{7.44}$$

The function f is a polynomial in u, v of degree Δ.

We can approximate the projected state, just as we did in the case of JK projection for

2/3 state:

$$\xi^A \approx \frac{1}{\Phi_1^A}\widehat{\mathcal{M}}_{\boldsymbol{\alpha}}^A[\Phi_1^A]^2 f_{\boldsymbol{\beta}}^A \prod_{i=1}^{N_A} u_i^{N-N_A-\Delta} \tag{7.45}$$

Since f has a small degree relative to other factors, we can ignore the action of the derivatives inside $\mathcal{M}_{\boldsymbol{\alpha}}^A$ on f.

Decomposing $[\phi_1^A]^2$ just as in the case of JK projection in terms of products of $J_i = \prod_{k=1,k\neq i}^{N_A}(u_i v_k - u_k v_i)$, we can make approximations similar to that in Eq. (7.36). The result is that we can replace the derivatives in $\widehat{\mathcal{M}}_{\boldsymbol{\alpha}}^A$ with the following

$$\begin{aligned}\partial_{u_j} &\rightarrow \frac{N-N_A}{u_j} + \sum_{k\neq j}\frac{v_k}{u_j v_k - v_j u_k},\\ \partial_{v_j} &\rightarrow \sum_{k\neq j}\frac{-u_k}{u_j v_k - v_j u_k}.\end{aligned} \tag{7.46}$$

which is a modification of the prescription given in Eq. 7.38.

Similar approximations when made on ξ^B result in the following prescription

$$\begin{aligned}\partial_{u_j} &\rightarrow \sum_{k\neq j}\frac{v_k}{u_j v_k - v_j u_k},\\ \partial_{v_j} &\rightarrow \frac{N-N_B}{v_j} + \sum_{k\neq j}\frac{-u_k}{u_j v_k - v_j u_k}.\end{aligned} \tag{7.47}$$

In the above expressions, we have approximated $N - \Delta \approx N$. The additional factors appearing in the above prescription relative to the JK case (Eq. (7.38)) are associated with the fact that ξ^A and ξ^B have particles occupying only one hemisphere. The large multiplicative factors of $\prod_i u_i$ and $\prod_i v_i$ in ξ^A and ξ^B ensure that the net wavefunction is still in the LLL Hilbert space, in spite of the reciprocal terms $1/u_i$ and $1/v_i$.

The sequence of approximations made here is in spirit similar to the JK projection which do produce reliable results in variational studies in the context of energetics. Nevertheless, the approximations here go beyond JK projection and are being used in the context of RSES. Approximate projections can generate spurious effects such as destroy linear dependencies of trial functions, [102] which could in general change the counting of RSES. Therefore these calculations based on such approximations need quantitative comparisons with exact answers, which we do in the following section.

We consider other related, plausible approximations as well as results of the RSES calculated using them in Sec. 7.3.4. These produce results that show less agreement with the exact RSES. One of these is methods is to define the projected EWFs by simply replacing the derivatives using Eq. 7.38. Note that when this is plugged into the right handside of EWF expansion (Eq. 7.25), this is not yield the JK projected CF state.

7.3 Numerical Results

In this section we present the numerical results comparing the RSES computed using different methods. To help keep track of which methods are being compared, we list them here

1. For RSES of the unprojected state obtained by using the Slater determinant expansion of the ground state of the TK Hamiltonian (Sec. 7.1), we use the name "unproj ED" in the figures.
2. For RSES of the projected state obtained by using the Slater determinant expansion of the LLL projected ground state of the TK Hamiltonian (Sec. 7.1), we use the name "proj ED" in the figures.
3. For RSES of the unprojected state obtained by using Monte Carlo integrations of the unprojected EWFs (Sec. 7.2.1), we use the name "unproj EWF MC " in the figures.
4. For RSES of the projected state obtained by using exact projection of the EWFs as described in Sec. 7.2.2, we use the name "exact proj EWF" in the figures.
5. For RSES of the projected state obtained by using approximate projection (Sec. 7.2.5), we use the name "approx proj EWF MC" in the figures.

7.3.1 Exact results using EWFs method

In this section, we demonstrate that methods using EWFs indeed produce exact results. This is expected as there were no approximations made in the scheme.

Figure 7.2 shows the RSES for unprojected (left panel) and projected (right panel) 2/5 CF state with $N = 8$ and $N_A = 4$. The RSES is computed using two methods. We use the method described in Sec. 7.1 to compute the exact RSES of the ground state of the TK Hamiltonian obtained from ED. The second method uses MC integrations as described in Sec. 7.2. As shown in the left panel, both methods produce exactly identical RSES. Note that the Monte Carlo method introduces an overall vertical shift in the RSES. We fix the shift by aligning both RSES such that lowest eigenvalue in the $L_z^A = 0$ sector is equal to zero. The MC method costs a tiny fraction of the computational time and can be extended to 100s of particles (even at this large system size, the bottleneck is not the computational time but the numerical precision of the wavefunction evaluations).

In the right panel of Fig. 7.2, we present the RSES for the projected 2/5 state. Exact results are obtained by using the method in Sec. 7.1 on the LLL projection of the ground state of the TK Hamiltonian. Secondly, we compute the RSES by exactly projecting the EWFs for the 2/5 CF state, as described in Sec. 7.2.2. As shown in the Fig. 7.2, since projection of the EWFs can be performed exactly, the second method produces

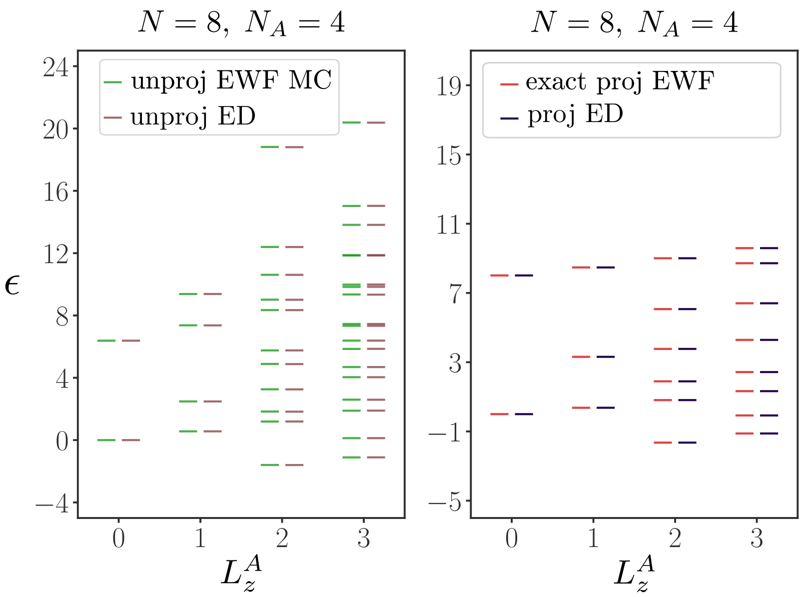

Figure 7.2: RSES for the unprojected (left panel) and projected (right panel) 2/5 CF state, for $N = 8$ and $N_A = 4$. The left panel compares the RSES computed using methods in Sec. 7.1 which uses ED ground state of TK Hamiltonian (brown) and the Monte Carlo from Sec. 7.2.1 (green), in given L_z^A-sectors. For small L_z^A values, both methods produce identical RSES (modulo an overall shift). In the right panel, we compare the RSES of the exact projected 2/5 CF state computed using method in Sec. 7.2.2 (red) with that of projected ground state of TK Hamiltonain, which uses method given in Sec. 7.1 (yellow) for $N = 8$ and $N_A = 4$, in given L_z^A-sectors. Both methods produce identical RSES. All RSES are shifted so that the least entanglement energy at L_z^A is equal to zero.

exact results. Since computation of exact projection is feasible only for small number of particles, the methods work for small systems only.

7.3.2 Effect of projection on RSES

Here we compare the RSES of the projected and unprojected CF states in small systems, where we can obtain results exactly without any artifact from approximate projections. Calculation of exactly projected 2/5 CF state is not feasible for larger systems. However, exact projection can be extended to larger systems ($N \sim 24$) for the case of 2/3 CF state. We compare the RSES of the unprojected and (exact) projected CF state at 2/3 in Fig. 7.3. For the unprojected case we use a Monte Carlo method (which, as mentioned earlier, is practically exact) whereas exact RSES for the projected state is computed using the methods in Sec. 7.2.2. RSES pattern is different for even and odd values of N_A and we present the two largest system sizes for each.

We see the RSES for the projected state shows the same counting as that of the unprojected state, though the RSES of the projected states show larger spread in the eigenvalues compared to that of the unprojected states. The numbers above the panels show the

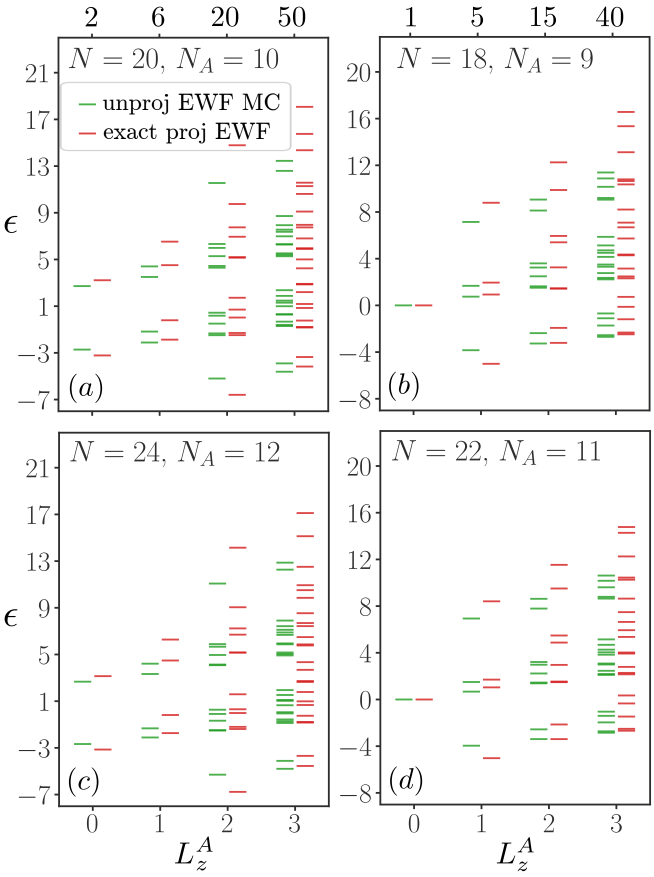

Figure 7.3: RSES for the unprojected (green) and exactly projected (red) bosonic 2/3 CF state. RSES for unprojected case is computed using Monte Carlo method from Sec. 7.2 whereas for exactly projected case, we use method presented in Sec. 7.2.2. RSES are shifted to make the mean entanglement energy equal to zero in $L_z^A = 0$ sector. (a) and (c) show the RSES for even N_A values, given by $N = 20$, $N_A = 10$ and $N = 24$, $N_A = 12$ respectively whereas (b) and (d) show the same for odd N_A values, given by $N = 18$, $N_A = 9$ and $N = 22$, $N_A = 11$ respectively. The numbers above the top axis of panel (a) and (b) represent the dimension of EWFs in each L_Z^A-sector for even and odd value of N_A, given the system is sufficiently large. Projected states have larger spread in the RSES for each L_z^A sectors compared to RSES of unprojected state but the counting remains the same.

number of EWFs in each L_z^A sector. The number of entanglement eigenvalues are smaller than that of the EWFs due to linear dependencies between them. The projection does not add further linear dependencies resulting in the same counting in both cases.

7.3.3 RSES from approximate projection of EWFs

In this section, we compare the exact RSES and the RSES obtained by approximating the LLL projection of the EWFs. As mentioned in the introduction, the comparison is not between RSES of exact projected CF state and RSES of the JK projected CF state - these two are likely to very similar to each other. The comparison is being made between the exact RSES and the RSES obtained after approximately projecting the EWFs.

Figure 7.4 shows the central result of this chapter comparing the RSES of exactly projected (Sec. 7.2.2) and approximately projected (Sec. 7.2.5) 2/3 CF state for small systems. To make the comparison easier, all RSES are shifted vertically to make mean entanglement energy in $L_z^A = 0$ sector equal to zero.

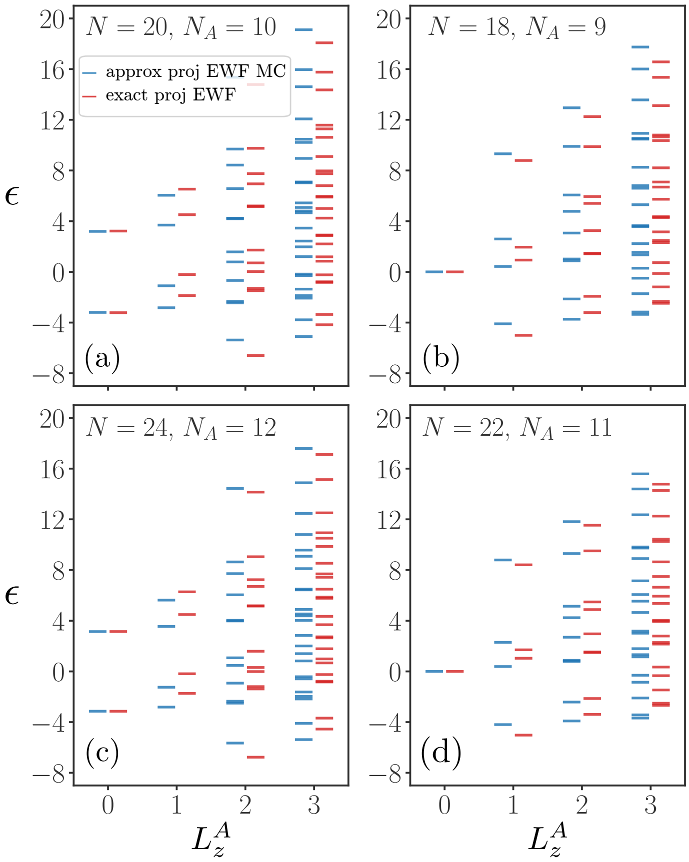

Figure 7.4: RSES for exactly projected (red) and approximately projected (blue) bosonic 2/3 CF state. RSES for the exactly projected state is compute using method in Sec. 7.2.2 and method in Sec. 7.2.5 is used for approximately projected state. Since even and odd N_A have different RSES pattern, we compare them separately. RSES in all L_z^A-sectors are shifted such that the mean entanglement energy at $L_z^A = 0$ is equal to zero. Panel (a) and (c) show RSES comparison for system sizes $N = 20$, $N_A = 10$ and $N = 24$, $N_A = 12$ respectively. Panels (b) and (d) show similar comparisons for system sizes $N = 18$, $N_A = 9$ and $N = 22$, $N_A = 11$ respectively.

Panels (a)-(d) in Fig. 7.4 present a side-by-side comparison of RSES for approximately projected and exactly projected 2/3 CF states for two largest systems where exact projection was feasible. Comparing the RSES for two different sizes, we see that the RSES for approximately projected state is close. Similar results were obtained even for smaller systems. Here too, the counting in different branches remain the same. It is noteworthy that the approximate projection does not destroy linear dependencies; this can be inferred from the identical counting in both cases.

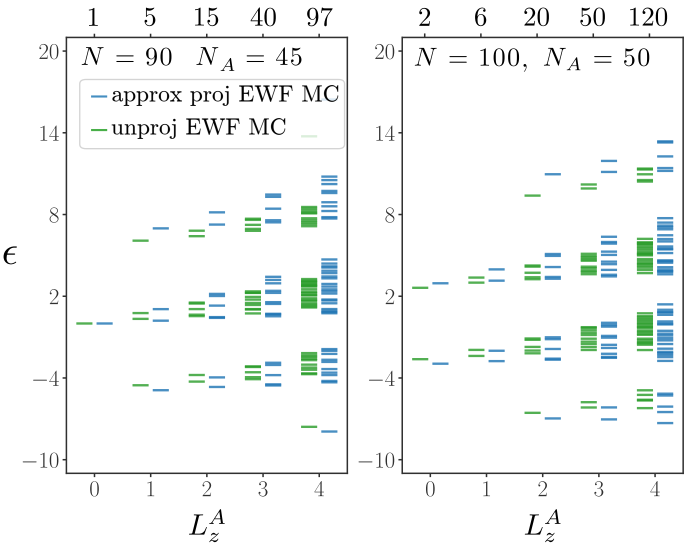

Figure 7.5: RSES for approximately projected (blue) and unprojected (green) bosonic 2/3 CF for system sizes $N = 90$, $N_A = 45$ (left) and $N = 100$, $N_A = 50$ (right). The RSES are shifted to make the mean entanglement energy in $L_z^A = 0$ sector equal to zero. We see that, except for a larger spread, RSES for the projected state is qualitatively identical to that of the unprojected state for large systems.

Finally, Fig. 7.5 shows the comparison between the unprojected and approximately projected 2/3 CF state for two large system sizes $N = 90$, $N_A = 45$ (left) and $N = 100$, $N_A = 50$ (right). Total number of EWFs in angular momentum-sectors given by $L_z^A = (0, 1, 2, 3, 4)$ for systems with even and odd N_A are $(2, 6, 20, 50, 120)$ and $(1, 5, 15, 40, 97)$ respectively. Although the RSES for the projected state has a larger spread as was observed in the case of smaller systems in Fig. 7.3, the branch structure is identical to that of the unprojected state. Qualitatively, the RSES of QH state does not change after projection.

7.3.4 Other approximations for LLL projection

In this section, we present the results comparing RSES of bosonic Jain 2/3 state computed using two different approximations for the LLL projection. First, we use the JK method given in Sec. 7.2.4, where LLL projection is equivalent to following replacement of derivatives

$$\begin{aligned} \partial_{u_j} &\rightarrow \sum_{k \neq j} \frac{v_k}{u_j v_k - v_j u_k}, \\ \partial_{v_j} &\rightarrow \sum_{k \neq j} \frac{-u_k}{u_j v_k - v_j u_k}. \end{aligned} \tag{7.48}$$

in all operators $\widehat{Y}_{Q,n,m}$, in Eq. (7.24). Fig. 7.6 shows the comparison of RSES generated using this method with that of the exactly projected state. Both RSES are shifted to make the mean entanglement energy in $L_z^A = 0$ sector equal to zero. Panel (a), (b) and (c) show the trend of entanglement energies for the two methods with increasing system size, in given L_z^A-sectors. We see, with increasing system size, both RSES appear to converge towards each other.

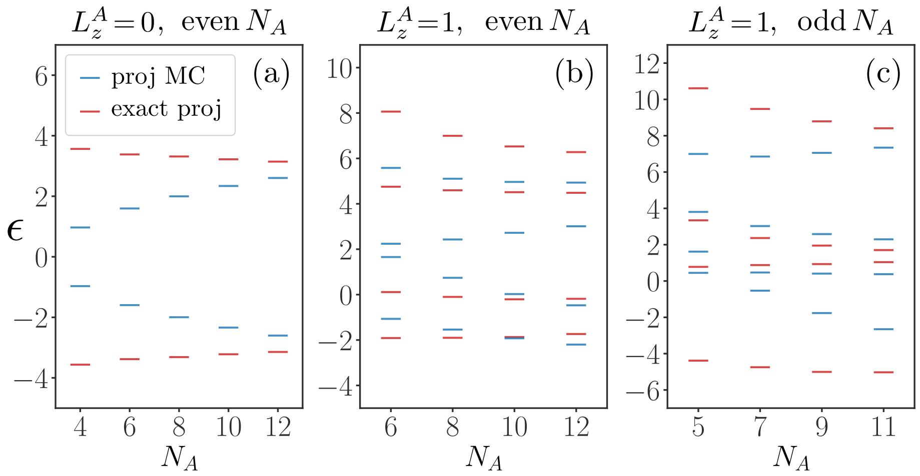

Figure 7.6: RSES for exactly projected (red) and approximately projected (blue) bosonic 2/3 CF state. RSES for the exactly projected state is compute using method in Sec. 7.2.2 and method in Sec. 7.2.5 is used for approximately projected state. Since even and odd N_A have different RSES pattern, we compare them separately. RSES in all L_z^A-sectors are shifted such that the mean entanglement energy at $L_z^A = 0$ is equal to zero. Panel (a) shows the comparison of RSES for exactly and approximately projected states in $L_z^A = 0$ sector. We see a clear convergence in RSES with N_A here. Comparison in $L_z^A = 0$ sector is trivial for odd N_A values as there is only one entanglement energy.

Panel $(d) - (g)$ of Fig. 7.7 show RSES comparison for fixed system size, each one for largest system sizes accessible for the exact projection. Compared to RSES (Fig. 7.4) of the approximation given in Sec. 7.2.5, we see larger mismatch with RSES of exactly projected state, which worsens in larger L_z^A-sectors. It is also apparent that the mismatch decreases with increasing system size.

For the second case, we approximate the projection of EWFs as

$$\xi^A = \mathcal{P}\mathcal{M}_{\boldsymbol{\alpha}}^A \mathcal{M}_{\boldsymbol{\beta}}^A = \widehat{\mathcal{M}}_{\boldsymbol{\alpha}}^A \mathcal{M}_{\boldsymbol{\beta}}^A \approx \frac{1}{\mathcal{M}_{\boldsymbol{\beta}}^A} \widehat{\mathcal{M}}_{\boldsymbol{\alpha}}^A [\mathcal{M}_{\boldsymbol{\beta}}^A]^2 \tag{7.49}$$

This approximation leads to following replacement of derivatives, given by

$$\begin{aligned} \partial_{u_j} &\rightarrow 2\frac{N - N_A}{u_j} + \sum_{k \neq j} \frac{v_k}{u_j v_k - v_j u_k}, \\ \partial_{v_j} &\rightarrow \sum_{k \neq j} \frac{-u_k}{u_j v_k - v_j u_k}. \end{aligned} \tag{7.50}$$

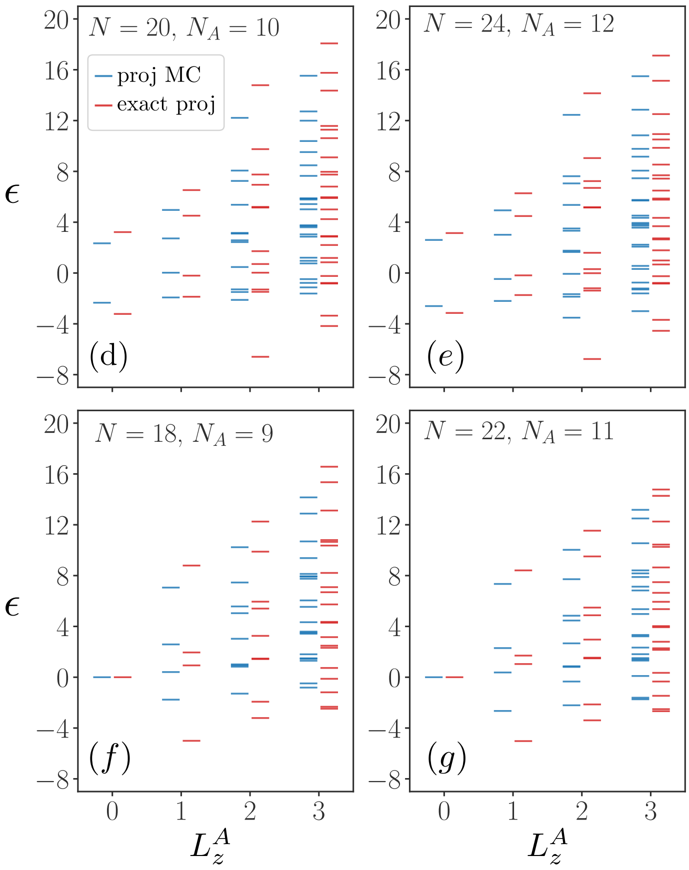

Figure 7.7: RSES for exactly projected (red) and approximately projected (blue) bosonic 2/3 CF state. Panel (d) and (e) show RSES comparison for system sizes $N = 20$, $N_A = 10$ and $N = 24$, $N_A = 12$ respectively. For same system size, RSES for approximately projected state has more spread compared to RSES of the exactly projected state. Panels (f) and (g) show similar comparisons for system sizes $N = 18$, $N_A = 9$ and $N = 22$, $N_A = 11$ respectively.

for A-subsection and for ξ^B, results in the following prescription

$$\begin{aligned}\partial_{u_j} &\to \sum_{k\neq j} \frac{v_k}{u_j v_k - v_j u_k},\\ \partial_{v_j} &\to 2\frac{N-N_B}{v_j} + \sum_{k\neq j} \frac{-u_k}{u_j v_k - v_j u_k}.\end{aligned} \tag{7.51}$$

Fig. 7.8 shows the similar comparison of resultant RSES with that of exactly projected Jain 2/3 state, for different system sizes. We notice that the RSES is significantly different than that of exactly projected state, with no clear entanglement gaps even in small L_z^A-sectors.

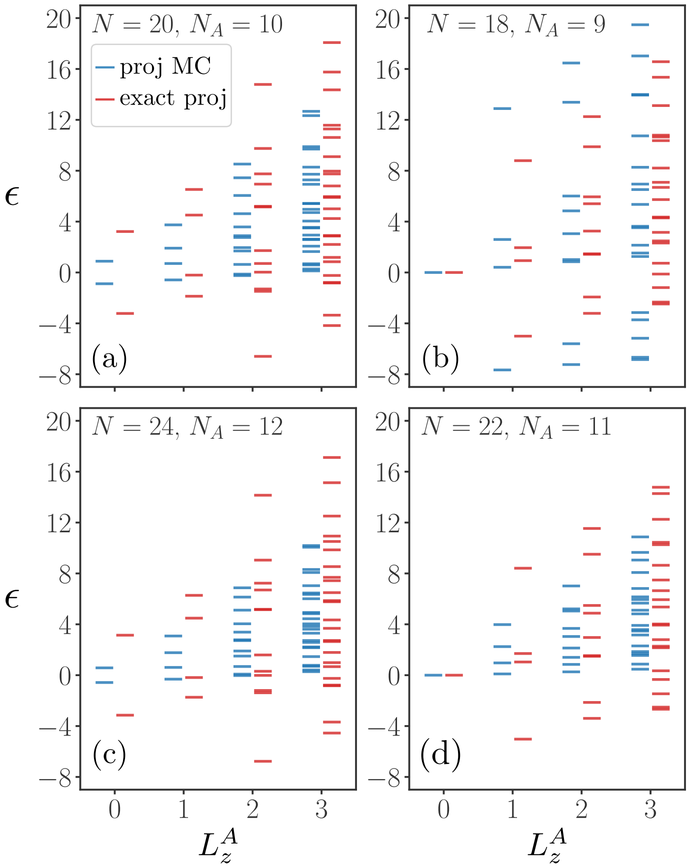

Figure 7.8: RSES for exactly projected (red) and approximately projected (blue) bosonic 2/3 CF state. RSES for the exactly projected state is compute using method in Sec. 7.2.2 and method in Sec. 7.2.5 is used for approximately projected state. Panel (*a*) and (*c*) show RSES comparison for system sizes $N = 20$, $N_A = 10$ and $N = 24$, $N_A = 12$ respectively. For same system size, RSES for approximately projected state has no clear entanglement gaps and does not look similar to the RSES of the exactly projected state. Panels (b) and (d) show similar comparisons for system sizes $N = 18$, $N_A = 9$ and $N = 22$, $N_A = 11$ respectively.

7.4 Conclusion

In this chapter, we carefully analyzed the Monte Carlo methods for RSES calculations. MC methods are useful to explore RSES of variational states in FQHE as they can be used to study much larger systems (upto 100 particles) than what is possible with any of the other methods (~ 10 particles). However when studying LLL projected CF states MC method needs adhoc approximations. This chapter attempts to address the question of the quality of these approximations. We present alternate methods with which exact RSES can be computed in small systems and we used them to benchmark the MC results.

The MC method proceeds by working with EWFs which are those states in individual subsystems which 'entangle' with the states in the complementary subsystem. These EWFs are far fewer in number when compared to the full dimension of the individual subsystems [102, 89, 65]. In case of Jain CF states and parton states [39, 41], EWFs can be explicitly written down due to the specific structure of these functions. MC method uses the fact that the density matrix can be compactly expressed in a basis of made of the EWFs. In particular the eigenvalues of the density matrix is determined by the overlap matrix of the EWFs.

Firstly, by comparing with the exact RSES of the unprojected Jain 2/5th state, we have shown that the MC method, using a fraction of a computational cost, produces practically exact results. Although this is expected, a quantitave verification is appealing. Comparison could be performed only in small systems, however we believe that the exact agreement extends to large systems as well.

Progress can be made in the case of the RSES of projected states provided that suitable approximation schemes can be devised. The EWFs have a structure different from the Jain states. It is not obvious that the naive application of the JK projection which works well in the Jain states would work for the EWFs. We present an approximation scheme for the EWFs that is in the spirit of the JK projection. In quantitative comparisons with the exact RSES of finite systems, the approximate method we presented works better than the one obtained by a naive application of the JK projection (see Sec. 7.3.4).

The approximate projection allows MC methods to be used in systems as large as 100 particles. We find that the RSES of the projected 2/3rd state is very close to that of the unprojected state. Independent of the quality of the approximations used for the projection, we find that the counting of the RSES states remain robust. These suggest that all these methods produce close to the correct projected state. Improved estimates of the RSES neverthelss can help in quantitative analysis of the scaling properties of the RSES.

Chapter 8

Conclusion

Several characteristic features of FQHE in the LLL cane be understood in terms of CF theory. In the first part of the thesis, we attempt to analyze a simplified model that abstracts some key features of the CF wavefunctions. Second part of the thesis deal with the study of RSES of parton states which generalizes the CF states.

The inverse problem of finding a parent Hamiltonian for LLL projected CF states has been a challenging one. Our attempt at solving this problem lead us to the model interaction presented in Ref. [103]. The model produces eigenstates that are very similar to CF state but are actually distinct from them. More precisely, a strong short-range interaction is presented for electrons in a magnetic field [103]. We write the model interaction in terms of pseudopotentials, where the energy of a pair of particles depends on their relative angular momentum. On the disk geometry, we can write the exact eigenstates for the QPs, QHs, and neutral excitations, in addition to the incompressible FQH state at the Jain sequence of filling fraction.

We extend the interaction to spherical geometry where the numerics are convenient. We show that the low-energy spectra of model interaction for a spherical system at Jain sequence of filling fractions *i.e.* $\nu = n/(2np+1)$ is identical to the spectra of IQH system at $\nu^* = n$. This correspondence is accurate, not only for incompressible states but their charged and neutral excitations as well. Although the interaction requires rotational symmetry, we argue that, since the model interaction is short-ranged, boundary conditions in the torus and cylinder should not affect the local physics. This argument led us to extend the model interaction to torus and cylinder geometries [104]. The complication of writing matrix elements of the model interaction in torus and cylinder basis is solved using the Fourier transform of the interaction on the disk. In both torus and cylinder geometries, the low-energy spectra of the model interaction show a correspondence to the IQHE spectra similar to what could be shown in the case of spherical geometry. In the torus case, however, the spectra of model interaction for the system at filling $\nu = n/(2np+1)$ shows the characteristic $(2np+1)$-fold degeneracy, which is related to the topology of a torus. Thus, the model interaction describes FQHE at the Jain sequence of filling fractions across many system geometries.

One key feature of this model interaction is that it is exactly solvable in the disk and cylinder geometry [103]. Ansatz eigenfunctions written for disk can be directly generalized to the cylinder geometry. However, similar generalization does not work for compact geometry like a sphere and torus, the reasons for which are explained below.

Although the eigenfunctions of the model interaction were inspired by CF wavefunctions and most of their properties, like fractional charge and statistics of charged excitations, are identical, the two are qualitatively different. In exact eigenfunctions, the IQH state is prepared in the actual magnetic field B, and the Jastrow factor is modified such that guiding-center coordinates replace the position coordinates. The modified Jastrow factor increases the relative angular momentum of each pair of particles by $2p$ without changing their LL indices. The key difference is that the modified Jastrow factor increases the area of the IQH Hall droplet instead of increasing the magnetic field. The resultant increment in the flux quanta changes the filling fraction from ν^* to ν. The increment in the area might explain why the ansatz wavefunction in the disk does not generalize to the sphere and torus geometry.

Unlike planar geometries, the concept of a guiding center is not well-defined on a sphere. Instead, the sphere has two mutually commuting $SU(2)$ algebras [59]. The first operator, called guiding-center momentum $\boldsymbol{L}$, forms ladder operators for angular momentum while preserving the LL of the eigenstate. On the other hand, ladder operators associated to the second operator, called cyclotron momentum $\boldsymbol{S}$, change the flux quantum number as well as LL index of the eigenstate. In order to generalize the disk eigenfunction on sphere, we need to construct a Jastrow factor which increments the area of IQH Hall droplet without scattering particles in LLs. In sphere, increase in size is equivalent to increment in the flux which, as we saw, is always accompanied by a change in the LL index. This prohibits the direct generalization of disk ansatz to spherical geometry. In torus, just like the sphere, the direct generalization fails. This is because the resultant eigenfunction breaks boundary conditions. However, we could still construct eigenstates for a few QPs of 1/3 in spherical and torus geometry using simplifications in the disk ansatz [104].

Rotational symmetry can also be broken using mass anisotropy [69, 70]. Studying the extension of model interaction, including such mass anisotropy, will be interesting. In its current form, the model interaction describes FQHE at the Jain sequence of filling fraction, which only hosts Abelian excitations. Naturally, possible extensions to the model interaction which captures the physics of FQHE at non-Abelian states and parton states make an exciting study [74]. This has been achieved for the specific case of Pfaffian and its excitations.

In the second half of this thesis, we study properties of a generalization of the CF states called parton states [97]. In particular, we investigate these states' entanglement spectrum (ES), quantifying the entanglement between various system parts. Additionally, it was argued in Ref. [63] that the ES of quantum Hall wavefunctions has a one-to-one correspondence with its edge spectra. In this thesis, we develop and generalize the Monte Carlo technique introduced in Ref. [65, 81] to calculate the real-space entanglement spectra (RSES). Direct calculation of entanglement spectra is numerically intensive, and we can study only small systems ($\sim$ 24 particles). In addition, entanglement spectra are sensitive to finite-size effects, so methods that allow the study of larger systems are desired. We use the Monte Carlo method to calculate the RSES of simple non-Abelian parton states, namely unprojected Φ_2^2, Φ_2^3 and Φ_3^2 with a system as large as $\sim$ 100 particles. Ref. [83] argues that the edge-spectra of parton state Φ_n^k is described by the highest weight representation of $\widehat{su}(n)_k \times u(1)$ affine Lie algebra. Since RSES and edge-spectra of FQH states have a one-to-one correspondence, we present a non-trivial demonstration of this correspondence by comparing the RSES of parton state Φ_n^k with the highest weight representations of $\widehat{su}(n)_k$ affine Lie algebra.

To verify that the RSES computed using the MC method is indeed correct, we compare it to the RSES of the direct but inefficient method for the unprojected and projected 2/5 CF state [105]. Where the direct way takes hours or even days with hundreds of processors for small systems ($\sim$ 20 particles) [101], the efficient method not only produces the correct RSES for similar system sizes in a few minutes on a processor but much larger systems with $\sim$ 100 particles can also be studied (for the unprojected case). Unfortunately, operation of exact projection becomes exponentially cumbersome with an increasing number of particles in higher LLs *i.e.*, $n > 0$, which limits the application of the efficient MC method for projected FQH states. Based on a technique given by Jain-Kamilla for LLL projection [98, 99], we devise an approximate projection prescription that enables efficient RSES computation of projected CF state for much larger systems ($\sim$ 100 particles). By comparing the RSES of exactly and approximately projected 2/3 CF state, we verify that the approximate method indeed produces qualitatively similar RSES. Thus, the approximation presented here opens up a way to study RSES of projected CF states for much more extensive system sizes.

In our study of entanglement spectra, we have only included CF states corresponding to filling fractions $\nu = n/(2pn + 1)$ where $n,\ p$ are positive integers. There are FQH states with filling fractions $\nu = n/(2pn - 1)$ where the composite fermions are in a reduced field B^* which is antiparallel to the actual physical field B. Edge theory of such FQH state predicts the presence of backward-moving neutral modes [106, 107, 108], which are seen experimentally as well [109]. Our approximation for LLL projection in the computation of RSES is based on the Jain-Kamilla projection method, which only works for CF states with filling fractions $\nu = n/(2pn + 1)$. This projection method can be generalized for CF states with $\nu = n/(2pn - 1)$, which have a negative effective magnetic field [100]. Since RSES of FQH states has a one-to-one correspondence with its edge spectra, RSES for CF states with counter-propagating edge modes is expected to have interesting features. Thus, extending the approximation discussed in Ref. [105] for such CF states would be particularly interesting, when applied to reverse flux attached states. Our current attempt at doing this was made difficult by the poor efficiency of MC.

Lastly, a word on the computational tool that was invaluable in our work. Most of the exciting results in the study of model interaction would only be possible with the usage of massively parallelized exact diagonalization routines available in PETSc [110] and SLEPc libraries [111]. PETSc is a toolkit that collects classes and data structures for scalable scientific problems like finding eigenpairs and solving partial differential equations. It supports MPI and GPUs through CUDA, HIP, or OpenCL, as well as hybrid MPI-GPU parallelism. SLEPc is a software library of PETSc for solving large-scale sparse eigenvalue problems on parallel computers. Using these tools, we could explore the spectra of much larger systems with dimensions too large to be tackled with standard methods. The code allows reliable calculation of degenerate states, which were crucial in the study discussed in Chapter 2. Extending these codes to matrix free Krylov methods can very useful in tackling versatile problems related to FQHE and other quantum many-body systems.

References

[1] K. v. Klitzing, G. Dorda, and M. Pepper. New method for high-accuracy determination of the fine-structure constant based on quantized hall resistance. *Phys. Rev. Lett.*, 45:494–497, Aug 1980.

[2] J T Chalker and P D Coddington. Percolation, quantum tunnelling and the integer hall effect. *Journal of Physics C: Solid State Physics*, 21(14):2665, may 1988.

[3] R. Willett, J. P. Eisenstein, H. L. Störmer, D. C. Tsui, A. C. Gossard, and J. H. English. Observation of an even-denominator quantum number in the fractional quantum hall effect. *Phys. Rev. Lett.*, 59:1776–1779, Oct 1987.

[4] Jainendra K. Jain. *Composite Fermions*. Cambridge University Press, 2007.

[5] Steven M. Girvin. The quantum hall effect: Novel excitations and broken symmetries, 1999.

[6] Ady Stern. Anyons and the quantum hall effect—a pedagogical review. *Annals of Physics*, 323(1):204–249, 2008. January Special Issue 2008.

[7] Chetan Nayak, Steven H. Simon, Ady Stern, Michael Freedman, and Sankar Das Sarma. Non-abelian anyons and topological quantum computation. *Rev. Mod. Phys.*, 80:1083–1159, Sep 2008.

[8] J.M. Leinaas and J. Myrheim. On the theory of identical particles. *Il Nuovo Cimento B Series 11*, 37(1):1–23, 1977.

[9] Frank Wilczek. Quantum mechanics of fractional-spin particles. *Phys. Rev. Lett.*, 49:957–959, Oct 1982.

[10] N. Read and Dmitry Green. Paired states of fermions in two dimensions with breaking of parity and time-reversal symmetries and the fractional quantum hall effect. *Phys. Rev. B*, 61:10267–10297, Apr 2000.

[11] Gregory Moore and Nicholas Read. Nonabelions in the fractional quantum hall effect. *Nuclear Physics B*, 360(2):362–396, 1991.

[12] Vito W. Scarola, Kwon Park, and Jainendra K. Jain. Cooper instability of composite fermions. *Nature*, 406:863–865, 2000.

[13] G. Möller and S. H. Simon. Paired composite-fermion wave functions. *Phys. Rev. B*, 77:075319, Feb 2008.

[14] Yang Liu, C. G. Pappas, M. Shayegan, L. N. Pfeiffer, K. W. West, and K. W. Baldwin. Observation of reentrant integer quantum hall states in the lowest landau level. *Phys. Rev. Lett.*, 109:036801, Jul 2012.

[15] Yang Liu, D. Kamburov, S. Hasdemir, M. Shayegan, L. N. Pfeiffer, K. W. West, and K. W. Baldwin. Fractional quantum hall effect and wigner crystal of interacting composite fermions. *Phys. Rev. Lett.*, 113:246803, Dec 2014.

[16] Hangmo Yi and H. A. Fertig. Laughlin-jastrow-correlated wigner crystal in a strong magnetic field. *Phys. Rev. B*, 58:4019–4027, Aug 1998.

[17] Chia-Chen Chang, Gun Sang Jeon, and Jainendra K. Jain. Microscopic verification of topological electron-vortex binding in the lowest landau-level crystal state. *Phys. Rev. Lett.*, 94:016809, Jan 2005.

[18] Sudhansu S. Mandal, Michael R. Peterson, and Jainendra K. Jain. Two-dimensional electron system in high magnetic fields: Wigner crystal versus composite-fermion liquid. *Phys. Rev. Lett.*, 90:106403, Mar 2003.

[19] Alexander C. Archer, Kwon Park, and Jainendra K. Jain. Competing crystal phases in the lowest landau level. *Phys. Rev. Lett.*, 111:146804, Oct 2013.

[20] Jianyun Zhao, Yuhe Zhang, and J. K. Jain. Crystallization in the fractional quantum hall regime induced by landau-level mixing. *Phys. Rev. Lett.*, 121:116802, Sep 2018.

[21] V. J. Goldman, B. Su, and J. K. Jain. Detection of composite fermions by magnetic focusing. *Phys. Rev. Lett.*, 72:2065–2068, Mar 1994.

[22] J. H. Smet, D. Weiss, R. H. Blick, G. Lütjering, K. von Klitzing, R. Fleischmann, R. Ketzmerick, T. Geisel, and G. Weimann. Magnetic focusing of composite fermions through arrays of cavities. *Phys. Rev. Lett.*, 77:2272–2275, Sep 1996.

[23] J. H. Smet, S. Jobst, K. von Klitzing, D. Weiss, W. Wegscheider, and V. Umansky. Commensurate composite fermions in weak periodic electrostatic potentials: Direct evidence of a periodic effective magnetic field. *Phys. Rev. Lett.*, 83:2620–2623, Sep 1999.

[24] R. L. Willett, R. R. Ruel, K. W. West, and L. N. Pfeiffer. Experimental demonstration of a fermi surface at one-half filling of the lowest landau level. *Phys. Rev. Lett.*, 71:3846–3849, Dec 1993.

[25] W. Kang, H. L. Stormer, L. N. Pfeiffer, K. W. Baldwin, and K. W. West. How real are composite fermions? *Phys. Rev. Lett.*, 71:3850–3853, Dec 1993.

[26] D. R. Leadley, R. J. Nicholas, C. T. Foxon, and J. J. Harris. Measurements of the effective mass and scattering times of composite fermions from magnetotransport analysis. *Phys. Rev. Lett.*, 72:1906–1909, Mar 1994.

[27] R.R. Du, H.L. Stormer, D.C. Tsui, L.N. Pfeiffer, and K.W. West. Shubnikov-dehaas oscillations around v = 12 landau level filling factor. *Solid State Communications*, 90(2):71–75, 1994.

[28] C. Kittel and P. McEuen. *Introduction to Solid State Physics.* John Wiley & Sons, Limited, 2018.

[29] F Delahaye and B Jeckelmann. Revised technical guidelines for reliable dc measurements of the quantized hall resistance. *Metrologia*, 40(5):217, sep 2003.

[30] D. J. Thouless, M. Kohmoto, M. P. Nightingale, and M. den Nijs. Quantized hall conductance in a two-dimensional periodic potential. *Phys. Rev. Lett.*, 49:405–408, Aug 1982.

[31] F. D. M. Haldane. Fractional quantization of the hall effect: A hierarchy of incompressible quantum fluid states. *Phys. Rev. Lett.*, 51:605–608, Aug 1983.

[32] Tai Tsun Wu and Chen Ning Yang. Dirac monopole without strings: Monopole harmonics. *Nuclear Physics B*, 107(3):365–380, 1976.

[33] Tai Tsun Wu and Chen Ning Yang. Some properties of monopole harmonics. *Phys. Rev. D*, 16:1018–1021, Aug 1977.

[34] F. D. M. Haldane and E. H. Rezayi. Periodic laughlin-jastrow wave functions for the fractional quantized hall effect. *Phys. Rev. B*, 31:2529–2531, Feb 1985.

[35] Martin Greiter, Vera Schnells, and Ronny Thomale. Laughlin states and their quasiparticle excitations on the torus. *Phys. Rev. B*, 93:245156, Jun 2016.

[36] David Mumford. *Tata Lectures on Theta I.* Birkhäuser Boston, MA, 2007.

[37] B. I. Halperin. Quantized hall conductance, current-carrying edge states, and the existence of extended states in a two-dimensional disordered potential. *Phys. Rev. B*, 25:2185–2190, Feb 1982.

[38] R. B. Laughlin. Anomalous quantum hall effect: An incompressible quantum fluid with fractionally charged excitations. *Phys. Rev. Lett.*, 50:1395–1398, May 1983.

[39] J. K. Jain. Composite-fermion approach for the fractional quantum hall effect. *Phys. Rev. Lett.*, 63:199–202, Jul 1989.

[40] Songyang Pu, Ying-Hai Wu, and J. K. Jain. Composite fermions on a torus. *Phys. Rev. B*, 96:195302, Nov 2017.

[41] J. K. Jain. Incompressible quantum hall states. *Phys. Rev. B*, 40:8079–8082, Oct 1989.

[42] N. Read and E. Rezayi. Beyond paired quantum hall states: Parafermions and incompressible states in the first excited landau level. *Phys. Rev. B*, 59:8084–8092, Mar 1999.

[43] D. C. Tsui, H. L. Stormer, and A. C. Gossard. Two-dimensional magnetotransport in the extreme quantum limit. *Phys. Rev. Lett.*, 48:1559–1562, May 1982.

[44] B. I. Halperin. Statistics of quasiparticles and the hierarchy of fractional quantized hall states. *Phys. Rev. Lett.*, 52:1583–1586, Apr 1984.

[45] B. I. Halperin, Patrick A. Lee, and Nicholas Read. Theory of the half-filled landau level. *Phys. Rev. B*, 47:7312–7343, Mar 1993.

[46] Ady Stern. Non-abelian states of matter. *Nature*, 464(7286):187–193, Mar 2010.

[47] S. A. Trugman and S. Kivelson. Exact results for the fractional quantum hall effect with general interactions. *Phys. Rev. B*, 31:5280–5284, Apr 1985.

[48] J. K. Jain, S. A. Kivelson, and Nandini Trivedi. Scaling theory of the fractional quantum hall effect. *Phys. Rev. Lett.*, 64:1297–1300, Mar 1990.

[49] J. K. Jain. Theory of the fractional quantum hall effect. *Phys. Rev. B*, 41:7653–7665, Apr 1990.

[50] E. H. Rezayi and A. H. MacDonald. Origin of the $\nu = 2/5$ fractional quantum hall effect. *Phys. Rev. B*, 44:8395–8398, Oct 1991.

[51] Martin Greiter, Xiao-Gang Wen, and Frank Wilczek. Paired hall state at half filling. *Phys. Rev. Lett.*, 66:3205–3208, Jun 1991.

[52] Steven H. Simon, E. H. Rezayi, N. R. Cooper, and I. Berdnikov. Construction of a paired wave function for spinless electrons at filling fraction $\nu = 2/5$. *Phys. Rev. B*, 75:075317, Feb 2007.

[53] Ying-Hai Wu, Tao Shi, and Jainendra K Jain. Non-abelian parton fractional quantum hall effect in multilayer graphene. *Nano Letters*, 17(8):4643–4647, Aug 2017.

[54] Sumanta Bandyopadhyay, Li Chen, Mostafa Tanhayi Ahari, Gerardo Ortiz, Zohar Nussinov, and Alexander Seidel. Entangled pauli principles: The dna of quantum hall fluids. *Phys. Rev. B*, 98:161118R, Oct 2018.

[55] Sumanta Bandyopadhyay, Gerardo Ortiz, Zohar Nussinov, and Alexander Seidel. Local two-body parent hamiltonians for the entire jain sequence. *Phys. Rev. Lett.*, 124:196803, May 2020.

[56] Steven H Simon. Wavefunctionology: The special structure of certain fractional quantum hall wavefunctions. In *Fractional Quantum Hall Effects: New Developments*, pages 377–434. World Scientific, 2020.

[57] Rachel Wooten and Joseph Macek. Configuration interaction matrix elements for the quantum hall effect. *arXiv preprint arXiv:1408.5379*, 2014.

[58] *NIST Digital Library of Mathematical Functions.* http://dlmf.nist.gov/, Release 1.1.7 of 2022-10-15. F. W. J. Olver, A. B. Olde Daalhuis, D. W. Lozier, B. I. Schneider, R. F. Boisvert, C. W. Clark, B. R. Miller, B. V. Saunders, H. S. Cohl, and M. A. McClain, eds.

[59] Martin Greiter. Landau level quantization on the sphere. *Phys. Rev. B*, 83:115129, Mar 2011.

[60] Y. W. Suen, L. W. Engel, M. B. Santos, M. Shayegan, and D. C. Tsui. Observation of a $\nu = 1/2$ fractional quantum hall state in a double-layer electron system. *Phys. Rev. Lett.*, 68:1379–1382, Mar 1992.

[61] D. Maryenko, A. McCollam, J. Falson, Y. Kozuka, J. Bruin, U. Zeitler, and M. Kawasaki. Composite fermion liquid to wigner solid transition in the lowest landau level of zinc oxide. *Nature communications*, 9(1):1–6, 2018.

[62] M. Shayegan. private communication, 2020.

[63] Hui Li and F. D. M. Haldane. Entanglement spectrum as a generalization of entanglement entropy: Identification of topological order in non-abelian fractional quantum hall effect states. *Phys. Rev. Lett.*, 101:010504, Jul 2008.

[64] N. Regnault, B. A. Bernevig, and F. D. M. Haldane. Topological entanglement and clustering of jain hierarchy states. *Phys. Rev. Lett.*, 103:016801, June 2009.

[65] Iván D. Rodríguez, Simon C. Davenport, Steven H. Simon, and J. K. Slingerland. Entanglement spectrum of composite fermion states in real space. *Phys. Rev. B*, 88:155307, Oct 2013.

[66] X. G. Wen and A. Zee. Shift and spin vector: New topological quantum numbers for the hall fluids. *Phys. Rev. Lett.*, 69:953–956, Aug 1992.

[67] F. D. M. Haldane. Many-particle translational symmetries of two-dimensional electrons at rational landau-level filling. *Phys. Rev. Lett.*, 55:2095–2098, Nov 1985.

[68] M. Hermanns. Composite fermion states on the torus. *Phys. Rev. B*, 87:235128, Jun 2013.

[69] F. D. M. Haldane. Geometrical description of the fractional quantum hall effect. *Phys. Rev. Lett.*, 107:116801, Sep 2011.

[70] R.-Z. Qiu, F. D. M. Haldane, Xin Wan, Kun Yang, and Su Yi. Model anisotropic quantum hall states. *Phys. Rev. B*, 85:115308, Mar 2012.

[71] G. W. Stewart. A krylov–schur algorithm for large eigenproblems. *SIAM Journal on Matrix Analysis and Applications*, 23(3):601–614, 2002.

[72] M. Fremling, T. H. Hansson, and J. Suorsa. Hall viscosity of hierarchical quantum hall states. *Phys. Rev. B*, 89:125303, Mar 2014.

[73] E. Brown. Bloch electrons in a uniform magnetic field. *Phys. Rev.*, 133:A1038–A1044, Feb 1964.

[74] Koji Kudo, A. Sharma, G. J. Sreejith, and J. K. Jain. Exactly solvable hamiltonian for non-abelian quasiparticles. *Phys. Rev. B*, 107:115163, Mar 2023.

[75] G. J. Sreejith, A. Wójs, and J. K. Jain. Unpaired composite fermion, topological exciton, and zero mode. *Phys. Rev. Lett.*, 107:136802, Sep 2011.

[76] G. J. Sreejith, C. Tőke, A. Wójs, and J. K. Jain. Bipartite composite fermion states. *Phys. Rev. Lett.*, 107:086806, Aug 2011.

[77] G. J. Sreejith, Ying-Hai Wu, A. Wójs, and J. K. Jain. Tripartite composite fermion states. *Phys. Rev. B*, 87:245125, Jun 2013.

[78] Anushya Chandran, M. Hermanns, N. Regnault, and B. Andrei Bernevig. Bulk-edge correspondence in entanglement spectra. *Phys. Rev. B*, 84:205136, Nov 2011.

[79] J. Dubail, N. Read, and E. H. Rezayi. Real-space entanglement spectrum of quantum hall systems. *Phys. Rev. B*, 85:115321, Mar 2012.

[80] Iván D. Rodríguez and Germán Sierra. Entanglement entropy of integer quantum hall states. *Phys. Rev. B*, 80:153303, Oct 2009.

[81] Greg J. Henderson, G. J. Sreejith, and Steven H. Simon. Entanglement action for the real-space entanglement spectra of chiral abelian quantum hall wave functions. *Phys. Rev. B*, 104:195434, Nov 2021.

[82] Xiao-Gang Wen. Topological orders and edge excitations in fractional quantum hall states. *Advances in Physics*, 44(5):405–473, 1995.

[83] X. G. Wen. Non-abelian statistics in the fractional quantum hall states. *Phys. Rev. Lett.*, 66:802–805, Feb 1991.

[84] Philippe Di Francesco, P. Mathieu, and D. Senechal. *Conformal Field Theory*. Graduate Texts in Contemporary Physics. Springer, 1997.

[85] W. Zhu, S. S. Gong, F. D. M. Haldane, and D. N. Sheng. Fractional quantum hall states at $\nu = 13/5$ and $12/5$ and their non-abelian nature. *Phys. Rev. Lett.*, 115:126805, Sep 2015.

[86] M. Tanhayi Ahari, S. Bandyopadhyay, Z. Nussinov, A. Seidel, and G. Ortiz. Partons as unique ground states of quantum hall parent hamiltonians: The case of fibonacci anyons, 2022.

[87] Nicolas Regnault. 165Entanglement spectroscopy and its application to the quantum Hall effects. In *Topological Aspects of Condensed Matter Physics: Lecture Notes of the Les Houches Summer School: Volume 103, August 2014*. Oxford University Press, 01 2017.

[88] G. J. Sreejith, M. Fremling, Gun Sang Jeon, and J. K. Jain. Search for exact local hamiltonians for general fractional quantum hall states. *Physical Review B*, 98:235139, 12 2018.

[89] Iván D. Rodríguez, Steven H. Simon, and J. K. Slingerland. Evaluation of ranks of real space and particle entanglement spectra for large systems. *Phys. Rev. Lett.*, 108:256806, Jun 2012.

[90] Ajit C. Balram, Csaba Töke, A. Wójs, and J. K. Jain. Fractional quantum hall effect in graphene: Quantitative comparison between theory and experiment. *Phys. Rev. B*, 92:075410, Aug 2015.

[91] Ajit C. Balram and J. K. Jain. Nature of composite fermions and the role of particle-hole symmetry: A microscopic account. *Phys. Rev. B*, 93:235152, Jun 2016.

[92] S. M. Girvin and Terrence Jach. Formalism for the quantum hall effect: Hilbert space of analytic functions. *Phys. Rev. B*, 29:5617–5625, May 1984.

[93] Ajit C. Balram, Maissam Barkeshli, and Mark S. Rudner. Parton construction of a wave function in the anti-pfaffian phase. *Phys. Rev. B*, 98:035127, Jul 2018.

[94] Ajit C. Balram, Sutirtha Mukherjee, Kwon Park, Maissam Barkeshli, Mark S. Rudner, and J. K. Jain. Fractional quantum hall effect at $\nu = 2 + 6/13$: The parton paradigm for the second landau level. *Phys. Rev. Lett.*, 121:186601, Nov 2018.

[95] S. Kass, R. V. Moody, J. Patera, and R. Slansky. *Affine Lie Algebras, Weight Multiplicities, and Branching Rules (2 Volume Set).* University of California Press, hardcover edition, 7 1991.

[96] G. J. Sreejith, Shivakumar Jolad, Diptiman Sen, and Jainendra K. Jain. Microscopic study of the $\frac{2}{5}$ fractional quantum hall edge. *Phys. Rev. B*, 84:245104, Dec 2011.

[97] Abhishek Anand, Rushikesh A. Patil, Ajit C. Balram, and G. J. Sreejith. Real-space entanglement spectra of parton states in fractional quantum hall systems. *Phys. Rev. B*, 106:085136, Aug 2022.

[98] J. K. Jain and R. K. Kamilla. Composite fermions in the hilbert space of the lowest electronic landau level. *Int. J. Mod. Phys. B*, 11(22):2621–2660, 1997.

[99] J. K. Jain and R. K. Kamilla. Quantitative study of large composite-fermion systems. *Phys. Rev. B*, 55:R4895–R4898, Feb 1997.

[100] Gunnar Möller and Steven H. Simon. Composite fermions in a negative effective magnetic field: A monte carlo study. *Phys. Rev. B*, 72:045344, Jul 2005.

[101] A. Sterdyniak, A. Chandran, N. Regnault, B. A. Bernevig, and Parsa Bonderson. Real-space entanglement spectrum of quantum hall states. *Phys. Rev. B*, 85:125308, Mar 2012.

[102] Ivan D. Rodriguez, A. Sterdyniak, M. Hermanns, J. K. Slingerland, and N. Regnault. Quasiparticles and excitons for the pfaffian quantum hall state. *Phys. Rev. B*, 85:035128, Jan 2012.

[103] Abhishek Anand, J. K. Jain, and G. J. Sreejith. Exactly solvable model for strongly interacting electrons in a magnetic field. *Phys. Rev. Lett.*, 126:136601, Mar 2021.

[104] Abhishek Anand, Songyang Pu, and G. J. Sreejith. Torus geometry eigenfunctions of an interacting multi-landau-level hamiltonian. *Phys. Rev. B*, 107:195126, May 2023.

[105] Abhishek Anand and G. J. Sreejith. Real-space entanglement spectra of lowest landau level projected fractional quantum hall states using monte carlo methods. *Phys. Rev. B*, 107:085101, Feb 2023.

[106] Xiao-Gang Wen. Theory of the edge states in fractional quantum hall effects. *International Journal of Modern Physics B*, 06(10):1711–1762, 1992.

[107] Ana Lopez and Eduardo Fradkin. Effective field theory for the bulk and edge states of quantum hall states in unpolarized single layer and bilayer systems. *Phys. Rev. B*, 63:085306, Feb 2001.

[108] C. L. Kane, Matthew P. A. Fisher, and J. Polchinski. Randomness at the edge: Theory of quantum hall transport at filling $\nu = 2/3$. *Phys. Rev. Lett.*, 72:4129–4132, Jun 1994.

[109] Aveek Bid, N. Ofek, H. Inoue, M. Heiblum, C. L. Kane, V. Umansky, and D. Mahalu. Observation of neutral modes in the fractional quantum hall regime. *Nature*, 466(7306):585–590, JUL 29 2010.

[110] Satish Balay, Shrirang Abhyankar, Mark F. Adams, Steven Benson, Jed Brown, Peter Brune, Kris Buschelman, Emil M. Constantinescu, Lisandro Dalcin, Alp Dener, Victor Eijkhout, Jacob Faibussowitsch, William D. Gropp, Václav Hapla, Tobin Isaac, Pierre Jolivet, Dmitry Karpeev, Dinesh Kaushik, Matthew G. Knepley, Fande Kong, Scott Kruger, Dave A. May, Lois Curfman McInnes, Richard Tran Mills, Lawrence Mitchell, Todd Munson, Jose E. Roman, Karl Rupp, Patrick Sanan, Jason Sarich, Barry F. Smith, Stefano Zampini, Hong Zhang, Hong Zhang, and Junchao Zhang. PETSc Web page. `https://petsc.org/`, 2022.

[111] Vicente Hernandez, Jose E. Roman, and Vicente Vidal. SLEPc: A scalable and flexible toolkit for the solution of eigenvalue problems. *ACM Trans. Math. Software*, 31(3):351–362, 2005.